GEOLOGY, GEOCHEMISTRY AND TECTONIC IMPORTANCE OF THE HORSE COVE COMPLEX: A LATE NEOPROTEROZOIC IGNEOUS COMPLEX IN THE EASTERN AVALON ZONE, NEWFOUNDLAND

By

Diane R. Skipton, B. Sc. (Hons.)

A thesis submitted to the School of Graduate Studies in partial fulfillment of the requirements for the degree of Master of Science

Department of Earth Sciences

Memorial University of Newfoundland

July 2011

St. John's Newfoundland

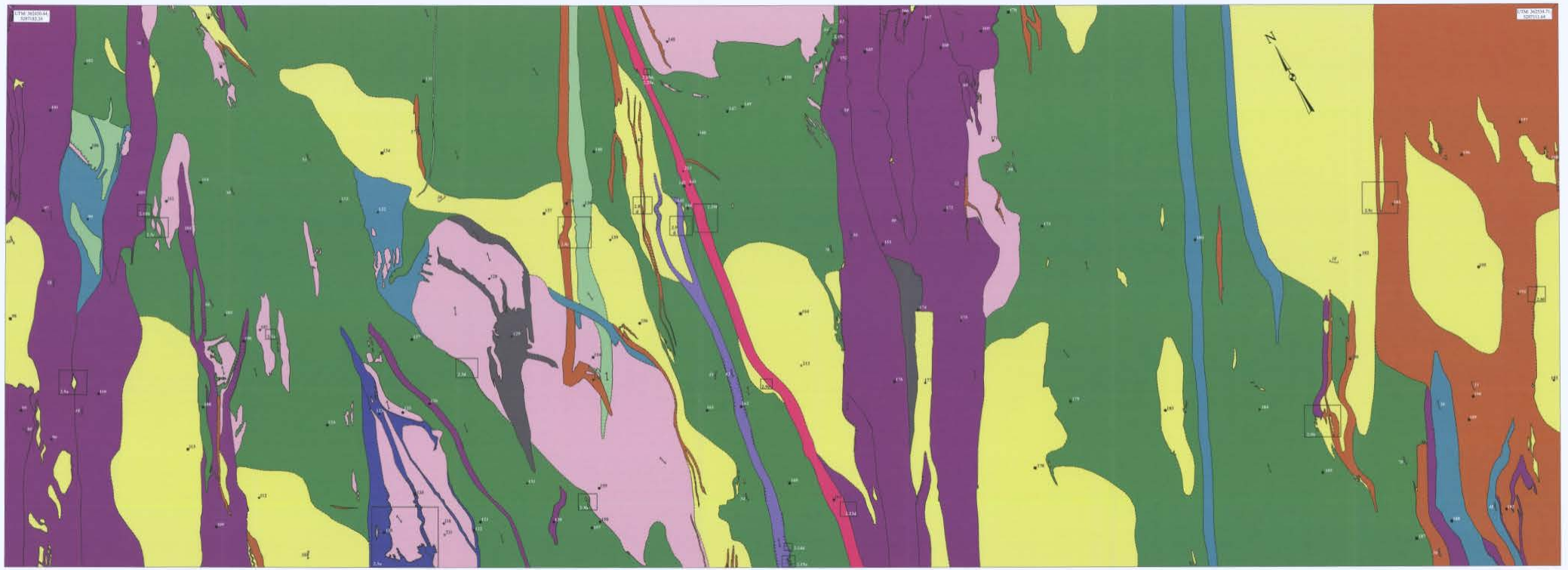

GEOLOGY OF THE HORSE COVE COMPLEX: MAP 1

by Diane Skipton

10 m

Projection: UTM Zone 22 (NAD 27 for Canada)

Legend

- Rhyolite Dykes
  Very fine-grained, white- weathering, locally foliated porphyritic dykes with light-green and dark-grey flow bands.
- Oxide-rich Basaltic Dykes
  Fine-grained, dark-grey- or white-weathering magnetic dykes.
- Oxide-rich Andesite Dykes
  Fine-grained, grey- or dark-purple-weathering magnetic dykes with compositional banding.
- Basaltic-Andesitic Dykes
  Fine-grained, dark-grey- and dark-brown-weathering dykes.
- Andesitic Dykes
  Fine-grained, light-brown-, light-grey- or light-greenish- green-weathering, feldspar-porphyritic dykes.
- Basaltic Dykes
  Fine-grained, dark-grey- and dark-brown-weathering, locally feldspar-porphyritic dykes.
- Hornblende Basaltic Dykes
  Fine-grained, dark-grey- and-dark-brown-weathering dykes.
- Hornblende-porphyritic Andesitic Dykes
  Fine-grained, dark brown- and light-brown-weathering dykes containing abundant feldspar and hornblende phenocrysts.
- Diorite
  Medium-grained, dark maroon-grey- to light greyish brown-weathering rocks with characteristic speckle- salt-and- pepper texture.
- Feldspar Porphyry
  White- or yellowish white-weathering rocks containing feldspar phenocrysts enclosed by a very fine-grained dark grey groundmass.
- Granodiorite
  Coarse-grained, white- to yellowish-white-weathering rocks, locally foliated or containing quartz veinlets.

- Defined contact
- Inferred contact (in outcrop)
- Inferred contact (covered)
- Intrusive (host rock)
- Defined shifted margin
- Cleavage with dip (B1f)
- Foliation (mineral lineation or cleavage trace)
- Joint set with dip (B1f)
- Joint set (dip unknown)
- 3.3a Plant location
- Representative sample
- Sample with thin section and whole-rock geochemistry data
- Sample with thin section (no geochemistry data)
- Geochronology sample

GEOLOGY OF THE HORSE COVE COMPLEX: MAPS 2 & 3, SECTIONS A-A' & C-C'

by Diane Skipton

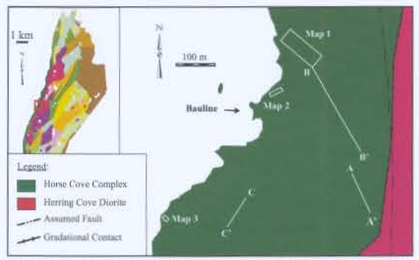

A map of the study area in and around the town of Bauline, showing the approximate locations of Maps 1, 2 and 3 and Sections A-A', B-B' and C-C'. The inset map shows the geology of the northeast coast of Conception Bay by Sparkes (2006), with the location of the study area marked in red.

Legend

- Rhyolitic Dykes — Very fine-grained, white-weathering, weakly feldspar-porphyritic dykes with light green and dark grey flow bands.
- Oxide-rich Basaltic Dykes — Fine-grained, dark grey- or black-weathering magnetic dykes.
- Oxide-rich Andesitic Dykes — Fine-grained, grey- or dark purple-weathering magnetic dykes with compositional banding.
- Basaltic-Andesitic Dykes — Fine-grained, dark grey- and dark brown-weathering dykes.
- Andesitic Dykes — Fine-grained, light brown, light grey- or light greyish- green-weathering, feldspar-porphyritic dykes.
- Basaltic Dykes — Fine-grained, dark grey- and dark brown-weathering, locally feldspar-porphyritic dykes.
- Hornblende Basaltic Dykes — Fine-grained, dark grey- and dark brown-weathering dykes. Dotted pattern indicates purplish-brown-weathering dykes with abundant (~10%) feldspar phenocrysts.
- Diorite — Medium-grained, dark brownish-grey- to light greyish-brown-weathering rocks with discontinuous epidotic veins and, locally, feldspar phenocrysts.
- Gabbro — Fine-to-medium-grained, dark brown-weathering rocks with rare feldspar phenocrysts and discontinuous epidotic veins.
- Feldspar Porphyry — White- or yellowish-white-weathering rocks containing feldspar phenocrysts enclosed by a very fine-grained dark grey groundmass.
- Granodiorite — Coarse-grained, white- to yellowish-white-weathering rocks, locally brecciated or containing quartz ribbons.
- Cover (vegetation, tidal pools, debris, etc.)
- Breccia
- Defined contact
- Inferred contact (in outcrop)
- Intrusion / Host rocks — Defined chilled margin
- Fault
- Cleavage with dip (RH)
- Foliation (mineral lineation or cleavage trace)
- 2.1c — Plate location
- Representative sample
- Sample with thin section and whole-rock geochemistry
- Sample with thin section (no geochemistry)
- Sample with geochemistry (no thin section)
- Geochronology sample

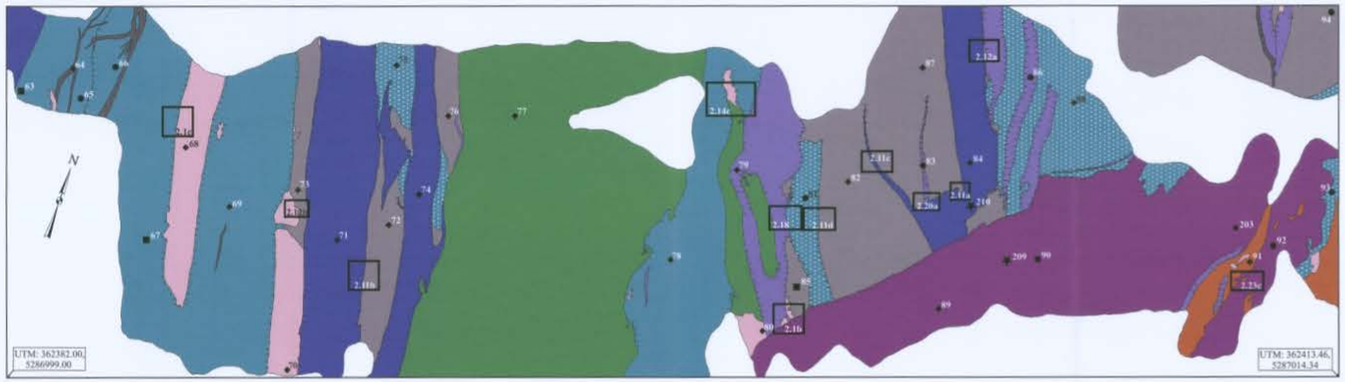

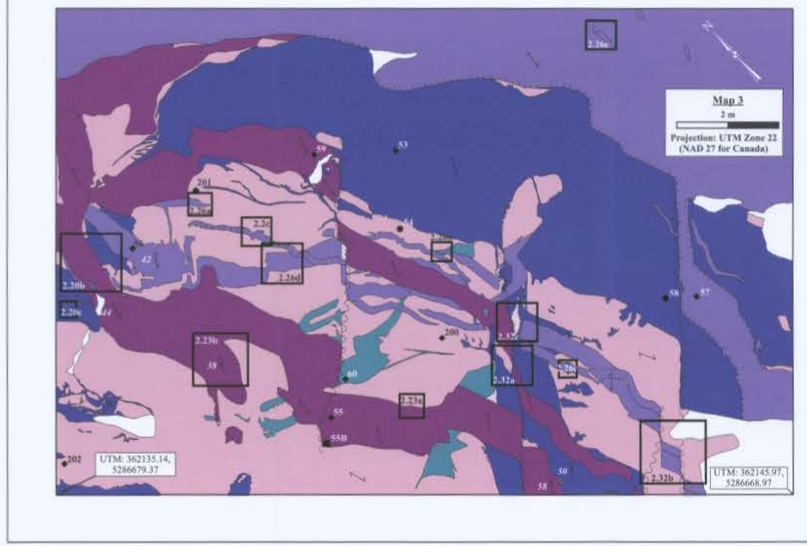

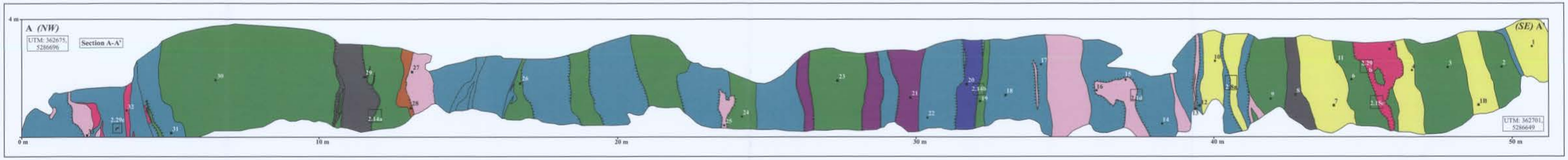

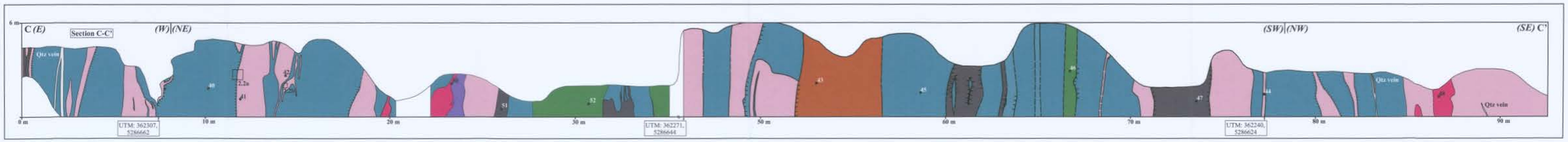

ABSTRACT

Mafic-to-felsic intrusive rocks of the Horse Cove Complex have been mapped in detail in the area surrounding Bauline on the east coast of Conception Bay in the Avalon Zone, Newfoundland. The Horse Cove Complex is characterized by a swarm of mafic-to-felsic dykes that coincide with the extrapolated trace of the Topsail Fault along the east coast of Conception Bay and are hosted by mafic submarine volcanic rocks and, locally, by diorite. In the Bauline area, the Horse Cove Complex is hosted by granodiorite, which has been dated at 625 ± 1.5 Ma using U/Pb zircon geochronology with the chemical abrasion thermal ionization mass spectrometry (CA-TIMS) method. This granodiorite is correlative to the felsic plutonic rocks of the Holyrood and White Hills intrusive suites, located south of Bauline, within and along the eastern margin of the Holyrood Horst. Based on detailed mapping and petrography in the Bauline area, the Horse Cove Complex has been divided into ten rock units. These rocks units include: feldspar porphyry, gabbro and diorite, which are the host rocks to the dyke swarm, and eight rock units that represent dykes of mafic-to-felsic composition. The Horse Cove Complex has been affected by greenschist-facies metamorphism, resulting in partial replacement of igneous mineral assemblages by greenschist-facies minerals, but igneous minerals and textures are still recognizable. The age of magmatism in the Horse Cove Complex has been bracketed by CA-TIMS U/Pb zircon ages of feldspar porphyry (580.6 ± 2.0 Ma) and an andesitic dyke (578.4 ± 2.3 Ma). Since field relationships indicate that these rock units represent the oldest and youngest datable rocks in the Complex, magmatism occurred over a period of 6.5 Ma or less: from 582.6 to 576.1 Ma, at maximum age limits. This age of

magmatism overlaps, within uncertainties, with several magmatic events on the NE Avalon Peninsula, including felsic volcanic and fine-grained intrusive rocks along the eastern margin of the Holyrood Horst and near Cape St. Francis. Based on lithogeochemistry, feldpsar porphyry and rhyolitic dykes in the Horse Cove Complex appear to represent volcanic arc magmatism and may be co-magmatic. The mafic to intermediate dykes and host rocks in the Horse Cove Complex are comprised of calc-alkaline and tholeiitic rocks that exhibit a range of compositions, from rocks with E-MORB-like geochemistry to rocks that are LREE-enriched and have negative Nb anomalies, comparable to subduction-related calc-alkaline basalts and andesites. There is an overall progression from rocks with E-MORB-like geochemistry to rocks with arc signatures, but exceptions exist due to the episodic emplacement and complex cross-cutting relationships of the dyke swarm. Seven rocks from the Horse Cove Complex, including a rhyolitic dyke and several mafic-to-intermediate rocks, have εNd values (at 580 Ma) ranging from +4.1 to +6.4. Thus, these rocks appear to have depleted mantle sources that have undergone various degrees of mixing or assimilation with older, LREE-enriched sources, such as continental crust and/or sediments in a subduction zone. The interpreted paleo-tectonic setting of the Horse Cove Complex is a back-arc basin environment, in which rocks with LREE-enriched mantle sources and subduction-contaminated sources were emplaced side-by-side and closely in time. The Horse Cove Complex may represent the last phase of subduction-related magmatism in the eastern Avalon Zone in Newfoundland prior to deep marine, deltaic and alluvial fan sedimentation during the late Neoproterozoic.

ACKNOWLEDGEMENTS

I would like to acknowledge numerous people who contributed to this project in a variety of ways. First of all, I would like to thank my supervisors, Greg Dunning and Greg Sparkes, for the opportunity of working on this project and for their generous guidance throughout the thesis. I am extremely fortunate to have had such dedicated and supportive supervisors, and I am very grateful for their constant encouragement and invaluable advice in all aspects of the project.

I extend thanks to George Jenner and Mark Wilson, together with several other professors in the MUN Department of Earth Sciences, for numerous helpful discussions. I am grateful to Michael Hutchings for his assistance in the field, Sherri Furey and Pam King for their detailed instruction and assistance in the geochronology laboratory and sample processing facilities at MUN, and Pauline Honarvar for her helpful advice regarding MapInfo. I would like to thank Alain Potrel and Sherri Furey at the MUN TIMS laboratory for obtaining Nd isotopic data and for explaining their analytical techniques. Thanks are also due to John Hanchar and Mark Wilson for providing geochemistry data from Cripple Cove and to Mark Cooper for providing U/Pb data from Cripple Cove. This project received financial assistance from the Buchans Fund of ASARCO Scholarship and from NSERC, in the form of a grant to Greg Dunning and an Alexander Graham Bell Canada Graduate Scholarship.

Finally, I would like to thank my family and friends for their support throughout the thesis, and my fiancé, Justin Emberley, for brightening my days and for his unwavering support and encouragement throughout this project, and always.

TABLE OF CONTENTS

LIST OF TABLES

LIST OF FIGURES

LIST OF PLATES

LIST OF ABBREVIATIONS

Minerals

Pl - plagioclase
Kfs - alkali feldspar
Fsp - feldspar (plagioclase or alkali)
Cpx - clinopyroxene
Opx - orthopyroxene
Hbl - hornblende
Act - actinolite
Epi - epidote
Chl - chlorite
Carb - carbonate
Ilm - ilmenite
Lx - leucoxene
Opq - opaque minerals (Fe-Ti oxides)
Ser - sericite
Ttn - titanite

Rock Units on the NE Avalon Peninsula

HIS - Holyrood Intrusive Suite
WHIS - White Hills Intrusive Suite
HHT - Hawke Hills Tuff
WMVS - White Mountain Volcanic Suite
MVS - Manuels Volcanic Suite
WHPC - Wych Hazel Pond Complex
HCD - Herring Cove Diorite
BHIS - Beaver Hat Intrusive Suite
HCC - Horse Cove Complex

Rock Types

N-MORB - normal mid-ocean ridge basalt
E-MORB - enriched mid-ocean ridge basalt
OIB - oceanic island basalt
IAT - island arc tholeiite
CAB - calc-alkaline basalt or andesite

LIST OF APPENDICES

CHAPTER 1: INTRODUCTION

1.1. Synopsis

The study area for this thesis is centered around the town of Bauline on the east coast of Conception Bay in the Avalon Zone in Newfoundland. This area offers the best exposure of the newly recognized and informally named Horse Cove Complex (HCC; Sparkes, 2006), which occurs over a distance of approximately 22 km along the east coast of Conception Bay. The HCC is a composite unit that consists of a mafic-to-felsic dyke swarm hosted by mafic volcanic rocks and diorite intrusions (Sparkes, 2006). Early studies of the geology of the Avalon Peninsula documented volcanic and felsic plutonic rocks of Neoproterozoic age and an overlying siliciclastic sequence that was deposited during the late Neoproterozoic (e.g. Rose, 1952; McCartney, 1967; Hsu, 1975; Williams and King, 1979; King, 1988, 1990). Recent studies investigated the geological complexity of the NE Avalon Peninsula (e.g. O'Brien *et al.,* 2001; Sparkes, 2005; Sparkes, 2006) and the resulting revised interpretation of the tectonic evolution of the Avalon Peninsula involved numerous periods of volcanic and plutonic activity and sedimentation during the late Neoproterozoic. However, due to the regional nature of previous studies, the geology of the HCC had not been examined in detail and its role in the tectonomagmatic history of the Avalon Peninsula is not known. Therefore, the aim of this thesis is to study the internal complexity, geochemistry and geochronological constraints of the HCC in order to determine its role in the tectonic history of the Avalon Zone in Newfoundland.

1.2. Geology of the Avalon Zone in Newfoundland

Subsequent to the amalgamation (ca. 1200-1000 Ma) and breakup (ca. 750-600 Ma) of the supercontinent of Rodinia, the ancient continent of Gondwana was formed by collisional and subduction-related events during ca. 650-520 Ma (e.g. Hoffman, 1991; Dalziel, 1997; Wingate and Giddins, 2000; Pisarevsky *et al.,* 2003, 2008). The formation of Gondwana is recorded in the rocks of the peri-Gondwanan terranes, which were located along or offshore of the northern margin of Gondwana into the Early Paleozoic (e.g. Theokritoff, 1979; O'Brien *et al.,* 1983, 1996; Murphy and Nance, 1989; Landing, 2005). Numerous peri-Gondwanan terranes were separated from the Gondwanan margin in the Late Cambrian-Early Ordovician, and were further displaced during the creation of the Appalachian-Caledonide-Variscan orogenic belt of present-day western Europe and eastern North America (e.g. van Staal *et al.,* 1998). One of these peri-Gondwanan terranes is the Avalon Terrane, or Avalonia, which occurs in numerous fault-bounded blocks from the Avalon Peninsula of Newfoundland to Nova Scotia, New Brunswick and New England (Williams, 1979). Although the pre-650 Ma tectonic setting of Avalonia is uncertain, subduction beneath the Gondwanan margin resulted in extensive arc-related magmatism in several parts of Avalonia during ca. 650-550 Ma (Nance and Murphy, 1994, 1996; Thompson *et al.,* 2007).

On the island of Newfoundland, remnants of the early Paleozoic Iapetus Ocean are preserved in the central mobile belt of the Appalachian orogen (Figure 1.1; Williams, 1964; Wilson, 1966). The central mobile belt is flanked by Proterozoic rocks that

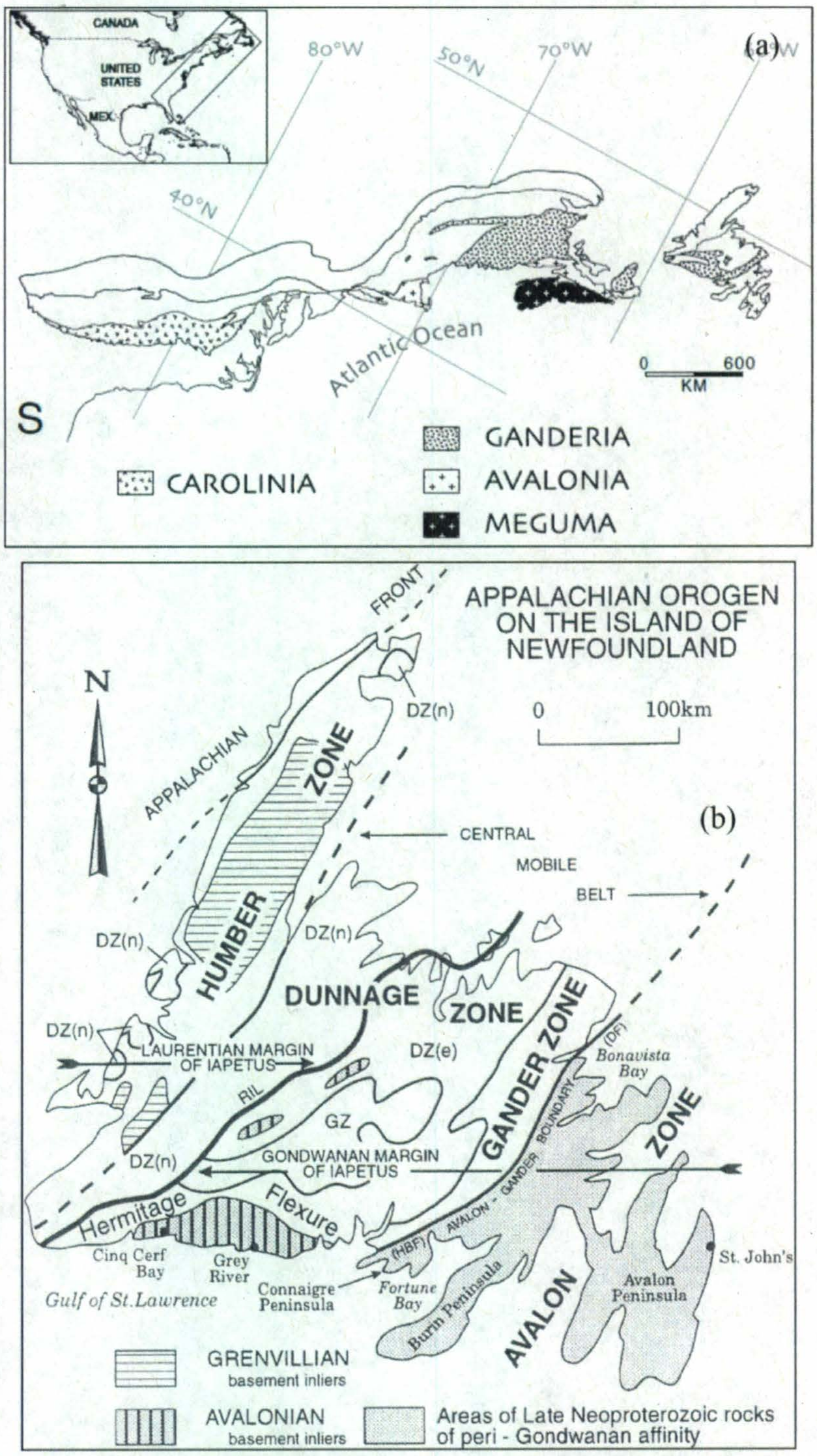

Figure 1.1: (a) Peri-Gondwanan terranes of the northern Appalachian orogen (Hibbard *et al.*, 2007). (b) Tectonic subdivision of the island of Newfoundland (O'Brien *et al.*,1996). DZ(e)=Dunnage Zone (Exploits subzone), DZ(n)=Dunnage Zone (Notre Dame subzone), GZ=Gander Zone, HBF=Hermitage Bay Fault, DF=Dover Fault, RIL=Red Indian Line.

represent the ancient Gondwanan and Laurentian margins of the Iapetus ocean (Williams, 1964; Wilson, 1966). The lithotectonically distinct Neoproterozoic rocks east of the central mobile belt are believed to have once been part of, or adjacent to, the ancient continent of Gondwana (Williams *et al.*, 1970), and are referred to as the Avalon Zone (Williams, 1979; O'Brien *et al.*, 1983). The Avalon Zone is separated from the outboard Iapetan continental margin rocks in the central mobile belt by the Dover-Hermitage Bay Fault (Figure 1.1; Blackwood and Kennedy, 1975). Basement inliers have been identified within the central mobile belt west of the Hermitage Bay Fault, including the basement block of the Hermitage Flexure and several smaller inliers in the Dunnage Zone (Dunning and O'Brien, 1989; Evans *et al.*, 1990; B. H. O'Brien *et al.*, 1991, 1993). These inliers were correlated with the Avalon Zone by Dunning and O'Brien (1989) but have been more recently correlated with Ganderia by some workers (e.g. Hibbard *et al.*, 2007; Lin *et al.*, 2007).

The Avalon Zone in Newfoundland is characterized by late Neoproterozoic (760-542 Ma) basement rocks, composed of volcanic, plutonic and clastic sedimentary rocks, covered by a terminal Neoproterozoic to early Ordovician sequence of fossiliferous siliciclastic rocks (e.g. Hutchinson, 1962; King, 1990; O'Brien *et al.*, 1996). Several tectonomagmatic and depositional events occurred in the Avalon Zone in Newfoundland during the late Neoproterozoic, at ca. 760 Ma, 730 Ma, 685-670 Ma, 640-590 Ma and 590-545 Ma (O'Brien *et al.*, 1996). The ca. 760, 730 and 685-670 Ma events are attributed to rifting and arc-related magmatism; the ca. 640-590 Ma events are interpreted to represent the development of volcanic arcs and arc-related basins; and magmatism and

sedimentation during ca. 590-545 is attributed to an orogenic and later extensional event (O'Brien *et al.,* 1996).

The Burin Group on the Burin Peninsula represents the oldest known subduction-related magmatism in the Avalon Terrane (Krogh *et al.,* 1988; Murphy *et al.,* 2008). The Burin Group consists of greenschist-facies submarine mafic rocks, including pillow basalt and breccia, as well as tuff and sedimentary rocks (Strong *et al.,* 1978). The Burin Group is intruded along most of its strike-length by a gabbroic sill, which has yielded an age of 763 ± 2 Ma (Krogh *et al.,* 1988). The plutonic and volcanic rocks in the Burin Group have predominantly oceanic tholeiitic chemistry, comparable to mafic igneous rocks of oceanic island arcs (Taylor, 1976; Strong and Dostal, 1980; Murphy *et al*., 2008).

A ca. 730 Ma felsic to intermediate volcanic succession followed the ca. 760 Ma arc-related magmatism of the Burin Group. Known as the Hawke Hills Tuff, these felsic volcanic rocks are preserved in the core of the Holyrood Horst on the Avalon Peninsula (Israel, 1998; O'Brien *et al.*, 2001). With a U/Pb zircon age of 729 ± 7 Ma (Israel, 1998), the Hawke Hills Tuff represents the oldest phase of felsic volcanism yet identified in the Avalonian terranes of the Appalachian orogenic belt (O'Brien *et al.,* 2001).

Arc-related, ca. 685-670 Ma old, predominantly felsic volcanic rocks occur in the Tickle Point Formation on the Connaigre Peninsula in the Avalon Zone in southern Newfoundland, where they are overlain by younger Neoproterozoic rocks (O'Brien *et al*., 1992, 1995). The Tickle Point Formation is dominantly composed of calc-alkaline rhyolite flows and pyroclastic rocks (O'Brien *et al.,* 1992). Two rhyolite samples from the Tickle Point Formation yielded U/Pb zircon ages of 682 ± 3 Ma (O'Brien *et al.,* 1994; Tucker, 1991, unpublished data) and 682.8 ± 1.6 Ma (Swinden and Hunt, 1991). In

addition, the Tickle Point Formation is intruded by co-magmatic granite and gabbro of the Furby's Cove Intrusive Suite. Granite from this suite yielded an age of 673 ± 3 Ma (O'Brien *et al.,* 1994; Tucker, 1991, unpublished data).

Rocks with ages between 685-670 Ma also occur in basement inliers south of the Hermitage Flexure in the Grey River and Cinq Cerf Bay areas. As noted above, these basement inliers have been correlated with Avalonia (Dunning and O'Brien, 1989) and, more recently, with Ganderia (Hibbard *et al.*, 2007; Lin *et al.,* 2007). A migmatite from the Grey River Gneiss was dated at 686 +33/-15 Ma (Dunning and O'Brien, 1989) and a granitic orthogneiss from the Cinq Cerf Gneiss was dated at 675 +12/-11 Ma (Valverde-Valquero *et al.,* 2006).

During about 640-590 Ma, the Avalon Zone in Newfoundland is characterized by plutonism, contemporaneous volcanic activity and related sedimentation. Although the magmatism and sedimentation are attributed to arc or arc-adjacent basin environments in a compressional tectonic setting, there is only minor structural and metamorphic evidence in eastern Newfoundland of a related collisional event (O'Brien *et al.,* 1996). Volcanic rocks from this period range in composition from basalt to rhyolite, and include calc-alkaline and tholeiitic rocks, as well as island-arc tholeiites associated with arc-rifting (Hussey, 1979; Sears, 1990; O'Brien *et al.,* 1990).

On the Avalon Peninsula, the calc-alkaline, dominantly felsic plutonic rocks of the Holyrood and White Hills instrusive suites have been dated at ca. 640-614 Ma by several workers (Krogh *et al.,* 1988; O'Brien *et al.,* 2001; Sparkes *et al.,* 2002; Sparkes, 2005) and intrude volcanic rocks of similar composition. Felsic volcanic rocks as young as 606

± 2 Ma (the Peak Tuff; Krogh *et al.,* 1988; O'Brien *et al.* 2001) are associated with this period of magmatism in the Holyrood Horst.

Calc-alkaline plutonism also occurred on the Connaigre Peninsula during 630-620 Ma, in the form of the mafic to felsic rocks of the Simmons Brook Intrusive Suite (Williams, 1971; O'Brien *et al.,* 1992), including a 621 ± 3 Ma granodiorite (Tucker, unpublished data; O'Brien *et al.,* 1994). These intrusions are hosted by the volcano-sedimentary rocks of the Connaigre Bay Group, from which a rhyolite was dated at 626 ± 3 Ma (Tucker, unpublished data; O'Brien *et al.,* 1994). Other ca. 620 Ma volcano-sedimentary sequences in the Avalon Zone in Newfoundland include the Love Cove Group in the Bonavista Bay area, and the conformably overlying Connecting Point Group in the Bonavista Bay and Burin Peninsula areas. A rhyolite from the Love Cove Group was dated at 620 ± 2 Ma (O'Brien *et al.,* 1989) and a tuff from the middle of the Connecting Point Group was dated at 610 ± 1 Ma (G. Dunning, unpublished data, in Dec *et al.,* 1992).

Turbiditic marine siliciclastic sedimentation occurred during the ca. 620-610 Ma period in association with arc-related volcanic activity. Examples of ca. 620-610 Ma marine siliciclastic successions include the Connaigre Bay Group (O'Brien *et al.,* 1995), the Connecting Point Group (Dec *et al.*, 1992), and the 621 +5/-4 Ma-and- younger (Israel, 1998) turbidity flows within the Holyrood Horst.

From about 590 to 545 Ma, the Avalon Zone in Newfoundland underwent extensive volcanism, plutonism and sedimentation. During about 590 to 570 Ma, widespread arc-related magmatism occurred in the Avalon terranes in arc or near-arc environments (O'Brien *et al.,* 1999). Magmatism during ca. 590-570 Ma resulted in calc-

alkaline and tholeiitic volcanic rocks, as well as calc-alkaline intrusions, whereas alkaline to peralkaline volcanic and intrusive rocks were produced during ca. 570 to 550 Ma (O'Brien *et al.,* 1996).

On the Burin Peninsula, the ca. 590-565 Ma Marystown Group represents a period of episodic and regionally extensive arc-related volcanism (O'Brien *et al.,* 1999). The Marystown Group is composed of calc-alkaline and tholeiitic subaerial volcanic rocks, with compositions ranging from basalt to rhyolite, and an upper sequence of continental alkaline basalts and rhyolites (O'Brien *et al.,* 1999). These rocks have been intruded by numerous plutons of ca. 580-570 Ma-aged granite, diorite and gabbro (O'Brien *et al.,* 1999). Dated rocks from the Marystown Group include a 620 +20/-7 Ma ash-flow tuff (Krogh et *al.,* 1988) and a ca. 572 Ma pyroclastic rock (Ketchum, unpublished data, 1998, in O'Brien *et al.,* 1999). Volcanism in the Marystown Group was followed by the marine volcano-sedimentary successions of the Musgravetown and Long Harbour Groups. Rhyolites from the base and top of the Long Harbour Group were dated at 568 ± 5 Ma and 552 ± 3 Ma, respectively (Tucker, unpublished data, O'Brien *et al.,* 1994) and rhyolite from the base of the Musgravetown Group was dated at 570 +5/-3 Ma (O'Brien *et al.,* 1989).

The Musgravetown Group extends to the Bonavista Bay area, where it is locally unconformable on the Connecting Point Group (O'Brien, 1993). The Louil Hills Intrusive Suite intrudes sub-Musgravetown Group strata in the Bonavista Bay area, and is interpreted to be comagmatic with Musgravetown Group volcanism (O'Brien *et al.,* 1989). The Louil Hills Intrusive Suite consists of peralkaline granite, dated at 572 +3/-2 Ma, related felsic dykes, gabbro and diabase dykes (O'Brien *et al.,* 1989).

On the Connaigre Peninsula, the ca. 570-550 deposition of the Long Harbour Group was accompanied by nearly coeval intrusions of granite, granodiorite, diorite and gabbro. These intrusions include the ca. 570 Ma Hardy's Cove, Harbour Breton and Grole intrusive suites, which intrude the Connaigre Bay Group and Tickle Point Formation (O'Brien *et al.,* 1995).

In the basement inlier in the Hermitage Flexure region, post-590 Ma magmatism includes a 584 +7/-6 Ma granodiorite that was emplaced into the Cinq Cerf Gneiss (Valverde-Vaquero *et al.,* 2006). The granodiorite intrusion coincided with deposition of the volcano-sedimentary Whittle Hill Sandstone and Third Pond Tuff sequence. This succession consists of conglomerate grading upward into sandstone and distal turbidites with felsic volcanic interbeds (Whittle Hill Sandstone) overlain by submarine mafic and felsic tuffs (Third Pond Tuff) (Dubé *et al.,* 1998). Felsic volcanic rocks from this sequence were dated at 583 +7/-3 Ma and 585 ± 5 Ma (Dubé *et al.,* 1998). These rocks were followed by ca. 576-562 Ma felsic intrusions of the Roti Intrusive Suite, which were emplaced along the tectonic boundary between the Whittle Hill Sandstone – Third Pond Tuff sequence and the Cinq Cerf Gneiss (O'Brien, 1987, 1988; O'Brien *et al*., 1991; Dunning and O'Brien, 1989).

Post-590 Ma magmatic events on the Avalon Peninsula include the arc-related, subaerial, mainly felsic volcanic rocks of the Manuels Volcanic Suite, which were deposited at about 584 Ma along the eastern margin of the Holyrood Horst (Sparkes, 2005). The ca. 582-and-younger marine siliciclastic strata and submarine mafic volcanic rocks of the Wych Hazel Pond Complex occur along the eastern margin of the Holyrood Horst and along the east coast of Conception Bay (Sparkes, 2006). These rocks are

overlain by the shallowing-upward siliciclastic sequence of the Conception, St. John's and Signal Hill Groups, which record a transition from a deep marine to a deltaic environment and then to an alluvial fan setting (King, 1990). The 565 ± 3 Ma age of a tuff bed near the top of the Conception Group (G. Dunning, 1988, unpublished data; Benus, in King 1988) provides the older age limit on the St. John's and Signal Hill Groups.

1.3. Overview of the Geology of the Avalon Peninsula

Major lithostratigraphic subdivisions of the Avalon Peninsula were carried out by early geological studies, including those of Jukes (1843), Murray (1869), Murray and Howley (1881), Bell (1892), Walcott (1900), Howley (1907) and Buddington (1916). Subsequent, regional-scale geological studies of the Avalon Peninsula include the maps and reports of Rose (1952), Hutchinson (1953), McCartney (1967), Hsu (1975), Williams and King (1979) and King (1988, 1990). As shown by Figure 1.2, the Avalon Peninsula consists of Neoproterozoic volcanic, sedimentary and plutonic rocks, locally unconformably overlain by a Cambrian to earliest Ordovician sedimentary cover sequence.

The Avalon Peninsula has undergone a southward-plunging, north-south-trending regional uplift, referred to as the Holyrood Horst (McCartney, 1969; O'Brien *et al.*, 2001). This structural feature divides the Avalon Peninsula into the lithotectonically distinct western, central and eastern blocks (Papezik, 1969, 1970). The centre of the Holyrood Horst is composed of subaerial felsic and mafic volcanic rocks of late Neoproterozoic age (ca. 730 to 580 Ma; O'Brien *et al.*, 1997, 2001), which were once

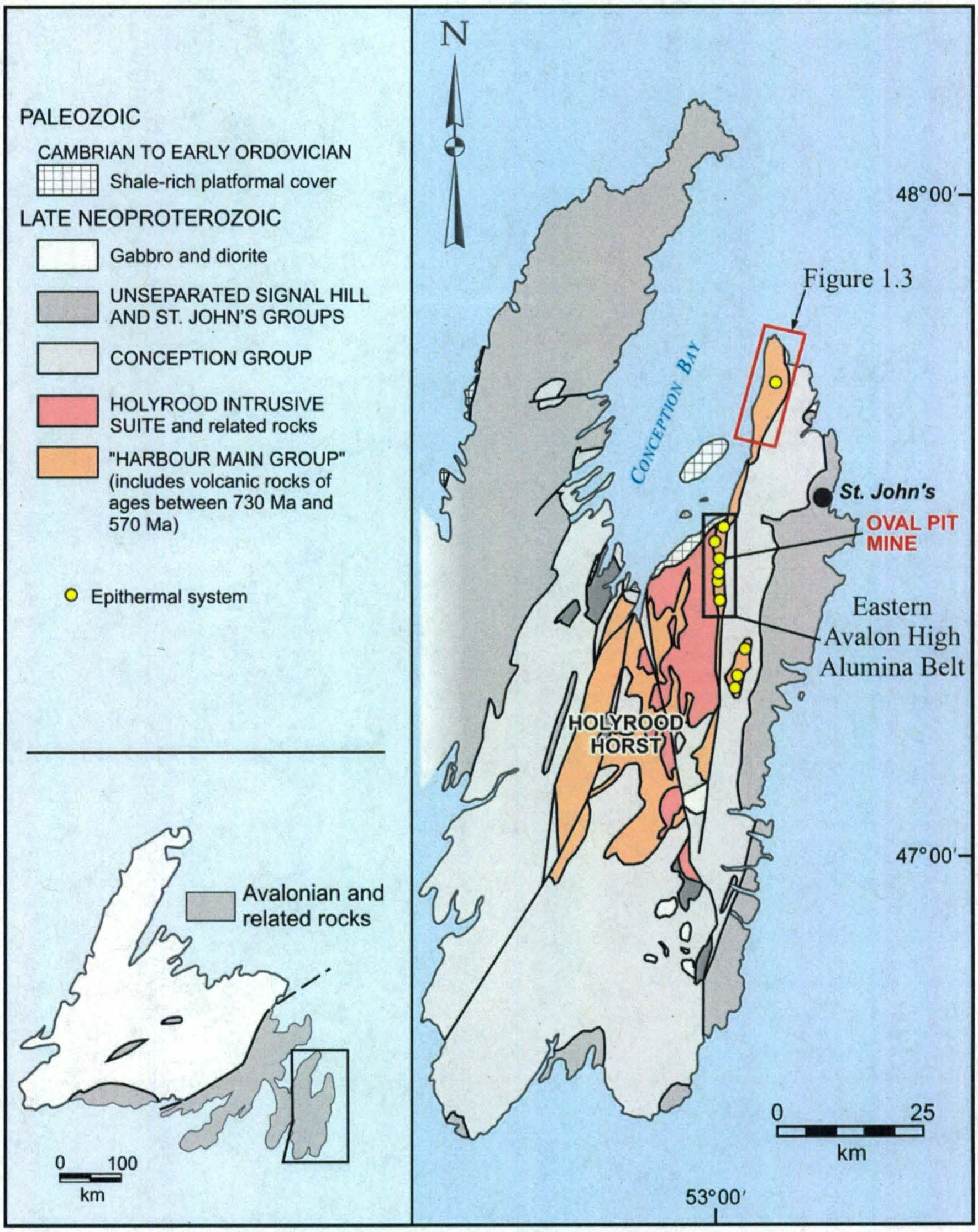

Figure 1.2: Regional geology of the Avalon Peninsula, showing the locations of high- and low-sulphidation style epithermal alteration systems, from Sparkes *et al.* (2005). The area shown in Figure 1.3 is outlined in red.

considered to be part of the Harbour Main Group of Rose (1952). Also within the Holyrood Horst are ca. 620 Ma felsic intrusive rocks, referred to as the Holyrood Intrusive Suite by King (1988) and the coeval White Hills Intrusive Suite of Sparkes *et al.* (2005). Adjacent to the Holyrood Horst are younger siliciclastic rocks of Neoproterozoic age, including the turbiditic Conception Group, the basinal-deltaic St. John's Group and the molasse-like Signal Hill Group (King, 1990). These rocks are overlain by remnants of a Cambrian-Ordovican platformal cover sequence that contain Atlantic-realm trilobites (King, 1990).

1.4. Geology of the NE Avalon Peninsula

1.4.1. Previous Work

In early geological studies of the Avalon Peninsula, the Neoproterozoic volcanic rocks were considered a stratigraphically continuous volcanic sequence, and were grouped under the Harbour Main Group of Rose (1952). The plutonic rocks in the region of the Holyrood Horst were believed to be coeval with the volcanic rocks, and were grouped together as the Holyrood Batholith (Rose, 1952), the Holyrood Plutonic Series (McCartney, 1967) or the Holyrood Intrusive Suite (King, 1988). In addition, siliciclastic rocks both inside and outside the Holyrood Horst were included in the Conception Group, forming the basal strata of the shoaling-upward succession of the Conception, St. John's and Signal Hill groups. However, several workers (e.g. Rose, 1952; O'Brien *et al.*, 2001) recognized conflicting geological relationships in earlier interpretations, and suspected that the Neoproterozoic succession on the Avalon Peninsula was formed by numerous periods of volcanism, sedimentation and plutonism over considerable time. As noted by

O'Brien *et al.* (2001), this model was supported by the complex and prolonged magmatic and lithostratigraphic evolution of western portions of the Avalon Zone in Newfoundland during the late Proterozoic (e.g. O'Brien *et al.,* 1995).

To investigate the Neoproterozoic rocks on the Avalon Peninsula in more detail, a bedrock mapping program was carried out in 2000 by the Geological Survey of Newfoundland and Labrador, at 1:50 000 scale, on the east-central Avalon Peninsula (NTS map areas 1N/3, 6, 7 and 11). The results of this mapping and corresponding geochronological data, reported in O'Brien *et al.* (2001), began a major revision of existing interpretations of the plutonic and volcano-stratigraphic development of the Avalon Peninsula.

East of the Topsail Fault, the Harbour Main Group was lithostratigraphically subdivided by King (1990) into the St. Phillips, Princes Lookout and Portugal Cove formations. O'Brien *et al.* (2001) divided the Neoproterozoic volcanic rocks west of the Topsail Fault into six regionally mappable units. These units are not only lithostratigraphically distinct, but their range in absolute age is about 160 Ma (O'Brien *et al.*, 2001). From oldest to youngest, they are: Hawke Hills Tuff, Triangle Andesite, Peak Tuff, Blue Hills Basalt, Manuels Volcanic Suite (MVS) and Wych Hazel Pond Complex (WHPC). Dated at 729 ± 7 Ma (Israel, 1998), the Hawke Hills Tuff represents the oldest known rock unit on the Avalon Peninsula. Subaerial rocks in the MVS host high-sulphidation style, pyrophyllite-diaspore alteration and low-sulphidation style, Au-Ag mineralization (e.g. O'Brien *et al.*, 1998). The ash-flow tuffs that host the pyrophyllite deposit in the Oval Pit Mine near Manuels were dated at 584 ± 2 Ma (later revised to 584

± 1 Ma by Sparkes *et al.*, 2005), providing an older age limit on the high-sulphidation system in the MVS (O'Brien *et al.,* 2001).

O'Brien *et al.* (2001) also determined that marine, turbiditic sedimentary rocks that are preserved in synclinal keels within the Holyrood Horst are older than the Neoproterozoic volcanic succession, and cannot be correlated with the Conception Group. On the east shore of Holyrood Bay, there is a conglomerate bed that contains granite clasts at the base of the marine sedimentary rocks. A rhyolitic tuff that overlies this unconformity was dated at 621 +5/-4 Ma (Israel, 1998), which indicates that the marine succession is up to 40 Ma older than the Neoproterozoic volcanic sequence (O'Brien *et al.,* 2001).

O'Brien *et al.* (2001) separated the Holyrood Intrusive Suite (HIS) of King (1988) into several distinct plutons according to age and lithology. These include, from oldest to youngest: 640 Ma monzonites, 635 – 630 Ma quartz-feldspar porphyries; 625 – 620 Ma quartz-rich granites and hydrothermally-altered post-620 Ma felsic intrusions. Historically, HIS magmatism was viewed as the heat source responsible for the development of epithermal alteration systems in the MVS (e.g. Rose, 1952; McCartney, 1967, 1969; Hughes and Brückner, 1971). However, the emplacement of these magmas pre-dated the ca. 585 Ma ash-flow tuffs that host the high-sulphidation style alteration system. Therefore, the heat that fuelled the epithermal systems cannot be attributed to the HIS, and must have been provided by younger magmatism (O'Brien *et al.,* 2001).

A study of the timing and setting of the epithermal systems and their relationship to gold mineralization on the eastern margin of the Holyrood Horst in the Eastern Avalon High Alumina Belt was carried out as a M. Sc. thesis by G. Sparkes (2005). The results

of this work, together with data from previous studies of the east-central Avalon Peninsula by the Geological Survey of Newfoundland and Labrador, are reported in Sparkes (2005) and Sparkes *et al.* (2004, 2005). This study also determined U/Pb zircon ages for nine different rock units along the eastern margin of the Holyrood Horst and developed a revised interpretation of the tectonomagmatic evolution of the Eastern Avalon High Alumina Belt.

The age of a granite from the HIS was found to be 622.5 ± 1.3 Ma (Sparkes *et al.*, 2005; modified from O'Brien *et al.,* 2001), in agreement with previously determined ages of 622 ± 2 Ma (Sparkes *et al.*, 2002) and 620 ± 2 Ma (Krogh *et al.*, 1988) from granites elsewhere in the suite.. On the eastern margin of the Holyrood Horst, monzonite, porphyry and silica-altered pyritic granite were assigned to the White Hills Intrusive Suite (WHIS), which shares a faulted or inferred intrusive contact with the HIS (Sparkes *et al.*, 2004; Sparkes, 2005). Sparkes *et al.* (2005) determined several U/Pb zircon ages in the WHIS, ranging from 625 ± 2.5 Ma to 614 ± 2 Ma, demonstrating that magmatism in the WHIS was coeval with much of the magmatism in the HIS.

In addition, Sparkes *et al.* (2005) reported U/Pb age constraints on the regional high- and low-sulphidation style epithermal systems. The older age limit to the high-sulphidation system was provided by the 584 ± 1 Ma crystallization age of a felsic volcanic rock from the MVS, collected from the core of the alteration zone in the Oval Pit Mine (O'Brien *et al.,* 2001; revised by Sparkes *et al.*, 2005). The advanced argillic alteration zone is overlain by sedimentary rocks belonging to the WHPC, which contain clasts of undeformed pyrophyllite-diaspore alteration (Sparkes *et al.*, 2005). A younger age limit of 582 ± 1.5 Ma for the high-sulphidation style alteration was determined by

Sparkes *et al.* (2005), from an unaltered pumiceous tuff that overlies the basal conglomerate of the WHPC. Thus, the formation, uplift and erosion of the high-sulphidation system occurred from ca. 585 to 580.5 Ma (Sparkes *et al.*, 2005).

A crystal rich ash-flow tuff provided the older age limit for the low-sulphidation style alteration system, at 582 ± 4 Ma (Sparkes *et al.*, 2005). The low-sulphidation style epithermal system is believed to have ceased by the early Cambrian, which is the age of fossils found in overlying platformal sedimentary rocks that contain low-sulphidation style epithermal clasts (Sparkes *et al.*, 2005).

U/Pb geochronological work by Sparkes *et al.* (2005) and earlier studies (e.g. O'Brien *et al.*, 2001) demonstrated that the ca. 625 to 620 Ma magmatism of the HIS and associated WHIS pre-dated the development of the high-sulphidation style epithermal system between 585 to 580.5 Ma. However, younger magmatism exists in the region, in the form of feldspar porphyry intrusions hosted by sedimentary rocks of the WHPC that overlie the 582 ± 1.5 Ma pumiceous tuff above the high-sulphidation style epithermal system (Sparkes, 2005). One such intrusion from the eastern margin of the Holyrood Horst, east of Manuels River, was dated by Sparkes (2005) at 585 ± 5 Ma. This age overlaps with the 582 ± 4 Ma eruption age of the ash-flow tuff that hosts low-sulphidation veining. Therefore, the magmatism that resulted in feldspar porphyry intrusions may be linked to the low-sulphidation alteration system (Sparkes *et al.*, 2005). Nevertheless, the source of heat and fluid for the high-sulphidation style alteration system remains uncertain.

Sparkes *et al.* (2005) recognized the potential for Au-bearing low-sulphidation epithermal vein systems on both the east and west margins of the Holyrood Horst,

particularly in areas with major faults, and/or regions that host post-620 Neoproterozoic porphyry intrusions. In part to evaluate the potential for mineralization, the Geological Survey of Newfoundland and Labrador embarked on a 1:25 000-scale regional mapping program during the summer of 2005. The study area is approximately 38 X 6 km, and extends along the east coast of Conception Bay, from Topsail northeast to Cape St. Francis. Another goal of this mapping project was to determine the northeastern extent of the geological units defined by O'Brien *et al.* (2001) west of the Topsail Fault.

The results of this project were reported in Sparkes (2006), together with updated mapping, and the northern portion of this map is shown in Figure 1.3. Sparkes (2006) confirmed that many of the units described by O'Brien *et al.* (2001) and Sparkes (2005) extend across the Topsail Fault up to Cape St. Francis, including the subaerial felsic volcanic rocks of the White Mountain Volcanic Suite, the felsic plutonic rocks of the HIS and the sedimentary and submarine mafic volcanic rocks of the WHPC.

Along the northeast coast of Conception Bay, the sedimentary and epidote-rich mafic volcanic rocks of the WHPC host diorite intrusions, informally-named the Herring Cove Diorite (HCD) by Sparkes (2006). In addition, the newly-recognized and informally named Horse Cove Complex (HCC) (Sparkes, 2006) consists of a swarm of mafic to felsic dykes hosted by the WHPC and, locally, by the HCD. The HCC extends along the east coast of Conception Bay, coincident with the extrapolated trace of the Topsail Fault, and corresponds to the St. Phillips Formation in the Harbour Main Group of King (1990). The youngest magmatism documented by Sparkes (2006) is that of the gabbroic intrusions of the Beaver Hat Intrusive Suite (BHIS). These intrusions display a close spatial association with the regional trace of the Topsail Fault. The BHIS locally

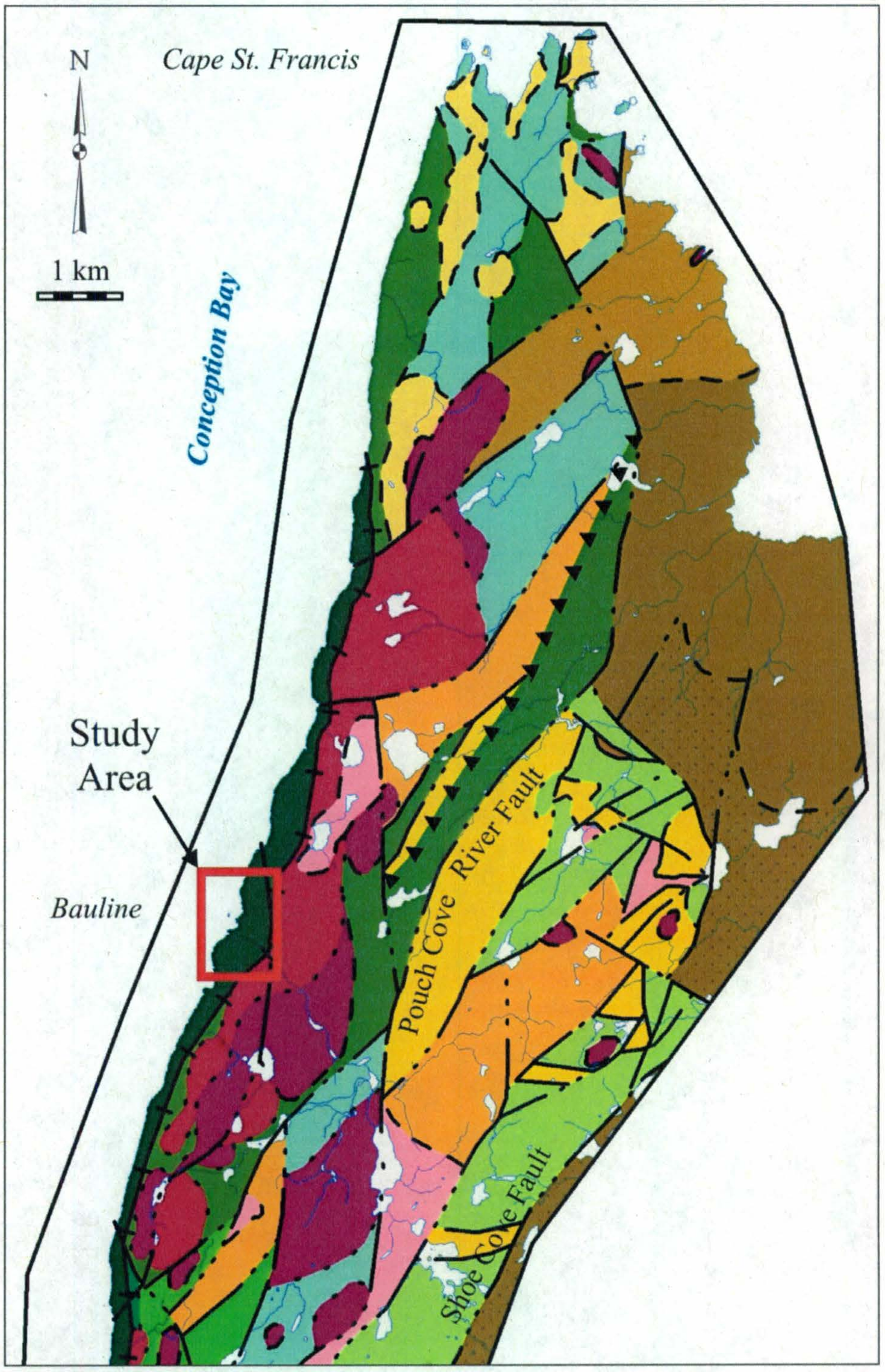

Figure 1.3: Geology of the Cape St. Francis area on the NE Avalon Peninsula in Newfoundland (Sparkes, 2006). The study area for this thesis is outlined in red.

Late Neoproterozoic

Beaver Hat Intrusive Suite

Fine- to coarse-grained, massive gabbro

Conception Group

Mannings Hill Member: Grey to dark green, medium- to coarse-grained sandstone and interbedded siltstone with minor chert

Torbay Member: Dark green, medium-grained sandstone, locally interbedded with Mannings Hill and Bauline Line Members; dotted pattern indicates siltstone interbedded with brown-weathering sandstone

Horse Cove Complex

Mafic to felsic swarm within submarine mafic volcanic rocks, volcaniclastic sandstone and diorite

Herring Cove Diorite

Fine- to medium-grained, massive diorite

Wych Hazel Pond Complex

Hematite-rich massive and pillowed basalt with rafts of siltstone and sandstone

Epidote-rich massive to locally-pillowed basalt

Siltstone interbedded with sandstone and minor pumiceous tuff

Flow-banded rhyolite

Holyrood Intrusive Suite

Pink-white-green-weathering, equigranular to quartz-phyric granite

White Mountain Volcanic Suite

Crystal-rich lapilli tuff

Rhyolite and minor fiamme-bearing ash-flow tuff

Geological contact (defined, approximate, assumed, gradational)

Fault (defined, approximate, assumed)

Thrust fault (approximate)

Figure 1.3 (continued): Legend for the regional geological map of the NE Avalon Peninsula (Sparkes, 2006).

intrudes the Mannings Hill Member of the late Neoproterozoic Conception Group, which is the stratigraphically highest unit exposed in the study area of Sparkes (2006). The BHIS is the youngest intrusive event yet identified on the NE Avalon Peninsula.

Sparkes (2006) acknowledged the ca. 580 Ma or younger HCD as a possible heat source for the low-sulphidation style epithermal system east of the Topsail Fault, since other candidates either pre-date or post-date the development of the alteration system. In addition, the occurrence of Au-bearing chalcedonic silica veins in the White Mountain Volcanic Suite east of the Topsail Fault illustrates the broad extent of low-sulphidation style alteration (Sparkes, 2006).

1.4.2. Summary of the magmatic and stratigraphic evolution of the NE Avalon Peninsula

The current interpretation of the tectonomagmatic development of the NE Avalon Peninsula is summarized in O'Brien *et al.* (2001), Sparkes (2005), Sparkes *et al.* (2005) and Sparkes (2006). The oldest rocks in the region are represented by the ca. 730 Ma felsic to intermediate volcanic succession of the Hawke Hills Tuff, which occupies the central and western portions of the Holyrood Horst. These rocks are bounded by younger intrusions that have been grouped into the HIS, including monzonite (640 ± 2 Ma; O'Brien *et al.,* 2001) and quartz-feldspar porphyry (631 ± 2 Ma; Krogh *et al.,* 1988). The Hawke Hills Tuff is associated with the Triangle Andesite, the Peak Tuff and the Blue Hills Basalt. The minimum age of the Triangle Andesite is provided by the 640 ± 2 Ma U/Pb age (O'Brien *et al.,* 2001) of a cross-cutting monzonitic pluton. Felsic volcanic rocks in the Peak Tuff provided an age of 606 ± 2 Ma (Krogh *et al.,* 1988; O'Brien *et al.,*

2001), which also represents the lower age limit of the overlying Blue Hills Basalt. On the eastern margin of the Holyrood Horst, an ash-flow tuff of the White Mountain Volcanic Suite yielded an age of 616 ± 2 Ma (Sparkes, 2005).

The most widespread plutonism in the NE Avalon region consists of quartz-rich granite of the HIS, which occupies much of the Holyrood Horst. Rocks from this pluton have been dated at 620 ± 2 Ma (Krogh *et al.,* 1988), 622 ± 2 Ma (Sparkes *et al.,* 2002) and 622.5 ± 1.3 Ma (O'Brien *et al.,* 2001; modified by Sparkes, 2005). The ca. 620 Ma intrusion of the HIS is believed to have driven hydrothermal alteration and related, syn-magmatic Au-bearing hydrothermal breccias (O'Brien *et al.,* 1998; Sparkes *et al.,* 2002). Several similarly-aged felsic plutonic rocks were dated in the WHIS on the eastern margin of the Holyrood Horst. These rocks include monzonite, granite and quartz-feldspar porphyry, which range in age from 625 ± 2.5 Ma to 614 ± 2 Ma (Sparkes, 2005). Together, the volcanic and plutonic rocks in the region of the Holyrood Horst represent ongoing plutonic and volcanic activity in an arc setting (King, 1988; Sparkes, 2005) from about 640 Ma to 606 Ma. Since the ca. 730 Ma Hawke Hills Tuff is locally intruded by HIS plutonic rocks, it is believed to represent the volcanic covering to subsequent volcano-plutonic arc magmatism (Sparkes, 2005).

Marine siliciclastic rocks appear to have been deposited in the region of the Holyrood Horst after the Hawke Hills Tuff and approximately coeval with the ca. 620 Ma magmatism of the HIS (O'Brien *et al.,* 2001). These turbiditic strata lie unconformably on the Hawke Hills Tuff and share either intrusive or unconformable contacts with plutonic rocks, and a rhyolitic tuff bed above a basal unconformity was dated at 621 +5/-4 Ma (Israel, 1998).

Younger subaerial, predominantly felsic volcanic rocks and ash-flow tuffs of the MVS occur along the eastern margin of the Holyrood Horst (Sparkes, 2005). A rhyolite that was collected from a zone of advanced argillic alteration in the MVS was dated at 584 ± 1 Ma, and an ash-flow tuff that contains low-sulphidation veins yielded an age of 584 ± 4 Ma (Sparkes, 2005). Thus, in the region of the Holyrood Horst, there was a gap in magmatism between the volcano-plutonic arc magmatism of about 640 to 606 Ma, and the onset of volcanism in the MVS at about 584 Ma.

Faulting appears to have occurred on a regional scale prior to the deposition of the overlying Cambrian cover sequence, resulting in the formation of the Mine Hill Shear Zone. Magmatic activity associated with the formation of the MVS is believed to have driven the convection of hydrothermal fluids along faults, concentrating fluids in the Mine Hill Shear Zone and causing the associated advanced argillic, high-sulphidation style alteration (Sparkes, 2005).

Arc-related volcanism began to wane between about 584 Ma and 582 Ma, as supported by the transition from the felsic volcanic rocks and tuffs of the MVS to the volcano-sedimentary succession of the WHPC (O'Brien *et al.,* 2001; Sparkes, 2005, 2006). During this period, significant erosion occurred and extensional stresses appear to have initiated normal faulting along the Mine Hill Shear Zone. This contributed to the present-day preservation of the MVS and its associated high-sulphidation alteration, whereas the volcanic rocks west of the Mine Hill Shear Zone were significantly eroded, exposing the lower-level HIS (Sparkes, 2005).

Ongoing extensional stresses appear to have caused submergence of the old arc complex and the creation of a Neoproterozoic basin that was infilled by the volcano-

sedimentary rocks of the WHPC. These rocks occur along the eastern margin of the Holyrood Horst, and extend east of the Topsail Fault and north to Cape St. Francis (Sparkes, 2006). The WHPC consists of siliceous sandstone and siltstone intercalated with mafic volcanic rocks, including pillowed basalt. In the lower WHPC, an ash-flow tuff near the base of the sedimentary succession that overlies high-sulphidation style alteration in the Oval Pit mine was dated at 582 ± 1.5 Ma (Sparkes, 2005).

East of the Topsail Fault and along the east coast of Conception Bay, the WHPC hosts intrusions of the HCD (Sparkes, 2006). Since the HCD exhibits similar trace-element patterns to those of the ca. 620 volcanic arc granites in the HIS, it is possible that the HCD represents a late pulse of volcanic arc magmatism with a similar source region to that of the HIS (Sparkes *et al.,* 2007). The HCD and the mafic volcanic rocks of the WHPC host a mafic-to-felsic dyke swarm that appears to follow the extrapolated trace of the Topsail Fault along the east coast of Conception Bay (Sparkes, 2006). This composite unit is the newly-recognized Horse Cove Complex, and its role in the tectonomagmatic history of the NE Avalon Peninsula is explored in this thesis.

Submarine mafic volcanism and sedimentation in the WHPC was followed by a succession of Neoproterozoic siliciclastic sedimentary rocks: the Conception, St. John's and Signal Hill groups. The stratigraphy of these rocks is described in Williams and King (1979) and King (1990). The Conception Group records a period of basinal sedimentation, dominated by south-flowing turbidity flows and intermittent felsic pyroclastic activity. King (1990) suggested that the felsic volcanic rocks in the former Harbour Main Group along the east coast of Conception Bay, including the rhyolite

domes at Cape St. Francis, represent the source of pyroclastic material in the Conception Group.

The occurrence of tuff interbeds within the package of Neoproterozoic sediments provides opportunities for precise dating, although limited data currently exist. A U/Pb zircon age of 565 ± 3 Ma (G. Dunning, unpublished data; Benus, 1988) was determined on a tuff bed that covers a fossiliferous surface in the Mistaken Point Formation near the top of the Conception Group on the southern Avalon Peninsula. This age provides an older age limit for the overlying St. John's and Signal Hill groups. Tuff beds in the glaciogenic Gaskiers Formation near the base of the Conception Group on the southern Avalon Peninsula were dated at ca. 580 Ma (Bowring *et al.,* 2003). Stratigraphically and sedimentologically, the Gaskier's Formation is comparable to the Bauline Line Member on the NE Avalon Peninsula, although no glaciogenic deposits have been found in the Bauline Line Member (King, 1990). Thus, the Conception Group on the NE Avalon Peninsula may also be as old as ca. 580.

The Conception Group is conformably overlain by shallowing-upward, fluvial-dominated, basinal-deltaic sedimentation in the St. John's Group. These strata are conformably overlain by the Signal Hill Group, which records the transition from a shallow marine environment to an alluvial fan. Tuff beds also occur locally in the St. John's and Signal Hill groups. The transition from the deep basin environment of the WHPC and Conception Group to the shallow marine and alluvial fan settings of the St. John's and Signal Hill groups, respectively, reflects a significant change from an extensional to compressional tectonic setting. The Signal Hill Group represents molasse-like deposits that resulted from tectonic uplift associated with the formation of a mountain

belt adjacent to the northern edge of the present-day Avalon Peninsula during the late Neoproterozoic Avalonian orogeny (King, 1990).

While the volcanic and sedimentary rocks west of the Topsail Fault lack a penetrative fabric, except in areas of argillic alteration, equivalent rocks east of the Topsail Fault are characterized by east-directed regional thrusting and penetrative foliation, indicative of regional compressional stresses (Sparkes, 2006). This deformation is probably related to east-directed thrusting and folding in the Flat Rock area, which has been attributed to the late Neoproterozoic Avalonian Orogeny (Calon, 2005). Strain along the Topsail Fault is believed to have formed a zone of penetrative, NE-trending foliation adjacent to the extrapolated trace of the Topsail Fault along the east coast of Conception Bay (Rose, 1952; King, 1988; Sparkes, 2006). The Topsail Fault has a complex deformational history, including oblique-slip and reverse-slip movements (Rose, 1952) and dextral, sinistral, horizontal and vertical motions (Sparkes, 2006). Numerous faults on the NE Avalon Peninsula are interpreted as splays from the Topsail Fault. For example, the White Mountain Volcanic Suite has been thrust eastward along the Pouch Cove River Fault over the WHPC (Sparkes, 2006), and sedimentary rocks of the WHPC have been thrust over those of the Conception Group (King, 1990; Smith, 1987). The older age limit for the onset of late Neoproterozoic deformation on the NE Avalon Peninsula is provided by the U/Pb age of a pumiceous ash-flow tuff at the base of the WHPC, dated at 582 ± 1.5 Ma (Sparkes, 2005, 2006).

Faulting during this period of compression is presumed to have exposed the Neoproterozoic succession of plutonic and volcanic rocks from underneath the WHPC succession (King, 1990; Sparkes, 2005). Erosion of the exposed volcanic and plutonic

rocks may be recorded in the Cabot Tower Member of the Signal Hill Group, in which up to 85% of clasts are rhyolite, rhyolite porphyry and ignimbrite and up to 10% are granite. King (1990) indicates that the granite clasts are comparable to the HIS granite, and that the felsic volcanic clasts are similar to the felsic volcanic rocks in the former Harbour Main Group.

The youngest identified intrusive event on the NE Avalon Peninsula consists of gabbroic dykes and plutons in the BHIS (Sparkes, 2006). These intrusions occur on the northern portion of the NE Avalon Peninsula, and cross-cut folded siliciclastic rocks of the Mannings Hill Member in the Conception Group (King, 1990; Sparkes, 2006). Similar intrusions were also recognized further south, near Manuels (Sparkes *et al.,* 2005) and in the Topsail Bluff area south of Portugal Cove (the Dogberry Hill Gabbro; King, 1990). Since the Mannings Hill Member lies in the Drook Formation, stratigraphically above the ca. 580 Ma Gaskiers Formation (Bowring *et al.,* 2003), the BHIS appears to be younger than ca. 580 Ma. Lithological and geochemical similarities between the BHIS and HCD suggest that they are co-genetic, and that they share a volcanic arc-related source region that is similar to that of the HIS granite (Sparkes *et al.,* 2007). Because intrusions of the BHIS cross-cut folded strata of the Conception Group near Cape St. Francis, the emplacement of BHIS represents the younger age limit on the late Neoproterozoic deformation associated with the Avalonian Orogeny (Sparkes, 2006). However, an attempt at U/Pb zircon geochronology of the BHIS yielded no datable minerals (G. Sparkes and G. Dunning, personal communication).

The late Neoproterozoic package of volcanic, plutonic and sedimentary rocks on the NE Avalon Peninsula is overlain by remnants of a fossiliferous Cambrian-Ordovician

platformal cover sequence (King, 1990). On the south coast of Conception Bay, these strata unconformably overlie Neoproterozoic volcanic and plutonic rocks in the Manuels River area (King, 1990). Minor magmatism is associated with the Cambrian-Ordovician cover sequence, in the form of Middle Cambrian alkaline basaltic pillow lavas, tuffs and gabbroic intrusions in the Cape St. Mary's area on the southern Avalon Peninsula (Greenough and Papezik, 1985).

Because the Cambrian-Ordovician succession is generally undeformed, the main phase of late Neoproterozoic deformation is believed to have ceased by the onset of the Cambrian at ca. 542 Ma (International Commission on Stratigraphy, www.stratigraphy.org). This is supported by ^{40}Ar-^{39}Ar data for sericite from the Mine Hill Shear Zone, which dated the last deformation event at 537 ± 3 Ma (Sparkes, 2005). However, isolated zones of deformation in the Cambrian strata west of the Topsail Fault (O'Brien, 2002; Sparkes *et al.,* 2004; Sparkes, 2005), and in Lower to Middle Cambrian shales along the Topsail Fault itself (Rose, 1952; Boyce and Hayes, 1991), indicate that localized deformation continued into the Cambrian.

1.5. Geology of the Horse Cove Complex

The dykes of the HCC are hosted by the ca. 580 Ma or younger HCD and the mafic volcanic rocks of the WHPC. The dyke swarm has an approximate strike length of 22 km along the east coast of Conception Bay, from south of Portugal Cove to north of Bauline. In the Bauline area, the dykes in the HCC are predominantly hosted by the HCD, and the absence of dykes east of Bauline marks a gradational contact between the two units (Sparkes, 2006). The dykes are characterized by sharp intrusive contacts with

chilled margins, and range in width from less than 20 cm to greater than 2 m (Sparkes, 2006). Several generations of dykes were mapped by Sparkes (2006), including, from oldest to youngest: diabase, feldspar porphyry, feldspar-phyric mafic dykes, and fine-grained, magnetic mafic dykes. Sparkes (2006) also recognized rare granitic dykes and flow-banded rhyolite. Preliminary geochemical results from Sparkes *et al.* (2007) showed that the mafic dykes sampled in the HCC have similar chemistry to mafic volcanic rocks from the WHPC. This implies that at least some of the mafic dykes served as feeder conduits to higher-level volcanism (Sparkes *et al.*, 2007).

However, after several regional geological studies that included the east coast of Conception Bay (e.g. Rose, 1952; Hsu, 1975; King, 1988, 1990; Sparkes, 2006; Sparkes *et al.,* 2007), the role of the HCC in the tectonic history of the Avalon Peninsula remained uncertain. The internal complexity and intrusive relationships within the HCC had not been studied in detail, and although the dykes were known to be younger than their ca. 580 Ma host rocks, the age of magmatism in the HCC remained undetermined. The geochemistry of the HCC had been investigated on a preliminary basis, but with no detailed mapping in the HCC, the geochemical data could not be linked to the complex magmatic development of the composite unit. Interpretations of the tectonomagmatic history of the HCC were also limited by the lack of extended trace element data.

The age of the HCC may have significant implications for the current geological interpretation of the NE Avalon Peninsula. For instance, magmatism in the HCC may be contemporaneous with magmatism elsewhere in the region, or it may be significantly younger. For example, Cambrian-aged magmatism has been identified in the Cape St. Mary's region (Greenough and Papezik, 1985) but has not yet been documented on the

NE Avalon Peninsula. An age determination for the dykes may also help to constrain the source of heat and fluids for the 585 to 580.5 Ma high-sulphidation style epithermal system hosted by the MVS.

A study of the age, geochemistry and geological history of the HCC may allow correlations with other rocks in the NE Avalon region. For example, the feldspar porphyry intrusions in the HCC are lithologically indistinguishable from feldspar porphyry intrusions hosted by the WHPC on the eastern margin of the Holyrood Horst (Sparkes, 2006). As well, mafic-to-intermediate magmatism in the HCC may be comparable to other magmatic events on the NE Avalon Peninsula, including the WHPC basalts, the HCD and the gabbroic BHIS, which represents the youngest identified intrusive event in the region (Sparkes, 2006). Understanding the relationships between the HCC and previously studied rocks in the region may refine the current understanding of the tectonomagmatic development of the Avalon Peninsula.

1.6. Project Goals

This study examines the internal complexity, age of magmatism, geochemistry and geological history of the HCC, and evaluates possible relationships between the HCC and other magmatic events on the NE Avalon Peninsula. In addition, this study investigates the role of the HCC in the current interpretation of the tectonic development of the Avalon Peninsula and the Avalon Zone in Newfoundland.

1.7. Methods

The town of Bauline was chosen as the study area for this project because the HCC is well-exposed in extensive coastal outcrops, as well as in numerous rock faces along the road leading into Bauline and in a quarry directly south of the town. The location of the study area is shown in Figure 1.3. The excellent exposure and fresh, lichen-free outcrop surfaces at Bauline allow the internal complexity of the HCC to be studied in detail. In addition, Bauline is accessible by road, and numerous outcrops are easily reached on foot. Geological mapping of the HCC focused on three separate areas of coastal outcrops (Maps 1-3) and three cross-sections along the road cut and quarry (Sections A-A', B-B' and C-C'). The maps and cross-sections are displayed on two posters in the pocket at the end of this volume: Map 1, the largest map, covers one poster, and the second poster includes Maps 2-3 and Sections A-A' and C-C'. The locations of the maps and cross-sections (Figure 1.4), together with outcrop exposure and methods of mapping, are described below.

For each of the rock units identified during mapping, several thin sections were analyzed for the purpose of characterizing the mineralogy and textures of each unit and to allow comparison with other units. Several rock units that had been separated on a preliminary basis in the field have similar field appearances and are so fine-grained that mineralogy could not be reliably determined with a hand lens. Therefore, thin section analysis was used to test the field-based division of these rocks. Because the HCC is a composite unit with multiple intrusive events and complex intrusive relationships, thin sections were strategically chosen to test the continuity of each rock unit across the study area.

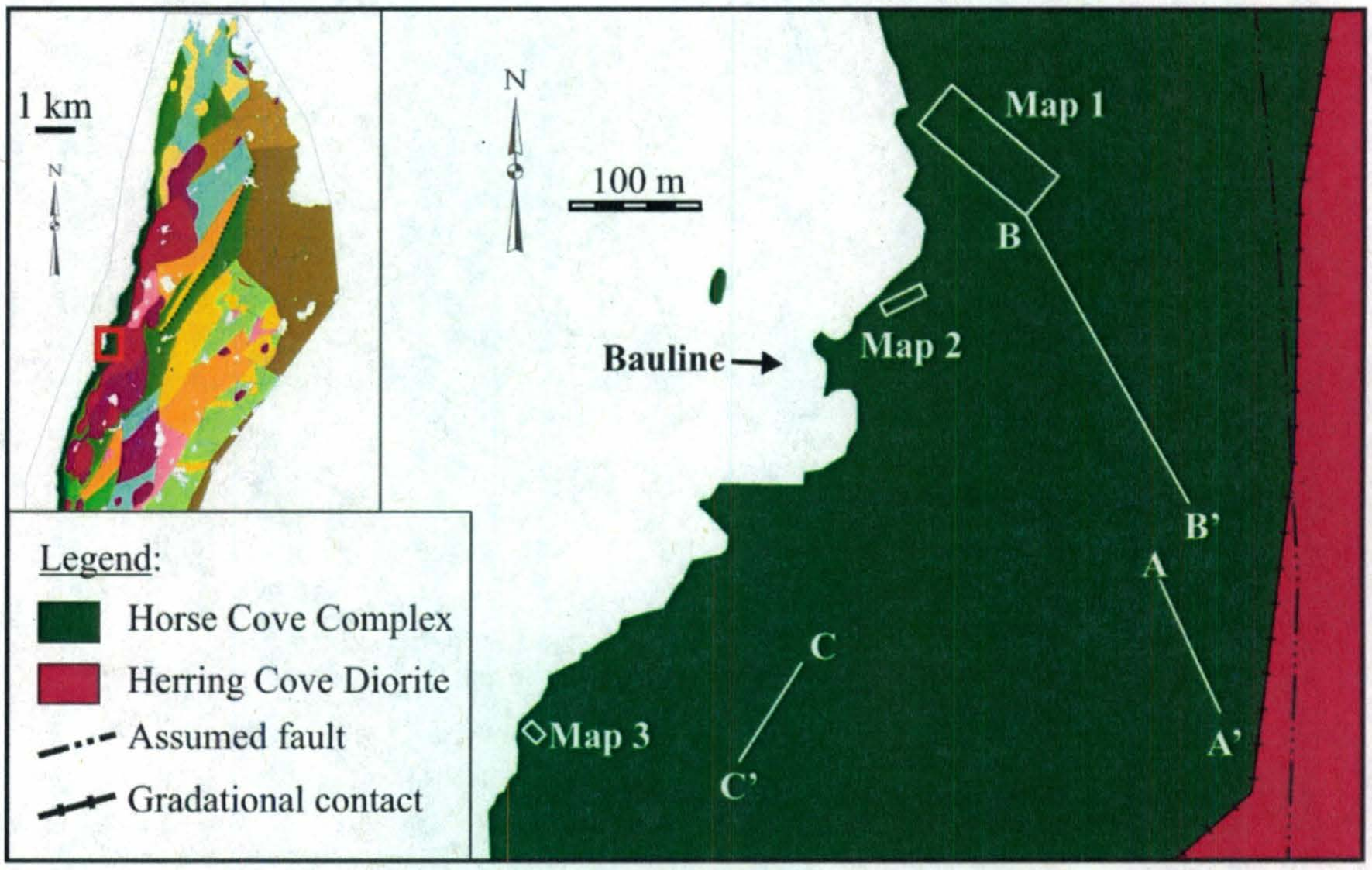

Figure 1.4: A map of the study area in and around the town of Bauline, showing the approximate locations of Maps 1, 2 and 3 and Sections A-A', B-B' and C-C'. The inset map shows the geology of the northeast coast of Conception Bay by Sparkes (2006), with the location of the study area marked in red.

Four key units were selected for U/Pb zircon geochronology to constrain the age of magmatism in the HCC. These units have well-defined field relationships, and include the youngest and oldest interpreted intrusions. They were analyzed using the chemical abrasion TIMS method (Mattinson, 2005) at Memorial University of Newfoundland. Sample preparation and analytical methods for U/Pb zircon geochronology are provided in Appendix B.

Sixty-six of the samples that were studied in thin section were chosen for whole-rock geochemical analysis. These samples were selected from Maps 1-3 because these areas have the most lithological variety and the best constrained field relationships. According to field relationships and petrography, these samples are representative of each rock unit in the study area. The rocks were analyzed for major and trace elements, including the REE, using the fusion ICP-MS method at Actlabs. Sample preparation and analytical methods for whole-rock geochemistry are provided in Appendix C. Whole-rock geochemistry was used to characterize each rock unit and identify igneous trends within the HCC. Geochemistry was also used to investigate source characteristics and the paleotectonic environment of the HCC. In addition, the geochemistry of the HCC was compared to that of selected rocks on the NE Avalon Peninsula that have been analyzed in previous studies (e.g. Sparkes, 2005; Sparkes *et al.,* 2007).

To further investigate the source characteristics of the HCC, seven samples were selected from the HCC for Nd isotopic analysis. The selection criteria for this limited sample set are explained in Chapter 4. Nd isotopic analysis was carried out at the TIMS lab at Memorial University of Newfoundland, and the analyticial methods are provided in Appendix F.

Lastly, all the findings from this study, including field relationships, U/Pb zircon ages, whole-rock geochemistry data and Nd isotopic data, were combined to reconstruct the magmatic evolution of the HCC and its role in the tectonic history of the NE Avalon Peninsula and the Avalon Zone in Newfoundland.

1.8. Mapping

1.8.1. Methods

Maps 1-3 represent three areas of coastal outcrops in the Bauline area that were mapped in detail using a grid-style. Each map area was carefully selected for maximum outcrop exposure, minimum weathering and lichen-cover, and for the lithological complexity that characterizes the HCC. The perimeter of each map was measured and marked with flagging tape, the bearings of the perimeter were measured, and UTM coordinates were determined for the corners of each map. The interior of each map area was marked at regular intervals to form a grid. For each map, the geology of each square of the grid was sketched and described in detail on gridded paper, including the locations of samples and field photographs. Each sheet of gridded paper was then scanned, and the resulting image was imported into Adobe Photoshop. The images were stitched together to form a mosaic of each map. Each mosaic of images, representing the geology of the mapped area, was imported into MapInfo and geo-referenced in using the UTM coordinates measured in the field. However, the uncertainty of coordinates measured with the GPS was approximately 7 m. Therefore, to geo-reference the map in MapInfo, the coordinates of three corners of the map were calculated using the measured coordinates of the fourth corner of the map and the bearings of the grid perimeter. Once

in MapInfo, the sketched geological contacts on the mosaic of images were digitized, together with structural data and the locations of samples and field photos. Because most samples are closely spaced and within the uncertainty on the GPS, the UTM coordinates of all samples were extracted from the geo-referenced maps in MapInfo.

The cross-sections were measured and marked at regular intervals with flagging tape, and UTM coordinates were determined at various points along each section. For Sections A-A' and B-B', overlapping photographs were taken along the cross-section and the geology was sketched and described on Mylar overlays on top of the photographs. Due to tall vegetation in front of the quarry walls, Section C-C' could not be photographed and was instead sketched in a field notebook. Sketches of Sections A-A' and C-C' were scanned, imported into MapInfo and digitized. Section B-B' was not digitized because the geology and field relationships in this cross-section are not well-constrained, as discussed below.

1.8.2. Map 1

With an area of 40 X 110 m, Map 1 is the largest map in the study area and covers west-sloping, partly vegetated terrain directly north of Bauline (Figure 1.5a). It is oriented NW-SE, oblique to the coastline of Conception Bay and approximately across-strike to the HCC. Some contacts are inferred because about 40% of Map 1 is covered by vegetation. In addition, contacts are difficult to see in some outcrops even though there is a clear change in lithology. This is due to locally developed shear fabrics, and because many outcrops are lichen-covered and surrounded by soil or ground-covering vegetation

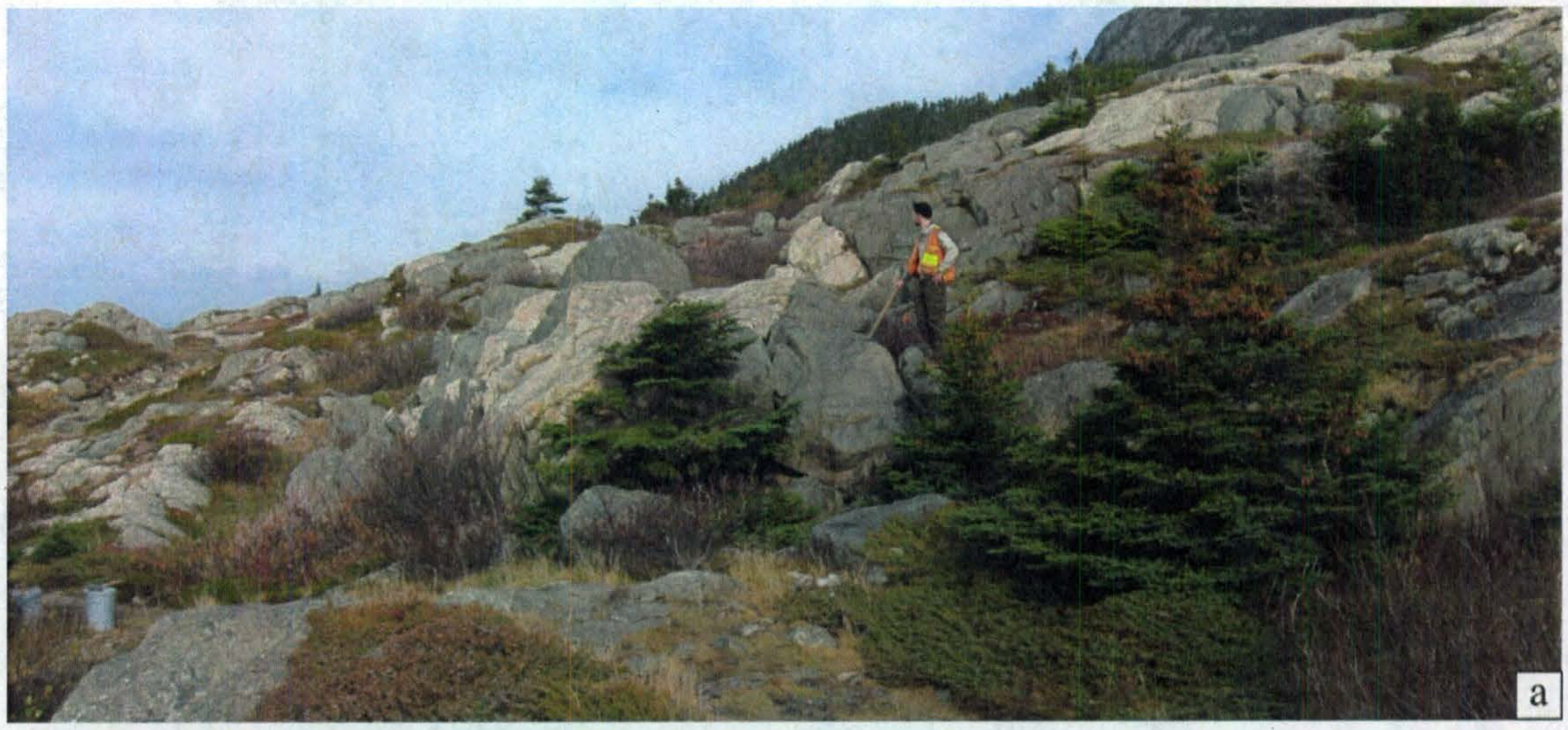

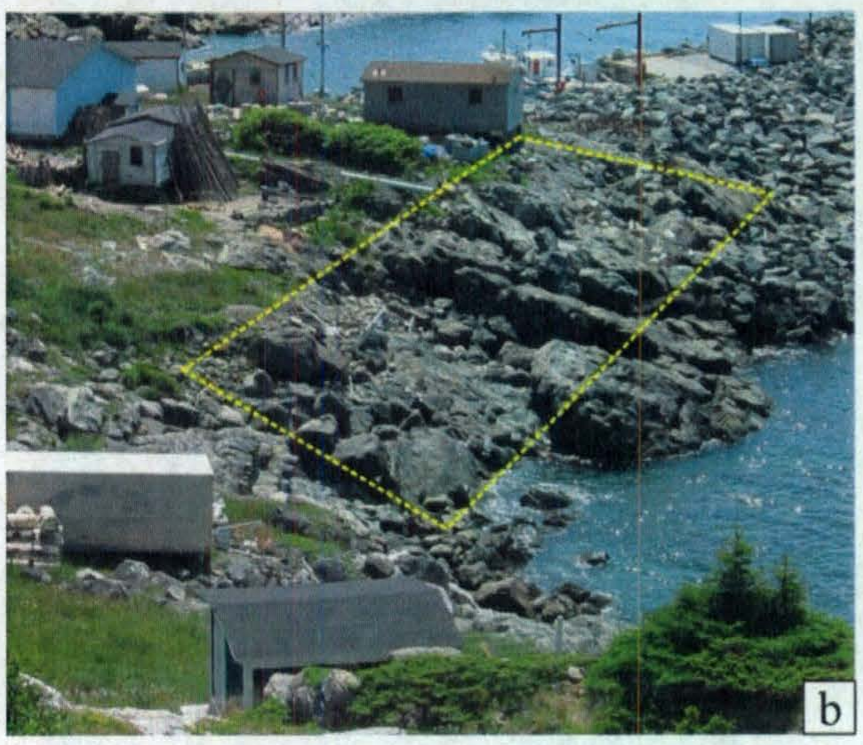

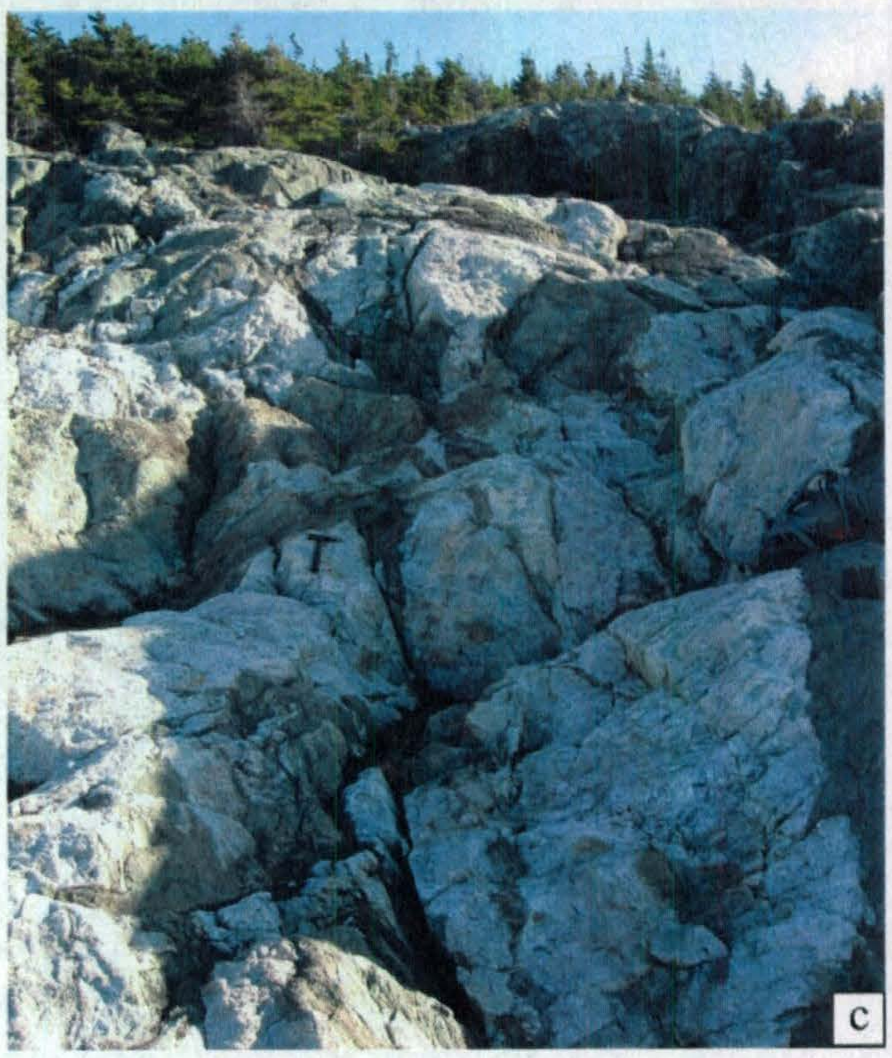

Figure 1.5: Field photographs of Maps 1-3. (a) View from the southern edge of Map 1, looking north. (b) View of Map 2, looking south. (c) View from the southwest corner of Map 3, looking east. Hammer in centre of photo is about 30 cm long.

that is not readily pulled back. Different line styles in Map 1 are used to distinguish inferred contacts in outcrop from those that are covered by vegetation.

1.8.3. Map 2

Map 2 covers 10 X 35 m of relatively flat coastal outcrops on the western edge of Bauline, directly east of the breakwater (Figure 1.5b). Map 2 is oriented NE-SW, and its western edge is bordered by the ocean, resulting in well-exposed outcrops that are wave-washed and lichen-free. Most contacts are clearly visible, but they are locally inferred due to pervasive brittle fractures.

1.8.4. Map 3

Map 3 has an area of 10 X 15 m and is located on west-sloping coastline directly south of Bauline (Figure 1.5c). Map 3 has nearly 100% outcrop exposure and the surfaces are lichen-free, resulting in clearly visible contacts. However, contacts are locally obscured by strong shear fabrics or brittle fractures.

1.8.5. Section A-A'

Section A-A' is about 51 m long, trends NW-SE and runs parallel to the road into Bauline. The blasted rock surfaces in Section A-A' (Figure 1.6a) are unweathered and lichen-free. Contacts are clearly identified, except in localized shear zones and densely fractured areas.

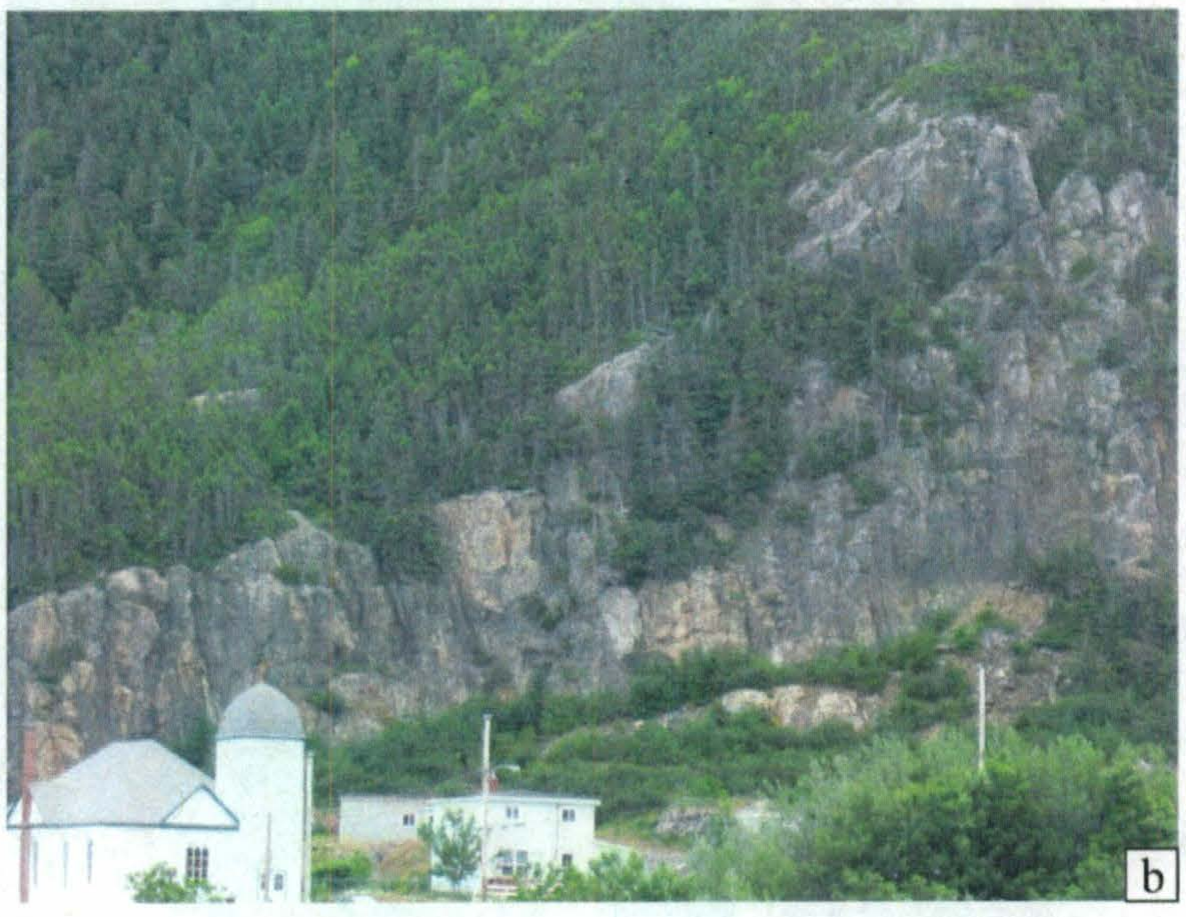

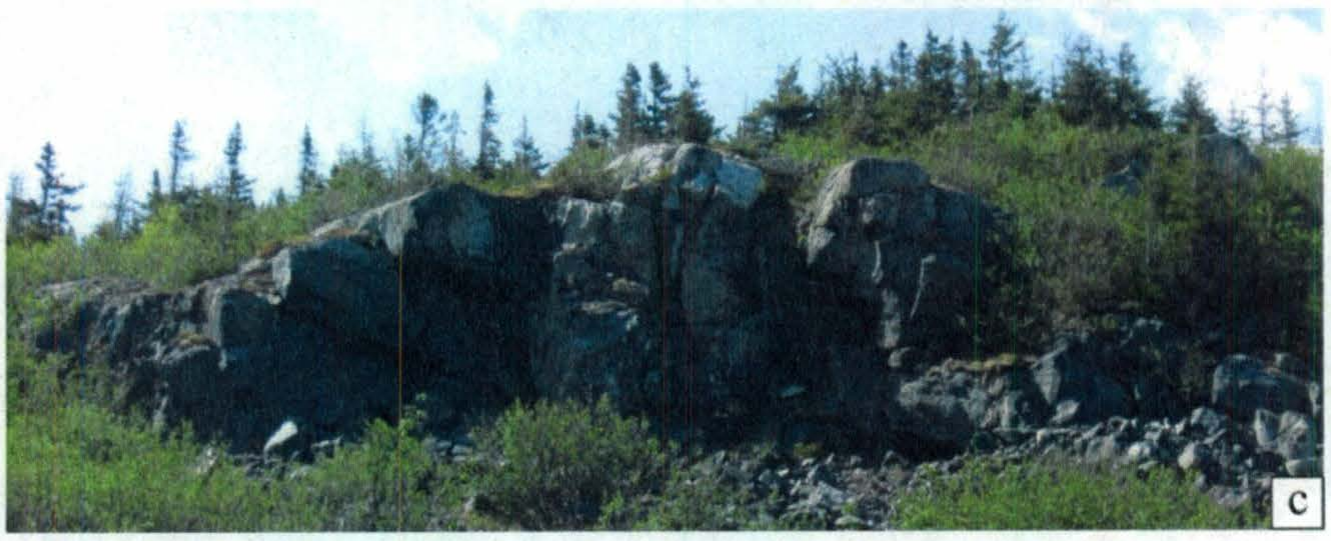

Figure 1.6: Field photographs of Sections A-A', B-B' and C-C'. (a) Part of Section A-A' (30-40 m along-section), viewed from the southwest. (b) The southeast end (80 m) of Section B-B', viewed from the southwest. (c) Part of Section C-C' (0-20 m along-section), viewed from the west.

1.8.6. Section B-B'

Section B-B' is about 360 m long and extends NW-SE along a steeply-dipping cliff on the NE edge of Bauline (Figure 1.6b). The NW end of this cross-section connects with the SE corner of Map 1, and the SE end of Section B-B' is about 50 m NE of the NW end of Section A-A'. Section B-B' was included in the mapping because: (1) the cliff provides up to 30 m of vertical outcrop and several hundred metres of outcrop along its base; and (2) together, Map 1 and Sections A-A' and B-B' form a complete cross-section across the strike of the HCC. However, Section B-B' displays less lithological variety than the other cross-sections. The rocks along Section B-B' are mostly massive, fine-to-medium-grained, dark grey- or green-weathering diorite. Mafic dykes and intrusive relationships between diorite and rare felsic rocks are not easily distinguished because the cliff is weathered, covered in lichen and exhibits a strong shear fabric. Therefore, field relationships are not well-constrained along Section B-B', few samples were collected and Section B-B' is not displayed in this study.

1.8.7. Section C-C'

Section C-C' is located in the quarry on the southern edge of Bauline (Figure 1.6c), about 100 m east of Map 3. Section C-C' is about 92.5 m long and has an overall NE-SW trend. Some portions of Section C-C' are covered by vegetation but the outcrop is unweathered and lichen-free. Contacts and intrusive relationships are therefore clearly visible except in localized sheared and fractured areas.

CHAPTER 2: ROCK UNIT DESCRIPTIONS

2.1. Introduction

The rocks at Bauline are divided into eleven lithologic units based on mapping and petrography. Although the rocks have undergone greenschist-facies metamorphism, the original igneous minerals have experienced minimal replacement by metamorphic minerals, and the rocks are grouped according to igneous mineral assemblages and textures. The distribution of these units is shown on the maps and cross-sections located in the back inside cover of this volume. Detailed descriptions of the field relationships, lithology and petrography of each unit are provided below, in the order of oldest to youngest interpreted ages. This chronological order of rock units, as represented in the legends for the maps and cross-sections, is an integrated interpretation of intrusive relationships observed throughout the study area. However, this chronological order is locally contradicted by some rock units in the dyke swarm due to the episodic emplacement of dykes that comprise each unit and the essentially coeval emplacement of certain rock units.

One hundred and seventeen thin sections were obtained from samples collected from across the study area, including from Sections A-A', B-B' and C-C' and from Maps 1, 2 and 3. Petrographic descriptions for each thin section are summarized in Appendix A, including modal proportions of phenocrysts and groundmass minerals, accessory minerals, grain sizes, textures, foliations and veins. The locations of field photos, thin sections and photomicrographs referred to in the unit descriptions are shown on maps and

cross-sections, and references to "station #" in the unit descriptions correspond to sample locations.

2.2. Lithology, field relationships and petrography of rock units in the study area

2.2.1. Granodiorite

2.2.1.1. Lithology and field relationships

This unit is coarse-grained, weathers white or yellowish-white, and its fresh surface is light greenish-grey. In Maps 1 and 2, granodiorite locally displays a deformation fabric defined by lozenge-shaped quartz ribbons that are up to 1.5 cm long (Plate 2.1a). Epidote veins are typically present throughout the unit but are particularly abundant at contacts, and are in places accompanied by veins of a pink mineral, which may be hematized albite.

This unit was observed in all grids and sections mapped at Bauline. It occurs as septa preserved between dykes and intrusions, blocks within diorite and as larger bodies that host mafic and intermediate dykes. Granodiorite septa occur throughout the study area and have various shapes and sizes ranging from ~30 cm long blocks (Plate 2.1b) to much larger slabs, such as the 7 m X 1 m septa in Map 2 and the 2 m wide blocks exposed in Section C-C'. Chilled margins in mafic and intermediate dykes against granodiorite septa were observed in areas where such features are not obscured by shearing, weathering or lichens. For example, hornblende basaltic dykes exhibit chilled margins against granodiorite septa in Map 2 (Plate 2.1c), Section A-A' (Plate 2.1d) and Section C-C' (Plate 2.2a). As well, in Section C-C', a hornblende basaltic dyke contains pieces of granodiorite (Plate 2.2b).

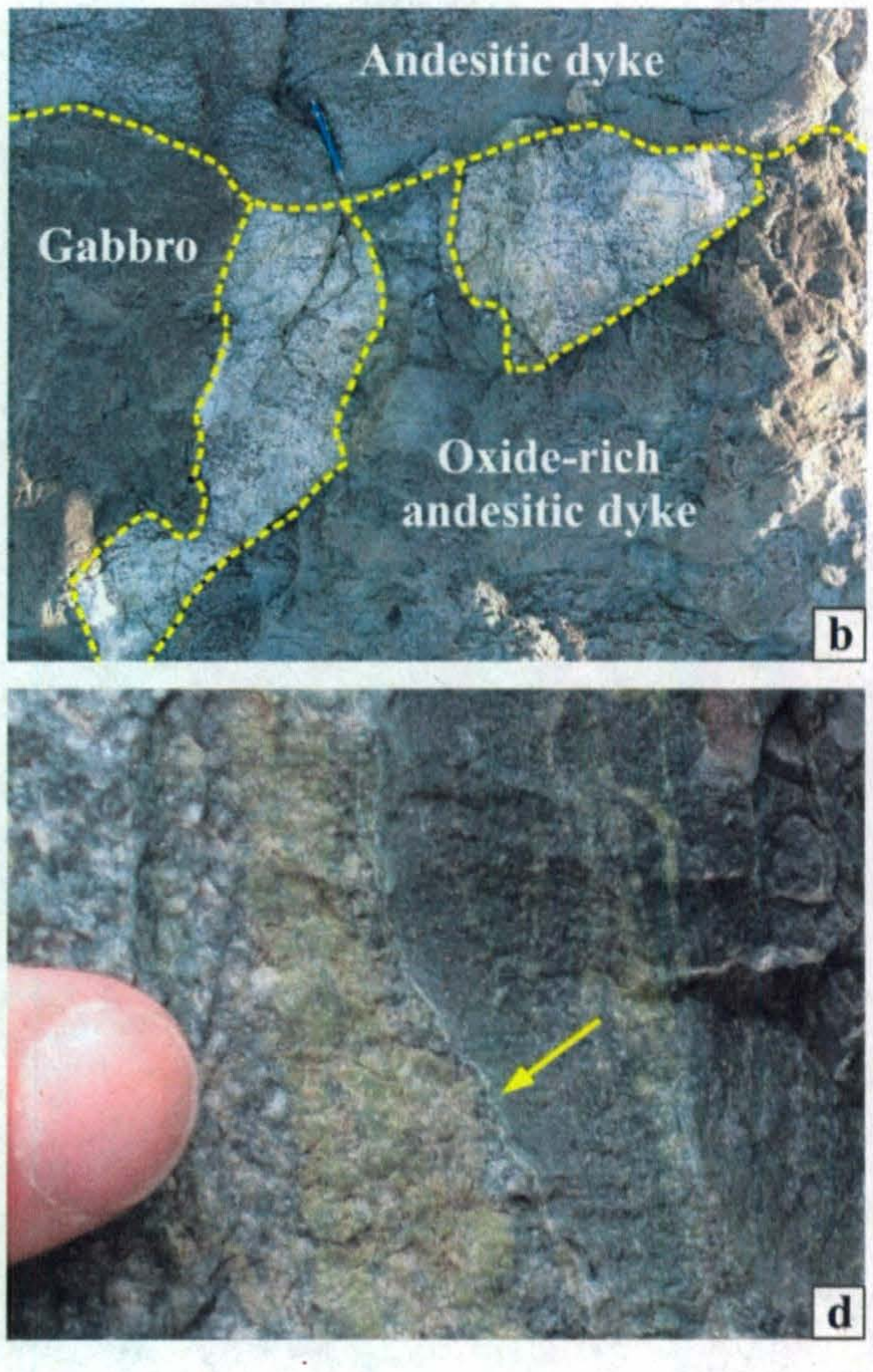

Plate 2.1: Field photographs of granodiorite. (a) ~1.5 cm long quartz ribbons trending NE-SW. (b) Small blocks of granodiorite between gabbro, an oxide-rich andesitic dyke and an andesitic dyke (Map 2). Chilled margins in hornblende basaltic dykes against granodiorite septa in Map 2 (c) and Section A-A' (d).

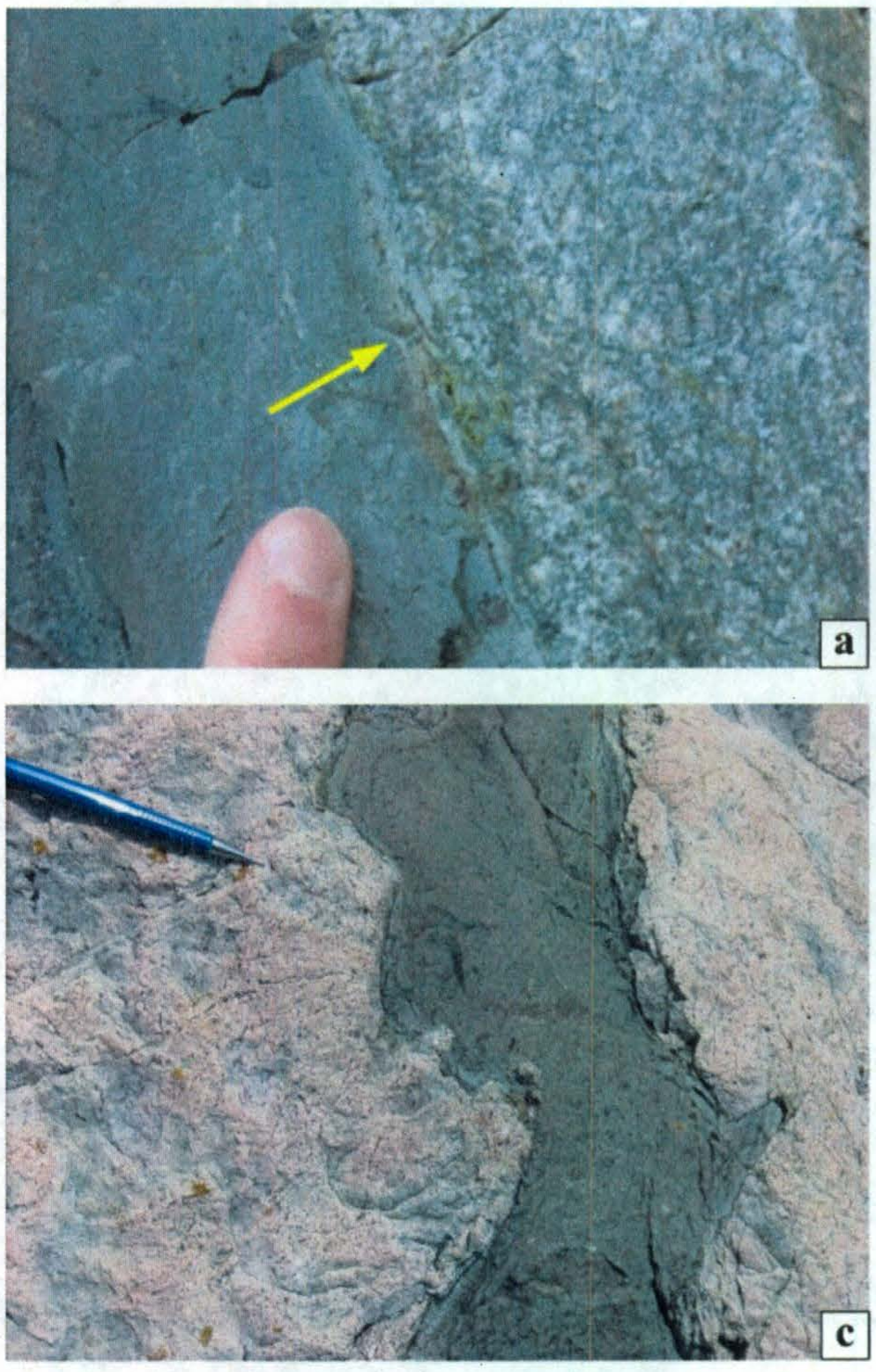

Plate 2.2: Field photographs of granodiorite. (a) A chilled margin in a hornblende basaltic dyke against granodiorite in Section C-C'. (b) An irregular contact between granodiorite and a hornblende basaltic dyke that contains pieces of granodiorite (Section C-C'). (c) An oxide-rich andesitic dyke chilled against granodiorite (Map 3).

In Map 3, granodiorite hosts a network of basaltic, oxide-rich andesitic and andesitic dykes, many of which exhibit chilled margins (Plate 2.2c). The most extensive exposure of granodiorite in the study area is in Map 1, where it forms large bodies, up to 5 m X 23 m in size, that are surrounded by diorite and host basaltic, oxide-rich basaltic, basaltic-andesitic, hornblende-porphyritic andesitic and andesitic dykes (Plate 2.3a). Because diorite encompasses these large granodiorite bodies and also contains many smaller blocks of granodiorite (Plate 2.3b and c), granodiorite appears to have been intruded by diorite. This interpretation is supported by a subtle chilled margin observed in diorite against granodiorite (Plate 2.3d).

Granodiorite also appears to predate feldspar porphyry and rhyolitic dykes. Because granodiorite and feldspar porphyry are usually separated by dykes or diorite, the contact between these two units is exposed in only two places in the study area: in one outcrop in Map 1, and along Section B-B'. In both places, granodiorite remains coarse-grained near the contact and feldspar porphyry is a slightly lighter colour at the boundary (Plate 2.3e), which suggests that feldspar porphyry postdates granodiorite. Granodiorite is in contact with a rhyolitic dyke along Section A-A', but intrusive relationships are ambiguous. However, since a rhyolitic dyke cross-cuts feldspar porphyry and diorite in Map 1, at least one rhyolitic dyke appears to be younger than granodiorite. Field relationships demonstrate that granodiorite is postdated by feldspar porphyry, diorite and mafic, intermediate and rhyolitic dykes, and it is therefore interpreted to be the oldest known unit in the study area. As well, the coarse grain size of granodiorite sets it apart from the fine-to-medium-grained rocks that comprise the other rock units in the study area, implying that granodiorite crystallized at a deeper level.

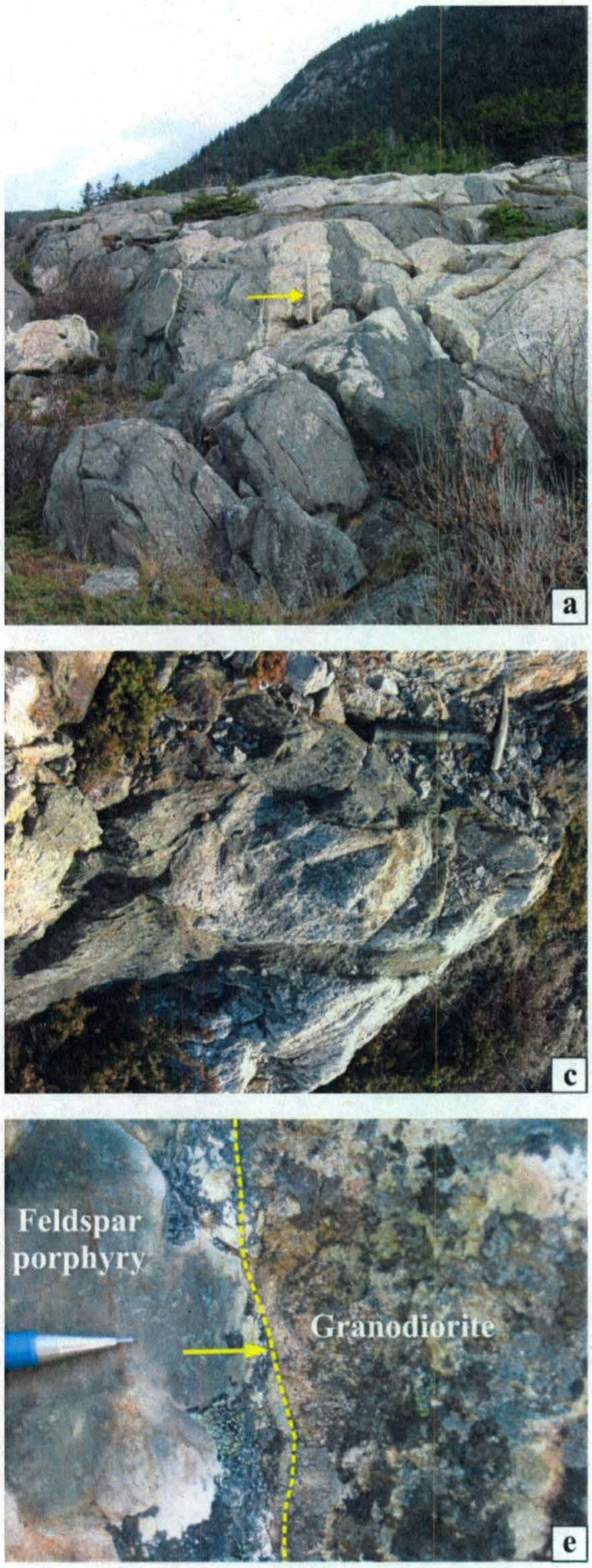

Plate 2.3: Field photographs of granodiorite. (a) View of part of Map 1, looking north, showing several basaltic dykes hosted by a large body of granodiorite. The hammer in the centre of the photo is about 0.7 m long. (b) & (c) Sheared blocks of granodiorite in diorite (Map 1). (d) Subtle chilled margin in diorite against granodiorite (Map 1). (e) Contact between granodiorite and feldspar porphyry (Section B-B').

2.2.1.2. Petrography

Granodiorite is composed of plagioclase, quartz, alkali feldspar and minor amounts of epidote, chlorite and actinolite. In thin section, plagioclase occurs as subhedral blocky laths that are typically ~1 mm long, but may be up to 4 mm long. Alkali feldspar forms anhedral and subhedral grains that are about the same size as plagioclase crystals and commonly display cross-hatch twinning (Plate 2.4a) or perthitic exsolution texture. In samples that have not undergone ductile deformation, quartz occurs as subhedral crystals and anhedral grains that range in size from about 0.5 to 2 mm and appear to fill spaces between feldspar grains (Plate 2.4a). Subhedral, tabular-shaped hornblende crystals were observed in minor amounts in some granodiorite thin sections (Plate 2.4b). Locally, chlorite, epidote, opaque minerals and actinolite form up to 1.5 mm long, tabular-shaped aggregates, which are lozenge-shaped in samples that have undergone ductile deformation (Plate 2.4c). These aggregates comprise less than 2% of each thin section, and they are interpreted to be pseudomorphs of primary hornblende. Secondary epidote and chlorite are concentrated at grain boundaries, and also occur as tiny blebs within feldspars. As well, chlorite and epidote fill fractures and form clots with opaque minerals.

All samples of granodiorite examined in thin section have undergone various degrees of brittle deformation. Feldspar crystals commonly contain fractures that result in offset lamellar twins, and many quartz and feldspar crystals are offset by fractures or have been reduced to crystal breccias (Plate 2.5a and b). Very fine-grained quartz and feldspar form vein-like networks surrounding regions of coarse-grained crystals that are fractured but remain otherwise intact (Plate 2.5b). This very fine-grained material is

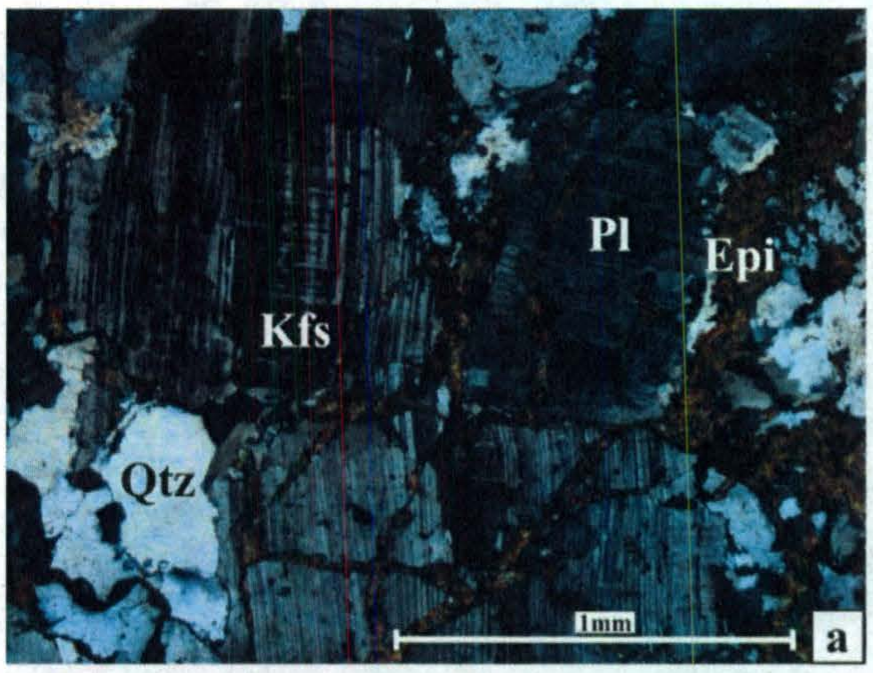

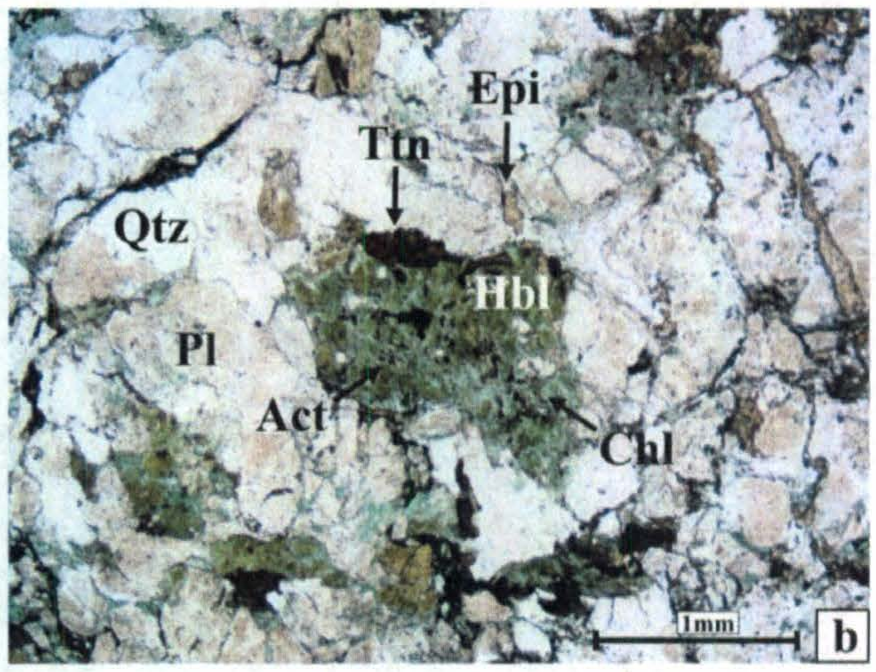

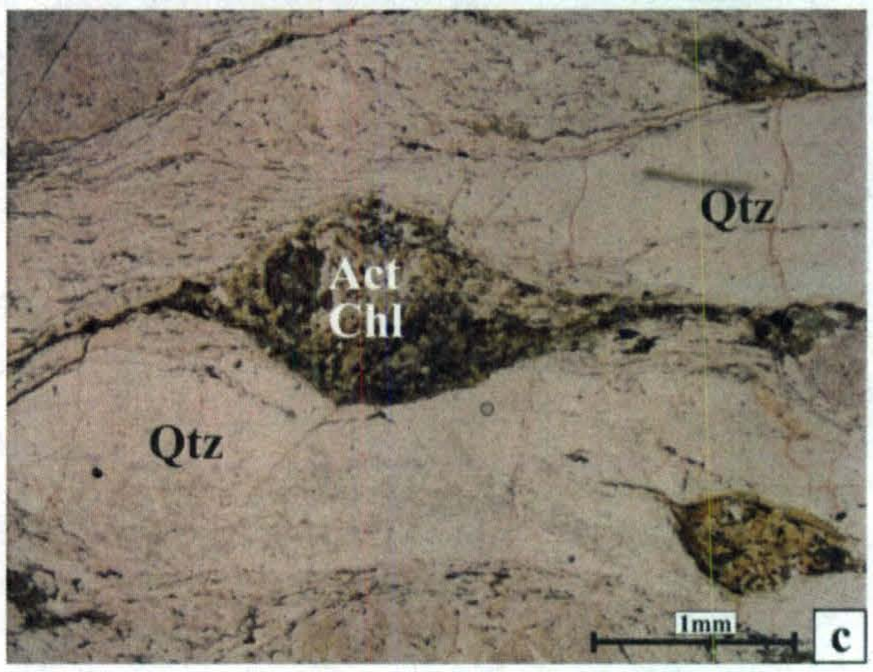

Plate 2.4: Photomicrographs of granodiorite in plane-polarized light, unless otherwise indicated. (a) Viewed under crossed polars, plagioclase exhibits lamellar twinning and cross-hatch twinning is visible in alkali feldspar. Feldspar and quartz are fractured by epidote veins (sample #13, Section A-A'). (b) Actinolite and chlorite have partially replaced hornblende, and abundant epidote-filled fractures have caused brecciation of quartz and feldspar (sample #33, Section A-A'). (c) A ductilely deformed aggregate of chlorite, actinolite and epidote pseudomorphing primary hornblende (sample #118, Map 1).

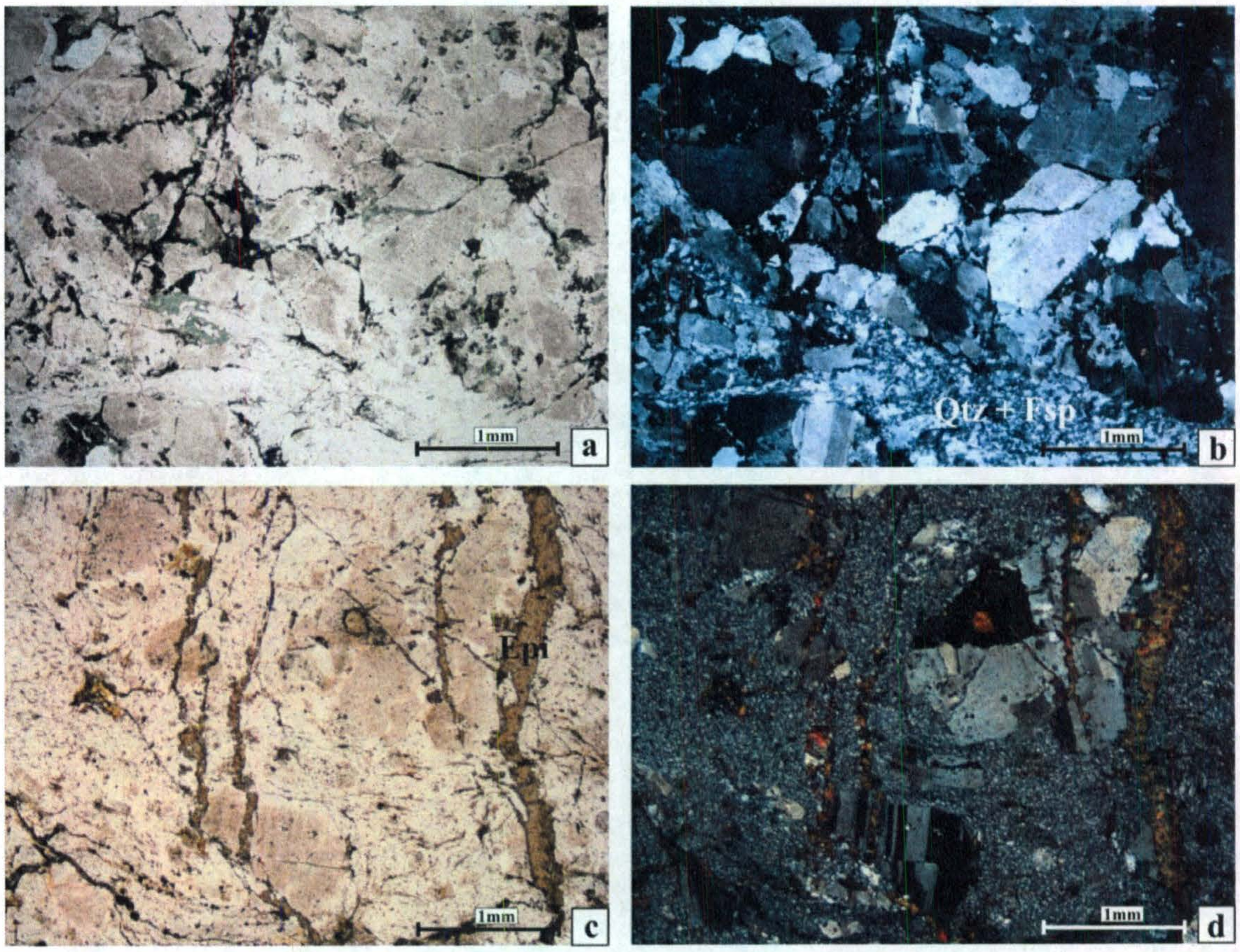

Plate 2.5: Photomicrographs of granodiorite in plane-polarized light, unless otherwise indicated. (a) Fractures filled with chlorite, epidote and opaque minerals (sample #200, Map 3). (b) Same view as (a) under crossed polars, showing brecciated feldspar grains and very fine-grained quartz and feldspar forming vein-like networks around patches of more coarse-grained material. (c) Blastomylonitic texture, with feldspar porphyroclasts cut by epidote veins and foliation defined by aligned chlorite and epidote in the groundmass (sample #107, Map 1). (d) Same view as (c) under crossed polars.

interpreted to be the product of crushed quartz and feldspar that has recrystallized in the presence of fluids.

In thin sections from samples #107, 118, 128 from Map 1, samples #68 and 80 from Map 2 and sample #199 from Section B-B', granodiorite exhibits blastomylonitic texture, which is characterized by fractured feldspar crystals and quartz grains enclosed by a groundmass of very fine-grained quartz + feldspar (Plate 2.5c and d, Plate 2.6a and b). This groundmass comprises ~65% of some granodiorite thin sections and is believed to be the result of significant brittle and/or ductile deformation, causing granulation and recrystallization. Foliation is preserved in the linear alignment of groundmass minerals, including chlorite and chains of tiny epidote crystals. In samples #118 and 128 from Map 1 and sample #68 from Map 2, blastomylonitic granodiorite has experienced ductile deformation, resulting in the stretching and partial recrystallization of quartz crystals into ribbons that are up to 1.5 cm-long and exhibit undulatory extinction (Plate 2.6a). In these granodiorite samples, foliation is defined by the parallel alignment of quartz ribbons, groundmass minerals and epidote veins. Some quartz ribbons are offset by epidote-filled fractures, indicating at least two generations of deformation (Plate 2.6b).

Several thin sections, including samples #148 from Map 1, #202 from Map 3 and #36 from Section A-A', appear to have undergone significant recrystallization. These thin sections consist of ~1 mm long subhedral, blocky feldspar laths enclosed by a fine-grained groundmass of relatively equigranular, subhedral quartz and feldspar (Plate 2.7a, b and c). Under high magnification, the grain boundaries of groundmass quartz and feldspar are occupied by very fine-grained quartz and feldspar, which indicates suturing and recrystallization of groundmass quartz and feldspar. In addition, groundmass quartz

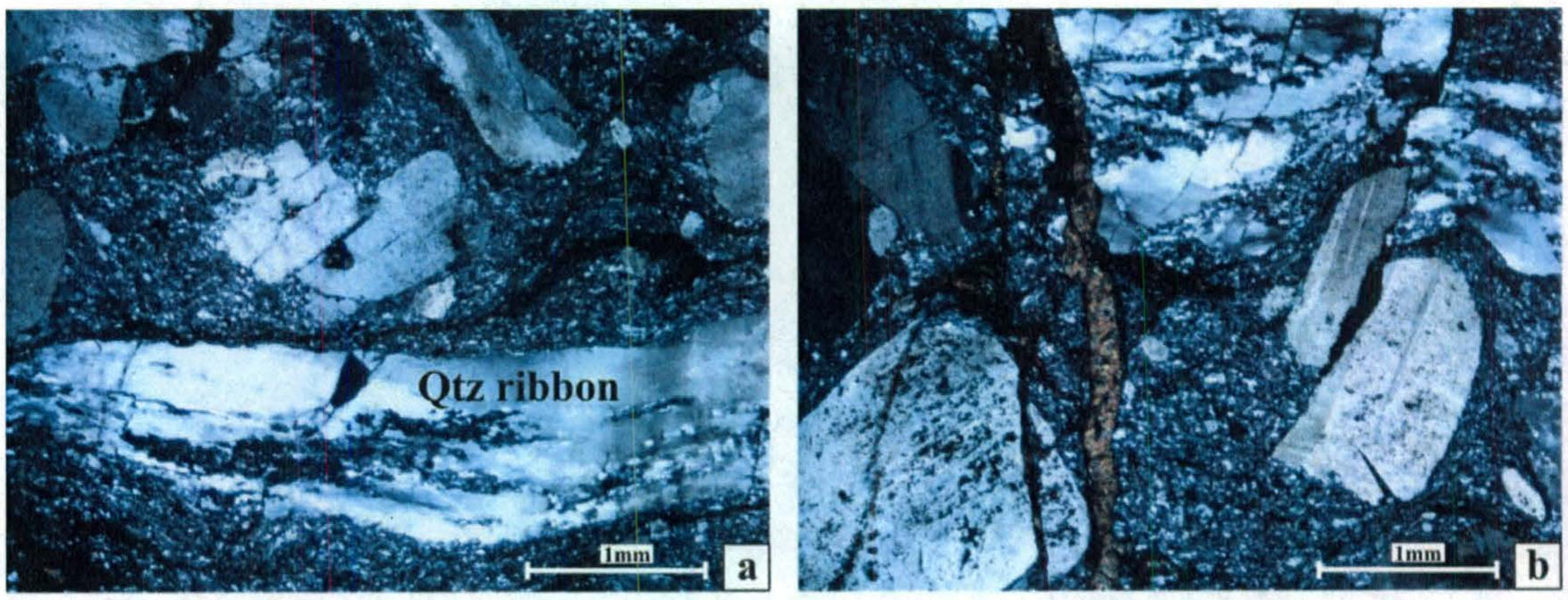

Plate 2.6: Photomicrographs of granodiorite in cross-polarized light. (a) Blastomylonitic texture with quartz ribbons, indicative of ductile deformation (sample #118, Map 1). (b) Blastomylonitic texture, with epidote veins aligned parallel to foliation and also off-setting feldspar porphyroclasts and quartz ribbons (sample #118, Map 1).

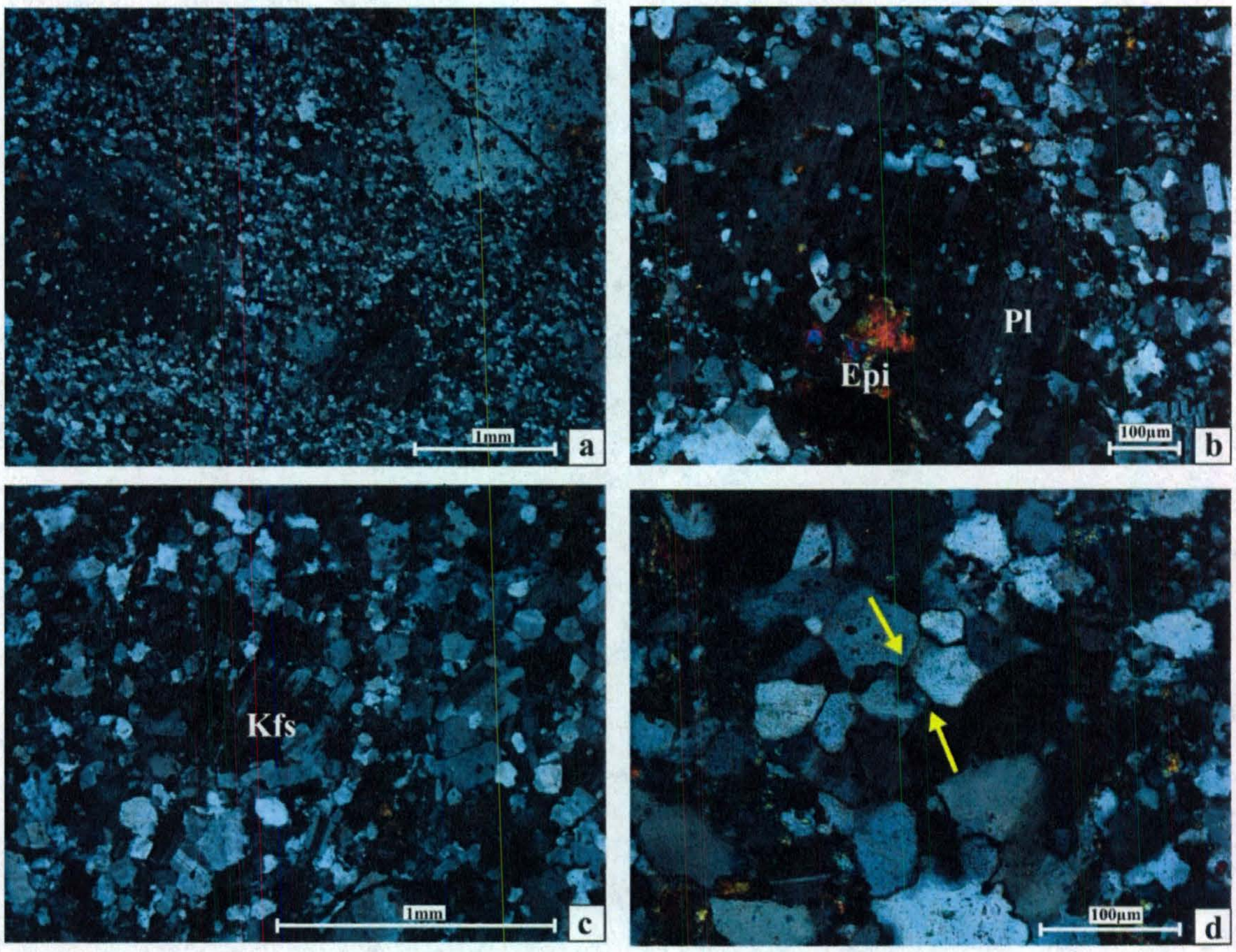

Plate 2.7: Photomicrographs of recrystallized granodiorite under crossed polars. (a) Subhedral, blocky feldspar laths enclosed by fine-grained, equigranular, recrystallized groundmass (sample #148, Map 1). (b) A lamellar-twinned plagioclase phenocryst with diffuse boundaries containing small, round quartz and feldspar crystals (sample #148, Map 1). (c) Cross-hatch twinning in alkali feldspar, surrounded by fine-grained recrystallized groundmass (sample #202, Map 3). (d) 120° triple junctions between feldspar and quartz grains in the groundmass (sample #148, Map 1).

and feldspar locally form annealing textures, characterized by euhedral crystals with sharp crystal faces that meet in 120° triple junctions (Plate 2.7d). Larger feldspar crystals range in length from about 0.5 to 5 mm, are about 1 mm long on average and locally display lamellar twinning. The large feldspar crystals contain round quartz and feldspar crystals that are similar to those in the groundmass, and have diffuse grain boundaries that grade into groundmass minerals, suggesting that the large feldspar grains have undergone partial recrystallization (Plate 2.7b). Thus, the large feldspar grains may be the only remnants of the original rock that are large enough to have resisted complete recrystallization. Because the large feldspar grains are similar in size to the largest feldspar grains observed in the granodiorite thin sections, and since they are, on average, larger and less elongate than feldspar phenocrysts in thin sections of feldspar porphyry, these samples may be granodiorite that has undergone extensive deformation and recrystallization.

2.2.2. Feldspar porphyry

2.2.2.1. Lithology and field relationships

This white- or yellowish-white-weathering unit has a very fine-grained, dark grey groundmass that encloses feldspar phenocrysts in about 10% abundance. Feldspar porphyry occurs extensively in Map 1 and is also found locally in Sections A-A' and B-B'. Like granodiorite, it appears to predate diorite and the mafic to felsic dyke swarm. In Sections A-A' and B-B', feldspar porphyry is exposed as sub-vertical, 0.5-20 m wide septa that are flanked by diorite, oxide-rich basaltic dykes, hornblende basaltic dykes or basaltic-andesitic dykes. In many cases, intrusive relationships are unclear due to

shearing at contacts, but chilled margins in mafic dykes against feldspar porphyry are preserved locally (Plate 2.8a). As well, intrusions adjacent to larger feldspar porphyry bodies enclose rafts of feldspar porphyry, such as those observed within a basaltic-andesitic dyke along Section B-B' (Plate 2.8b).

In Map 1, feldspar porphyry forms numerous large bodies, up to ~20 m X 40 m, that are separated by diorite. Because thin sections from feldspar porphyry bodies throughout Map 1 are petrographically indistinguishable, the feldspar porphyry bodies represent the remnants of a feldspar porphyry intrusion that has been infiltrated by diorite and, subsequently, by a swarm of mafic to felsic dykes. This is supported by the abundance of feldspar porphyry blocks within diorite, both adjacent to larger feldspar porphyry bodies and isolated within diorite. Large feldspar porphyry bodies in Map 1 host several types of dykes, including andesitic, basaltic-andesitic, oxide-rich andesitic and hornblende-porphyritic andesitic dykes, which locally display chilled margins (Plate 2.8c-f) and often separate or contain blocks of feldspar porphyry (Plate 2.9a-d). Feldspar porphyry is also cross-cut by a rhyolitic dyke in Map 1, as well as along Section A-A'. Although the rhyolitic dykes are dark grey and glassy-textured throughout, and chilled margins are not evident, their younger age is substantiated by flow banding that is parallel to contacts with feldspar porphyry (Plate 2.9e).

The age relationship between feldspar porphyry and granodiorite is poorly defined by field relationships but feldspar porphyry is interpreted to be younger than granodiorite. Therefore, because feldspar porphyry appears to be younger than granodiorite but older than diorite and the swarm of mafic to felsic dykes, it is interpreted to be the second oldest mapped unit in the study area.

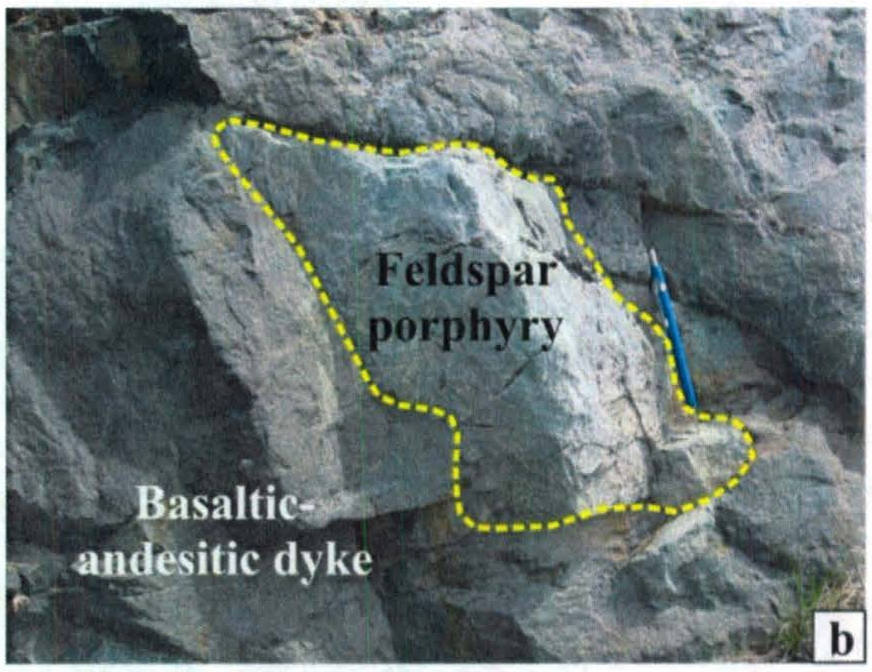

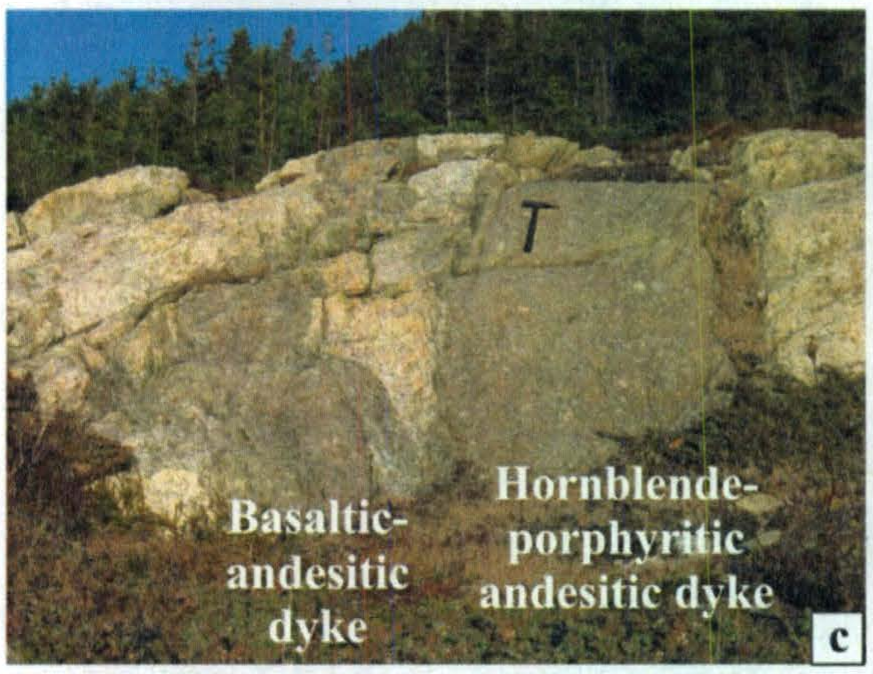

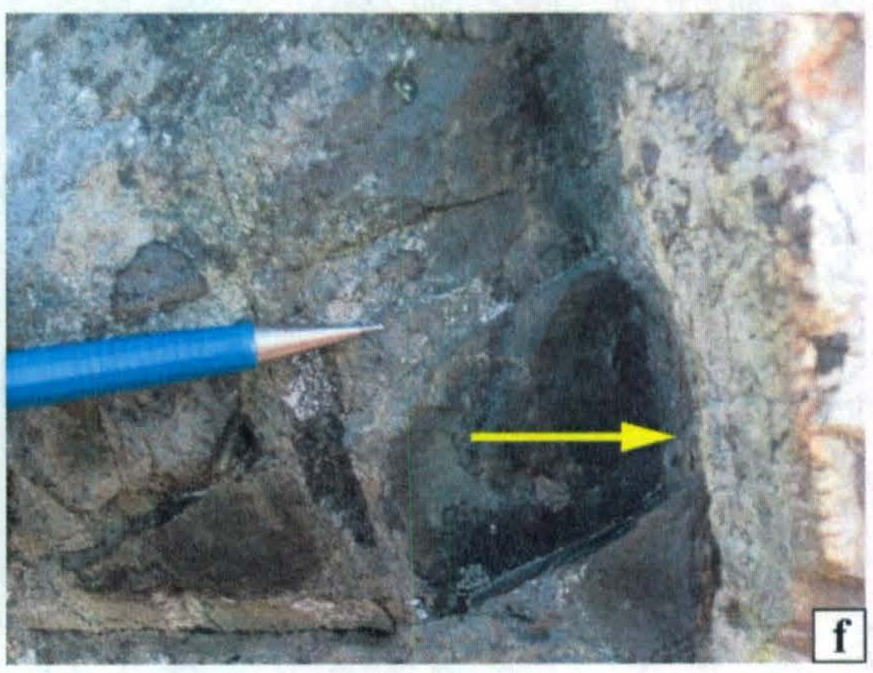

Plate 2.8: Field photographs of feldspar porphyry. (a) A chilled margin in an unsampled mafic dyke against feldspar porphyry (Section A-A'). (b) A raft of feldspar porphyry within a basaltic-andesitic dyke (Section B-B'). (c) A hornblende-porphyritic andesitic dyke and a basaltic-andesitic dyke hosted by feldspar porphyry (Map 1). (d) Thin, basaltic-andesitic dykes hosted by feldspar porphyry (Map 1). (e) An unsampled mafic or intermediate dyke offset within feldspar porphyry (directly north of Map 1). (f) A chilled margin in a basaltic-andesitic dyke against feldspar porphyry (Map 1).

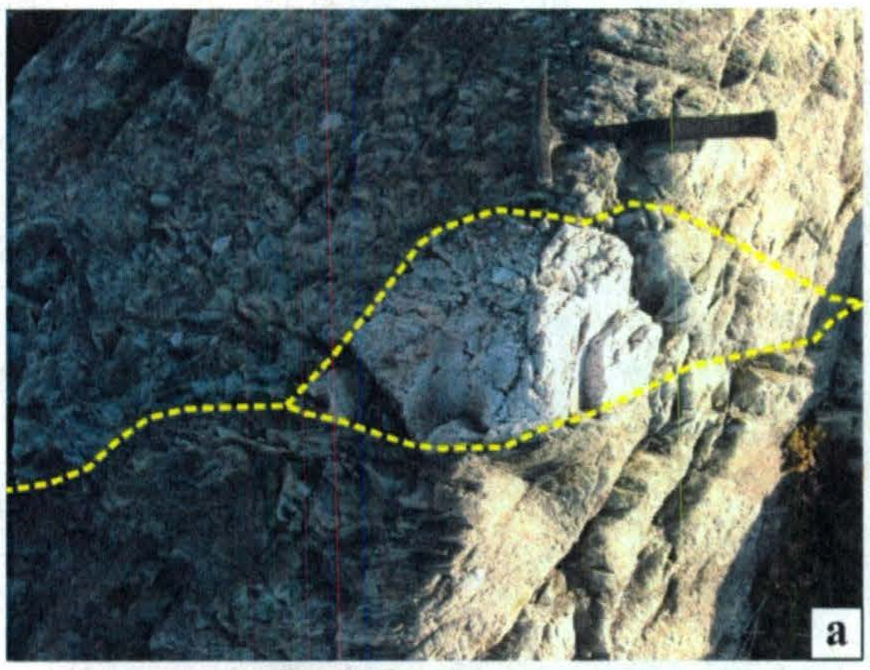

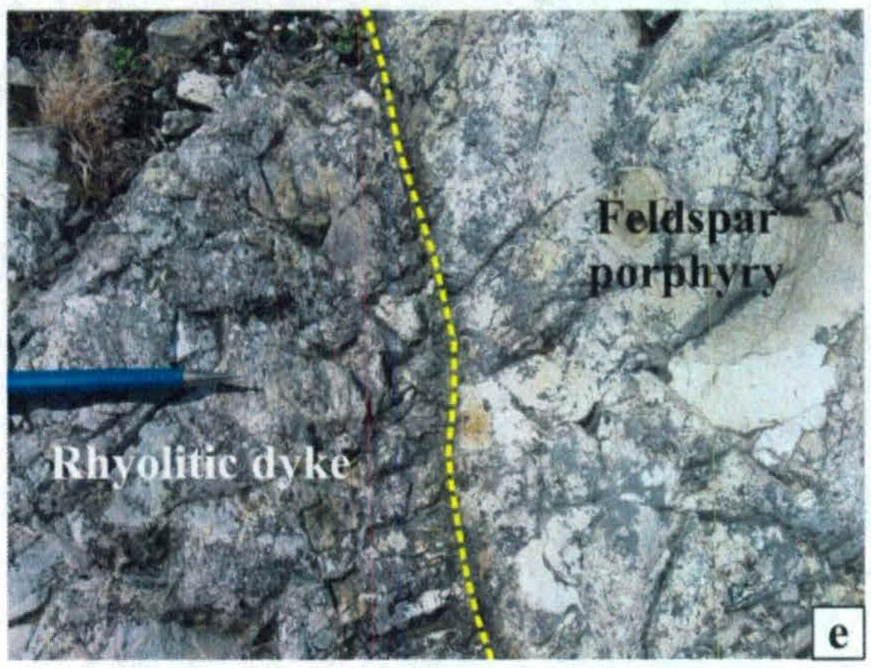

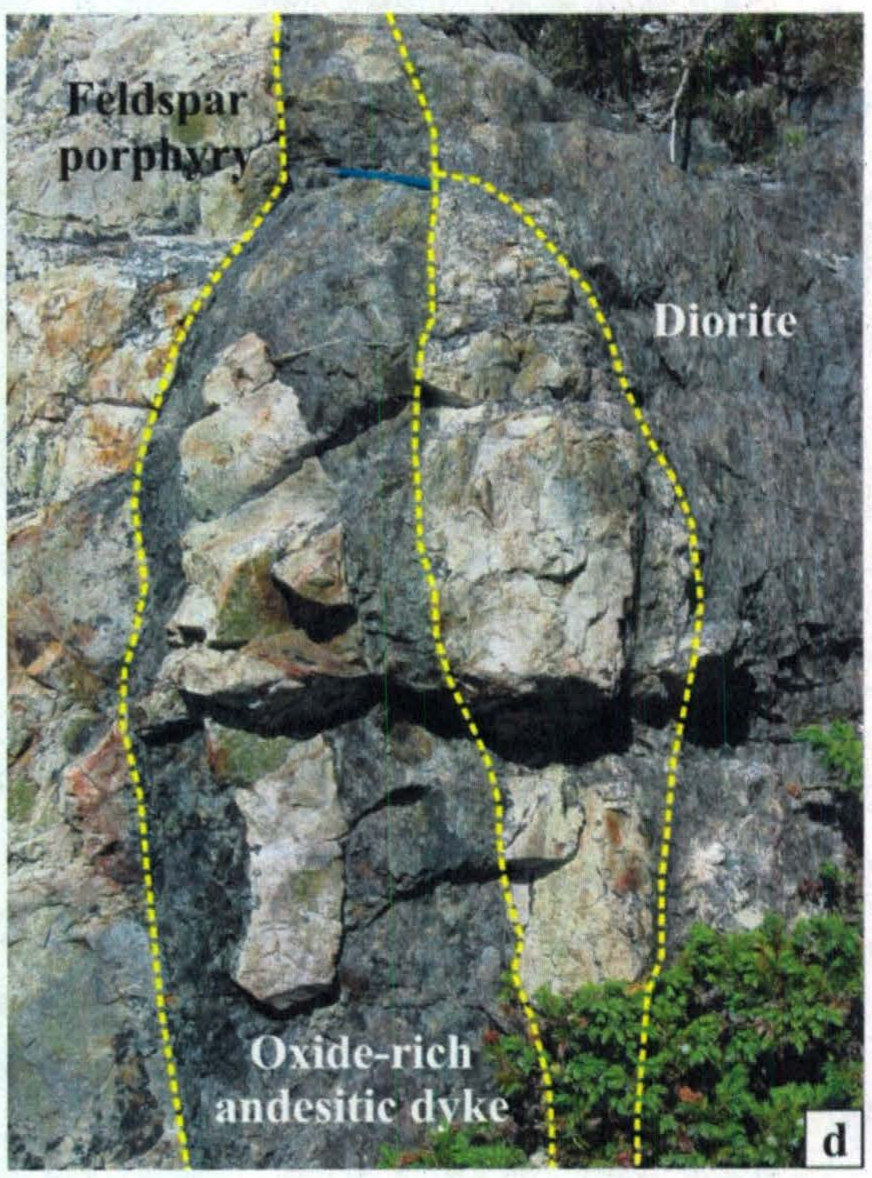

Plate 2.9: Field photographs of feldspar porphyry in Map 1. (a) A block of feldspar porphyry between two andesitic dykes. (b) Slivers of feldspar porphyry between andesitic and basaltic-andesitic dykes. (c) A block of feldspar porphyry within a basaltic-andesitic dyke. (d) A block of feldspar porphyry within an oxide-rich andesitic dyke and a second block of feldspar porphyry between an oxide-rich andesitic dyke and diorite. (e) A rhyolitic dyke with flow-banding parallel to the contact with feldspar porphyry.

2.2.2.2. Petrography

In thin section, plagioclase and alkali feldspar phenocrysts are subhedral to euhedral, elongate and blocky laths that range in length from 0.5 to 4 mm, and are about 1 mm long on average (Plate 2.10a). The phenocrysts display simple and lamellar twinning and some crystals exhibit undulatory extinction. They typically form clusters of up to 5 intergrown crystals. The phenocrysts are surrounded by a groundmass that consists of small (~150 μm) subhedral feldspar laths enclosed by patches of anhedral quartz and feldspar. These patches of quartz and feldspar commonly display granophyric texture, characterized by vermicular intergrowths of quartz and feldspar that radiate outwards from central feldspar laths (Plate 2.10b). Granophyric texture is thought to represent simultaneous crystallization of quartz and feldspar from a late-stage igneous melt (Nesse, 2000).

Feldspar porphyry contains minor amounts of opaque minerals that occur as anhedral blebs disseminated throughout the groundmass, as well as larger (up to ~250 μm) subhedral crystals. Secondary chlorite and epidote occur as anhedral blebs and aggregates throughout the groundmass and in minor amounts in feldspar phenocrysts, which also contain tiny opaque inclusions and sericite (Plate 2.10c). Locally, feldspar phenocrysts have been partially or fully replaced by aggregates of epidote. Although feldspar porphyry is rarely foliated, parallel alignment of opaque minerals, clots of chlorite and chains of epidote crystals define weak foliations in some thin sections. Feldspar porphyry contains veins that are filled with quartz or epidote, which is often accompanied by opaque minerals and/or chlorite.

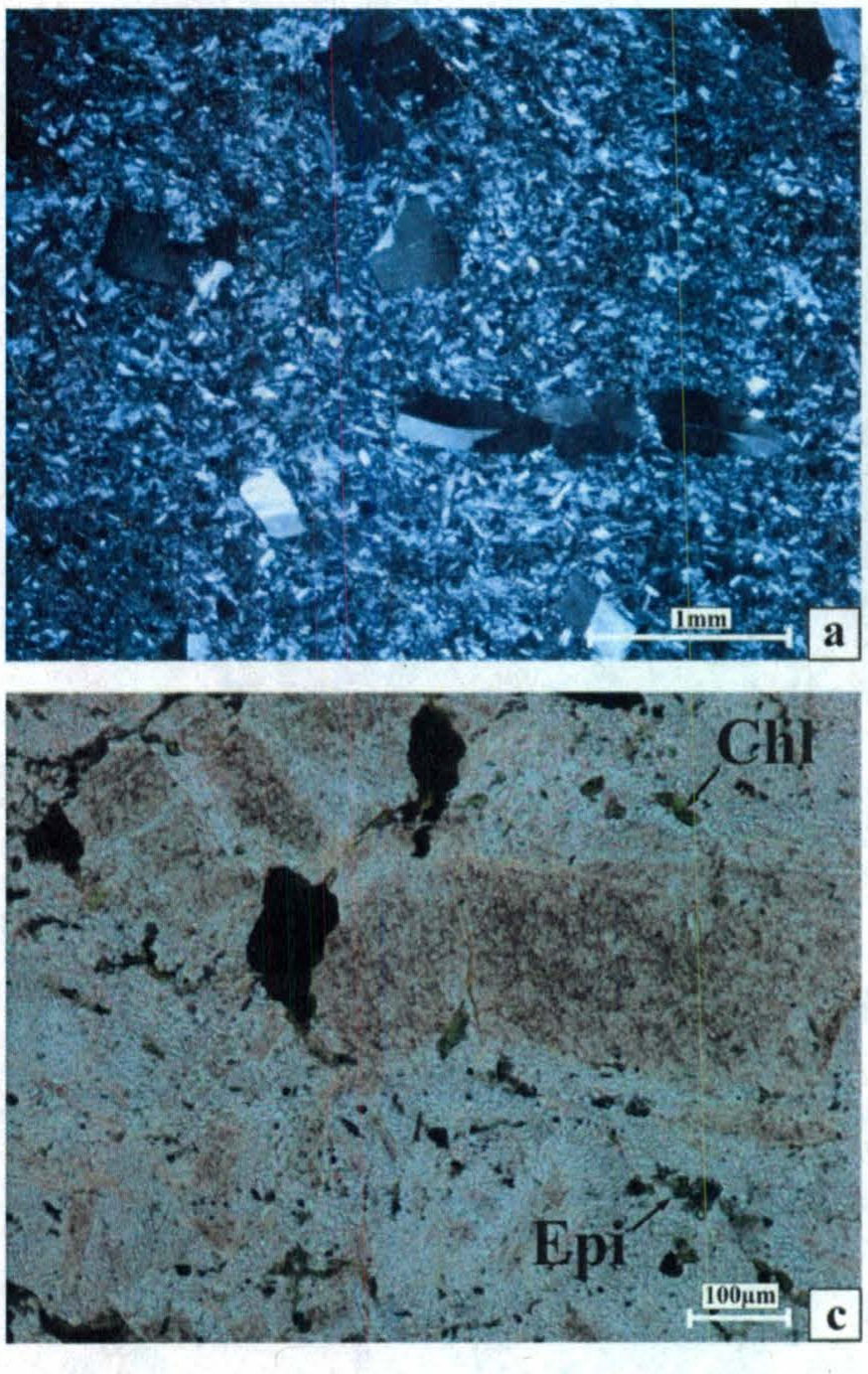

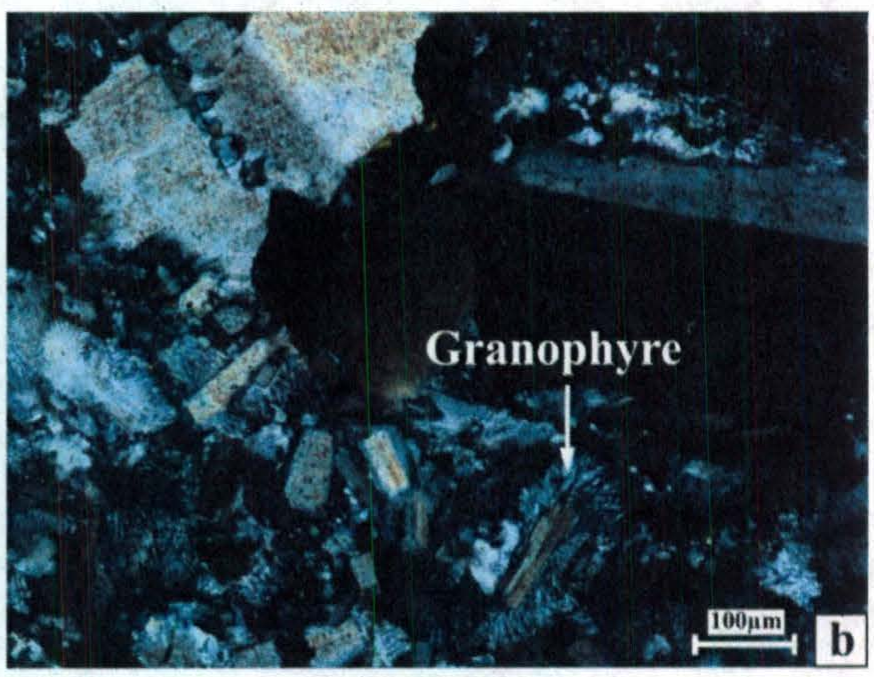

Plate 2.10: Photomicrographs of feldspar porphyry, under crossed polars unless otherwise indicated. (a) Feldspar phenocrysts with simple twins, locally exhibiting undulatory extinction (sample #112, Map 1). (b) Granophyre surrounds feldspar laths in the groundmass near a cluster of feldspar phenocrysts (sample #98, Map 1). (c) Same view as (b) in plane polarized light, showing chlorite and epidote throughout the groundmass, and sericite and tiny opaque inclusions in feldspar phenocrysts.

2.2.3. Gabbro

2.2.3.1. Lithology and field relationships

This dark brown-weathering, fine- to medium-grained gabbro is dark green on fresh surfaces and contains abundant discontinuous epidote veins. It is sparsely feldspar-porphyritic (<3%) with subhedral, blocky plagioclase phenocrysts that range in length from 1.5 to 4 mm. Gabbro occurs only in Map 2 and is interpreted to be the oldest mafic unit in the study area. Gabbro hosts several mafic and intermediate dykes and locally occurs as septa between dykes. Clear chilled margins are present in andesitic and basaltic dykes at contacts with gabbro, and a thin, subtle chilled margin occurs in a feldspar-porphyritic hornblende basaltic dyke (Plate 2.11). As well, slivers of gabbro host rocks are preserved at the contact between a basaltic dyke and an oxide-rich andesitic dyke (Plate 2.12a). In addition, gabbro shares an irregular contact with a block of granodiorite (Plate 2.12b), and contains fragments of granodiorite surrounded by chilled margins.

While intrusive relationships indicate without doubt that gabbro post-dates granodiorite and hosts basaltic, hornblende basaltic and andesitic dykes, the age relationship between gabbro and diorite remains uncertain. Although diorite shares a contact with gabbro, the contact is partially inferred along a fractured boundary, and no chilled margin is present in either unit along the exposed part of the contact. Hence, the relative ages of diorite and gabbro are ambiguous. Because gabbro is relatively fine-grained and no volcanic features were observed in outcrop or thin section, it is interpreted to be a shallow-level intrusion.

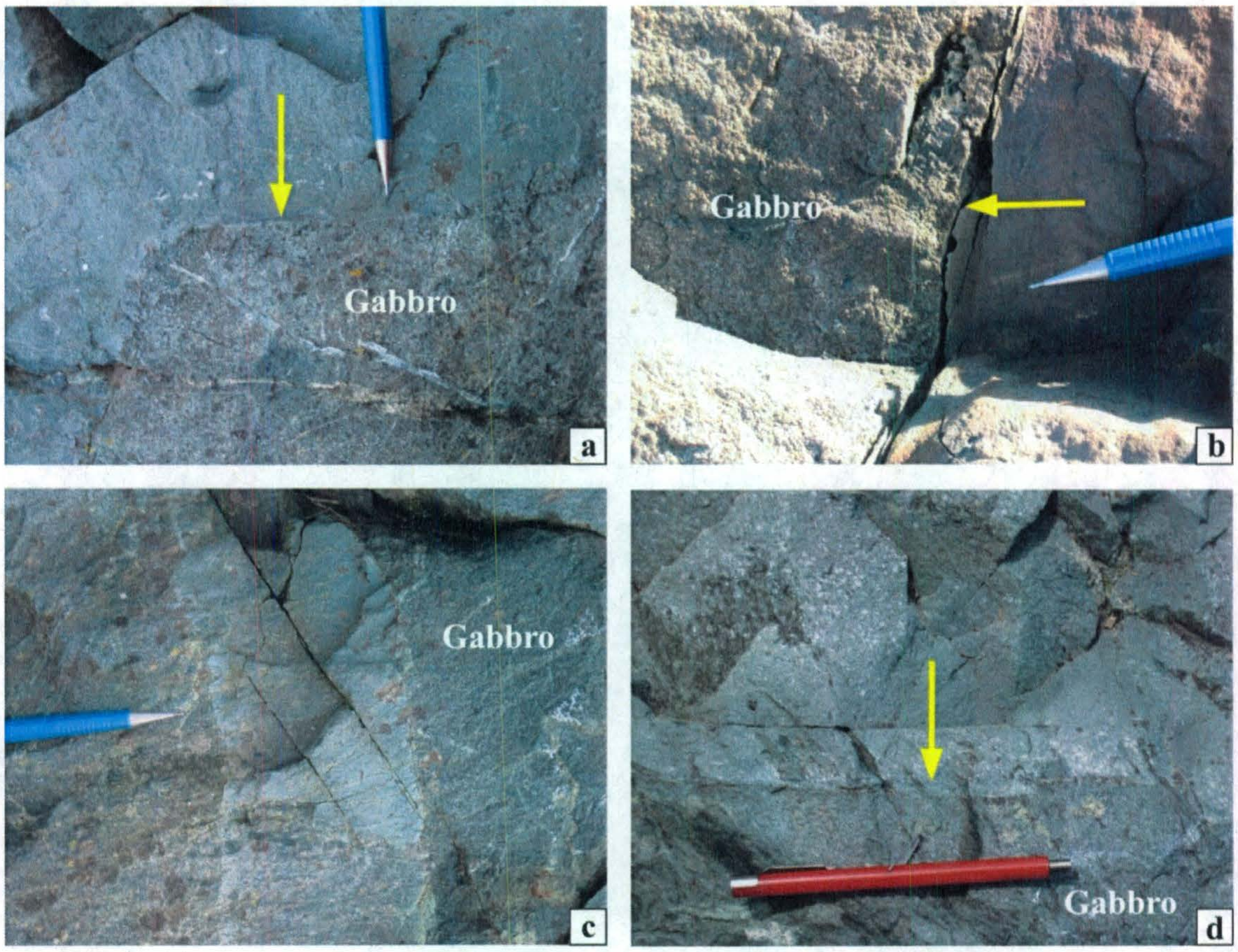

Plate 2.11: Field photographs of gabbro in Map 2. (a) & (b) Well-developed chilled margins in basaltic dykes against gabbro host rocks. (c) An offshoot of a basaltic dyke chilled against gabbro host rocks. (d) A subtle chilled margin in a feldspar-porphyritic hornblende basaltic dyke against gabbro host rocks.

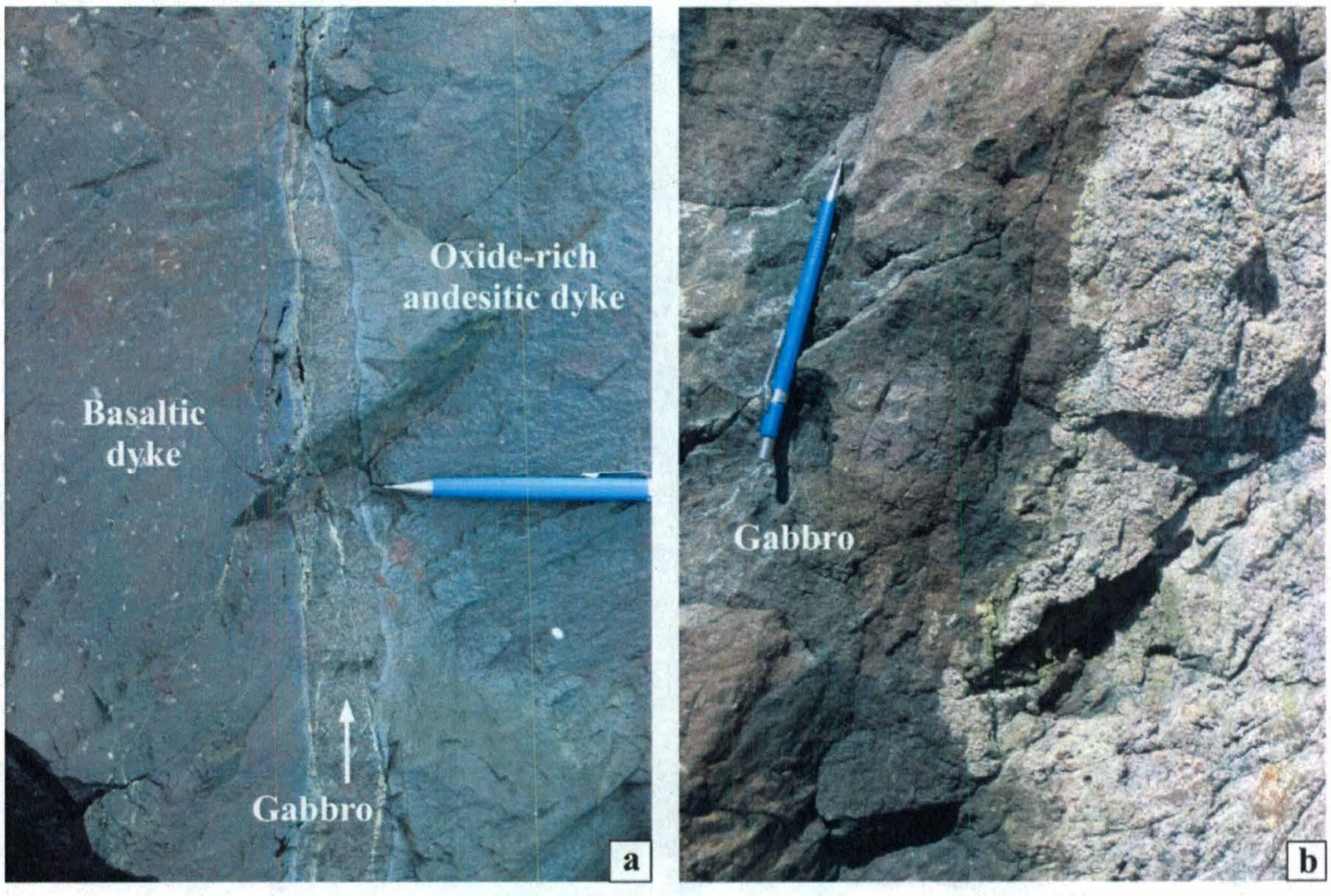

Plate 2.12: Field photographs of gabbro in Map 2. (a) A basaltic dyke and an oxide-rich andesitic dyke chilled against a sliver of gabbro. (b) An irregular contact between gabbro and a block of granodiorite.

2.2.3.2. Petrography

In thin section, sub-ophitic texture is locally displayed by anhedral clinopyroxene grains that partially enclose subhedral plagioclase laths in the groundmass (Plate 2.13a and b). Clinopyroxene is fringed by needles of actinolite, and clinopyroxene crystals are commonly partially replaced by patches of actinolite ± chlorite. Many clinopyroxene grains have been reduced to remnants surrounded by aggregates of actinolite ± chlorite pseudomorphing the original clinopyroxene grain (Plate 2.13c and d). Subhedral, tabular hornblende crystals are also observed in thin section, and are partially replaced by aggregates of actinolite ± chlorite. In many cases, optically-continuous, tabular-shaped aggregates of actinolite ± chlorite appear to have fully replaced igneous hornblende.

Opaque minerals form angularly and irregularly shaped aggregates that are interpreted to be ilmeno-magnetite that has been altered to ilmenite and leucoxene (Plate 2.13c). Locally, chlorite forms elongate clots with subhedral, bladed epidote crystals concentrated at the edges. These aggregates are up to 2 mm long, and while many are irregular in shape, some are lath-shaped and may be pseudomorphing another mineral. Extensive greenschist-facies metamorphism is evident not only in the partial replacement of clinopyroxene and hornblende, but also in the occurrence of chlorite, actinolite and epidote as tiny (< 50 μm) crystals within and between all igneous minerals. This includes plagioclase, which has also been significantly sericitized. In addition to epidote veins, which are ubiquitous in thin section and locally contain carbonate or Fe-Ti-oxides, minor quartz veins were also observed.

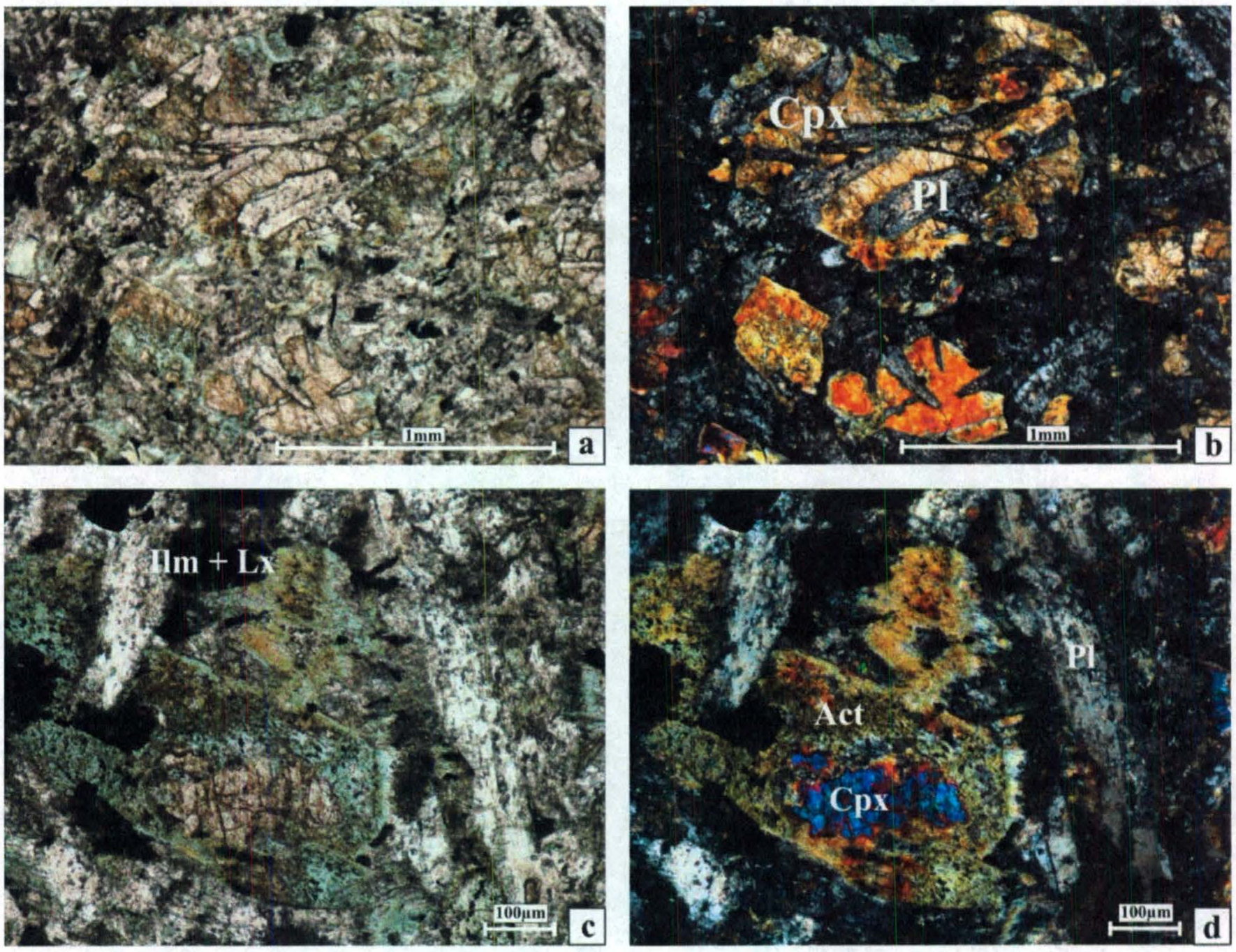

Plate 2.13: Photomicrographs of gabbro (sample #82, Map 2) in plane polarized light, unless otherwise indicated. (a) Intense alteration of clinopyroxene, plagioclase, hornblende and opaque minerals under greenschist-facies conditions has produced abundant chlorite, actinolite and epidote. (b) Same view as (a) under crossed polars, highlighting sub-ophitic texture formed by clinopyroxene enclosing plagioclase laths. (c) A remnant of clinopyroxene surrounded by an optically-continuous, tabular aggregate of actinolite and chlorite. Also note the occurrence of opaque minerals as aggregates of ilmenite and leucoxene, which are interpreted to be altered ilmeno-magnetites. (d) Same view as (c) under crossed polars.

2.2.4. Diorite

2.2.4.1. Lithology and field relationships

This unit consists of magnetic diorite that is dark green on fresh surfaces, weathers dark brownish-grey to light greyish-brown and locally contains discontinuous epidote veins. Unlike most mafic and intermediate units in the study area, diorite is medium-grained. It is weakly feldspar-porphyritic (<5%) with subhedral, 1-4 mm long, blocky plagioclase phenocrysts.

Diorite is the most widespread of the mafic-to-intermediate units in the study area and hosts many dykes of different lithologies. This unit hosts several dykes along Section A-A', including an oxide-rich basaltic dyke with a clear chilled margin (Plate 2.14a). Diorite also forms septa between mafic dykes in Section A-A', including a ~1 m wide sliver of diorite that is flanked by a hornblende basaltic dyke and a basaltic dyke with a clear chilled margin (Plate 2.14b). In Map 2, diorite is flanked by basaltic and hornblende basaltic dykes with chilled margins, and occurs as blocks between dykes (Plate 2.14c) and within oxide-rich andesitic dykes.

In Map 1, diorite contains blocks of granodiorite and feldspar porphyry. Some blocks are isolated within diorite, several metres away from the nearest felsic block, whereas others are adjacent to contacts with larger felsic bodies (Plate 2.3b and c). The shapes of some of these blocks are matched by irregular edges on neighbouring felsic bodies, evidence for the plucking of blocks from larger felsic bodies by intruding diorite melt. Most chilled margins in Map 1 are obscured by lichen and shearing along contacts, but a subtle chilled margin is present in diorite against granodiorite (Plate 2.3d). In Map 1, diorite hosts at least twenty-five individual dykes representing several different

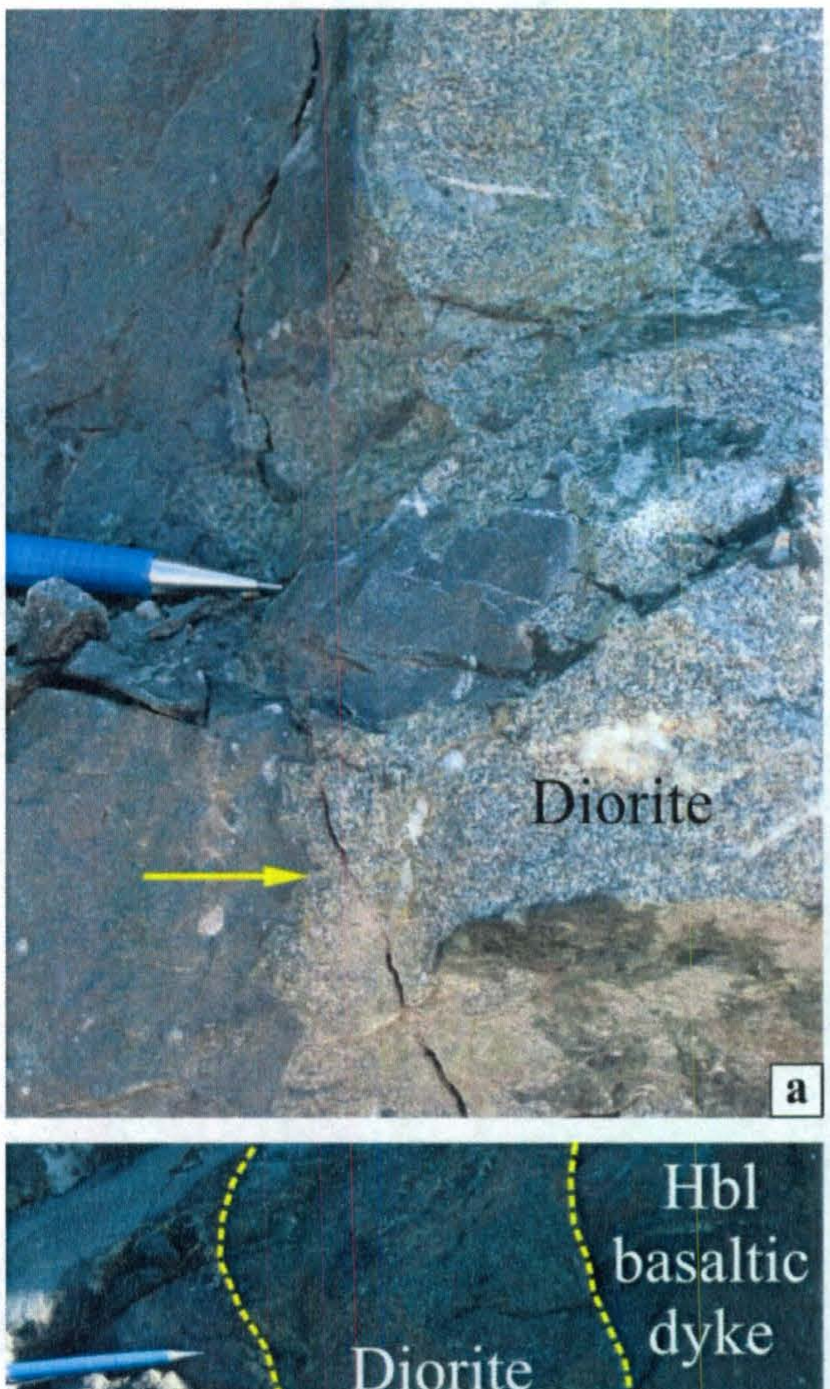

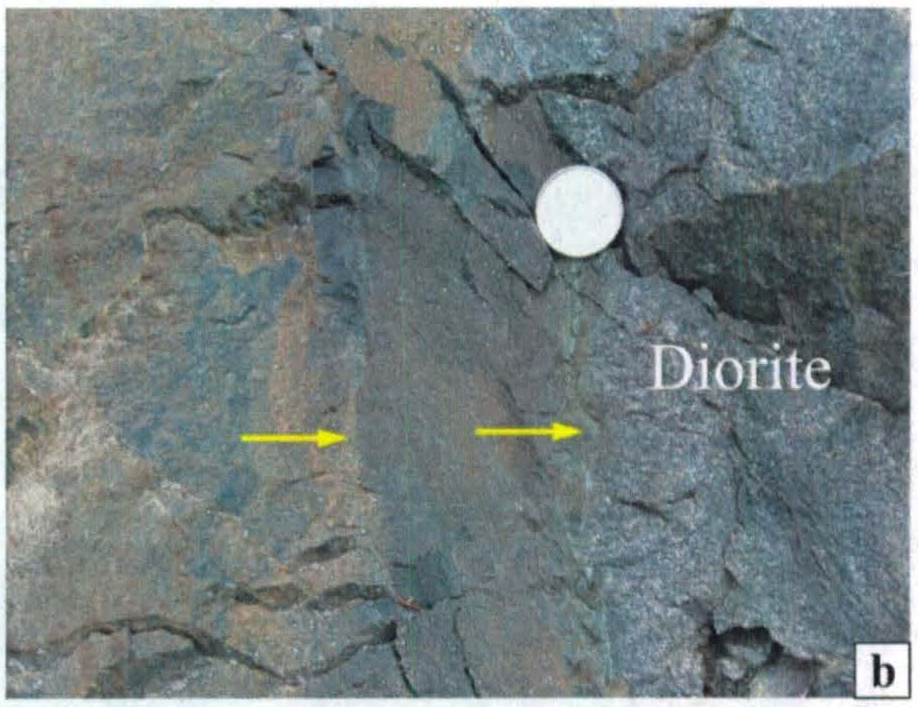

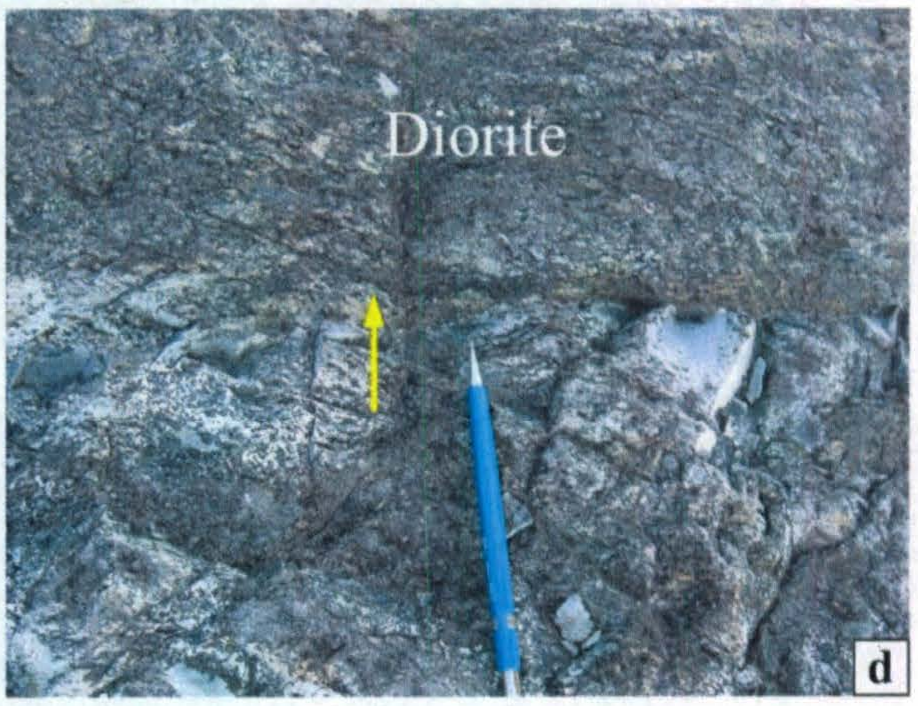

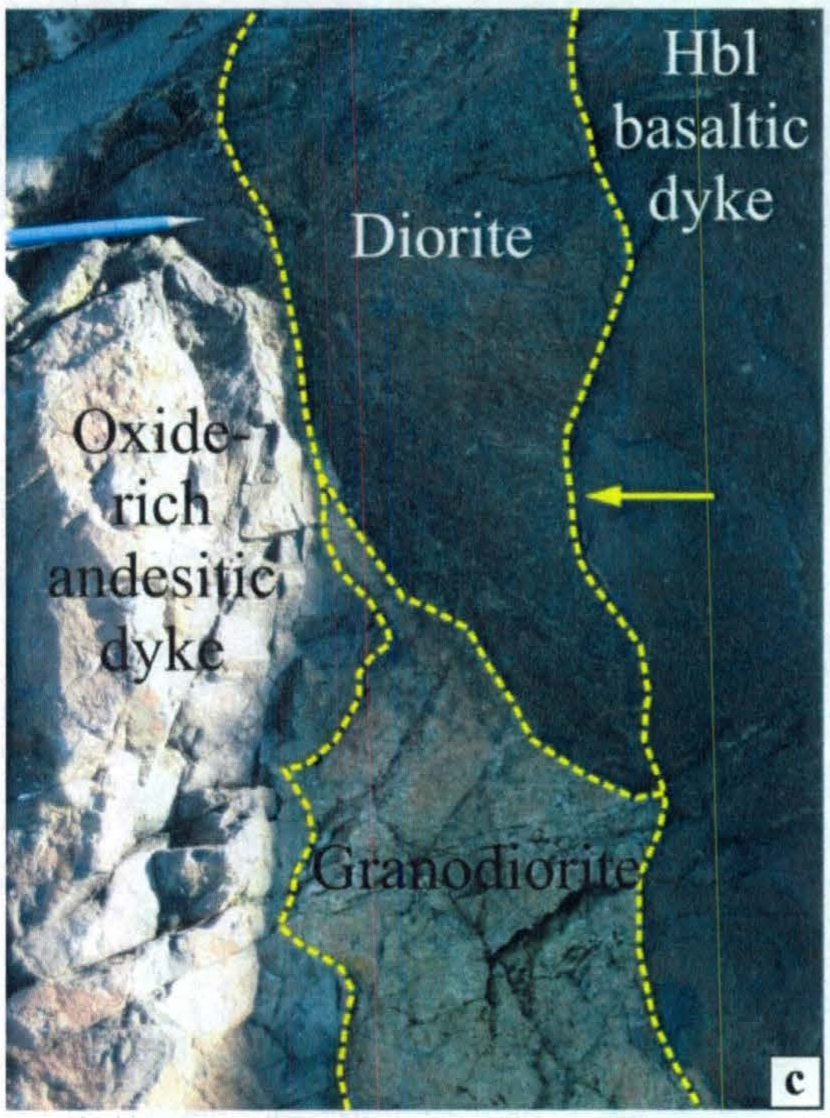

Plate 2.14: Field photographs of diorite. (a) An irregular contact with a clear chilled margin in an oxide-rich basaltic dyke against diorite (Section A-A'). (b) A well-developed chilled margin in a basaltic dyke against diorite. Note the second chilled margin in the basaltic dyke, indicating multiple injections of basaltic melt (Section A-A'). (c) A hornblende basaltic dyke with a chilled margin against blocks of diorite and granodiorite (Map 2). (d) A chilled margin in an oxide-rich andesitic dyke against diorite (Map 1).

lithologies, including dykes from every mafic and intermediate unit described below. For example, an oxide-rich andesitic dyke displays clear chilled margins against diorite and encloses a diorite block (Plates 2.14d and 2.15a). Chilled margins are also present in andesitic dykes against diorite (Plate 2.15b and c). As well, a rhyolitic dyke cross-cuts diorite, and its younger age is supported by flow banding that is parallel to the contact with diorite (Plate 2.15d). Furthermore, there is a subtle chilled margin in a rhyolitic dyke against diorite in Section A-A' (Plate 2.15e).

Due to its relatively small grain size and lack of extrusive features, diorite is interpreted to be a shallow-level intrusion. Field relationships indicate that diorite intruded at least the northern portion of the study area after the emplacement and crystallization of granodiorite and feldspar porphyry. As a result, discontinuous bodies of granodiorite and feldspar porphyry occur throughout diorite, and many smaller blocks were entrained in the diorite melt. The intrusion of diorite appears to have been followed by a swarm of mafic to intermediate dykes and rare felsic dykes, which occur throughout the study area and cross-cut diorite and gabbro, as well as older granodiorite and feldspar porphyry.

2.2.4.2. Petrography

In thin section, hornblende occurs as green to light green pleochroic, subhedral tabular crystals that have all undergone some degree of replacement by actinolite ± chlorite (Plate 2.16a-d). Twinned hornblende crystals are occasionally observed through the actinolite ± chlorite metamorphic overprint. Commonly, parallel actinolite needles form aggregates that are optically continuous and define a tabular shape, although some actinolite needles typically extend into adjacent plagioclase grains. This texture is

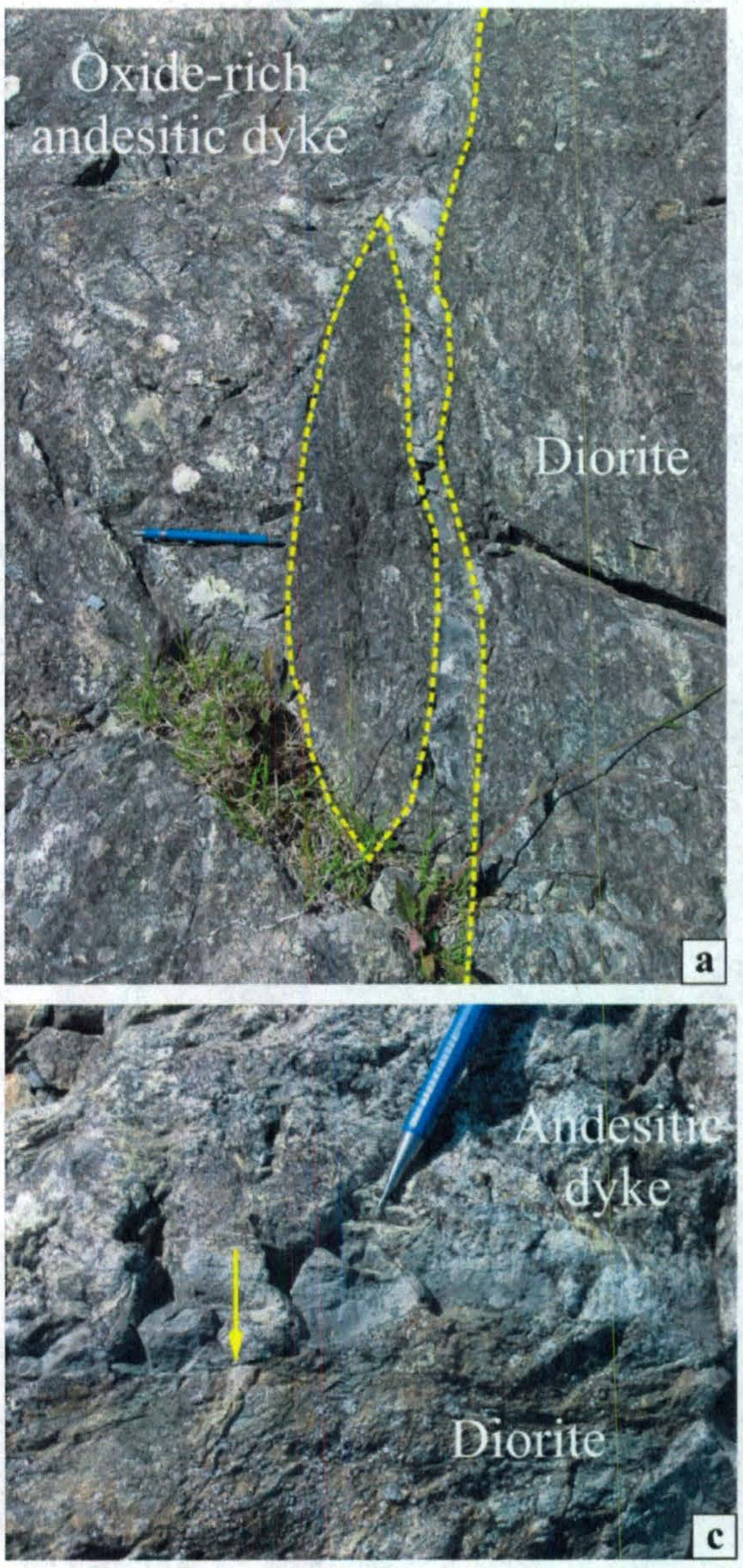

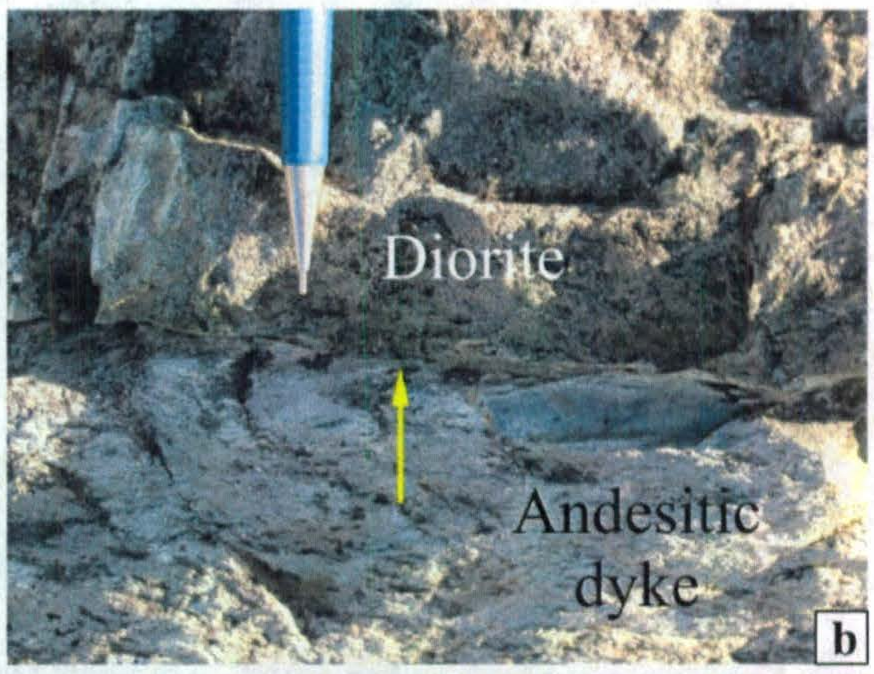

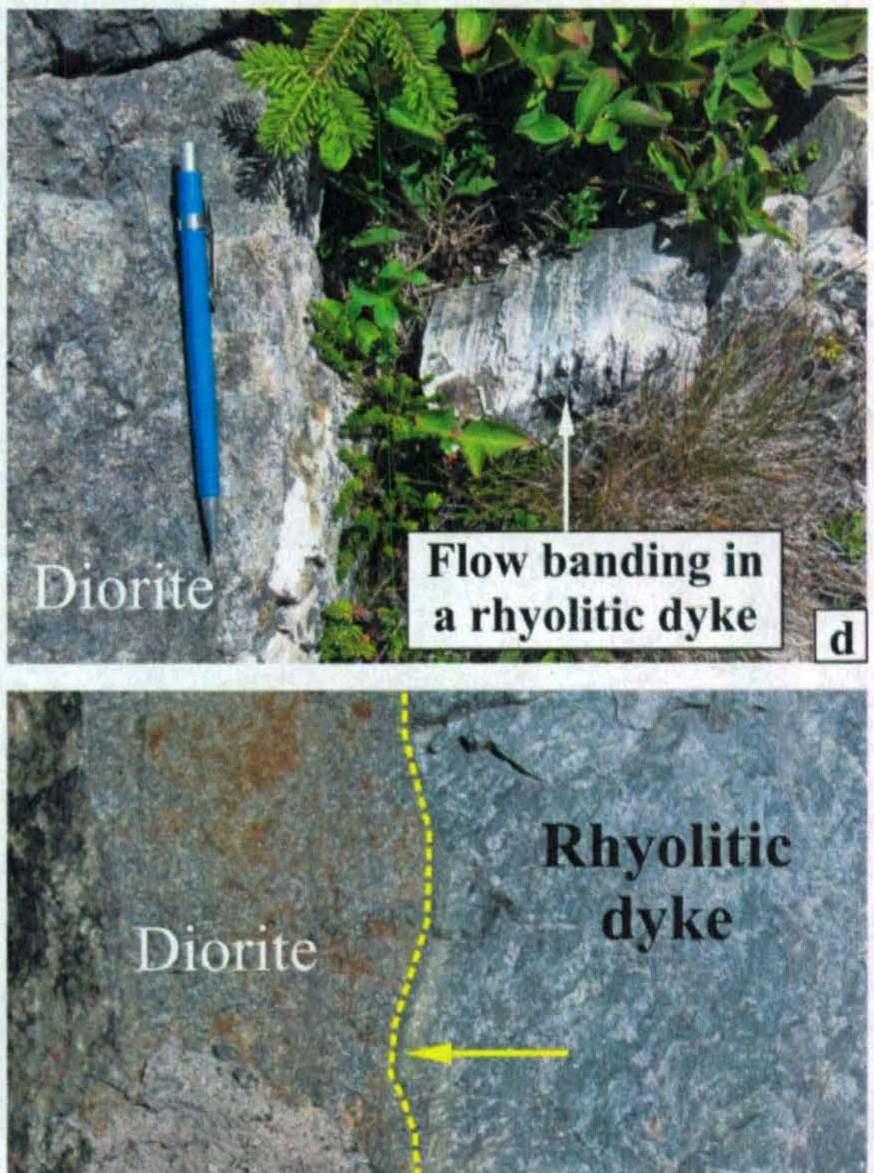

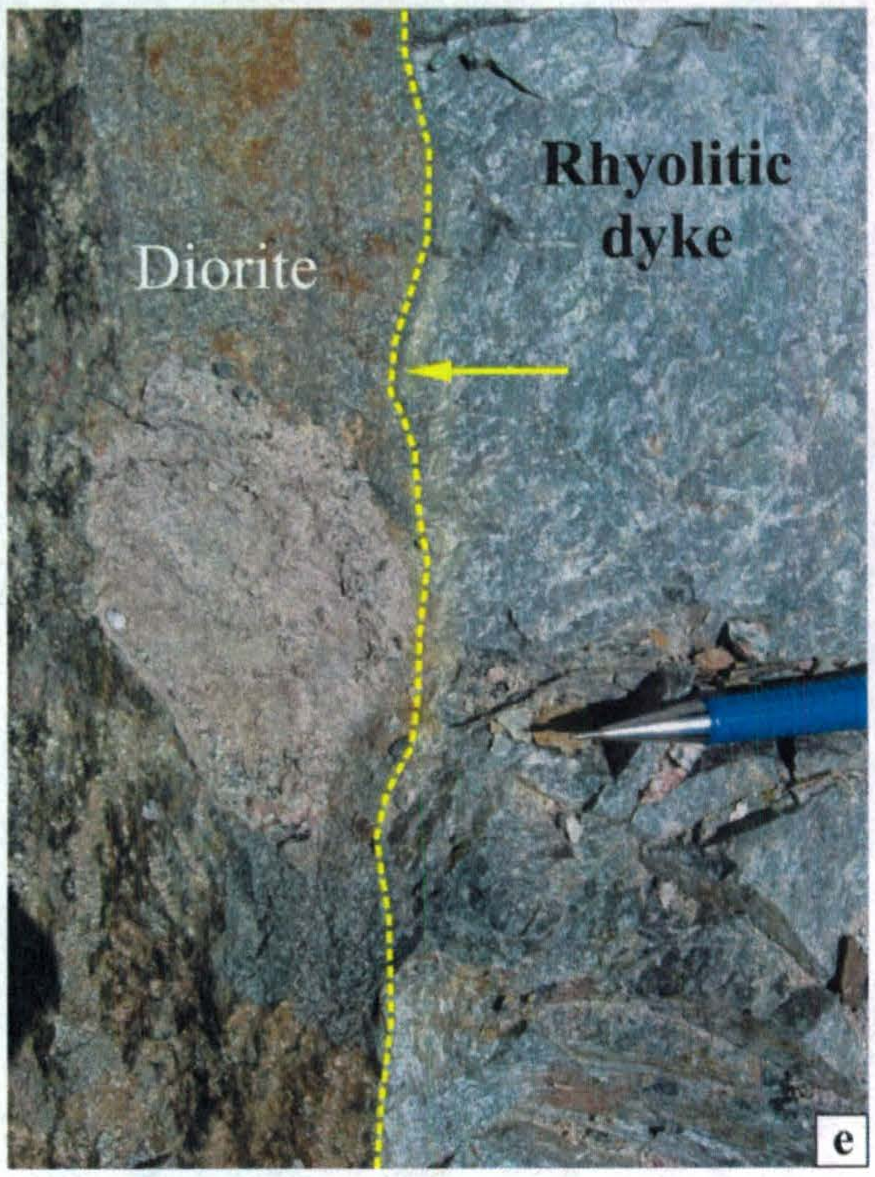

Plate 2.15: Field photographs of diorite. (a) The same oxide-rich andesitic dyke in Plate 2.14d containing a block of diorite. (b) An andesitic dyke chilled against diorite (Map 1). (c) A chilled margin in an andesitic dyke against diorite (Map 1). (d) A rhyolitic dyke hosted by diorite with flow-banding parallel to dyke margins (Map 1). (e) A subtle, light-green coloured chilled margin in a rhyolitic dyke against diorite (Section A-A').

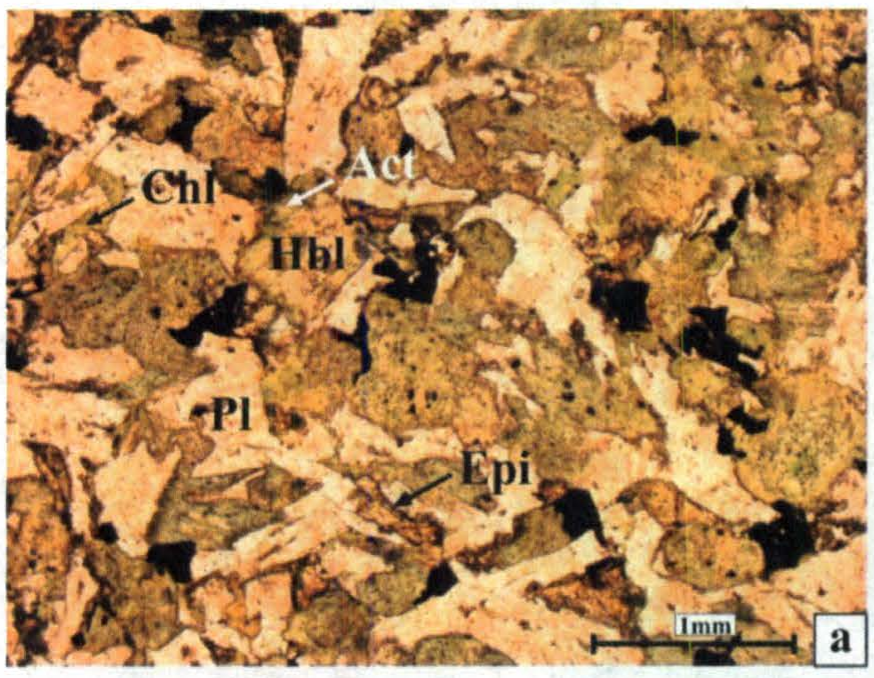

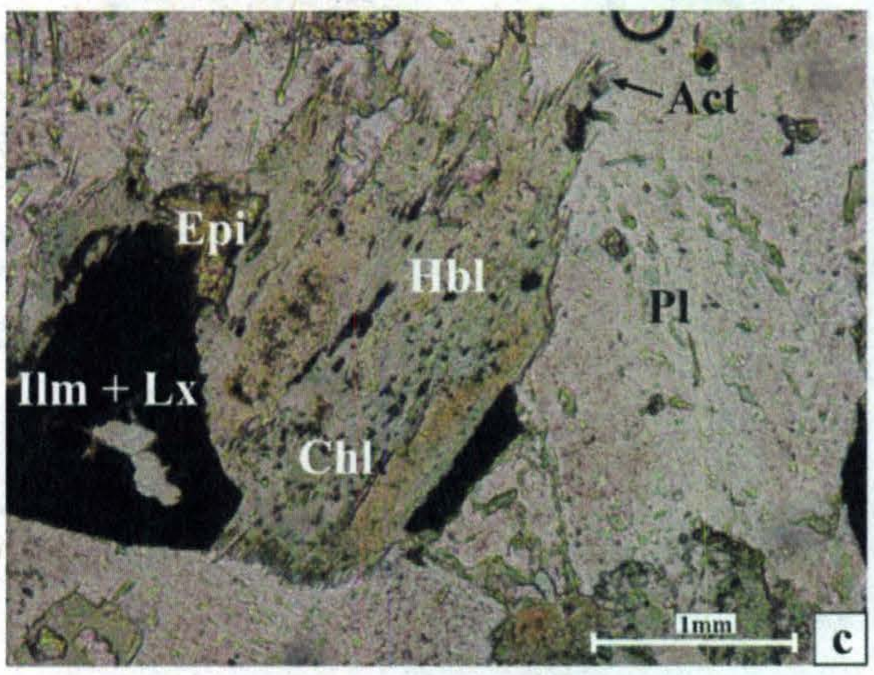

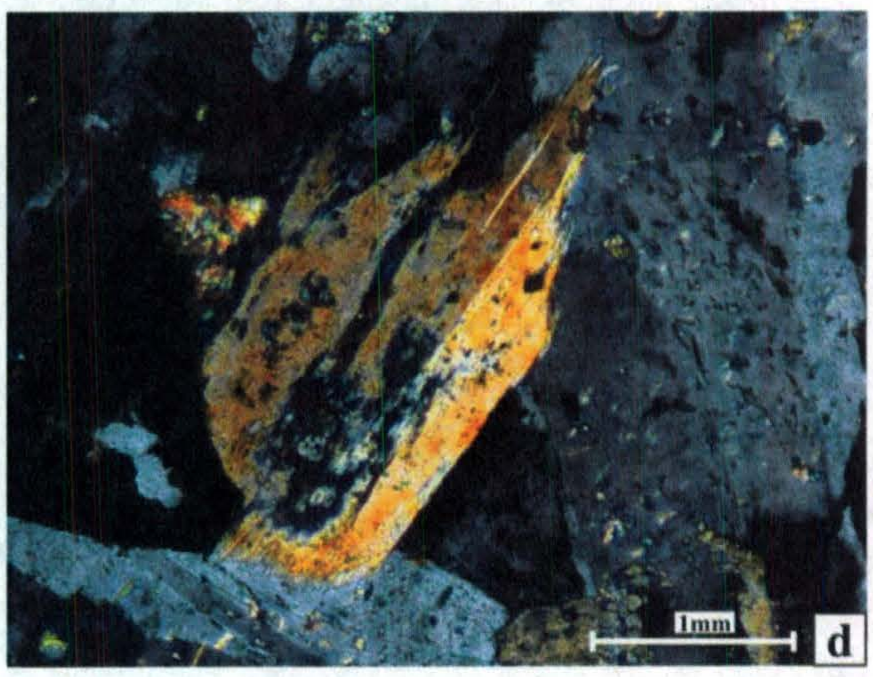

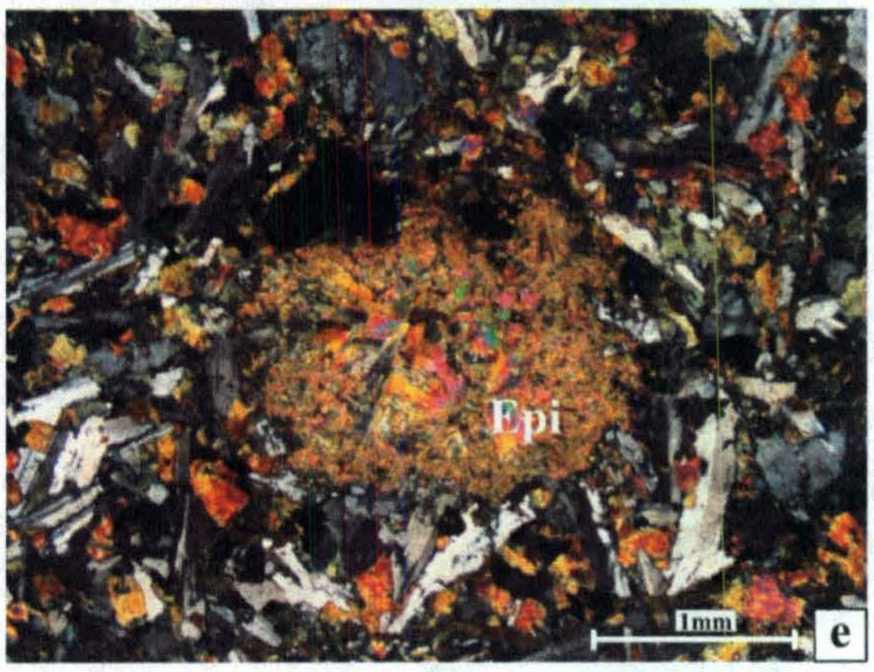

Plate 2.16: Photomicrographs of diorite in plane-polarized light, unless otherwise indicated. (a) The dominant mineral assemblage consists of medium-grained hornblende, plagioclase and opaque minerals (sample #102, Map 1). (b) Same view as (a) under crossed polars, showing patches and rims of chlorite and actinolite on hornblende. (c) Hornblende has been partially replaced by actinolite and chlorite. Also note blebs of epidote and chlorite in plagioclase (sample #77, Map 2). (d) Same view as (c) under crossed polars, showing a twin in hornblende, and optically continuous bundles of actinolite needles extending into plagioclase. (e) Viewed under crossed polars, a rectangular aggregate of epidote crystals appears to be pseudomorphing another mineral (sample #102, Map 1).

interpreted to represent the transitional replacement of igneous hornblende by actinolite under greenschist-facies metamorphic conditions. Plagioclase occurs in the groundmass as subhedral, blocky or elongate laths averaging 1 mm in length, although anhedral plagioclase grains commonly fill spaces between plagioclase laths and other minerals. Plagioclase has undergone various degrees of sericitization and contains actinolite needles, anhedral blebs of epidote and chlorite and nearly submicroscopic Fe-Ti-oxide inclusions (Plate 2.16c). Opaque minerals are concentrated in angular and square-shaped aggregates along with a dark grey-brown alteration material; these are interpreted to be ilmeno-magnetite altered to ilmenite + leucoxene (Plate 2.16c). Epidote locally forms round or irregularly-shaped aggregates of radial crystals, and also forms rectangular aggregates up to 2.5 mm long (Plate 2.16e). These are probably pseudomorphs of another mineral, such as plagioclase phenocrysts. Where this unit is in or near shear zones, it has developed a weak foliation defined predominantly by the parallel alignment of Fe-Ti oxides, hornblende and greenschist-facies alteration minerals.

2.2.5. Hornblende-porphyritic andesitic dykes

2.2.5.1. Lithology and field relationships

This unit consists of two fine-grained andesitic dykes in Map 1 that are abundantly feldspar- and hornblende-porphyritic (~10% and ~10%, respectively). The easternmost dyke weathers dark brown and has a dark green groundmass, and the westernmost dyke weathers light brown and has a dark grey groundmass. The easternmost dyke cross-cuts diorite, feldspar porphyry (Plate 2.8c) and granodiorite, and is cross-cut by a basaltic-andesitic dyke. The hornblende-porphyritic andesitic dyke on

the west end of Map 1 also cross-cuts diorite and is cross-cut by an andesitic dyke and several hornblende basaltic dykes.

2.2.5.2. Petrography

The easternmost dyke consists of a plagioclase-rich groundmass that surrounds 0.5-3 mm long plagioclase phenocrysts and ~1 mm long hornblende phenocrysts (Plate 2.17a and b). In thin section (sample #138), plagioclase phenocrysts are subhedral-to-euhedral blocky crystals that contain abundant sericite and blebs of epidote, chlorite and actinolite. The hornblende phenocrysts are dark green-to-light green pleochroic, subhedral tabular crystals that contain patches of chlorite and actinolite (Plate 2.17b). A weak foliation is defined by the parallel alignment of Fe-Ti oxides, aggregates of chlorite and actinolite and chains of epidote throughout the groundmass.

The westernmost hornblende-porphyritic andesitic dyke consists of a plagioclase-rich groundmass that encloses 0.5-2.5 mm long plagioclase phenocrysts and ~0.5 mm long hornblende phenocrysts (Plate 2.17c and d). In thin section (sample #100), plagioclase phenocrysts are similar to those in the other hornblende-porphyritic andesitic dyke, but hornblende phenocrysts are unique: they are subhedral to euhedral tabular crystals with distinctive dark brown to light brown pleochroism. Twinned grains are common, and many grains exhibit growth zoning characterized by rims containing exsolved Fe-Ti oxide needles (Plate 2.17e). Hornblende is fringed by actinolite needles ± chlorite, and locally contains patches with green to light brown pleochroism, which may represent the onset of alteration. Well-developed foliation in this rock is defined by the parallel alignment of hornblende phenocrysts, along with chlorite, epidote and actinolite aggregates throughout the groundmass.

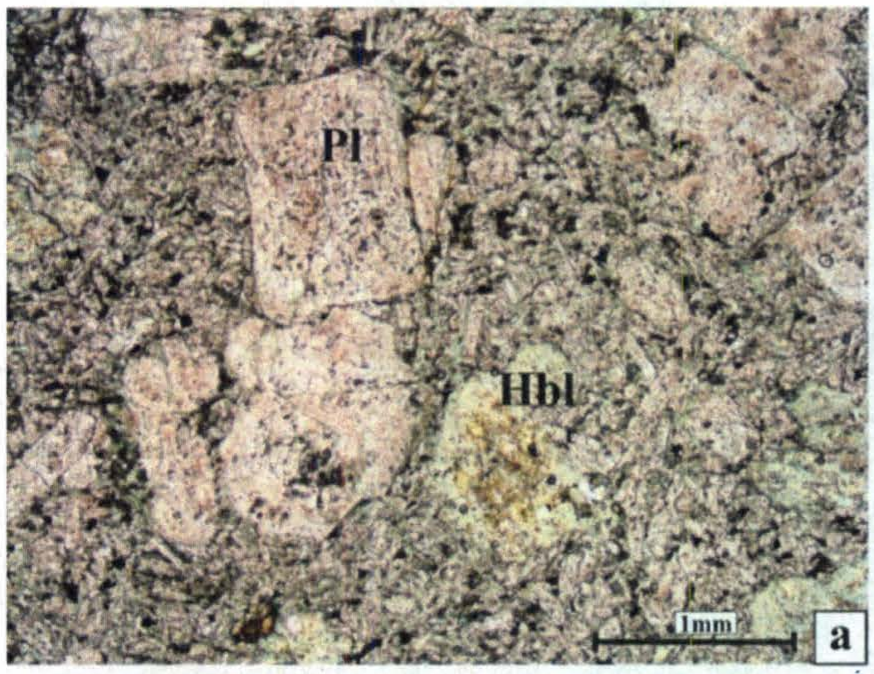

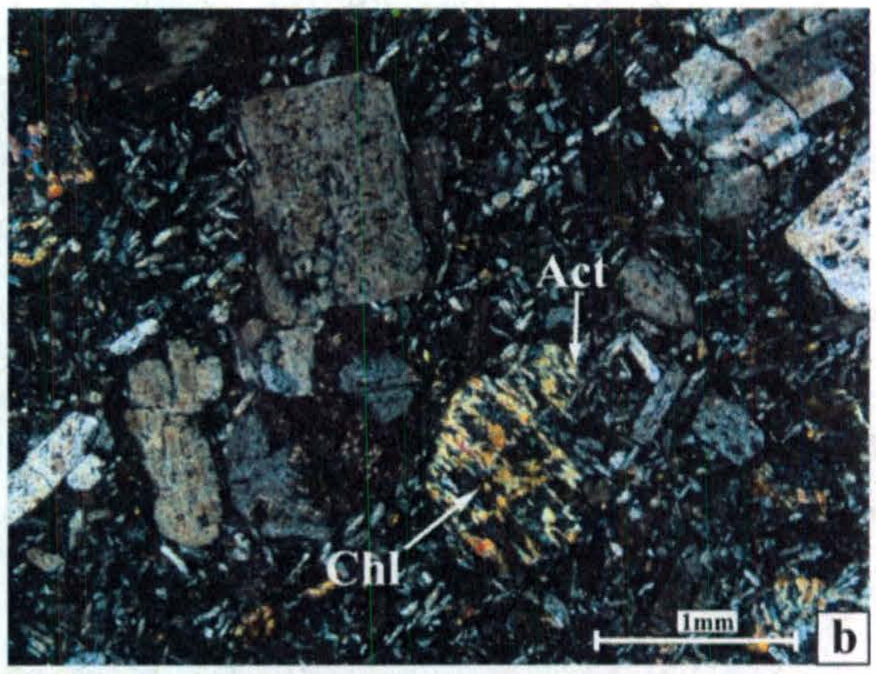

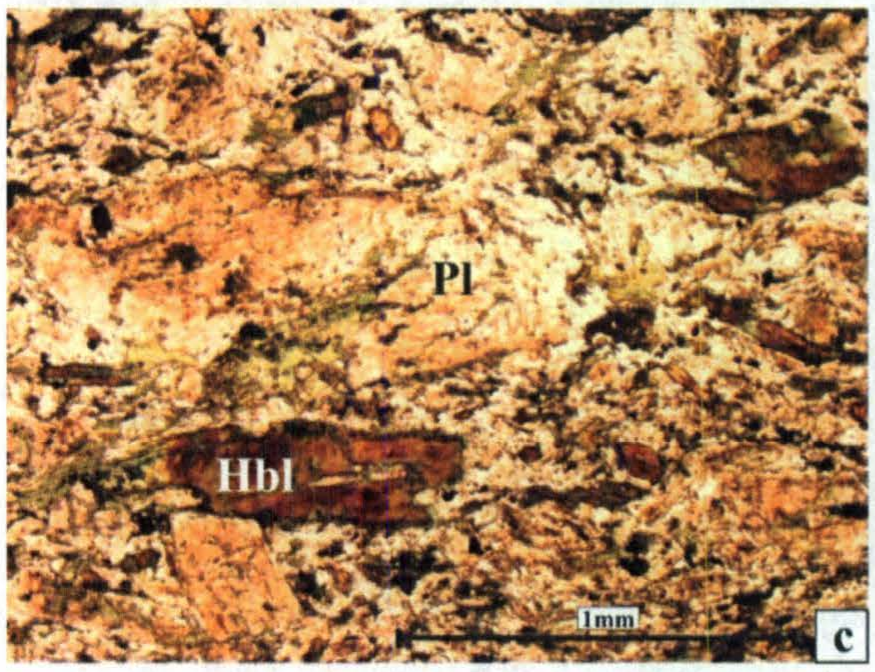

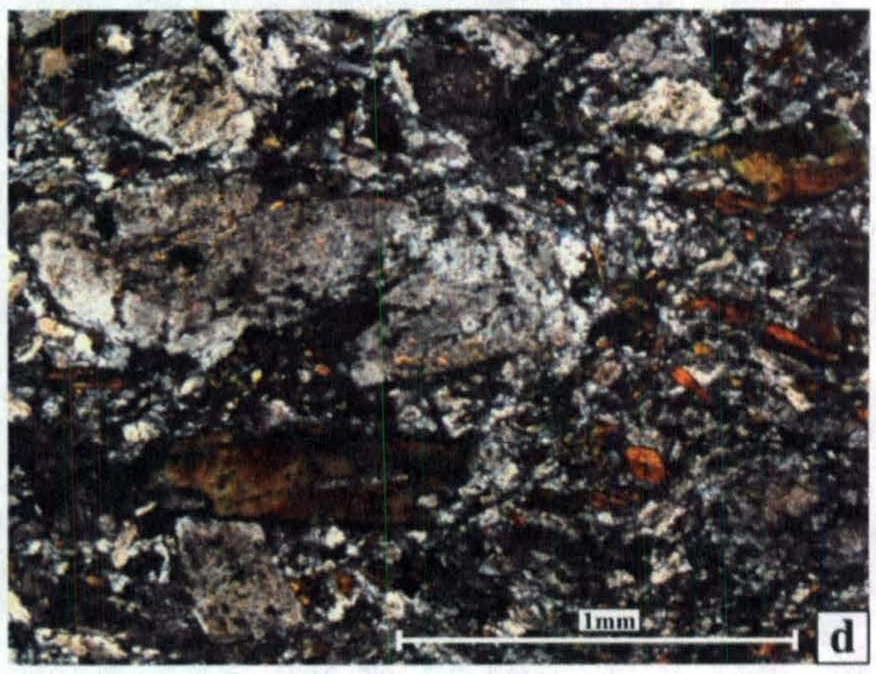

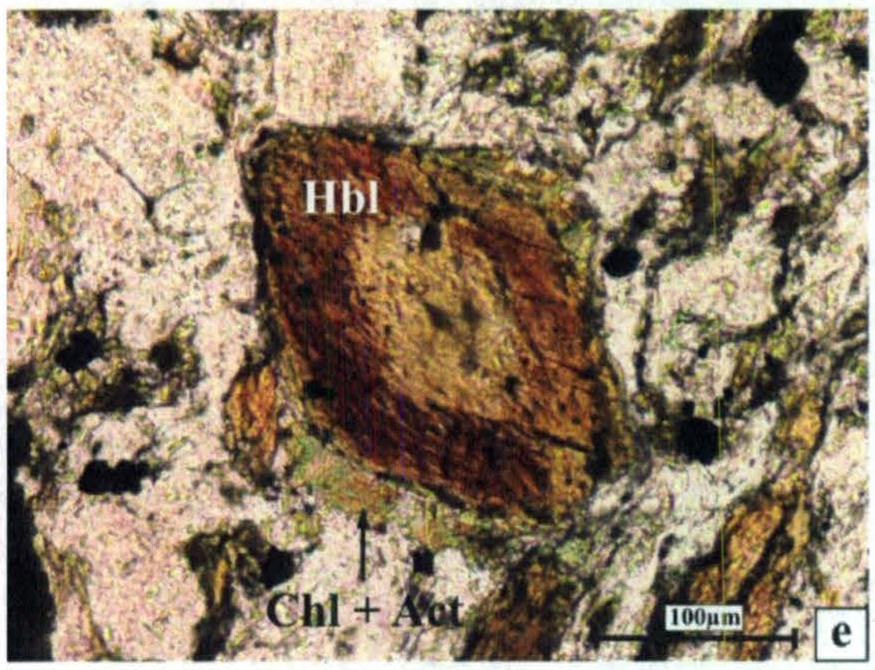

Plate 2.17: Photomicrographs of hornblende-porphyritic andesitic dykes in plane-polarized light, unless otherwise indicated. (a) Plagioclase and hornblende phenocrysts in a groundmass of plagioclase, opaque minerals, chlorite, epidote and actinolite (sample #138, Map 1). (b) Same view as (a) under crossed polars, showing partial replacement of hornblende by chlorite and actinolite. (c) Plagioclase phenocrysts and dark brown to light-brown pleochroic hornblende phenocrysts aligned parallel to foliation (sample #100, Map 1). (d) Same view as (c) under crossed polars. (e) A euhedral basal section of a hornblende phenocryst showing zoning defined by exsolved Fe-Ti oxides in the outer rim. Also note abundant chlorite, epidote and actinolite throughout groundmass, and chlorite and actinolite surrounding hornblende (sample #100, Map 1).

2.2.6. Hornblende basaltic dykes

2.2.6.1. Lithology and field relationships

This unit is composed of fine-grained, non-porphyritic, dark brown- and dark grey-weathering dykes with dark green fresh surfaces. This unit also includes purplish-brown-weathering, abundantly feldspar-porphyritic (~15%) dykes, which are limited to Map 2. The hornblende basaltic dykes have different relative ages, but they are all interpreted to be younger than diorite, gabbro, granodiorite and feldspar porphyry, and older than the andesitic dykes. The purplish-brown-weathering, feldspar-porphyritic hornblende basaltic dykes are interpreted to be the oldest dykes in Map 2. They are hosted by gabbro (Plate 2.11d) and are cross-cut by basaltic dykes with chilled margins, oxide-rich andesitic dykes with chilled margins (Plate 2.18), and an andesitic dyke with chilled margins. A non-porphyritic hornblende basaltic dyke (station #78) is chilled against the same oxide-rich andesitic dyke that cross-cuts the purplish-brown-weathering, feldspar-porphyritic hornblende basaltic dyke in Plate 2.18. Hence, this particular non-porphyritic hornblende basaltic dyke, and perhaps others from this unit, is younger than the purplish-brown-weathering, feldspar-porphyritic hornblende basaltic dykes.

Non-porphyritic hornblende basaltic dykes in Map 2 have well-developed chilled margins against diorite (Plate 2.14c), gabbro and blocks of granodiorite (Plate 2.1c). In Sections A-A' and C-C', hornblende basaltic dykes enclose rafts and septa of diorite and granodiorite, and often display clear intrusive contacts and chilled margins (Plates 2.1d and 2.2a and b). In Map 1, as in other areas, dykes from this unit are hosted by diorite or granodiorite and are cross-cut by andesitic dykes with chilled margins. In addition, a hornblende basaltic dyke (station #99) has intruded a hornblende-porphyritic andesitic

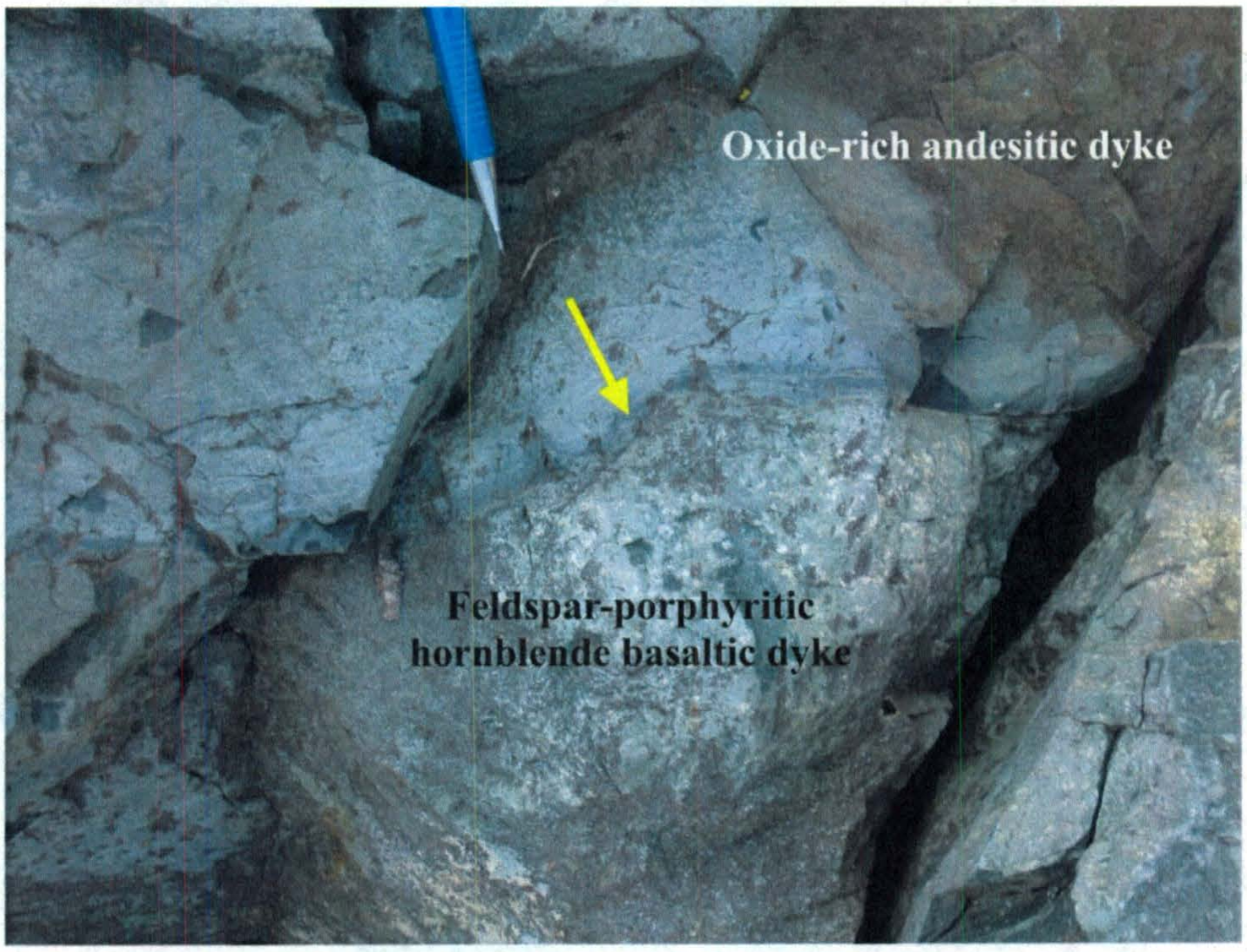

Plate 2.18: Field photograph of a well-developed chilled margin in an oxide-rich andesitic dyke against a purplish-brown-weathering, feldspar-porphyritic hornblende basaltic dyke (Map 2).

dyke (station #100), which implies that other dykes in this unit are also younger than the hornblende-porphyritic andesitic dykes.

2.2.6.2. Petrography

In thin section, hornblende forms subhedral tabular-shaped crystals and anhedral crystals that appear to fill spaces between plagioclase laths (Plate 2.19a and b). Hornblende has dark green-to-light green pleochroism, contains patches of actinolite ± chlorite and has fringes of actinolite needles ± chlorite at grain boundaries. Optically continuous bundles of actinolite needles appear to be pseudomorphing hornblende, a texture also observed in diorite. Indeed, all hornblende in the hornblende basaltic dykes seems to have been partially or almost entirely replaced by actinolite ± chlorite. Plagioclase occurs as subhedral elongate and blocky laths, as well as anhedral grains that appear to fill spaces between plagioclase laths and hornblende crystals. Fe-Ti oxides occur throughout the dykes and are interpreted to be ilmeno-magnetite altered to ilmenite and leucoxene. Greenschist-facies metamorphic minerals, including epidote, chlorite and actinolite, occur as tiny (<50 μm) crystals forming aggregates at plagioclase and hornblende grain boundaries, and also occur within plagioclase, along with sericite. In certain hornblende basaltic dykes (e.g. sample #99 in Map 1 and samples #69, 78 and 88 in Map 2), weak foliations were observed in thin section, defined by the parallel alignment of opaque minerals, hornblende and aggregates of actinolite, chlorite and epidote (Plate 2.19c). Epidote veins are common but are typically less than 1 mm wide and comprise no more than 3% of each thin section analyzed.

The purplish-brown-weathering, feldspar-porphyritic dykes in Map 2 (samples #75 and 88) contain about 12% subhedral, blocky plagioclase phenocrysts that range in

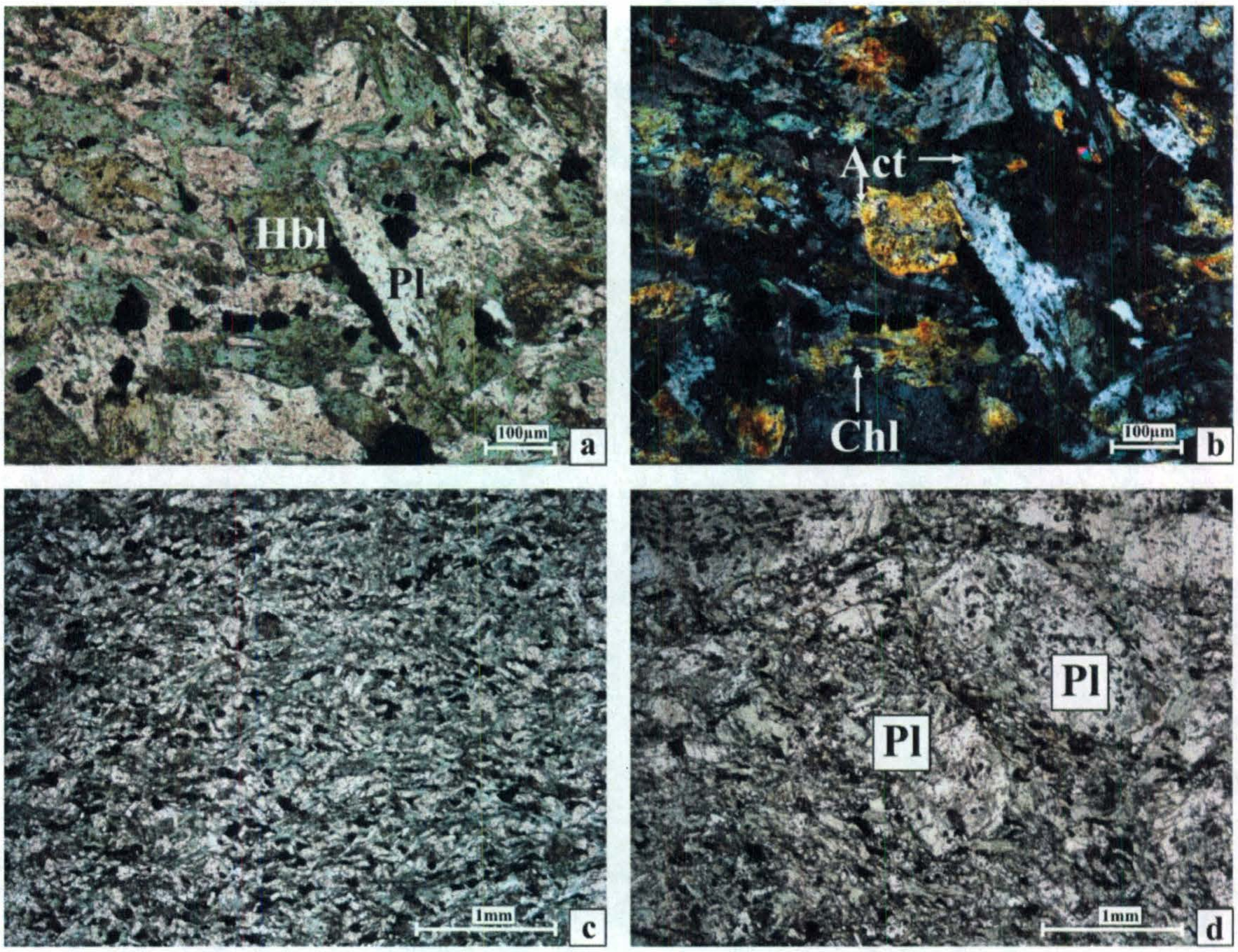

Plate 2.19: Photomicrographs of hornblende basaltic dykes in plane-polarized light, unless otherwise indicated. (a) Plagioclase, hornblende and opaque minerals with secondary chlorite, epidote (sample #99, Map 1). (b) Same view as (a) under crossed polars, highlighting tabular hornblende grains with fringes of actinolite and chlorite, as well as hornblende containing patches of chlorite and bundles of actinolite needles. (c) A weak foliation defined by aligned hornblende, opaque minerals and aggregates of actinolite, chlorite and epidote (sample #78, Map 2). (d) Plagioclase phenocrysts are occupied by greenschist-facies minerals, including chlorite, epidote and actinolite (sample #88, Map 2).

length from less than 1 mm to 6 mm, with an average length of 2 mm (Plate 2.19d). The plagioclase phenocrysts have undergone extensive sericitization, obscuring any twinning or zoning, and contain abundant inclusions of Fe-Ti oxides and secondary chlorite, actinolite and epidote. The phenocrysts also have embayed boundaries and fractures occupied by alteration minerals invading from the groundmass. These dykes locally contain irregularly-shaped chlorite clots, which are up to 2 mm long and are bordered by aggregates of subhedral epidote crystals.

2.2.7. Basaltic dykes

2.2.7.1. Lithology and field relationships

This unit includes fine-grained, dark brown- and dark grey-weathering basaltic dykes that are dark green on fresh surfaces. Some of these dykes are sparsely populated (<5%) by subhedral to euhedral, 2-5 mm long, blocky plagioclase phenocrysts.

Together with other dykes in the study area, the basaltic dykes appear to be younger than gabbro, diorite and granodiorite. For example, a large granodiorite body in Map 1 hosts a network of basaltic dykes (Plate 2.3a). Along Section A-A', a basaltic dyke with chilled margins (Plate 2.14b) has intruded along the contact between a hornblende basaltic dyke and a raft of diorite. In Map 2, a basaltic dyke (station #71) is chilled against granodiorite and gabbro (Plate 2.11b), as well as a purplish-brown-weathering, feldspar-porphyritic hornblende basaltic dyke. Another basaltic dyke in Map 2 (station #84) is hosted by gabbro (Plate 2.11a), cross-cuts an oxide-rich andesitic dyke (Plate 2.20a) and is cross-cut by an andesitic dyke. In Map 3, a basaltic dyke is hosted by

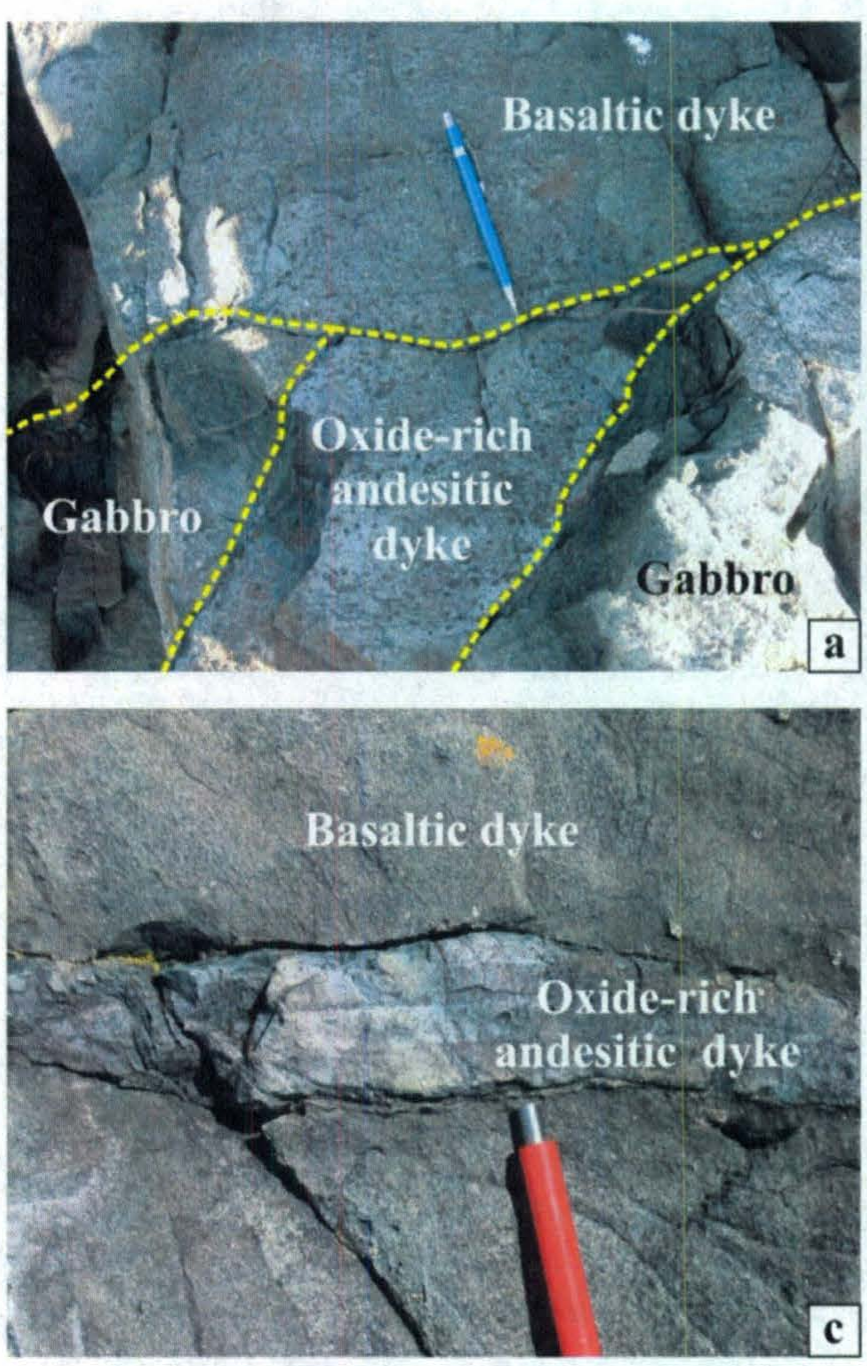

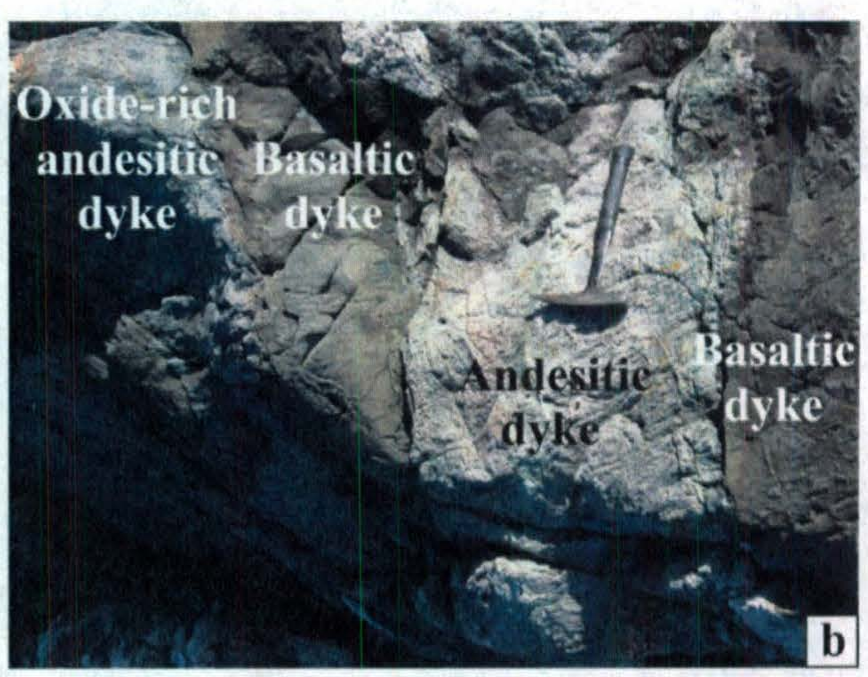

Plate 2.20: Field photographs of basaltic dykes. (a) A basaltic dyke cross-cuts a ~25 cm wide oxide-rich andesitic dyke (Map 2). (b) A basaltic dyke is cross-cut by a light-greyish-green-weathering andesitic dyke and a dark-purple-weathering oxide-rich andesitic dyke (Map 3). (c) A ~5 cm-wide dark-purple-weathering oxide-rich andesitic dyke is hosted by a basaltic dyke (Map 3).

granodiorite and is cross-cut by oxide-rich andesitic dykes and andesitic dykes (Plate 2.20b and c).

In summary, field relationships indicate that the basaltic dykes are younger than gabbro, diorite, granodiorite and feldspar porphyry and are older than the andesitic dykes. However, the oxide-rich andesitic dykes are both older and younger than the basaltic dykes, suggesting that these two units overlap in age. Locally, the basaltic dykes are younger than the hornblende basaltic dykes, but relative age relationships with other types of dykes remain uncertain.

2.2.7.2. Petrography

In thin section, clinopyroxene occurs as anhedral to subhedral crystal remnants that exhibit weak colourless-to-beige pleochroism (Plate 2.21a). Optically continuous remnants of clinopyroxene grains are surrounded by aggregates of actinolite and chlorite, indicating partial replacement of larger, igneous clinopyroxene by greenschist-facies metamorphic minerals (Plate 2.21a and b). The clinopyroxene remnants and their associated actinolite and chlorite aggregates often enclose plagioclase laths in the groundmass, demonstrating sub-ophitic texture.

As in other rocks in the study area, greenschist-facies metamorphic minerals occur throughout the basaltic dykes. Actinolite, chlorite and epidote occur within plagioclase phenocrysts and form aggregates between groundmass plagioclase laths, and igneous clinopyroxene seems to have undergone partial replacement by actinolite and chlorite. Locally, chlorite is concentrated in large (~250 μm) aggregates with euhedral epidote crystals (Plate 2.21c and d, Plate 2.22a). Hornblende was observed only rarely in the basaltic dykes (Plate 2.21c and d), perhaps due to the complete replacement of the

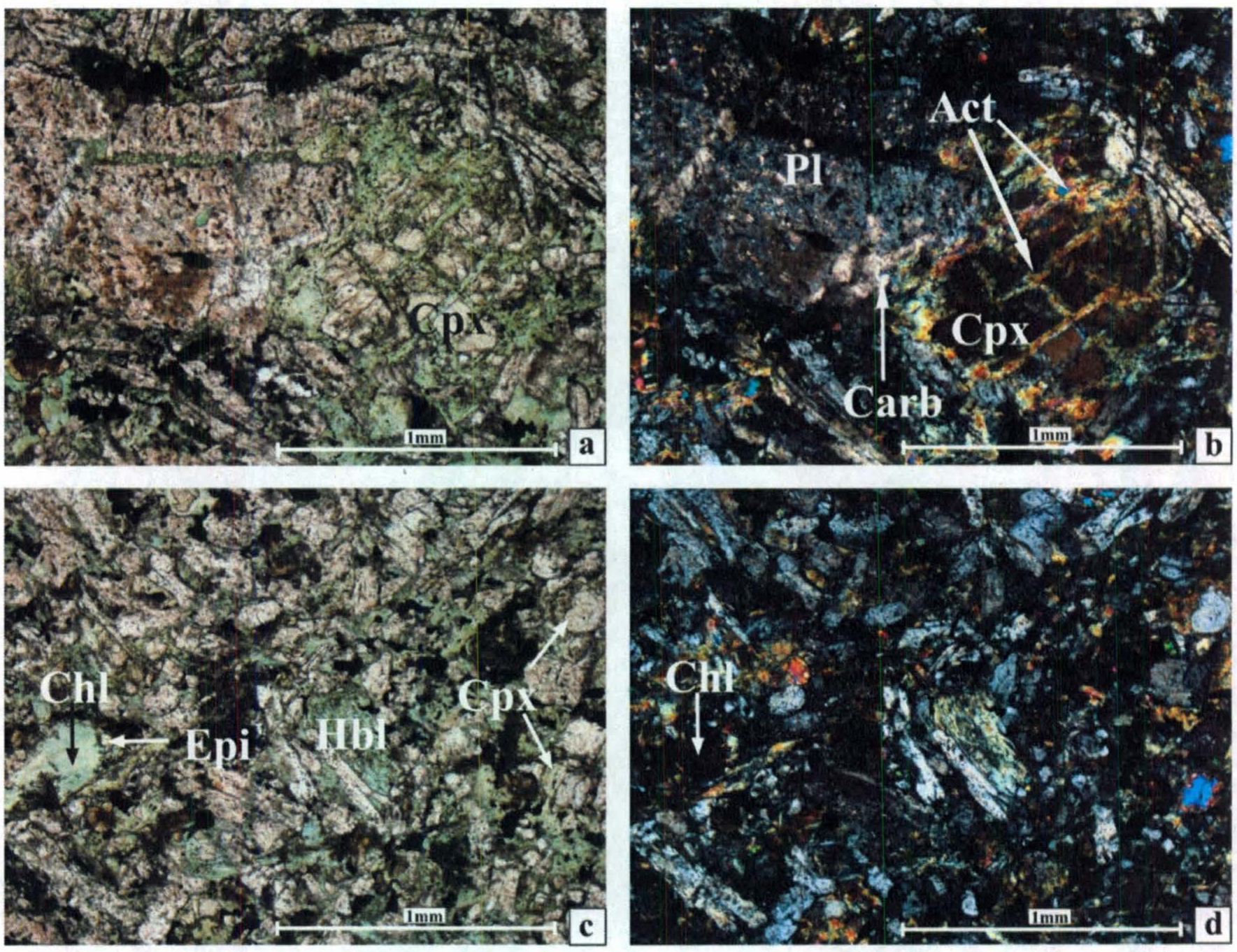

Plate 2.21: Photomicrographs of basaltic dykes in plane-polarized light, unless otherwise indicated. (a) Remnants of a clinopyroxene grain are surrounded by actinolite and minor chlorite, and abundant epidote, chlorite and actinolite occur between and within plagioclase grains (sample #71, Map 2). (b) Same view as (a) under crossed polars, showing actinolite surrounding and filling fractures in clinopyroxene, as well as a plagioclase phenocryst with abundant sericite, chlorite and epidote. (c) Several remnants of clinopyroxene are surrounded by greenschist-facies minerals, and chlorite forms an aggregate bordered by epidote crystals. As well, hornblende has resisted complete replacement by actinolite and chlorite (sample #71, Map 2). (d) Same view as (c) under crossed polars.

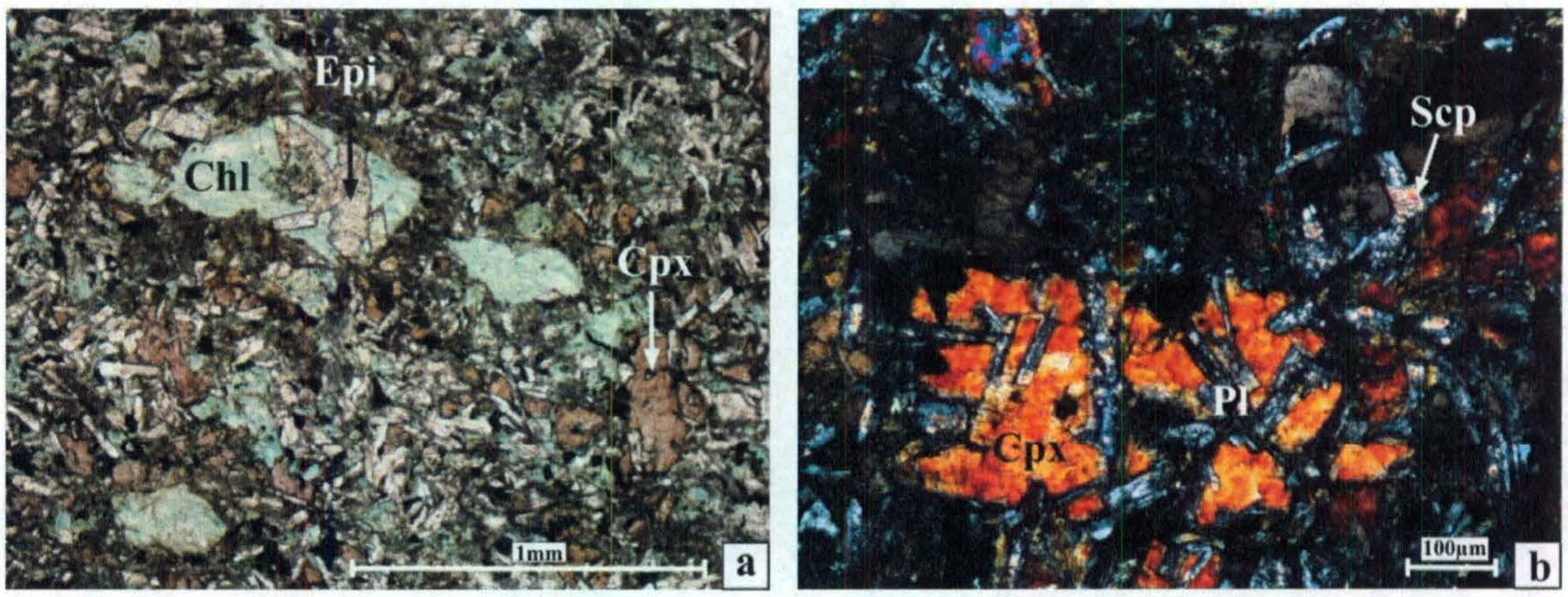

Plate 2.22: Photomicrographs of basaltic dyke sample #123, Map 1. (a) Pinkish-brown-coloured clinopyroxene shows little alteration or replacement by greenschist-facies alteration minerals. Clinopyroxene partially encloses plagioclase laths, demonstrating sub-ophitic texture. Chlorite forms up to ~1 mm long aggregates that locally contain euhedral epidote crystals (plane-polarized light). (b) Detail of sub-ophitic texture formed by clinopyroxene and plagioclase. Also note partial replacement of plagioclase by scapolite (cross-polarized light).

majority of hornblende by actinolite and chlorite. Aggregates of ilmenite and leucoxene are ubiquitous in the basaltic dykes, and appear to represent altered ilmeno-magnetite. In addition, minor epidote veining was observed in some thin sections and, locally, weak foliations in the basaltic dykes are defined by the alignment of aggregates of greenschist-facies alteration minerals.

Some petrographic differences exist between a basaltic dyke that occurs in Map 1 (sample #123) and other basaltic dykes in the study area. Clinopyroxene in this dyke is much more abundant and it exhibits strong pinkish-brown-to-light-pinkish-brown pleochroism (Plate 2.22a). It has undergone significantly less replacement by actinolite and chlorite compared to clinopyroxene in the other dykes, and sub-ophitic texture is well-preserved by clinopyroxene edged by fringes of actinolite needles ± chlorite (Plate 2.22b). In addition, plagioclase in the basaltic dyke in Map 1 has been partially replaced by scapolite (Plate 2.22b).

2.2.8. Andesitic dykes

2.2.8.1. Lithology and field relationships

The light brown, grey or greyish-green weathering colours that characterize these dykes readily distinguish them from the dark brown- and dark grey-weathering mafic dykes in the study area. The fresh surfaces of the andesitic dykes consist of a fine-grained, greyish-green or purplish-grey groundmass that encloses ~1 mm long plagioclase feldspar phenocrysts (<6%). Light greyish-green-weathering andesitic dykes in Map 3 (stations #55 and 59) contain vesicles concentrated in dyke interiors, and are

characterized by thin (<1 mm thick), white, parallel bands that are spaced about 0.5-1 cm apart and are generally parallel to dyke margins (Plate 2.23a and b).

The andesitic dykes are interpreted to be among the youngest dykes in the study area. They exhibit clear cross-cutting relationships with several types of dykes and commonly display well-developed chilled margins. For example, in Map 3, andesitic dykes are hosted by granodiorite (Plate 2.23a and b) and cross-cut basaltic dykes (Plate 2.20b) and oxide-rich andesitic dykes. However, one of the andesitic dykes is cross-cut by a thin oxide-rich andesitic dyke, which suggests that these two units are broadly coeval.

The andesitic dyke in Map 2 (station #89) cross-cuts gabbro and several types of mafic and intermediate dykes, including a basaltic dyke, feldspar-porphyritic hornblende basaltic dykes and oxide-rich andesitic dykes (Plate 2.1b). This andesitic dyke is cross-cut by a dark-grey-weathering basaltic-andesitic dyke (station #91), which represents one of the few magmatic events that is interpreted to be younger than the andesitic dykes. Mafic enclaves observed in the andesitic dyke adjacent to the cross-cutting basaltic-andesitic dyke (Plate 2.23c) may be evidence of magma mixing, or alternatively, they may be inclusions of mafic host rocks.

Andesitic dykes are common throughout Map 1 and are hosted by granodiorite, feldspar porphyry and diorite (Plate 2.15b and c), locally displaying chilled margins against these units. Andesitic dykes also cross-cut hornblende basaltic dykes. In Map 1, andesitic dykes are rarely cross-cut by mafic or other intermediate dykes, and these occurrences are not well-constrained due to shearing, fracturing and/or limited exposure

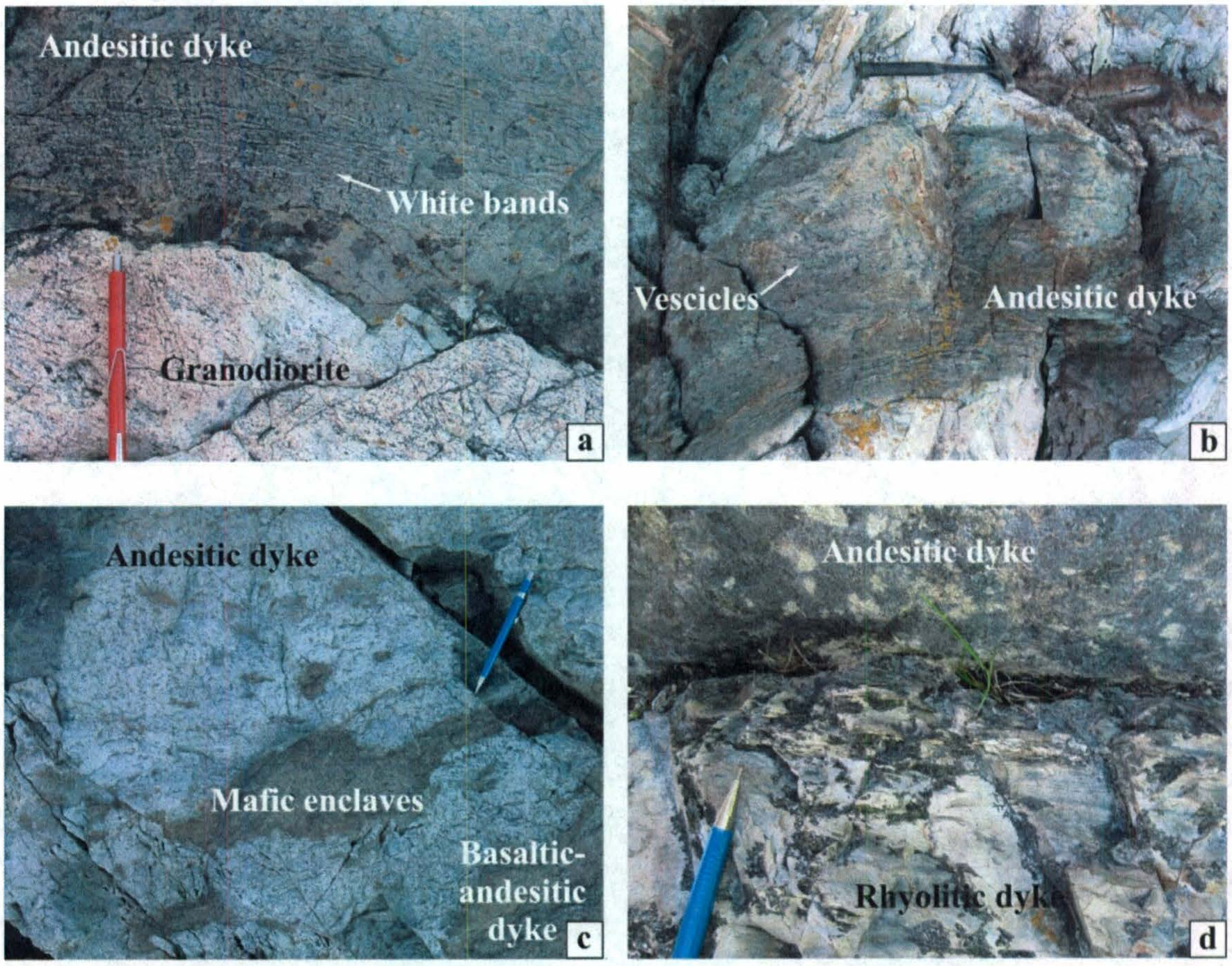

Plate 2.23: Field photographs of andesitic dykes. (a) An irregular contact between a light greyish-green-weathering andesitic dyke and granodiorite, with thin, white bands parallel to dyke margin (Map 3). (b) A light greyish-green-weathering andesitic dyke hosted by granodiorite. Note the vesicles in the dyke interior and white bands near dyke margins (Map 3). (c) Mafic enclaves in an andesitic dyke adjacent to a younger basaltic-andesitic dyke (Map 2). (d) Flow banding in a rhyolitic dyke parallel to the contact with an andesitic dyke (Map 1).

along contacts. However, an andesitic dyke is cross-cut by a rhyolitic dyke in Map 1 (Plate 2.23d). Hence, this rhyolitic dyke, along with the basaltic-andesitic dyke in Map 2 and the thin oxide-rich andesitic dyke in Map 3, represents the only magmatic event that is constrained by field relationships to be younger than an andesitic dyke.

2.2.8.2. Petrography

With about 60-75% plagioclase, including phenocrysts, the andesitic dykes are plagioclase-rich and contain minor proportions of other igneous minerals. In thin section, plagioclase phenocrysts are subhedral to euhedral, blocky, lath-shaped crystals, whereas groundmass plagioclase forms thinner, elongate, subhedral lath-shaped crystals (Plate 2.24). Hornblende was rarely observed in thin section, and occurs as subhedral, ~0.5 mm long, tabular phenocrysts that are partially replaced by actinolite and chlorite. Fe-Ti oxides are disseminated throughout each thin section as subhedral to euhedral, blocky crystals, which also form clusters of 2-5 crystals.

Greenschist-facies minerals, which consist of actinolite, chlorite and epidote, are concentrated in aggregates between plagioclase grains, and actinolite tends to form elongate bundles of acicular crystals at grain boundaries (Plate 2.24c). Actinolite, chlorite and epidote are also present as tiny inclusions within plagioclase, although in lesser amounts than in the mafic rocks. Locally, a foliation is defined by the parallel alignment of groundmass plagioclase and associated aggregates of greenschist-facies minerals (Plate 2.24d). In addition, veins filled with carbonate, quartz ± chlorite or epidote ± chlorite were observed in several thin sections.

One of the andesitic dykes in Map 1 (sample #103) is distinct from the other andesitic dykes due to the presence of clinopyroxene. This dyke contains about 4%

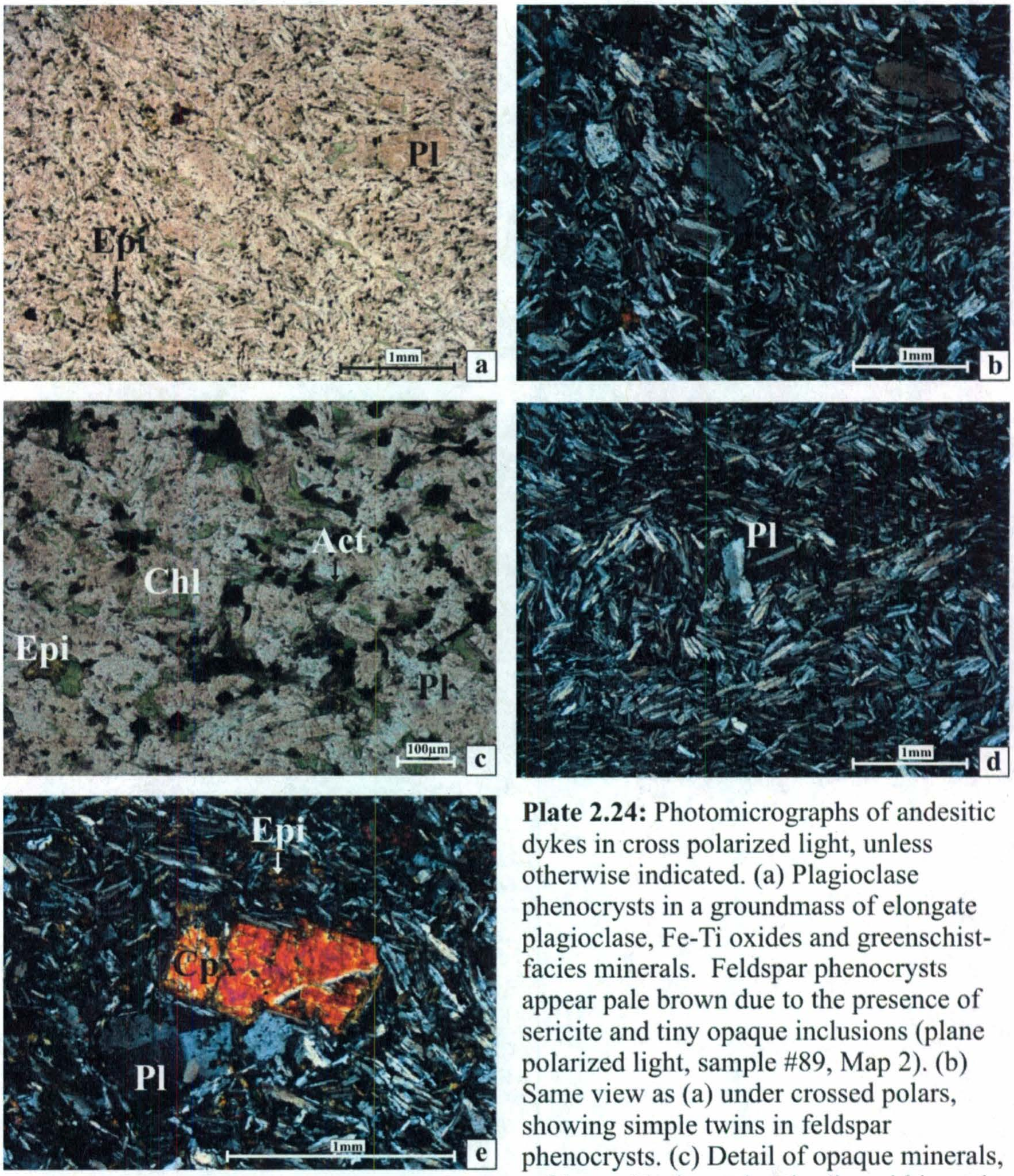

Plate 2.24: Photomicrographs of andesitic dykes in cross polarized light, unless otherwise indicated. (a) Plagioclase phenocrysts in a groundmass of elongate plagioclase, Fe-Ti oxides and greenschist-facies minerals. Feldspar phenocrysts appear pale brown due to the presence of sericite and tiny opaque inclusions (plane polarized light, sample #89, Map 2). (b) Same view as (a) under crossed polars, showing simple twins in feldspar phenocrysts. (c) Detail of opaque minerals, epidote, chlorite and actinolite within and between groundmass plagioclase laths (plane polarized light, sample #89, Map 2). (d) A weak foliation defined by groundmass plagioclase (sample #167, Map 1). (e) A subhedral clinopyroxene phenocryst accompanied by a feldspar phenocryst (sample #103, Map 1).

clinopyroxene phenocrysts, which occur as subhedral, tabular-shaped crystals that are, on average, ~0.5 mm long (Plate 2.24e). Actinolite and chlorite fill fractures and form fringes around clinopyroxene, and clinopyroxene locally occurs as crystal remnants within aggregates of actinolite and chlorite.

As described above, the light greyish-green-weathered andesitic dykes in Map 3 (samples #55 and 59) contain thin, white, parallel bands that are generally parallel to dyke margins. In thin section, these ~300 μm thick bands are composed of very fine-grained, intergrown quartz and feldspar. The light greyish-green-weathering andesitic dykes in Map 3 exhibit additional petrographic differences from the other andesitic dykes: they contain significantly fewer plagioclase phenocrysts, groundmass plagioclase laths are more fine-grained, and they contain numerous ~0.5 mm wide aggregates of anhedral quartz grains. These quartz aggregates are typically accompanied by epidote ± chlorite, and may have crystallized from SiO_2- and trace element-enriched late-stage magmatic fluids.

2.2.9. Basaltic-andesitic dykes

2.2.9.1. Lithology and field relationships

This unit consists of fine-grained, dark brown- and dark grey-weathering dykes that are dark green on fresh surfaces. Most of the basaltic-andesitic dykes are hosted by diorite, feldspar porphyry (Plate 2.8c, d, f and Plate 2.9c) or granodiorite and do not share cross-cutting relationships with other dykes. However, one basaltic-andesitic dyke in Map 1 (station #155) cross-cuts a hornblende-porphyritic andesitic dyke and is cross-cut by an un-sampled mafic dyke that is assumed to be a hornblende basaltic dyke. In

addition, a basaltic-andesitic dyke (station #91) cross-cuts the andesitic dyke in Map 2 (Plate 2.23c), and is therefore among the youngest known magmatic events in the study area.

2.2.9.2. Petrography

In thin section, these dykes are composed of plagioclase and Fe-Ti oxides with greenschist-facies minerals surrounding and filling spaces between plagioclase crystals (Plate 2.25a and b). Apart from plagioclase and opaque minerals, which are assumed to be igneous, no other primary minerals or pseudomorphs of primary minerals were observed in thin section. This distinguishes the basaltic-andesitic dykes from the mafic dykes in the study area, which all contain hornblende or clinopyroxene or greenschist-facies pseudomorphs of these minerals. The basaltic-andesitic dykes are petrographically similar to the andesitic dykes except for their higher abundances of opaque minerals and chlorite, epidote and actinolite. There are some textural variations among the basaltic-andesitic dykes, including unique, elongate plagioclase laths in a dyke in Map 1 (sample #155; Plate 2.25c and d). Plagioclase crystals in the groundmass of this dyke have length to width ratios of up to 15, whereas plagioclase in other mafic and intermediate dykes in the study area is much less elongate. Another basaltic-andesitic dyke in Map 1 (sample #143) has been permeated by veins of epidote and opaque minerals, resulting in brecciation of nearly all plagioclase crystals. As well, a dyke from this unit in Section C-C' (sample #43) contains abundant subhedral, blocky, lath-shaped plagioclase phenocrysts that are up to 1 cm long.

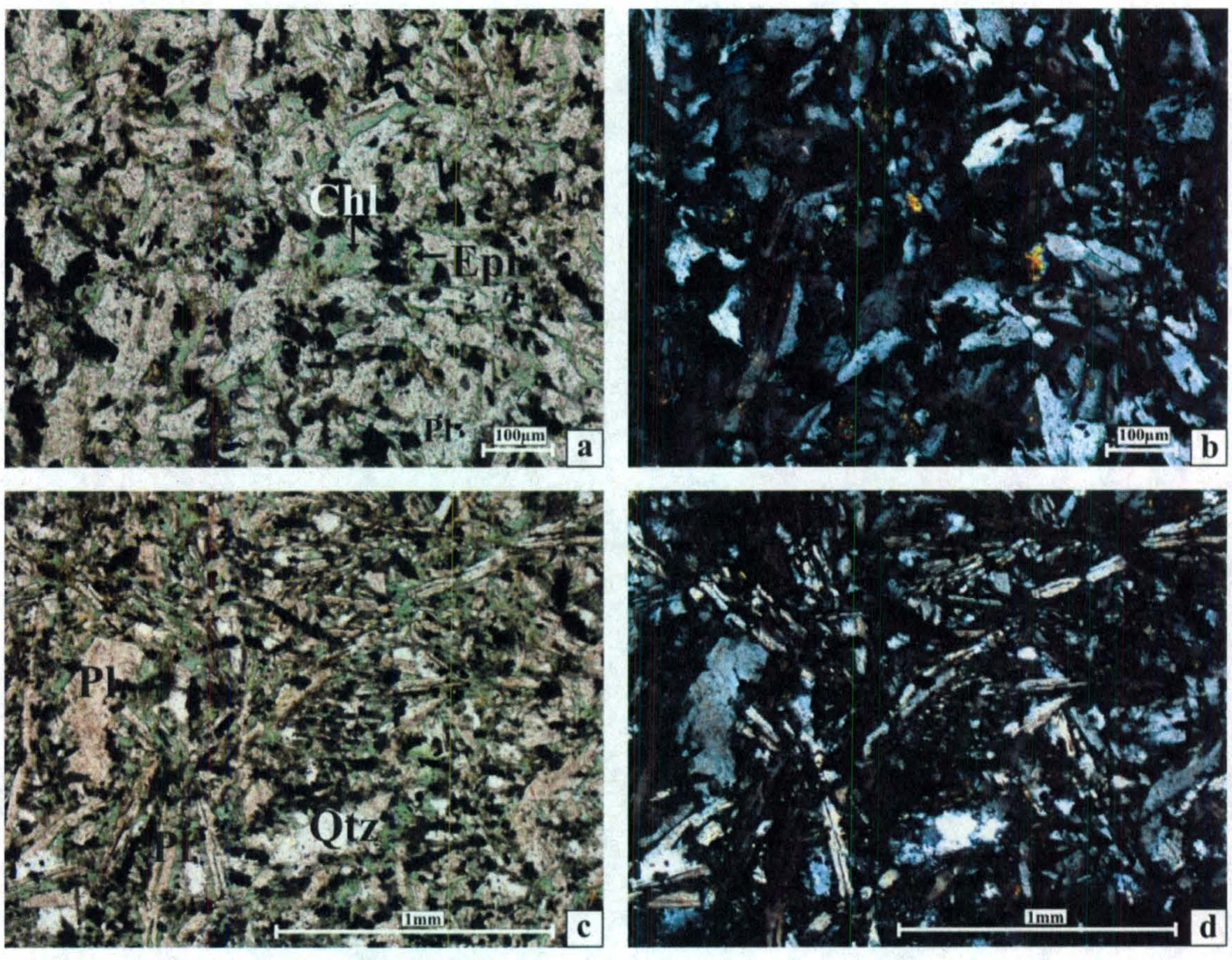

Plate 2.25: Photomicrographs of basaltic-andesitic dykes in plane polarized light, unless otherwise indicated. (a) The dominant mineral assemblage consists of plagioclase and opaque minerals with secondary chlorite, epidote and minor actinolite that do not appear to be pseudomorphing igneous minerals (sample #91, Map 2). (b) Same view as (a) under crossed polars, demonstrating that the green mineral in (a) is mostly chlorite. (c) Unique, elongate plagioclase laths and opaque minerals in the groundmass surrounding a plagioclase phenocryst (sample #155, Map 1). (d) Same view as (c) under crossed polars.

2.2.10. Oxide-rich basaltic and andesitic dykes

2.2.10.1. Lithology and field relationships

This unit includes dark grey-weathering oxide-rich basaltic dykes that are dark grey on fresh surfaces, as well as grey- or dark purple-weathering oxide-rich andesitic dykes that are dark purple on fresh surfaces. The dykes in this unit range in width from 5 cm to 1.5 m and have a very fine-grained groundmass that often encloses rare ~0.5 mm long plagioclase phenocrysts (<5%). The dykes are strongly magnetic and commonly exhibit compositional bands in different shades of purple or grey that form parallel to dyke margins (Plates 2.18 and 2.20c). In Map 3, several dark purple-weathering oxide-rich andesitic dykes display an unusual pattern of banding (Plate 2.26a-c), which is interpreted to represent the preserved chilled margins of multiple magma injections within the dykes.

Like the other dykes in the study area, the oxide-rich andesitic and basaltic dykes are interpreted to post-date granodiorite, feldspar porphyry, gabbro and diorite. Although they are broadly coeval with the dyke swarm, the oxide-rich andesitic and basaltic dykes have multiple generations. In Map 3, oxide-rich andesitic dykes are hosted by granodiorite (Plates 2.2c and 2.26a-d) and cross-cut basaltic dykes (Plate 2.20b and c). Many oxide-rich andesitic dykes in Map 3 are cross-cut by light greenish-grey-weathered andesitic dykes, but one andesitic dyke is cross-cut by a thin, dark-purple-weathering, compositionally banded dyke that is interpreted to be an oxide-rich andesitic dyke. This suggests that the oxide-rich andesitic dykes are multi-generational and they are broadly coeval with the andesitic dykes in Map 3. The episodic nature of the oxide-rich andesitic

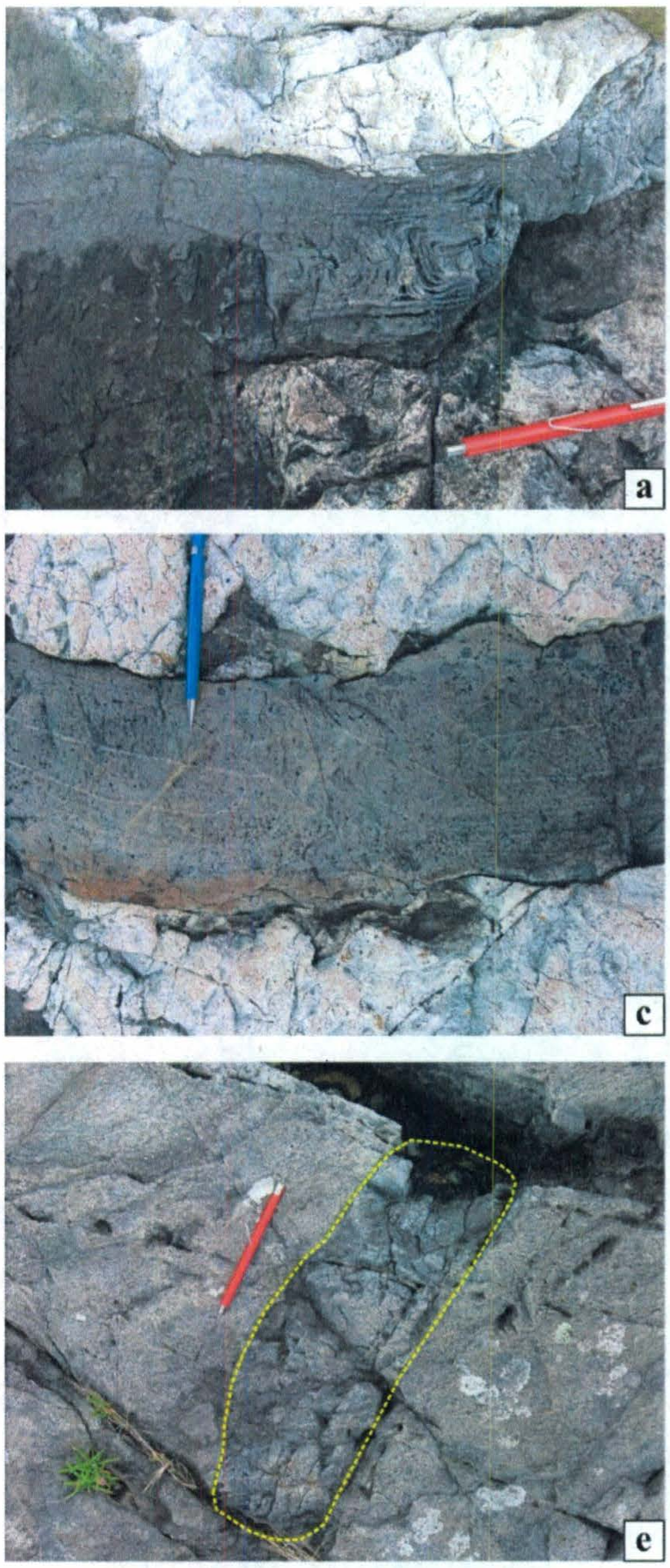

Plate 2.26: Field photographs of dark-purple-weathering oxide-rich andesitic dykes in Map 3. (a) to (c) Distinctive banding may represent multiple chilled margins from melt injections within the dykes. (d) An irregularly shaped dark-purple-weathering oxide-rich andesitic dyke hosted by granodiorite. (e) A block of a dark-purple-weathering oxide-rich andesitic dyke within another oxide-rich andesitic dyke.

dykes is supported by the occurrence of numerous blocks of oxide-rich andesitic dykes within another oxide-rich andesitic dyke (Plate 2.26e).

In Map 2, oxide-rich basaltic dykes are hosted by hornblende basaltic dykes and gabbro. Oxide-rich andesitic dykes are hosted by gabbro and diorite, and they cross-cut feldspar-porphyritic hornblende basaltic dykes (Plate 2.18). The oxide-rich andesitic dykes are cross-cut by a basaltic dyke (Plate 2.20a), a non-porphyritic hornblende basaltic dyke and an andesitic dyke. However, thin, dark-purple-weathering, compositionally banded dykes occur within the same hornblende basaltic dyke and the same andesitic dyke that cross-cut oxide-rich andesitic dykes. This indicates that there are at least two generations of oxide-rich andesitic dykes in Map 2, and that they are broadly coeval with hornblende basaltic dykes and andesitic dykes.

In Map 1, an oxide-rich andesitic dyke is hosted by diorite (Plates 2.14d and 2.15a) and feldspar porphyry (Plate 2.9d) but does not have any exposed cross-cutting relationships with other dykes. One of the oxide-rich basaltic dykes (station #129) in this area is hosted by granodiorite but does not have any exposed cross-cutting relationships with other dykes. A possible chilled margin is present in an oxide-rich basaltic dyke (station #174) against a block of feldspar porphyry. This dyke is surrounded by andesitic dykes, but contact relationships between the two units are obscured by shearing and fracturing.

In Section C-C', an oxide-rich andesitic dyke shares a contact with a rhyolitic dyke (station #50). However, due to quartz veins along the contact, no chilled margin was observed in either unit in outcrop or in thin section. An oxide-rich basaltic dyke (station #51) in Section C-C' has a well-developed chilled margin against a block of

granodiorite, and is cross-cut by an un-sampled mafic dyke that is assumed to be a hornblende basaltic dyke. An oxide-rich basaltic dyke in Section A-A' displays an irregular intrusive contact with diorite (Plate 2.14a).

2.2.10.2. Petrography

In thin section, the most striking features of these dykes are their very fine grain size and high proportion of opaque minerals. Groundmass plagioclase forms subhedral, elongate laths that are typically ~100 μm long. Groundmass plagioclase crystals are surrounded by aggregates of secondary chlorite, actinolite and epidote that fill grain boundaries and tend to encroach on plagioclase grains (Plate 2.27). Opaque minerals occur as nearly sub-microscopic blebs disseminated throughout each thin section, and commonly form chains of tiny (<25 μm) euhedral crystals (Plates 2.27a and 2.28a). These opaque minerals are believed to be igneous magnetite, which would explain the strongly magnetic character of the dykes. Opaque minerals also locally form larger aggregates (up to 0.5 mm) with epidote ± chlorite ± actinolite.

Where compositional banding was observed in the field, thin sections reveal that the ~3 mm wide bands are defined by different proportions of disseminated opaque minerals, and the bands are accompanied by parallel, ~100 μm thick bands of anhedral feldspar ± quartz. Compositional banding is interpreted to have formed as a result of magma flow, evidence of which is also locally preserved in igneous flow foliations around plagioclase phenocrysts (Plate 2.27b).

All the oxide-rich andesitic dykes analyzed in thin section, and some of the oxide-rich basaltic dykes, contain round or oval-shaped quartz grains that are significantly larger than groundmass minerals (Plate 2.27a, c and d). Quartz is generally accompanied

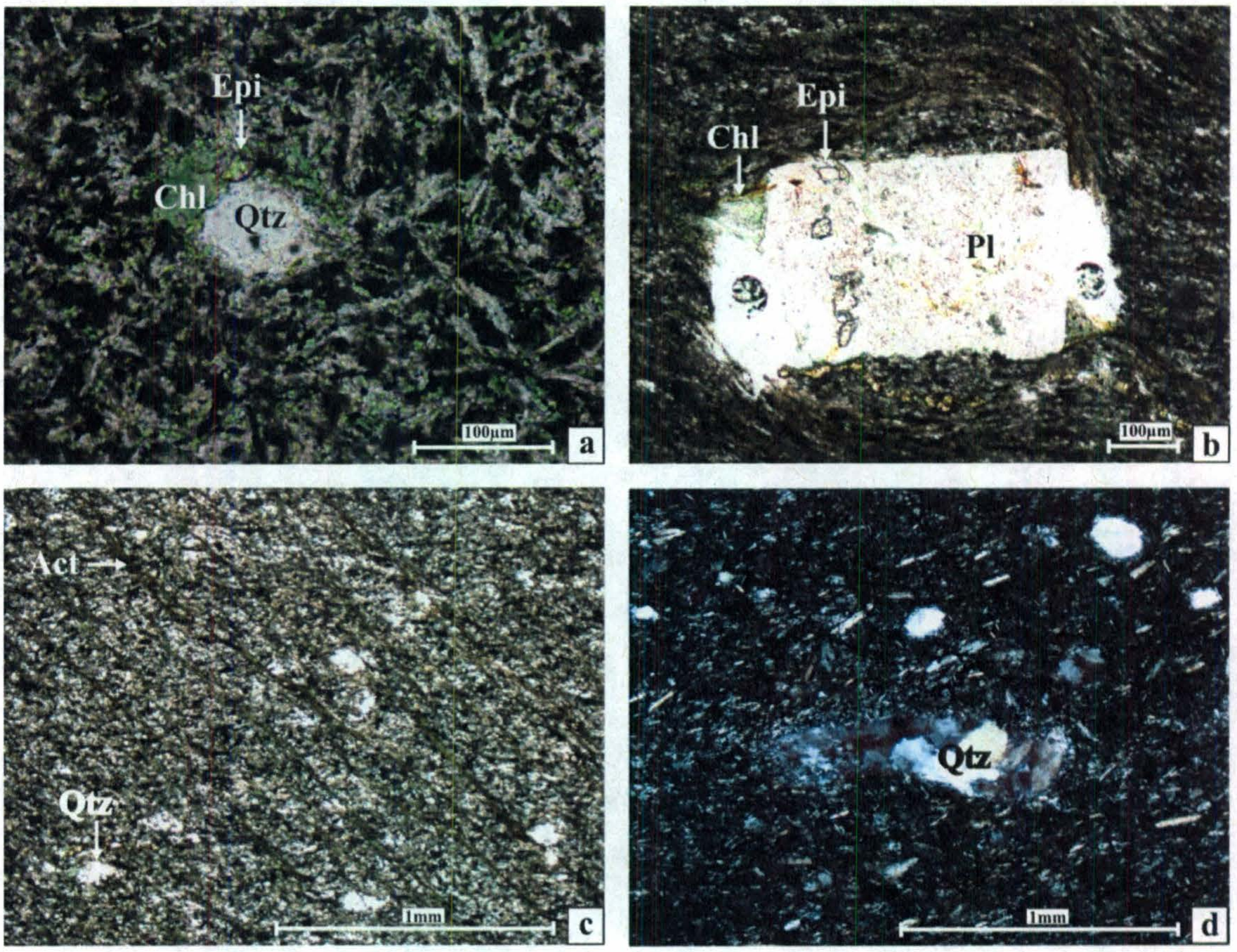

Plate 2.27: Photomicrographs of oxide-rich basaltic (a) and andesitic dykes (b-d) in plane polarized light, unless otherwise indicated. (a) Quartz, surrounded by chlorite and epidote, enclosed by a groundmass of tiny feldpsar laths, aggregates and chains of Fe-Ti oxides and secondary chlorite, epidote and actinolite (sample #129, Map 1). (b) A flow fabric preserved in the groundmass that surrounds a feldspar phenocryst (sample #56, Map 3). (c) Groundmass minerals and larger quartz grains define a fabric that is oriented horizontally in the photo. This fabric is cross-cut diagonally by a second fabric defined by ribbons of actinolite (sample #56, Map 3). (d) Viewed in cross polarized light, quartz forms round and oval-shaped grains and elongate aggregates of anhedral grains (sample #145, Map 1).

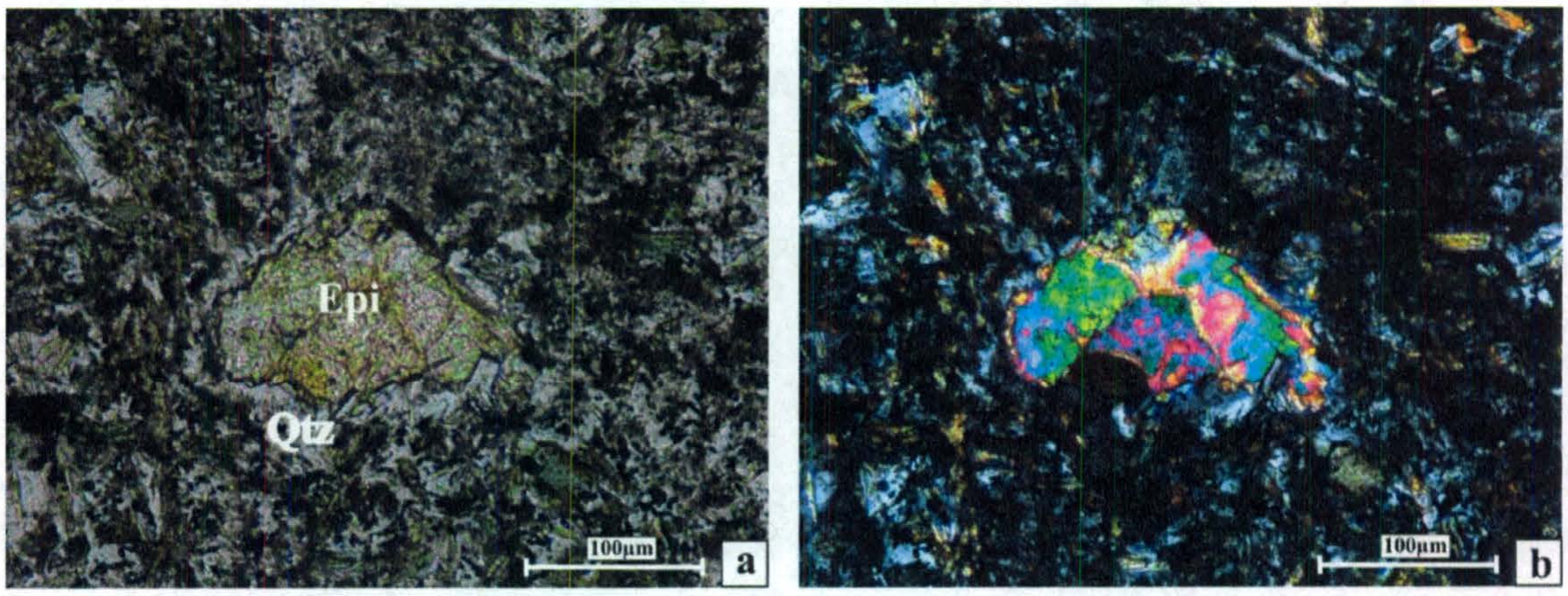

Plate 2.28: Photomicrographs of oxide-rich andesitic dyke sample #79, Map 2. (a) An aggregate of epidote crystals, surrounded by quartz, is enclosed by a groundmass of plagioclase, greenschist-facies minerals and aggregates and chains of Fe-Ti oxides (plane polarized light). (b) Same view as (a) under crossed polars.

by smaller aggregates of chlorite or epidote, and may represent pockets of SiO_2- rich late-stage igneous fluids. Quartz locally forms elongate aggregates that are up to 5 mm long (Plate 2.27d). As well, epidote locally forms large (>100 μm) aggregates that tend to be surrounded by quartz or feldspar (Plate 2.28a and b), which may represent igneous epidote that crystallized in pockets of SiO_2- and trace element-rich late-stage magmatic fluid. One of the oxide-rich andesitic dykes in Map 3 (sample #56) contains a 3 mm long aggregate enriched in chlorite and opaque minerals, as well as anomalously large plagioclase phenocrysts with embayed boundaries that appear to have undergone resorption. These features imply that this dyke incorporated lithic fragments and xenocrysts prior to or during emplacement.

The dykes in this unit are characterized by parallel alignment of compositional bands and elongate quartz aggregates, as well as plagioclase, opaque minerals and greenschist-facies minerals in the groundmass. This fabric is thought to have developed during igneous flow. However, in a thin section from an oxide-rich andesitic dyke in Map 3 (sample #56), flow foliation is intersected by a second fabric, which is interpreted to have formed during deformation (Plate 2.27c).

2.2.11. Rhyolitic dykes

2.2.11.1. Lithology and field relationships

In these white-weathering dykes, tiny feldspar phenocrysts (<5%) are enclosed by a very fine-grained, glassy, dark grey groundmass. Rhyolitic dykes often resemble feldspar porphyry septa, but they are distinguished by their darker grey, glassy groundmass, white weathering colour, smaller, less abundant feldspar phenocrysts and the

presence of flow banding. Alternating light green and dark grey flow bands range in width from 1 mm to 1 cm and occur throughout rhyolitic dykes (Plate 2.29a). The flow bands are most well-developed near dyke margins and are parallel to contacts with host rocks (Plates 2.9e, 2.15d and 2.23d). Locally, rhyolitic dykes also display autobrecciation (Plate 2.29b).

Twenty cm- to-1 m wide rhyolitic dykes were mapped in Sections A-A', B-B' and C-C', as well as in Map 1, and they represent some of the youngest magmatic events in the study area. In Section A-A', a rhyolitic dyke seems to have intruded along the contact between feldspar porphyry and diorite (Plate 2.15e), displaying subtle chilled margins against both units. Flow banding that is parallel to the contact with feldspar porphyry and autobrecciation adjacent to the contact with diorite (Plate 2.29b) also suggest that the rhyolitic dyke is younger than both units. However, a rhyolitic dyke in Section A-A' appears to be cross-cut by an unsampled mafic dyke. This mafic dyke contains blocks of rhyolitic composition that seem to have been plucked from the adjacent rhyolitic dyke (Plate 2.29c).

In Section B-B', rhyolitic dykes are chilled against dark grey-weathering mafic rocks that are believed to be mafic dykes and diorite (Plate 2.29d). In addition, a ~4 m wide rhyolitic dyke outcrops along Section B-B', in the hillside immediately east of Map 1 (Plate 2.29e). Flow banding in this rhyolitic dyke is parallel to dyke margins and it is hosted by mafic rocks that are thought to be diorite. This dyke is unique among the rhyolitic dykes in the study area because the centre of the dyke is occupied by a dark-grey-weathering mafic dyke with the same orientation. The mafic dyke may have intruded the rhyolitic dyke after it was crystallized, although no chilled margins were

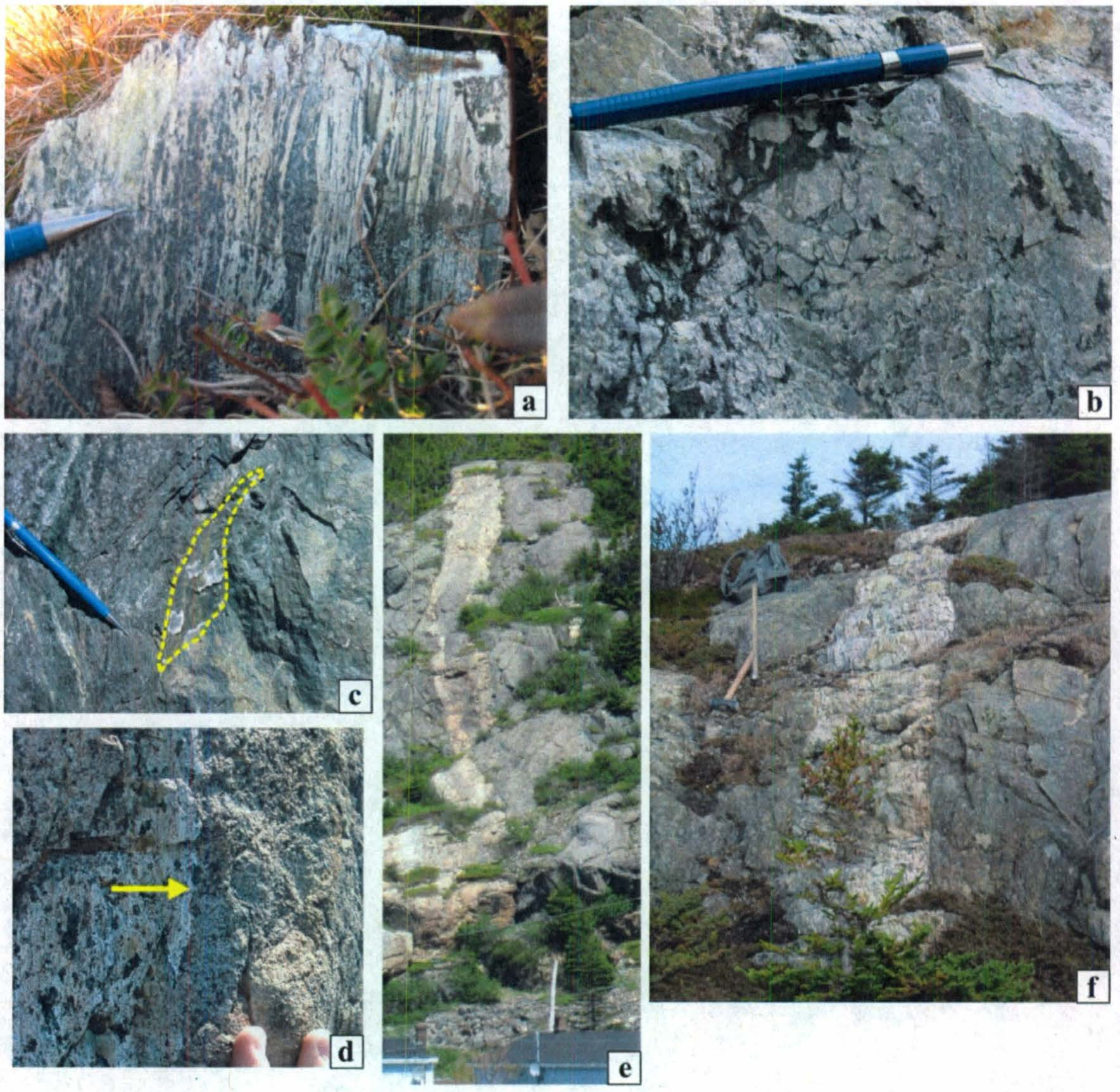

Plate 2.29: Field photographs of rhyolitic dykes. (a) Alternating light green and grey flow bands parallel to the dyke margin (Map 1). (b) Autobrecciation in the dyke margin adjacent to the contact with diorite (Section A-A'). (c) A piece of a rhyolitic dyke within a mafic dyke (Section A-A'). (d) A chilled margin in a rhyolitic dyke against mafic rocks (Section B-B'). (e) A ~4 m wide rhyolitic dyke with a mafic interior, which may be a mafic dyke. Photomicrographs of this rhyolitic dyke are shown in Plate 2.31a and b (Section B-B'). (f) A rhyolitic dyke hosted by diorite. Flow banding in this dyke is shown in (a). Photomicrographs of this dyke are shown in Plates 2.30 and 2.31c and d (Map 1).

observed in the mafic dyke, perhaps due to shearing along contacts. Another possibility is that the mafic dyke and rhyolitic dyke were emplaced simultaneously.

A 1 m thick rhyolitic dyke extends for at least 45 m across Map 1, hosted by feldspar porphyry and diorite (Plate 2.29f). This dyke has well-developed flow banding that is parallel to contacts with both host rocks (Plates 2.9e and 2.15), and it also cross-cuts an andesitic dyke (Plate 2.23d). Because andesitic dykes represent some of the youngest magmatism in the study area, this rhyolitic dyke must also be one of the latest magmatic events.

2.2.11.2. Petrography

In thin section, plagioclase and alkali feldspar phenocrysts form euhedral blocky laths with simple twins, and some plagioclase crystals display lamellar twinning (Plate 2.30a-c). The phenocrysts range in size from ~250 μm to 1.5 mm but are about 0.5 mm on average. They are surrounded by a very fine-grained groundmass that consists of tiny (<50 μm) subhedral to euhedral elongate plagioclase laths enclosed by anhedral quartz and feldspar, which locally form oval-shaped patches (Plate 2.30a-d). Anhedral quartz and feldspar in the groundmass are interpreted to be products of the devitrification of glass. In many rhyolitic dykes, aggregates of anhedral quartz grains form tails on feldspar phenocrysts and also occur as up to 2.5 mm long elongate pods that may have crystallized from pockets of residual, SiO_2-rich igneous melt (Plate 2.30d). Epidote, chlorite and opaque minerals occur as anhedral blebs and clots throughout the groundmass (Plate 2.30b), and epidote veins are common.

In addition to feldspar phenocrysts, one rhyolitic dyke in Section B-B' (sample #204) contains minor amounts of euhedral, light-to-dark brown pleochroic, ~0.5 mm long

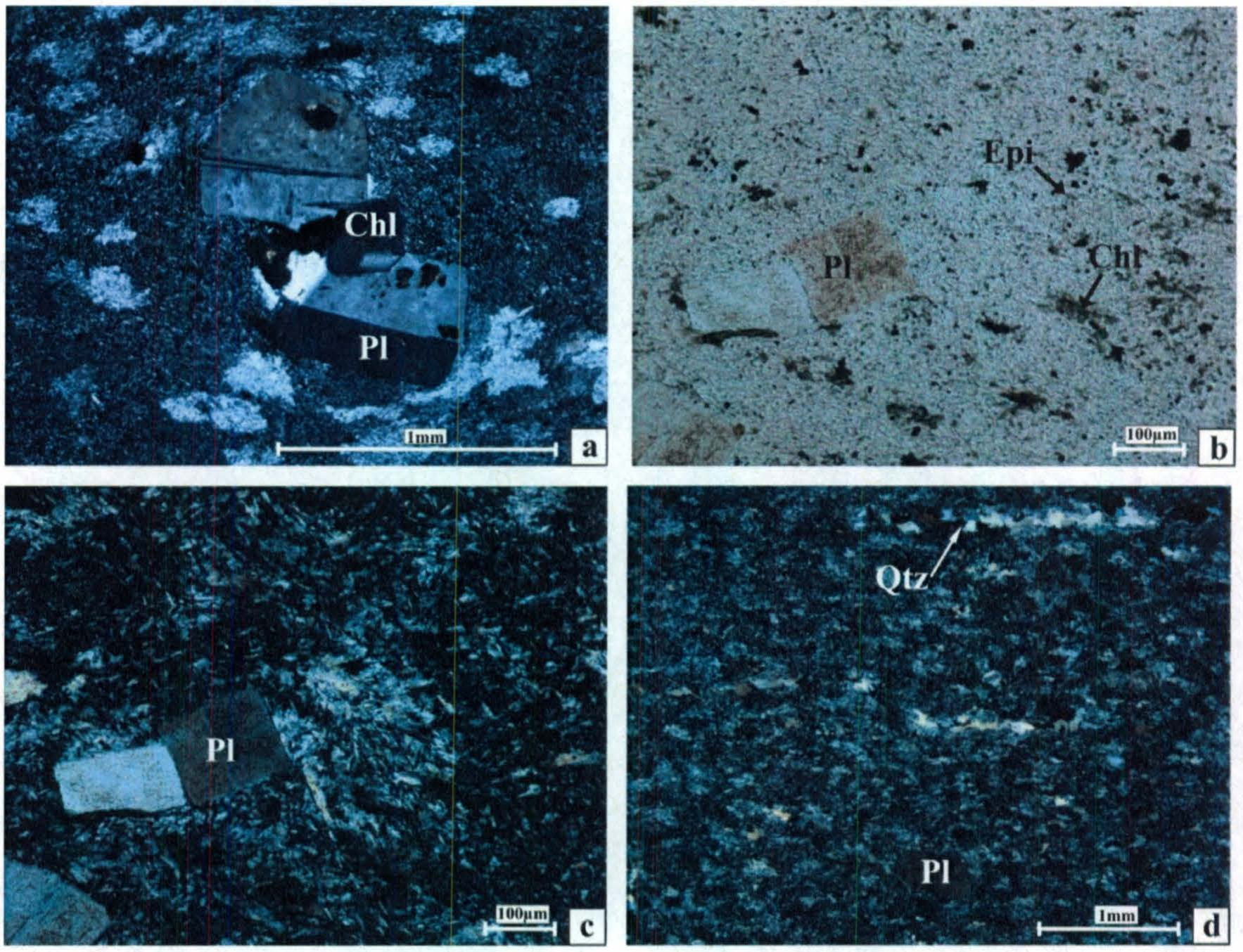

Plate 2.30: Photomicrographs of the rhyolitic dyke in Map 1 under crossed polars, unless otherwise indicated. (a) A cluster of feldspar phenocrysts, accompanied by an aggregate of chlorite (sample #142). (b) A feldspar phenocryst surrounded by a very fine-grained groundmass that includes clots of chlorite and Fe-Ti-oxides (plane polarized light, sample #141). (c) Same view in (b) under crossed polars, showing an oval-shaped patch of feldspar enclosing feldspar laths in the groundmass. (d) Igneous flow foliation at the centre of a rhyolitic dyke, defined by the parallel orientation of feldspar phenocrysts and elongate quartz aggregates, as well as feldspar patches and chlorite clots in the groundmass (sample #141).

hornblende phenocrysts (Plate 2.31a and b). The feldspar phenocrysts in this dyke exhibit signs of deformation, including undulatory extinction, irregular, wavy boundaries and tails filled with chlorite (Plate 2.31a and b). This deformation may have occurred during igneous flow.

Flow banding is typically formed by bands enriched in feldspar patches in the groundmass alternating with bands enriched in chlorite and opaque minerals (Plate 2.31c and d), although some rhyolitic dykes exhibit more subtle flow banding defined by different concentrations of disseminated opaque minerals. Along dyke margins, where flow banding is most apparent, as well as in dyke interiors, most minerals are oriented parallel to the direction of flow, including elongate quartz aggregates, chains of epidote crystals and opaque minerals, clots of chlorite, oval-shaped patches of feldspar and feldspar laths in the groundmass.

2.3. Structural elements of the HCC

Several deformation features were observed during mapping at Bauline, including cleavage, joints and faults. As well, the occurrence of the dyke swarm signifies numerous fractures in the study area. However, deformation did not uniformly affect the study area, and variations in structural data indicate a complex deformational history. While a complete structural analysis is beyond the scope of this study, a synopsis of deformation in the study area is provided below, and structural data are shown in Figure 2.1.

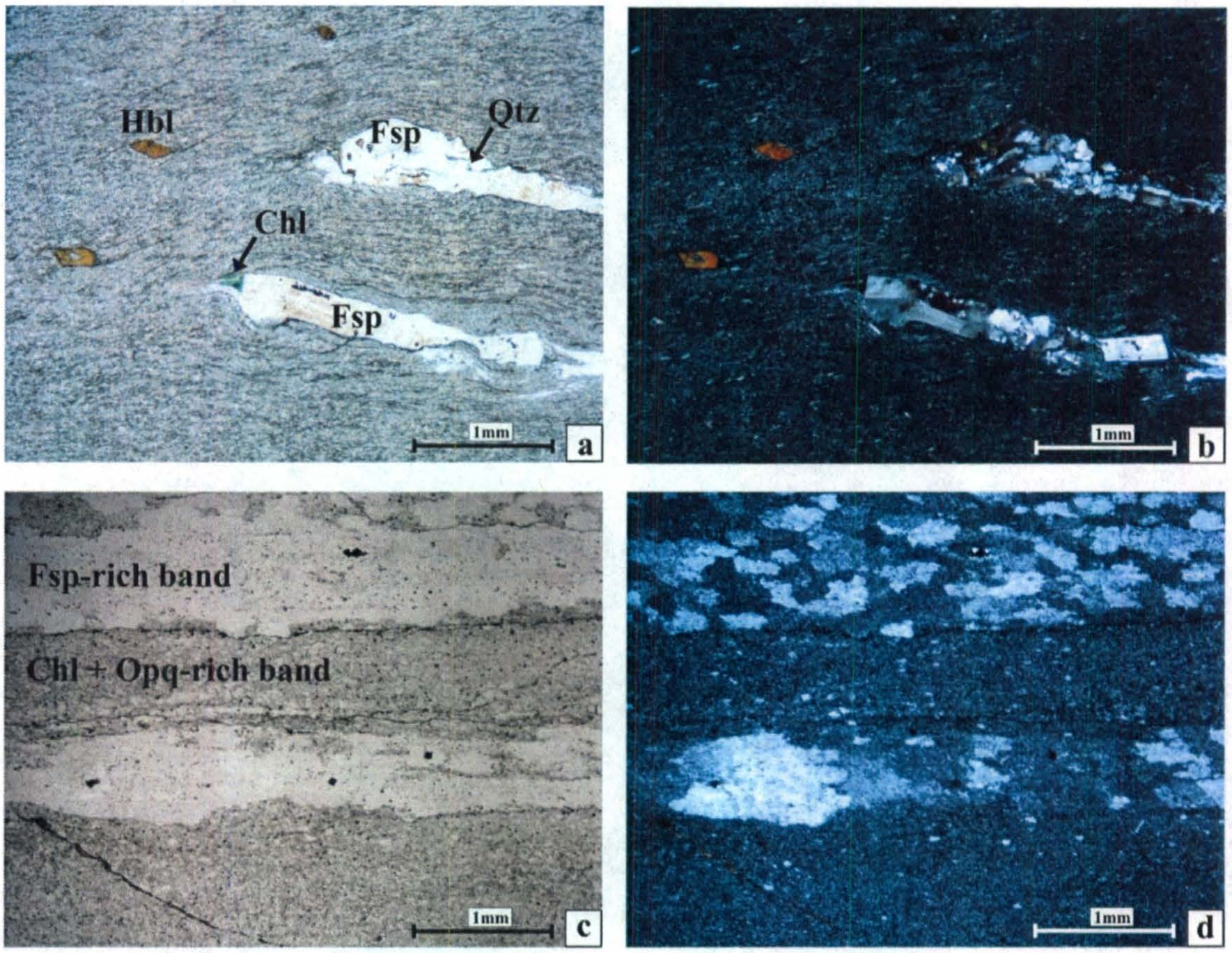

Plate 2.31: Photomicrographs of rhyolitic dykes in plane polarized light, unless otherwise indicated. (a) The alignment of hornblende and feldspar phenocrysts and groundmass minerals defines a foliation that may be attributed to igneous flow. Note the "tails" of chlorite on feldspar phenocrysts (sample #204, Section B-B'). (b) Same view as (a) under crossed polars, showing deformation and partial recrystallization of feldspar phenocrysts. (c) Well-developed flow banding near dyke margin, defined by feldspar-rich bands alternating with chlorite- and Fe-Ti-oxide-rich bands (sample #142, Map 1). (d) Same view as (c) under crossed polars, highlighting oval-shaped feldspar patches in feldspar-rich flow bands.

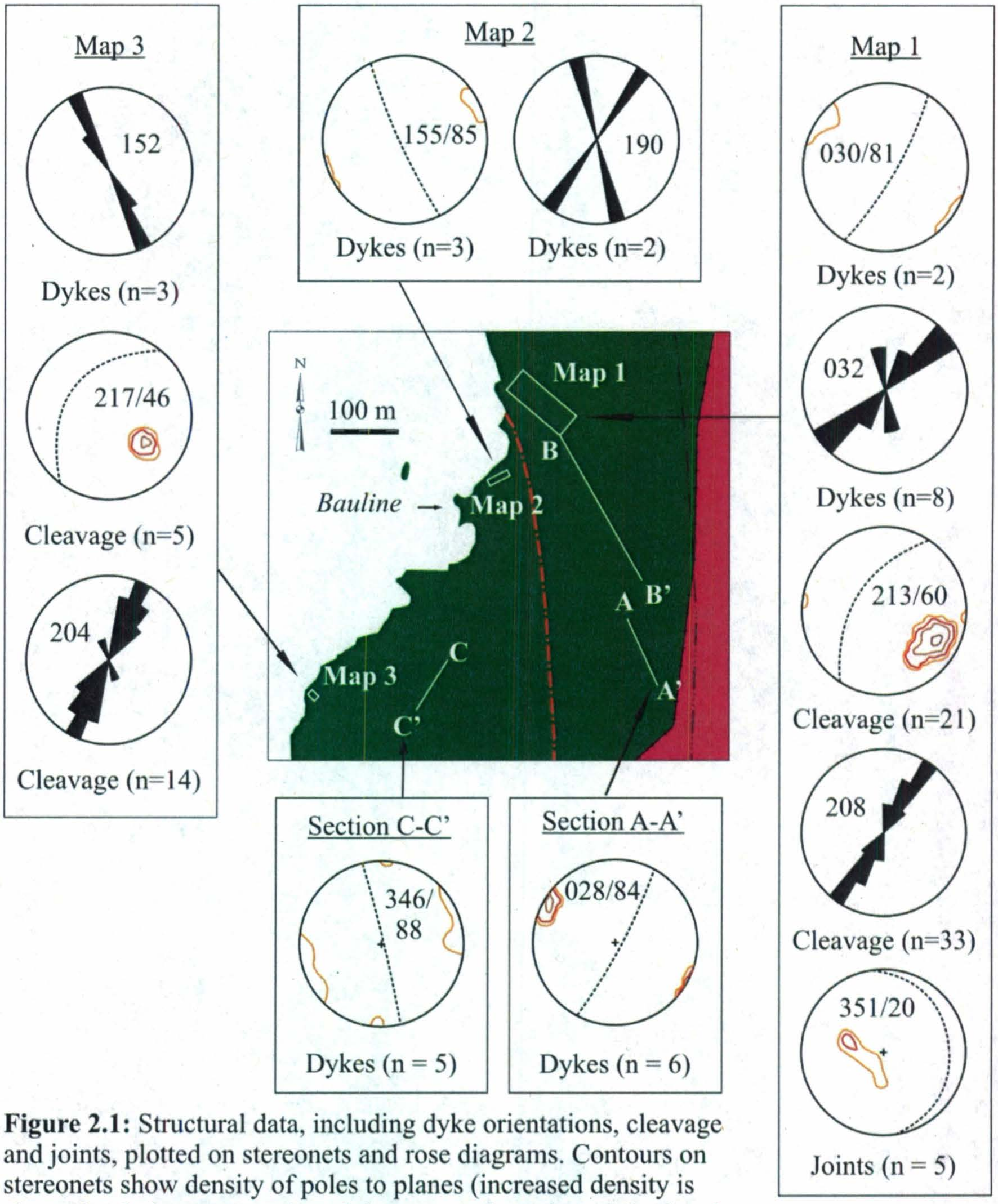

Figure 2.1: Structural data, including dyke orientations, cleavage and joints, plotted on stereonets and rose diagrams. Contours on stereonets show density of poles to planes (increased density is shown by darker contours), and the mean orientation of the data is given in strike/dip (RH) and plotted as a great circle. Since dip could not be measured for some dykes and cleavage planes, strike data are plotted on rose diagrams. The inset map of the study area indicates the locations of the structural data. Pink=Herring Cove Diorite; Green=Horse Cove Complex. The red dotted line indicates the location of an inferred fault.

2.3.1. Dyke orientations

The orientations of several dykes were measured in each of the maps and cross-sections in the study area, except for Section B-B'. Individual dykes are difficult to identify in this cross-section, due to shearing and lichen-cover. Orientations were determined for only a fraction of the dykes in the study area because there are a limited number of dykes with the necessary exposure to reliably measure strike and dip. For some dykes in Maps 1-3, dip could not be measured and strike data are plotted on rose diagrams in Figure 2.1. While the dykes in the study area are all steeply dipping, dykes on the east side of the study area in Map 1 and Section A-A' strike NE-SW, whereas dykes on the west side of the study area in Maps 2 & 3 and Section C-C' strike NW-SE (Figure 2.1).

2.3.2. Joints

Joint sets were observed in some rock units in Map 1. In feldspar porphyry throughout Map 1, E-W and NW-SE-striking fractures are spaced about 5-10 cm apart and dip 10-30° to the east. Joints are also common in the andesitic dykes in the centre of Map 1, and have similar orientations to those in feldspar porphyry. Joints were also observed in certain hornblende basaltic and basaltic-andesitic dykes in the western end of Map 1. These fractures are spaced 5-10 cm apart, strike NE-SW and dip about 35° to the east. The orientations of five joint sets are plotted on a stereonet in Figure 2.1.

2.3.3. Faults

Because the dykes in Map 1 and Section A-A' strike in a different direction from the dykes in Maps 2 & 3 and Section C-C', it is possible that the original dyke orientations were altered by a fault that separates the east and west sides of the study area. The trace of this interpreted fault is shown on the inset map in Figure 2.1. In Map 3, several smaller-scale, NE-SW-striking faults have produced dextral, ~ 1 m offsets towards the SW (200º). Granodiorite and several types of dykes are offset, including basaltic, andesitic (Plate 2.32a) and oxide-rich andesitic dykes (Plate 2.32b). Gravel-sized granodiorite breccia was observed along the faults, and one fault zone is occupied by a sheared basaltic dyke that contains lozenge-shaped, brecciated fragments of granodiorite and oxide-rich andesitic dykes (Plate 2.32c).

2.3.4. Shear zones and cleavage

NE-SW-striking, W-dipping deformation cleavage occurs extensively in Maps 1 and 3 (Figure 2.1). Although cleavage was observed throughout Map 1, the most strongly developed cleavage is concentrated in localized, NE-SW-striking shear zones that are approximately 2-5 m wide. These shear zones are characterized by deformed, lozenge-shaped blocks of granodiorite hosted by strongly sheared mafic-to-intermediate rocks (Plate 2.3b and c). While cleavage seems to affect all mafic-to-intermediate rock units, cleavage was not observed in feldspar porphyry or rhyolitic dykes, although granodiorite locally displays NE-SW-trending quartz ribbons (Plate 2.1a).

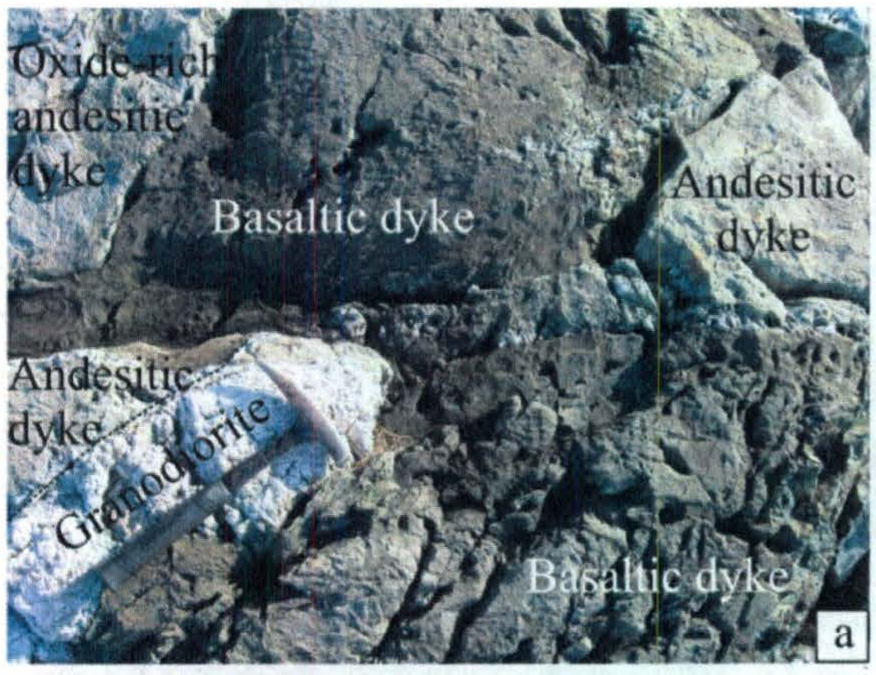

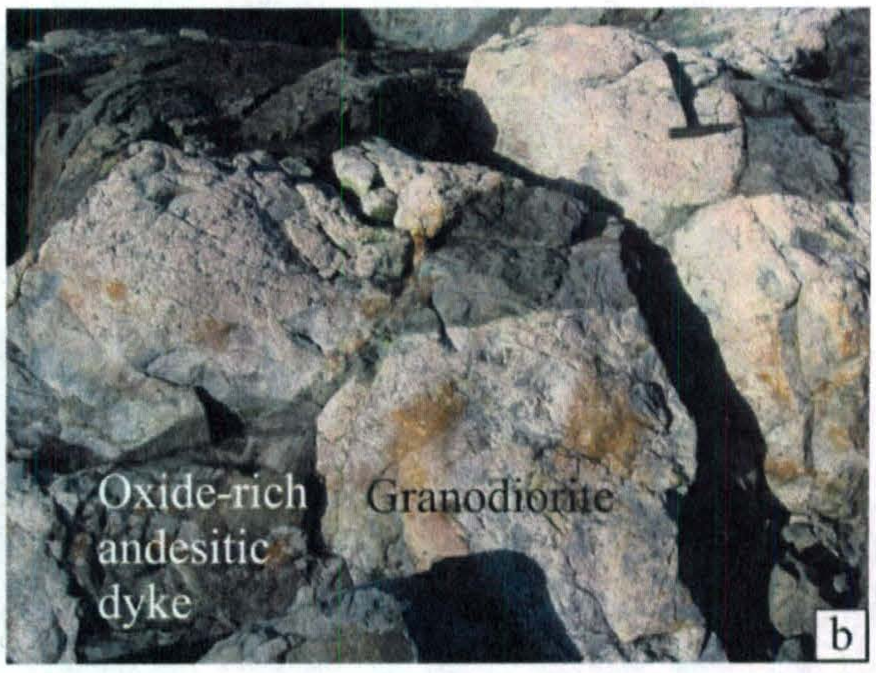

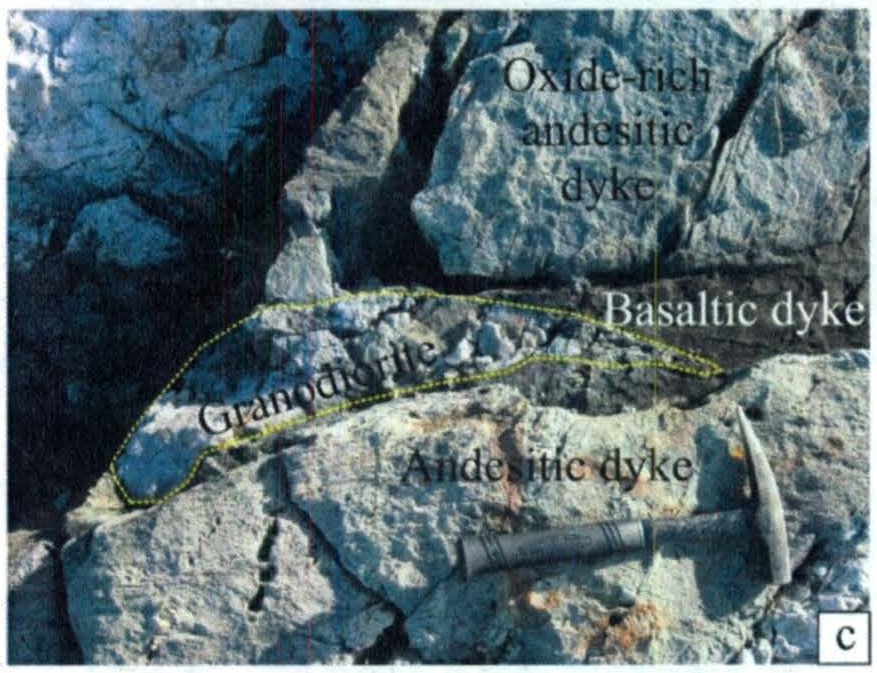

Plate 2.32: Field photographs of faults in Map 3. (a) Dextral offset of an andesitic dyke. (b) Dextral offsets of an oxide-rich andesitic dyke. (c) Fault zone occupied by a basaltic dyke and a lozenge-shaped, brecciated block of granodiorite.

Deformation fabrics are not present in Map 2, but subtle foliations occur in some mafic thin sections (e.g. Plate 2.19c). As well, one of the granodiorite blocks in Map 2 displays blastomylonitic texture and quartz ribbons in thin section (sample #68).

The rocks in all three cross-sections locally display shear fabrics, most commonly in mafic-to-intermediate dykes, but these fabrics were rarely measured because they are typically parallel to wavy, irregular dyke boundaries. In general, deformation cleavage is more extensive and more strongly developed proximal to the coast of Conception Bay.

2.3.5. Interpretation of structural elements

As mentioned in Chapter 1, the NE-trending Topsail Fault is exposed southwest of the study area and the trace of the fault can be extrapolated along the east coast of Conception Bay. In rocks east of the Topsail Fault, previous studies (e.g. King, 1988, 1990) have found evidence of polyphase deformation associated with the Topsail Fault, including sinistral, dextral and olique-slip motions and an overall eastward directed thrusting. Thus, many of the structures observed in the study area may be attributed to the proximity of the Topsail Fault.

The extensive dyke swarm in the study area, and along other sections of the east coast of Conception Bay, indicates a period of extension accompanied by magmatism. Extension may have occurred before the development of the Topsail Fault, or it may represent one of many episodes of deformation during the polyphase deformation history of the Topsail Fault. The difference in orientation of the dykes across the study area implies that either the fractures that accommodate the dykes opened in two different

directions, or that the east and west sides of the study area are separated by an unexposed fault that altered the orientations of the dykes.

King (1990) stated that NE-trending faults on the NE Avalon Peninsula, including the Pouch Cove River and Shoe Cove faults (Figure 1.3), may be splays from the nearby Topsail Fault. Thus, the inferred fault at Bauline that is interpreted to separate the east and west sides of the study area may also represent a splay from the Topsail Fault that postdates the emplacement of the dyke swarm. However, the sense of movement along this inferred fault remains uncertain, especially in light of the complex, multi-directional deformation history of the Topsail Fault.

Because cleavage in Maps 1 and 3 strikes NE-SW and dips about 45-60W, both areas, and perhaps the entire study area, appear to have been affected by the same cleavage-forming deformation event. As granodiorite appears to be the oldest rock in the study area, it is possible that the quartz ribbons in granodiorite formed during an earlier deformation event. Since the NE-SW orientation of quartz ribbons is parallel to the orientation of cleavage in other rock units, both fabrics may have developed under similar deformational stresses. The absence of cleavage in rhyolitic dykes and feldspar porphyry may be explained by the relative structural competence of these rock types. As well, since the strike of the cleavage is roughly parallel to the direction of offset of the small-scale faults in Map 3, the faults may have formed during a dextral strike-slip component of the cleavage-forming deformation event.

Because the area in which Map 2 is located is relatively undeformed, it may lie on a structural block that was isolated from the cleavage-forming deformation event. However, subtle deformation fabrics observed in thin sections of certain mafic dykes (e.g.

Plate 2.19c, sample #78) suggest that the area in which Map 2 is located has undergone weak deformation. The blastomylonitic texture and quartz ribbons observed in a granodiorite thin section from Map 2 (sample #68) indicate that, like granodiorite in Map 1, granodiorite in Map 2 has been locally affected by ductile deformation. Since the deformed granodiorite block is surrounded by younger, undeformed mafic dykes, granodiorite appears to have undergone deformation prior to the intrusion of the adjacent mafic dykes. If the deformed granodiorite block is not *in situ*, it may have undergone deformation at depth or elsewhere, prior to the magmatic or structural transport of the granodiorite block to its current position.

Cleavage development is interpreted to be post-magmatic, since it affects almost all rock units, including those with the youngest interpreted ages. The faults in Map 3, like the cleavage, appear to post-date magmatism, because offsets were observed in several rock units of different interpreted ages. Furthermore, cleavage seems to have developed after inferred movement along the fault that is interpreted to separate the east and west sides of the study area because cleavage has a nearly uniform orientation on both sides of the inferred fault.

As discussed in Chapter 1, the east coast of Conception Bay is affected by a NE-trending regional foliation that is attributed to deformation along the Topsail Fault (Sparkes, 2006). Because the deformation cleavage that affects the rocks in Bauline also strikes NE-SW, and since Bauline is in close proximity to the extrapolated trace of the Topsail Fault, the cleavage in the study area is probably equivalent to the regional NE-trending foliation that is associated with the Topsail Fault.

The spatial correlation of the HCC dyke swarm with the extrapolated trace of the Topsail Fault suggests a relationship between these two events. The Topsail Fault may have propagated along the zone of weakness formed by the HCC dyke swarm. Alternatively, the Topsail Fault may have provided a zone of weakness for the emplacement of the dyke swarm, and NE-SW-oriented cleavage may have developed in the dykes during the prolonged deformational history of the Topsail Fault.

The relationship between the joint sets in Map 1 and the other deformation features in the study area is uncertain, although the orientations of the joints are different from the orientations of dykes, cleavage and faults. It is possible that these fractures are synchronous with other brittle structures on the NE Avalon Peninsula, such as the E-W-trending Portugal Cove-Windsor Lake Fault (King, 1990). Similar to this fault, the joints in the study area may post-date eastward directed thrusting and could be related to late-stage folding, or alternatively, may represent unrelated deformation events.

CHAPTER 3: GEOCHRONOLOGY

3.1. Sample selection

To constrain the age of magmatism in the Horse Cove Complex (HCC), four rock units were selected for U/Pb zircon geochronology, including granodiorite, feldspar porphyry, an andesitic dyke and a rhyolitic dyke. These units were selected for dating based on well-defined field relationships that bracket the age of magmatism in the HCC and because their compositions favour the formation of zircon. A sample (#210) was also collected from a feldspar porphyritic basaltic dyke in Map 2 but no datable minerals were found after processing. The locations of the geochronology samples are shown in Figures 3.1 and 3.2. The samples were dated using the chemical abrasion TIMS method (Mattinson, 2005). Sample preparation and analysis are described in Appendix B. The U and Pb concentrations, isotopic data, ages and uncertainties of the four samples analyzed in this study are compiled in Table 3.1, and concordia diagrams are shown in Figure 3.3.

Granodiorite was chosen for U/Pb zircon geochronology because field relationships throughout the study area indicate that it predates all other magmatism and therefore provides the older age limit for the HCC. The granodiorite sample that was selected for dating (#211) is from a large granodiorite body in the centre of Map 1. Samples were collected from the rhyolitic dyke in Map 1 (#212) and the andesitic dyke in Map 2 (#209) to define a younger age limit for the HCC. Since the andesitic dyke in Map 2 cross-cuts several other dykes, it is known to be among the youngest magmatic events in the study area. As well, the rhyolitic dyke in Map 1 is hosted by feldspar porphyry and

Figure 3.1: Detail of Map 1, showing the locations of U/Pb zircon geochronology samples DS-09-211 in granodiorite, DS-09-212 in a rhyolitic dyke and DS-09-213 in feldspar porphyry. Note the occurence of granodiorite and feldspar porphyry as blocks surrounded by diorite and dykes, and that feldspar porphyry and diorite are cross-cut by the rhyolitic dyke.

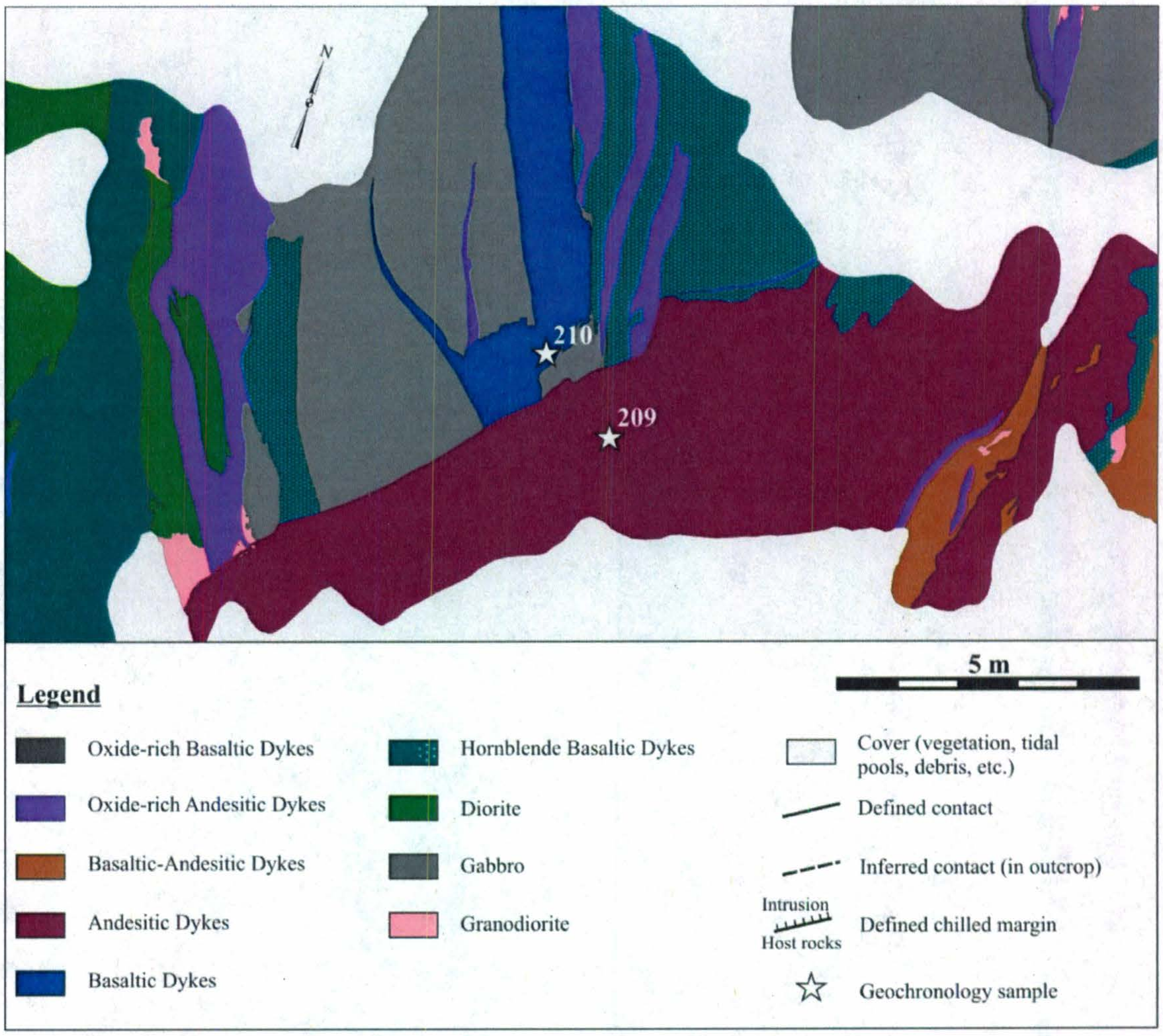

Figure 3.2: Detail of Map 2, showing the locations of U/Pb zircon geochronology samples DS-09-209 in an andesitic dyke and DS-09-210 in a basaltic dyke. Note that the andesitic dyke cross-cuts numerous rock units, including gabbro, feldspar-porphyritic hornblende basaltic dykes, oxide-rich andesitic dykes and a basaltic dyke. The andesitic dyke is cross-cut by a basaltic-andesitic dyke and oxide-rich andesitic dykes, although the contacts and intrusive relationships of these dykes are not well defined.

Table 3.1: U/Pb isotopic data for four rock samples from the Bauline area in the Avalon Zone, Conception Bay, Newfoundland. Samples #211-213 are from Map 1 and sample #209 is from Map 2.

Fraction	Concentration Measured				Corrected Atomic Ratios								Age (Ma)		
	Weight	U	Pb rad	total common Pb	206Pb / 204Pb	208Pb / 206Pb	206Pb / 238U	±	207Pb / 235U	±	207Pb / 206Pb	±	206Pb / 238U	207Pb / 235U	207Pb / 206Pb
	(mg)	(ppm)	(ppm)	(pg)											
Andesitic Dyke: DS-09-209 (362404, 5287013)															
Z1 6 clr prm & frag	0.006	82	8.9	9	359	0.2719	0.09387	50	0.7712	70	0.05959	46	578	580	589
Z2 3 clr prm & frag	0.003	109	11.9	7	307	0.2831	0.09386	64	0.7712	148	0.05959	100	578	580	589
Z3 6 clr prm	0.006	68	10.1	6	588	0.1726	0.13868	142	1.4283	124	0.07470	52	837	901	1060
Granodiorite: DS-09-211 (362450, 5287134)															
Z1 4 euh prm	0.006	217	24.5	2	4574	0.2225	0.10181	58	0.8489	48	0.06047	22	625	624	621
Z2 7 clr euh prm	0.010	370	40.9	2	12589	0.2032	0.10181	38	0.8502	28	0.06056	14	625	625	624
Z3 4 clr euh prm	0.006	251	27.6	8	1259	0.2016	0.10147	56	0.8487	68	0.06066	38	623	624	627
Z4 4 clr euh prm	0.006	430	48.0	2	7900	0.2096	0.10203	42	0.8508	34	0.06048	12	626	625	621
Rhyolitic Dyke: DS-09-212 (362480, 5287142)															
Z1 4 clr prm	0.006	134	14.4	1	3631	0.2573	0.09428	72	0.7720	68	0.05939	50	581	581	581
Z2 6 clr euh prm	0.009	114	12.0	1	5663	0.2316	0.09449	56	0.7722	44	0.05927	30	582	581	577
Z3 3 clr prm	0.004	197	21.0	1	4626	0.2516	0.09452	56	0.7732	46	0.05933	24	582	582	579
Z4 4 clr prm	0.006	89	9.4	2	1903	0.2465	0.09416	128	0.7706	96	0.05936	56	580	580	580
Z5 3 clr prm	0.004	71	7.4	1	1519	0.2336	0.09374	94	0.7664	82	0.05930	46	578	578	578
Feldspar Porphyry: DS-09-213 (362477, 5287127)															
Z1 6 clr euh prm	0.006	142	15.3	5	961	0.2613	0.09429	50	0.7721	90	0.05939	58	581	581	582
Z2 4 clr euh prm	0.004	132	14.0	15	224	0.2502	0.09411	80	0.7759	64	0.05980	40	580	583	596
Z3 2 clr euh prm	0.002	84	9.0	9	134	0.2623	0.09492	76	0.7838	320	0.05989	224	585	588	600
Z4 4 clr euh prm	0.004	120	13.0	6	505	0.2755	0.09427	62	0.7732	86	0.05948	58	581	582	585

Notes: All zircons were chemically abraded (Mattinson 2005) prior to dissolution; Z=zircon; 3,6, etc.=number of grains in analysis; clr=clear; euh=euhedral; prm=prisms; frag=fragments, mg=milligrams, ppm=parts per million, pg=picograms; UTM's (easting, northing) after sample number (NAD 27, Zone 22); errors reported after ratios are two sigma uncertainties.

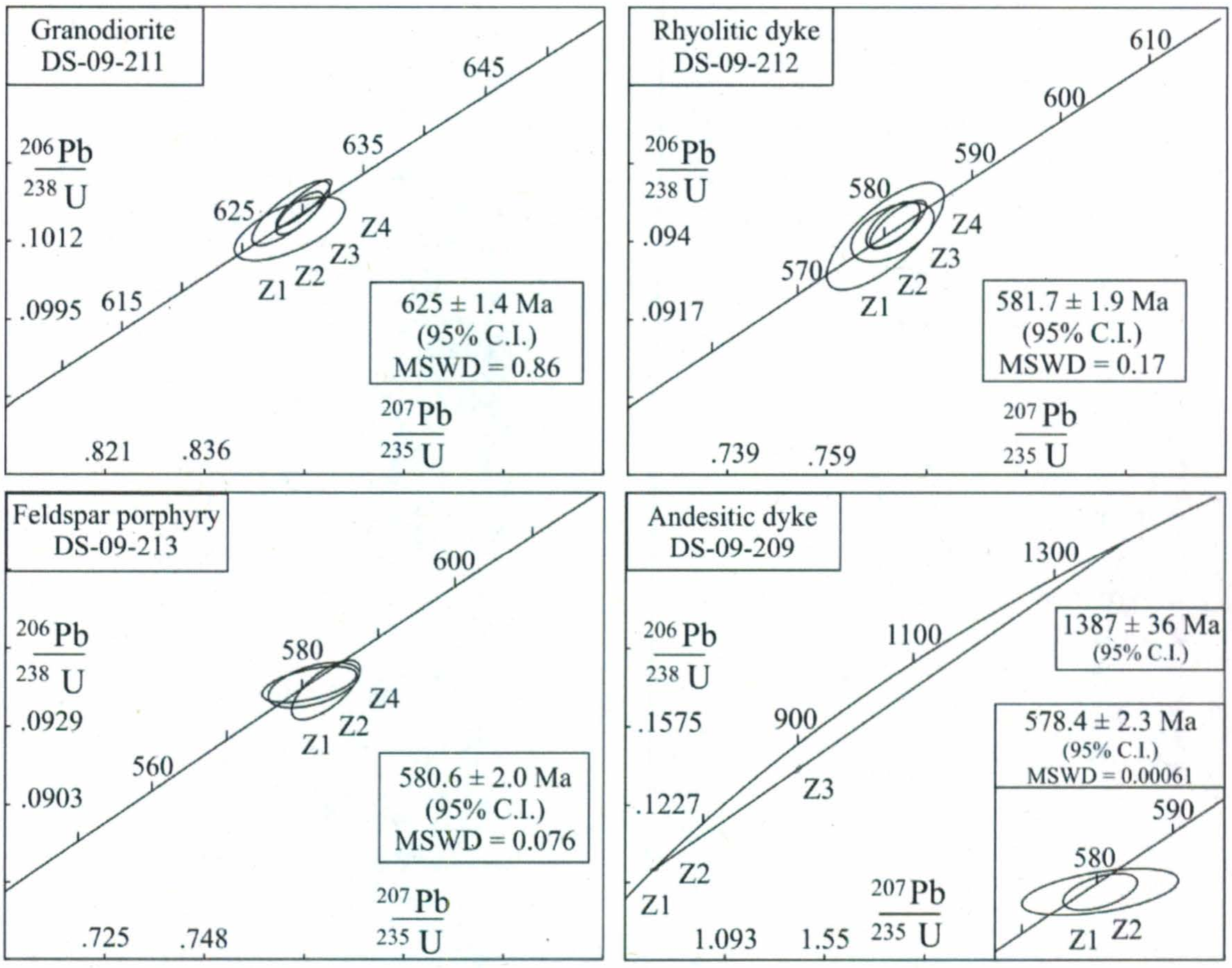

Figure 3.3: Concordia diagrams for the four samples selected for U/Pb geochronology from the Horse Cove Complex. U/Pb zircon ages are indicated in inset boxes.

diorite and appears to cross-cut an andesitic dyke. Therefore, the rhyolitic dyke is also a candidate for the youngest magmatic event in the HCC. The fourth U/Pb geochronology sample was taken from a large body of feldspar porphyry in Map 1 (#213). This feldspar porphyry body is cross-cut by the rhyolitic dyke from which sample #212 was taken. Because field evidence indicates that feldspar porphyry is younger than granodiorite but older than diorite and the swarm of mafic to felsic dykes, the U/Pb age of feldspar porphyry provides an intermediate age for magmatism in the study area. This age further constrains the timing of magmatism in the HCC within the age range bracketed by granodiorite and the rhyolitic and andesitic dykes.

3.2. Results

3.2.1. Granodiorite

Granodiorite yielded abundant, clear, euhedral zircons that formed 2:1 prisms (Plate 3.1a), and cathodeluminesence (CL) images show clear igneous growth zoning (Plate 3.2a). With U concentrations in the four measured fractions ranging from 217 ppm to 430 ppm, and a mean U concentration of 317 ppm, the zircons in granodiorite had the highest U concentrations of the four samples analyzed. The zircons in granodiorite also had the lowest $^{208}Pb/^{206}Pb$ ratio of the four rocks analyzed, signifying lower Th/U in the granodiorite melt. At the 95% confidence interval, this sample yielded a U/Pb age of 625 ± 1.4 Ma (MSWD = 0.86).

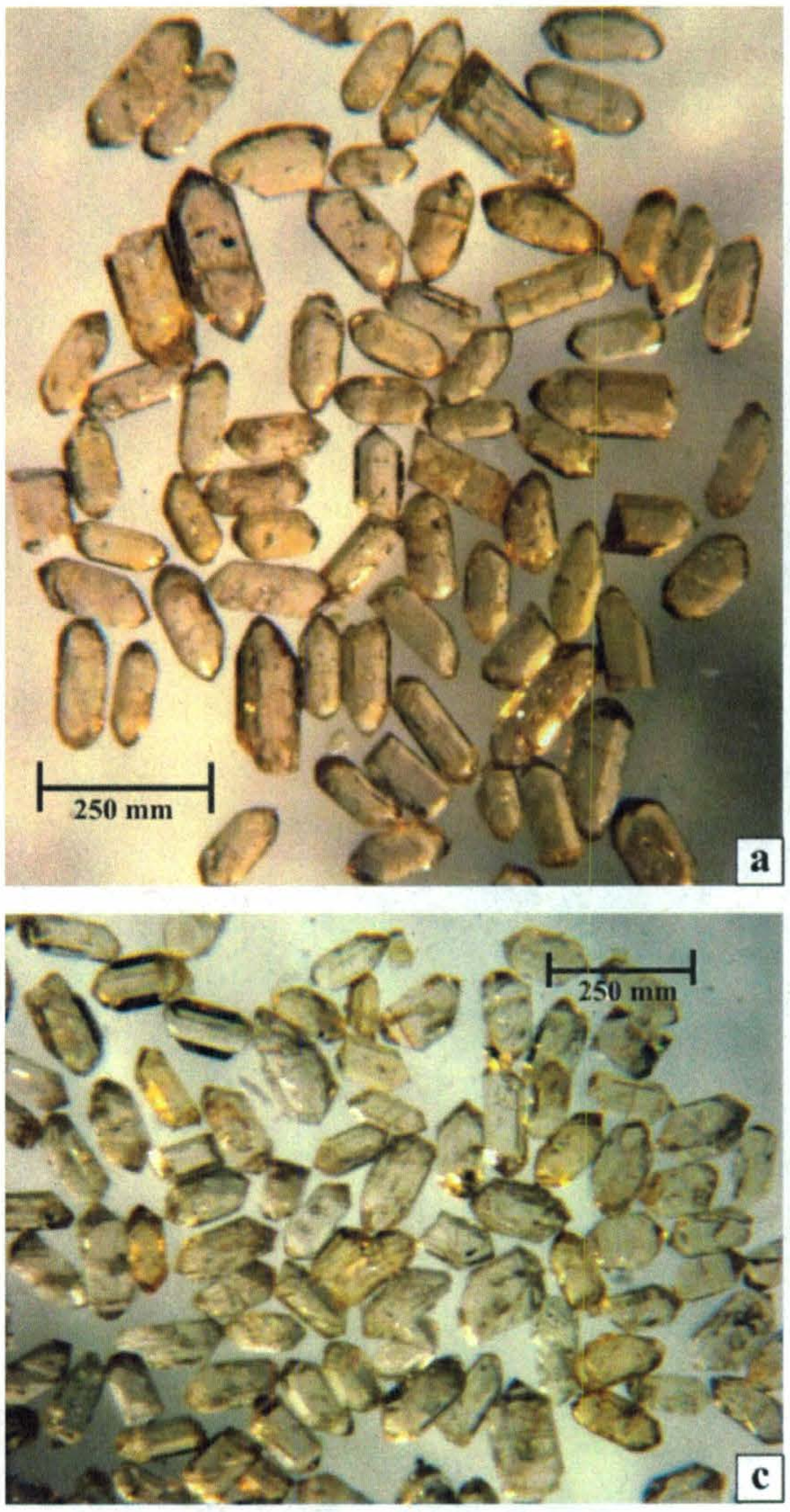

Plate 3.1: Plane polarized light photomicrographs of zircon from each of the samples selected for U/Pb geochronology. (a) Clear, euhedral 2:1 prisms from granodiorite (sample DS-09-211). (b) Clear, euhedral 3:1 prisms from a rhyolitic dyke (sample DS-09-212). (c) Clear, euhredral 2:1 prisms from feldspar porphyry (sample DS-09-213). (d) Clear 2:1 prisms from an andesitic dyke (sample DS-09-209), including subhedral crystals, smaller subrounded grains and crystal fragments.

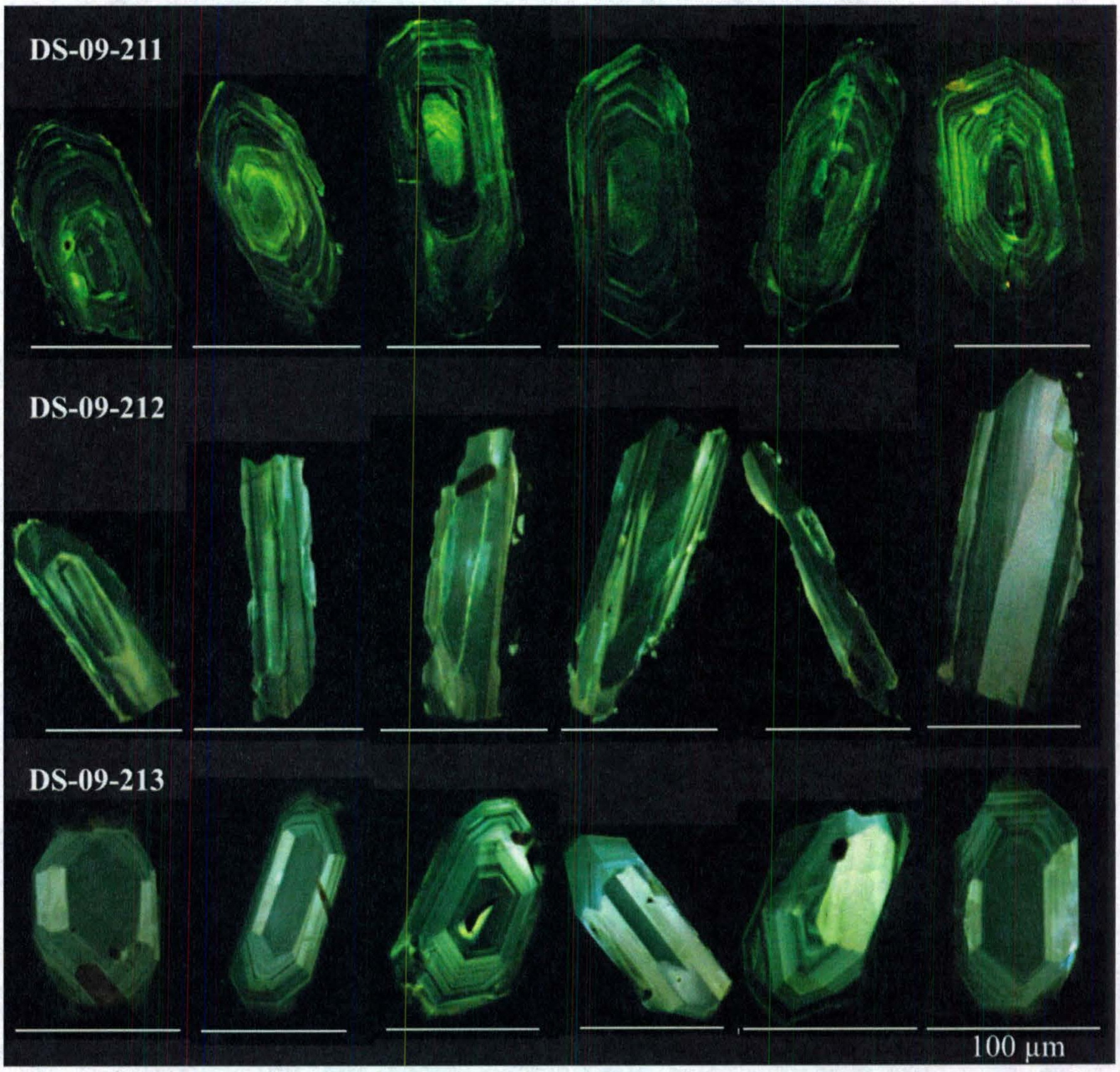

Plate 3.2: Cathodeluminescence images of zircon from three of the four samples chosen for U/Pb geochronology, including granodiorite (DS-09-211), a rhyolitic dyke (DS-09-212) and feldspar porphyry (DS-09-213). All scale bars are 100 µm.

3.2.2. Rhyolitic dyke

The rhyolitic dyke contained abundant zircons that formed clear, euhedral 3:1 prisms (Plate 3.1b) with longitudinal zoning visible in CL (Plate 3.2b). The five measured fractions yield a U/Pb age of 581.2 ± 1.8 Ma (MSWD = 0.61). However, the $^{206}Pb/^{238}U$ ratio for fraction Z5 is significantly lower than all the other fractions, perhaps because it has some Pb loss that was not eliminated by chemical abrasion. When the U/Pb age is calculated for fractions Z1-Z4, the U/Pb age is 581.7 ± 1.9 Ma (MSWD = 0.17) at the 95% confidence interval. This age is accepted as the age of the rhyolitic dyke because it avoids possible Pb loss from fraction Z5 and has a lower MSWD than the age calculated using all five fractions.

3.2.3. Feldspar porphyry

This sample contained the most abundant, best quality zircons of all the samples dated. The zircons in this sample occurred as very clear, euhedral 2:1 prisms and well-developed igneous growth zoning was revealed by cathodoluminescence (Plates 3.1c and 3.2c). The U concentrations and $^{208}Pb/^{206}Pb$ ratios of the zircons measured in this sample were similar to those in the zircons in the rhyolitic dyke. At the 95% confidence interval, the four measured fractions from this sample yielded a U/Pb age of 581.4 ± 1.8 Ma (MSWD = 0.91). However, fraction Z3 had a significantly higher proportion of common Pb and it is shifted to the right on the Concordia diagram, rendering it less reliable than the other fractions. Calculated without fraction Z3, the U/Pb age for this sample is 580.6 ± 2.0 Ma at the 95% confidence interval (MSWD = 0.076). This age has a much lower MSWD and is the accepted age for feldspar porphyry.

3.2.4. Andesitic dyke

The andesitic dyke contained clear, subhedral 2:1 prisms of various sizes that represent three populations: small, sub-rounded zircons; larger zircons with one or more crystal faces; and crystal fragments that did not match either of these groups. The largest zircons with the best-developed crystal faces (Plate 3.1d) were selected for dating, but none of these zircons could be spared for CL imaging. Two of the three measured fractions gave a U/Pb age of 578.4 ± 2.3 Ma (MSWD = 0.00061) at the 95% confidence interval. These two fractions have the highest $^{208}Pb/^{206}Pb$ ratios of all samples, but the U concentrations were similar to those in the zircons from the rhyolitic dyke and feldspar porphyry.

Fraction Z3 was not used to calculate the U/Pb age of the andesitic dyke because it plotted below Concordia and gave an anomalously older U/Pb age of about 900 Ma. The age of this fraction can be attributed to one or more inherited zircon crystals or inherited cores among the six crystals analyzed in fraction Z3. The inherited component of fraction Z3 yielded an average age of 1387 ± 36 Ma at the 95% confidence interval. Fraction Z3 also has a lower $^{208}Pb/^{206}Pb$ ratio than the other two fractions in this sample, indicating that the inherited component in this fraction may have crystallized in a melt with a lower Th/U than that for fractions Z1 and Z2.

3.3. Discussion

3.3.1. Age of the Horse Cove Complex

With a U/Pb age of 625 ± 1.4 Ma, granodiorite is the oldest unit among the four units that were dated using U/Pb geochronology. This supports the interpretation of field

relationships discussed in Chapter 2, which indicate that granodiorite predates all other rocks in the study area. U/Pb geochronology has revealed that the rhyolitic dyke, feldspar porphyry and the andesitic dyke, with U/Pb ages of 581 ± 1.9 Ma, 580.6 ± 2.0 Ma and 578.4 ± 2.3 Ma, respectively, are all at least 40 Ma younger than the granodiorite. The U/Pb ages of these three units overlap within their combined uncertainties, raising the possibility that they were emplaced simultaneously. However, as discussed in Chapter 2, field relationships indicate that the 581.7 ± 1.9 Ma rhyolitic dyke is younger than the 580.6 ± 2.0 Ma feldspar porphyry. Therefore, the rhyolitic dyke is no older than 582.6 Ma, and it may be as much as 2.8 Ma younger than feldspar porphyry.

The 578.4 ± 2.3 Ma U/Pb age of the andesitic dyke implies that it is the youngest rock unit of those dated in the study area. The lack of field relationships between the andesitic dyke that was selected for U/Pb geochronology and the 581.7 ± 1.9 Ma rhyolitic dyke and the 580.6 ± 2.0 Ma feldspar porphyry does not allow their direct comparison. Nevertheless, because the 581.7 ± 1.9 Ma rhyolitic dyke cross-cuts an unsampled, light grey-weathering dyke that is interpreted to be an andesitic dyke, it appears to be younger than at least one andesitic dyke in the study area. However, since this andesitic dyke was not sampled, its petrographic and geochemical equivalence to the 578.4 ± 2.3 Ma andesitic dyke cannot be proven. Furthermore, even if they were found to be from equivalent melts, the two andesitic dykes need not be the same age. Thus, it remains uncertain whether the 578.4 ± 2.3 Ma andesitic dyke is indeed younger than the 581.7 ± 1.9 Ma rhyolitic dyke, but the two rocks must have been emplaced within 6.5 Ma of each other.

U/Pb geochronology indicates that the 578.4 ± 2.3 Ma andesitic dyke and the 580.6 ± 2.0 Ma feldspar porphyry also crystallized within 6.5 Ma of each other. Because the 578.4 ± 2.3 Ma andesitic dyke is not in contact with feldspar porphyry, and their U/Pb ages overlap in uncertainty, their age relationship is ambiguous. However, feldspar porphyry in Map 1, including the feldspar porphyry body that was dated at 580.6 ± 2.0 Ma, is cross-cut by numerous andesitic dykes that are geochemically and petrographically similar to the 578.4 ± 2.3 Ma andesitic dyke in Map 2. Therefore, it is likely that the 578.4 ± 2.3 Ma andesitic dyke is also younger than feldspar porphyry.

Regardless of the relative age relationships between the feldspar porphyry, rhyolitic dyke and andesitic dyke that were selected for U/Pb geochronology, it is clear that they bracket a narrow window of magmatism spanning, at most, 6.5 Ma. The ages of these units, together with the U/Pb age of 625 ± 1.4 Ma for granodiorite, record ~40 Ma of geological history in the study area. However, field relationships demonstrate that the majority of rocks in the study area postdate feldspar porphyry. For instance, diorite is interpreted to be younger than feldspar porphyry because it surrounds numerous blocks of feldspar porphyry that are petrographically and geochemically comparable. Because field evidence suggests that diorite is younger than the 580.6 ± 2.0 Ma feldspar porphyry, and it is clearly cross-cut by the 581.7 ± 1.9 Ma rhyolitic dyke, the age of diorite is constrained between 582.6 Ma and 579.8 Ma.

Feldspar porphyry is cross-cut by several types of dykes in Map 1 and Section A-A', including dykes of rhyolitic, andesitic, oxide-rich andesitic, basaltic-andesitic and hornblende-porphyritic andesitic compositions. Because many dykes in the study area do not share cross-cutting relationships with feldspar porphyry, it is impossible to know

whether the entire dyke swarm postdates feldspar porphyry. However, many of the dykes that are not in contact with feldspar porphyry are hosted by diorite, or are known to be younger than those hosted by diorite, which is interpreted to be younger than feldspar porphyry. Therefore, it is plausible that the entire dyke swarm in the study area is younger than feldspar porphyry, and that the U/Pb zircon age of 580.6 ± 2.0 Ma for the feldspar porphyry provides the older age limit for the entire dyke swarm. Nevertheless, complex cross-cutting relationships validate the episodic nature of the dyke swarm, preventing absolute proof that all dykes are younger than feldspar porphyry.

The 578.4 ± 2.3 Ma andesitic dyke in Map 2 cross-cuts several rock units, including gabbro, feldspar-porphyritic hornblende basaltic dykes, oxide-rich andesitic dykes and a basaltic dyke. Since it represents a single magmatic event that is unmistakably younger than several dykes, the 578.4 ± 2.3 Ma andesitic dyke provides the best estimate for the younger age limit of magmatism in the HCC. Throughout the study area, andesitic dykes commonly cross-cut other dykes of various compositions and are seldom cross-cut by other intrusions. Therefore, it is reasonable to assume that other andesitic dykes also represent the youngest magmatism in the HCC in the study area, and that they are coeval with the 578.4 ± 2.3 Ma andesitic dyke. There are, however, certain dykes that appear to postdate the andesitic dykes, as mentioned in Chapter 2. For instance, oxide-rich andesitic dykes and a basaltic-andesitic dyke cross-cut the 578.4 ± 2.3 Ma andesitic dyke in Map 2, and a ~5 cm wide oxide-rich andesitic dyke cross-cuts an andesitic dyke in Map 3. As well, andesitic dykes in Map 1 appear to be locally intruded by unsampled mafic dykes and an oxide-rich basaltic dyke, although deformation has partially obscured contacts and intrusive relationships are unclear. Despite limited

evidence of magmatism following the andesitic dykes, the best estimate of the younger limit of magmatism in the HCC is the U/Pb age of 578.4 ± 2.3 Ma for the andesitic dyke in Map 2.

In summary, U/Pb geochronology of four key rock units has revealed a ~40 Ma age gap between the crystallization of granodiorite and the emplacement of all other mapped magmatic events in the study area. The U/Pb age of 625 ± 1.4 Ma for granodiorite confirms that granodiorite is either the *in situ* host rock for subsequent magmatism, or was tectonically or magmatically transported as blocks from an older intrusion. Because nearly all the magmatism in the HCC in the Bauline area appears to have occurred after the intrusion of feldspar porphyry and before the emplacement of the andesitic dykes, the best estimate for the duration of the majority of magmatism in the HCC is provided by the U/Pb zircon ages of these two units. Thus, most magmatism in the Bauline area appears to have occurred during a relatively short period of up to 6.5 Ma, between about 582.6 Ma and 576.1 Ma. At the other limit of interpretation, all dykes could have been emplaced very rapidly, within, for example, 100 000 years. The inferred sequence of magmatic events in the HCC is summarized schematically in Figure 3.4.

The U/Pb age determination for magmatism in the HCC has implications for the age of deformation in the study area. The fractures that now accommodate dykes must have opened during emplacement of the dyke swarm, between about 582.6 Ma and 576.1 Ma. As discussed in Chapter 2, the difference in orientation of the dykes across the study area may be due to movement along an unexposed fault. Displacement along this fault must have occurred either during or after the emplacement of the dyke swarm, after about 582.6 Ma. As examined in Chapter 2, the timing of the deformation event responsible for

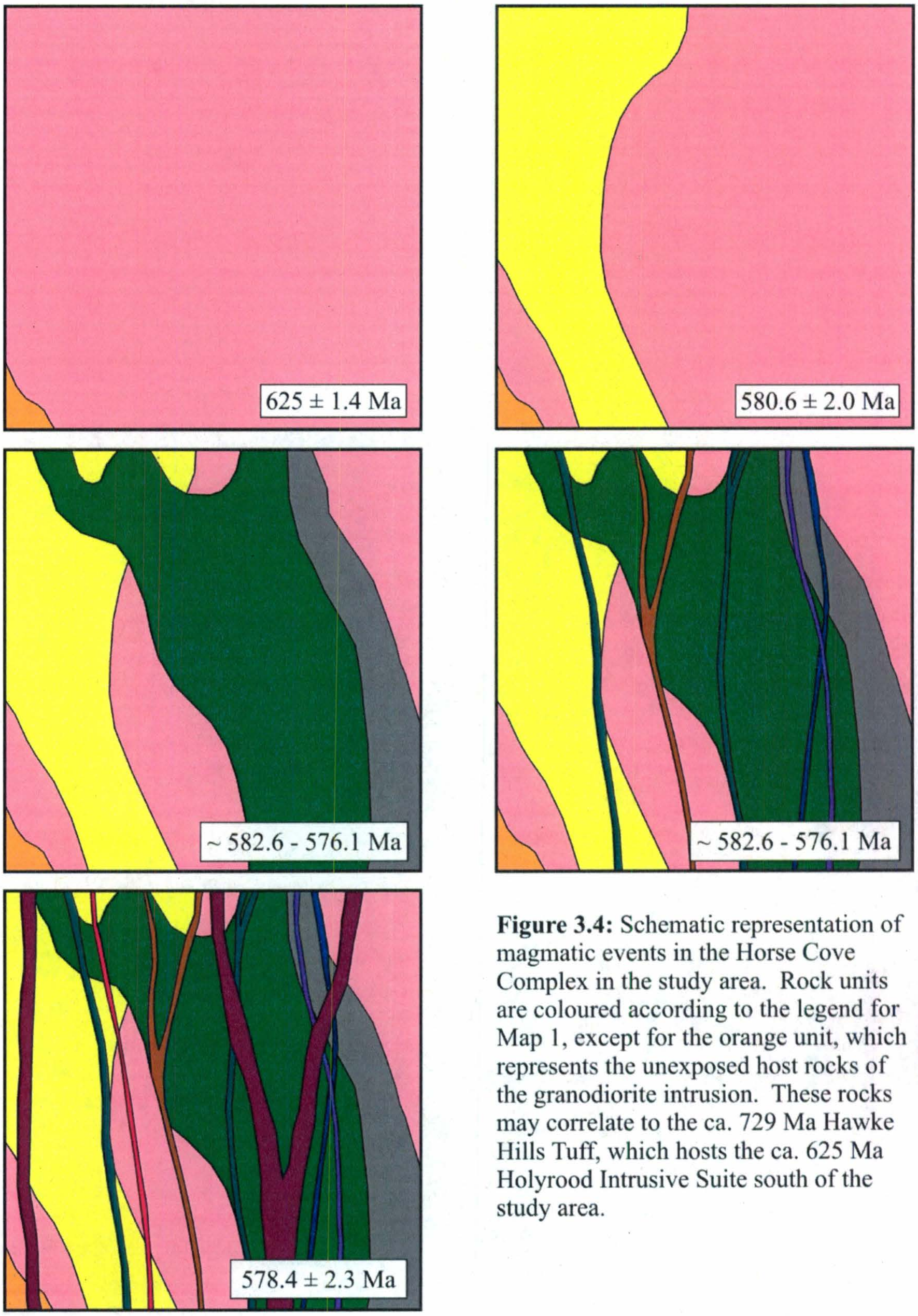

Figure 3.4: Schematic representation of magmatic events in the Horse Cove Complex in the study area. Rock units are coloured according to the legend for Map 1, except for the orange unit, which represents the unexposed host rocks of the granodiorite intrusion. These rocks may correlate to the ca. 729 Ma Hawke Hills Tuff, which hosts the ca. 625 Ma Holyrood Intrusive Suite south of the study area.

the formation of NE-SW-oriented cleavage is a complex issue. All rock units in the study area, except for those in Map 2, exhibit NE-SW-oriented cleavage, and therefore must pre-date the deformation event that created the cleavage. It is possible that this deformation event occurred after the dyke swarm, post-576.1 Ma, but left the area studied in Map 2 unaffected on an isolated structural block. Another theory is that the deformation event that formed the NE-SW-oriented cleavage is younger than all the rocks in the study area except for those in Map 2. In this case, the deformation event would be bracketed between 582.6 Ma, the older age limit on the dyke swarm, and 580.7 Ma, the older age limit on the andesitic dyke in Map 2. It is possible that quartz ribbons in granodiorite, including those in the dated sample, formed during the deformation event that formed NE-SW-oriented cleavage because the quartz ribbons are also oriented NE-SW. However, quartz ribbons, granulation and other brittle and ductile deformation features observed in granodiorite may be the products of a complex and protracted deformation history, as permitted by the significantly older age of this rock.

3.3.2. Regional age correlations

U/Pb geochronology of four key rock units at Bauline allows temporal correlations to be made with other dated rocks on the NE Avalon Peninsula. A summary of all known post-630 Ma U/Pb ages from the NE Avalon Peninsula is provided in Figure 3.5. The U/Pb zircon age of 625 ± 1.4 Ma for granodiorite in this study overlaps with established U/Pb zircon ages of granitoid rocks in the Holyrood Intrusive Suite (HIS). These rocks include the 622.5 ± 1.3 Ma pink, white and green granite dated by Sparkes

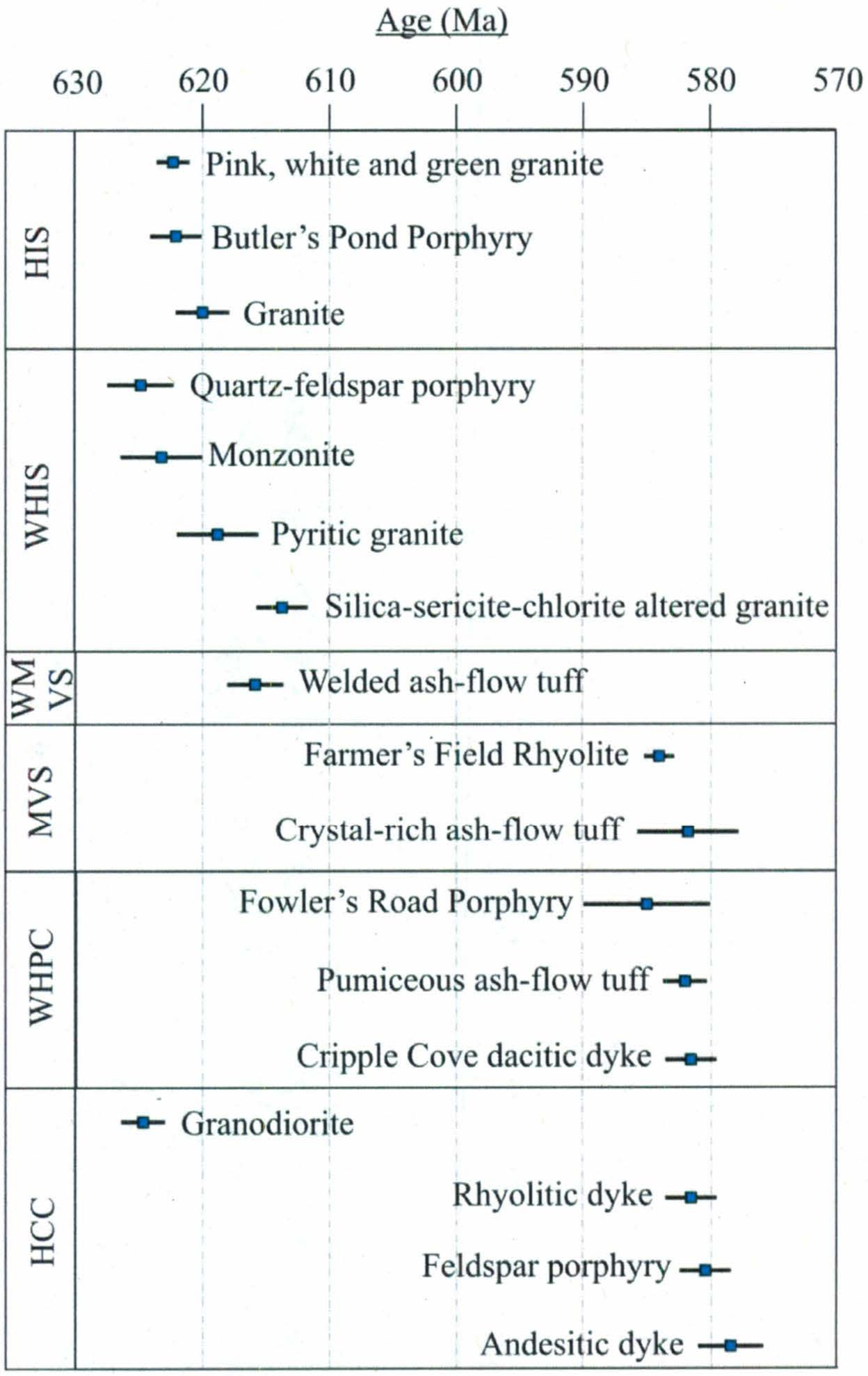

Figure 3.5: A summary of U/Pb zircon geochronological data for the NE Avalon Peninsula after 630 Ma, modified after Sparkes (2005). HIS=Holyrood Intrusive Suite; WHIS=White Hills Intrusive Suite; WMVS=White Mountain Volcanic Suite; WHPC=Wych Hazel Pond Complex; MVS=Manuels Volcanic Suite; HCC=Horse Cove Complex. Except for the HCC ages from this study, all U/Pb ages were determined by Sparkes (2005), apart from the ages of the HIS pink, white and green granite (O'Brien *et al.* 2001; modified by Sparkes 2005), the HIS Butler's Pond Porphyry (Sparkes *et al.* 2002), the HIS granite (Krogh *et al.* 1988) and the Cripple Cove dacitic dyke (Cooper, 2011).

(2005), modified from the age initially determined by O'Brien *et al.* (2001), and the 622 ± 2 Ma Butler's Pond Porphyry dated by Sparkes *et al.* (2002). The granodiorite from Bauline also overlaps in age with two rocks from the White Hills Intrusive Suite (WHIS), which occurs near the eastern margin of the Holyrood Horst and shares a faulted or inferred intrusive contact with granite of the HIS (Sparkes, 2005). The dated rocks from the WHIS include a 623.5 ± 3.5 Ma monzonite and a quartz-feldspar porphyry that crystallized at 625 ± 2.5 Ma (Sparkes, 2005; Sparkes *et al.*, 2005). In addition, the 625 ± 1.4 Ma granodiorite is close in age to a HIS granite that was dated at 620 ± 2 Ma by Krogh *et al.* (1988), as well as a 619 ± 3 Ma pyritic granite from the WHIS, dated by Sparkes (2005).

The U/Pb age of 625 ± 1.4 Ma for the granodiorite from Bauline is the first evidence of this age of magmatism east of the Topsail Fault and so far north, and confirms that the granodiorite is contemporaneous with several granitoid rocks in the Holyrood and White Hills intrusive suites. The 625 ± 1.4 Ma age of the granodiorite from Bauline supports the mapping of Sparkes (2006), in which granitoid rocks along the east coast of Conception Bay were assigned to the HIS. Rather than including the 625 ± 1.4 Ma granodiorite from Bauline in the HCC, it is more appropriately correlated with the HIS and WHIS because it is synchronous with the HIS and WHIS and predates magmatism in the HCC by ca. 40 Ma.

The feldspar porphyry, rhyolitic and andesitic dykes from the HCC overlap in age, within uncertainties, with several felsic magmatic events on the NE Avalon Peninsula. For example, these three units overlap in age with a dacitic dyke that cross-cuts mafic volcaniclastic rocks in the Wych Hazel Pond Complex (WHPC) at Cripple Cove, north of

the study area, which was dated at 581.7 ± 1.8 Ma (Cooper, 2011). In addition, feldspar porphyry, rhyolitic and andesitic dykes from the HCC overlap in age with a pumiceous ash-flow tuff in the WHPC that was dated at 582 ± 1.5 Ma (Sparkes, 2005), and with a crystal-rich ash-flow tuff in the Manuels Volcanic Suite (MVS) that hosts low-sulphidation alteration, dated at 584 ± 4 Ma (Sparkes, 2005). The U/Pb ages for the HCC feldspar porphyry, rhyolitic dyke and andesitic dyke also coincide with the 585 ± 5 Ma Fowler's Road Porphyry, which is hosted by siltstones in the upper WHPC (Sparkes, 2005). As well, the 584 ± 1 Ma Farmer's Field Rhyolite of the MVS overlaps in age with the HCC rhyolitic dyke but is postdated by the feldspar porphyry and andesitic dyke. The Farmer's Field Rhyolite, which was dated by Sparkes (2005), hosts the high-sulphidation alteration system in the Oval Pit Mine.

The overlapping U/Pb ages of the HCC feldspar porphyry, rhyolitic dyke and andesitic dyke at Bauline with numerous felsic volcanic and intrusive rocks on the eastern margin of the Holyrood Horst, and with a dacitic dyke at Cripple Cove, indicate that felsic magmatism occurred simultaneously in all three locations, spanning a distance of about 35 km. Several intermediate to mafic intrusive events also occurred in the HCC during this period, as bracketed by the ages of feldspar porphyry and the andesitic dyke in the study area. Furthermore, the ages of the HCC feldspar porphyry, rhyolitic dyke and andesitic dyke coincide with the 585 to 580.5 Ma high-sulphidation style alteration system and the 584 ± 4 Ma-and-younger low-sulphidation style alteration system in the Eastern Avalon High-Alumina Belt (Sparkes, 2005).

CHAPTER 4: GEOCHEMISTRY

4.1. Introduction

Sixty-six samples were collected from Maps 1-3 for major and trace element geochemical analysis because these areas have the greatest lithological variety and the best-defined field relationships. Rocks were analysed from each of the units identified in the Horse Cove Complex (HCC) in the study area. The samples are referred to in the text by sample number, without the prefix "DS-09", and the locations of the analysed samples are shown on Maps 1-3. The samples were powdered at the rock preparation facilities at Memorial University of Newfoundland and sent to Actlabs, where they were prepared for analysis using the lithium metaborate/tetraborate fusion technique. At Actlabs, the samples were analysed using the inductively coupled plasma emission spectrometer (ICP-ES) and the inductively coupled plasma mass spectrometer (ICP-MS). To test complete dissolution of samples analyzed using ICP methods, twenty samples were analyzed at Memorial University of Newfoundland using the X-ray fluorescence (XRF) technique. Sample preparation and methods of analysis are described in Appendix C and the major and trace element geochemical data from the HCC are reported in Appendix D. Analyses of standard reference materials and duplicates, as well as a discussion of data quality, are provided in Appendix E. Seven samples were selected for Nd isotopic analysis, and were analysed using the thermal ionization mass spectrometer (TIMS) at Memorial University of Newfoundland. Methods of Nd isotopic analysis are described in Appendix F.

Prior to plotting and interpreting the geochemical data, average values were calculated for all duplicate and triplicate analyses. As well, because data that approach

limits of detection may not be quantitative, values that were less than 1.5 times the limit of detection were removed from the dataset (G. Jenner, personal communication, 2010). This included the removal of some trace element data for several samples, and the removal of all As, Mo, In and Bi analyses. Since the ICP-ES analysis did not differentiate between ferrous and ferric Fe, the Fe data were converted to total Fe as FeO, denoted as FeO*, where $FeO^*=Fe_2O_3*0.8998$. The data were recalculated volatile free to a total of 100%. The trace element data were modified using the recalculation factor determined from corresponding major element analyses.

The major and trace element geochemistry of each rock unit mapped in the study area is described below, followed by a discussion of geochemical trends and similarities between rock units and implications for the tectonic setting of the HCC. In addition, the geochemistry of the HCC in the study area is compared to data from other rocks on the NE Avalon Peninsula acquired by previous studies.

4.2. Alteration

As evidenced by significant epidote veining thoughout the map area and greenschist-facies mineralogy observed in thin section, the rocks at Bauline have been affected by alteration/metamorphism. Therefore, caution must be used when interpreting the concentrations of potentially mobile elements. For example, the total alkali-silica plot of Le Bas *et al.* (1986) puts many samples in the trachyandesite and trachydacite fields, whereas classification diagrams that use less mobile elements, including the Nb/Y vs. Zr/TiO_2 plot of Pearce (1996; Figure 4.1a) and the Zr/TiO_2 vs. SiO_2 plot of Winchester and Floyd (1977; Figure 4.1b), place these samples in the andesite and dacite fields. This

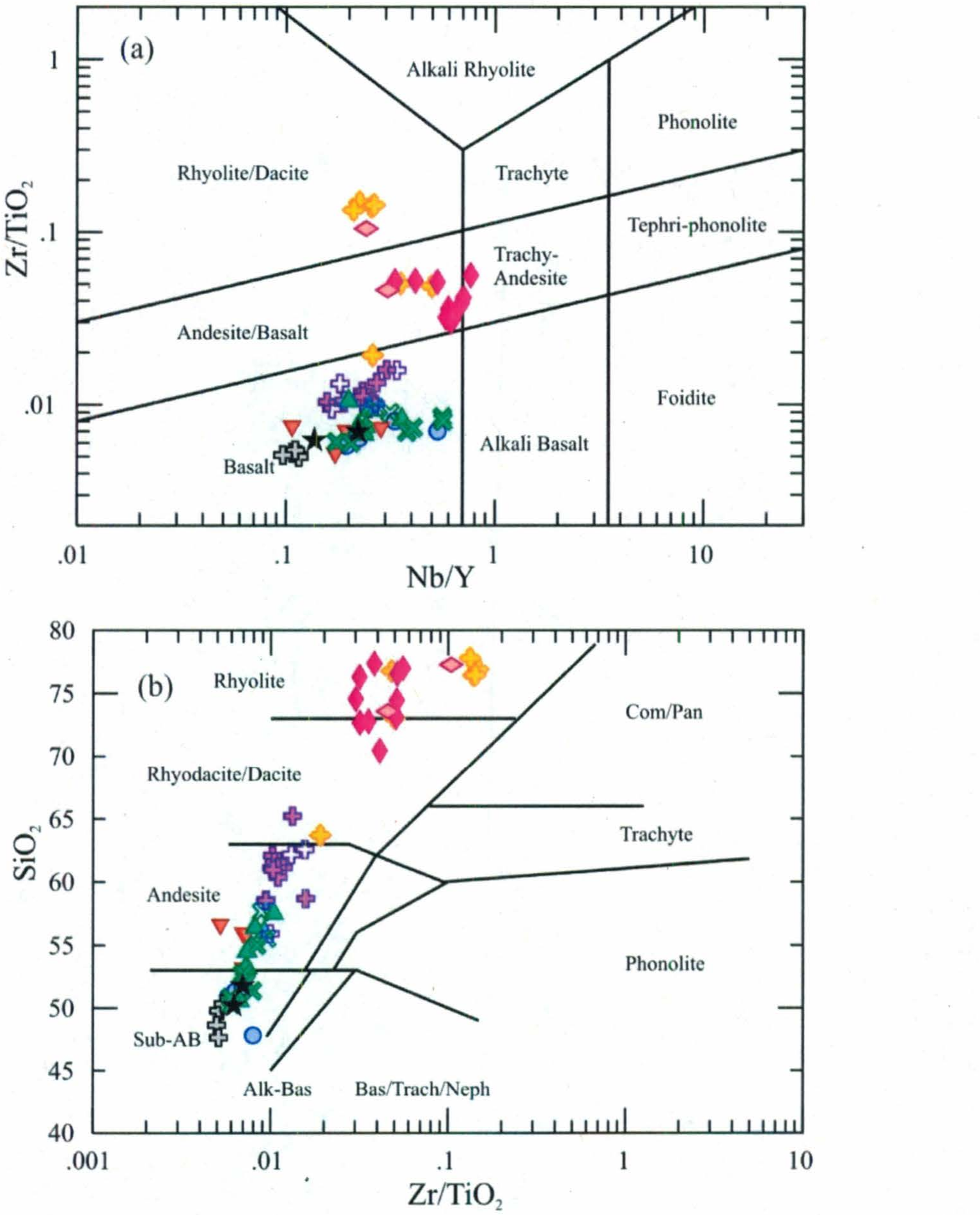

Figure 4.1: Classification diagrams of (a) Pearce (1996) and (b) Winchester and Floyd (1977).

shows that alteration in the rocks at Bauline has caused enrichment of Na_2O and/or K_2O. As well, the alteration plot of Hughes (1973; Figure 4.2) shows that many of the rocks in the dataset have been affected by Na-metasomatism. Therefore, elements that are potentially mobile (e.g. Na_2O, K_2O, Rb, Ba, Sr, CaO) cannot be trusted to characterize the rocks geochemically. Instead, only elements that are known to resist mobility under alteration conditions will be used to characterize the rocks and identify geochemical trends. Although major elements tend to be mobile, certain major elements (e.g. SiO_2, MgO, FeO) will be used to characterize the rocks because they do not appear to have been significantly affected by alteration, as analyses of these elements are clustered by lithology or display trends consistent with igneous fractionation.

4.3. Methodology

The samples are grouped according to rock unit in order to maintain the context of lithology, petrography and relative ages, as described in Chapter 2. However, all samples in a given rock unit are not always geochemically equivalent and, in many cases, share geochemical traits with samples from other units. The geochemistry of each rock unit is described below and followed by a brief interpretation, and finally, a discussion of similarities between data from different rock units and implications regarding the formation of the HCC.

4.3.1. Classification

In the geochemical descriptions of each rock unit, the classification diagrams of Winchester and Floyd (1977) and Pearce (1996) are used to show the general composition

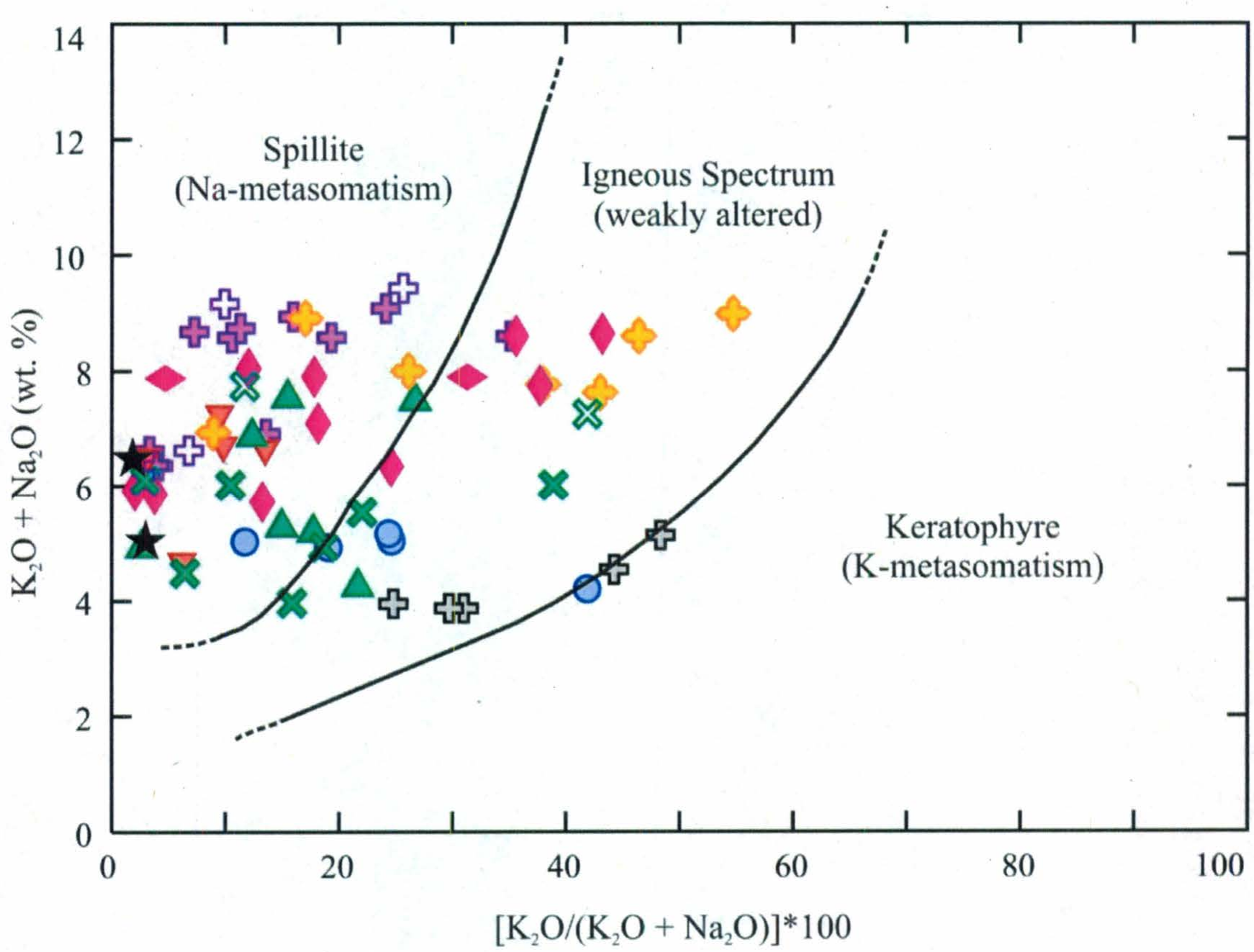

Figure 4.2: Diagram of alkali parameters, after Hughes (1973). Symbols are as in Figure 4.1.

of the samples and how they compare to other rock units. Because all samples have undergone alteration, normative mineralogy is not representative of original mineralogy, and is not used to classify or characterize the rocks in this study. Instead, the Jensen (1976) cation plot is used to classify the mafic-to-intermediate rocks.

In granitoid rocks, many trace elements are not incompatible and cannot be relied upon for classification because they occur in accessory mineral phases, such as zircon and monazite (Bea, 1996; Frost *et al.*, 2001). Alternative classification schemes have been developed, such as the scheme of Frost *et al.* (2001), which relies on Fe number, the modified alkali-lime index and the alumina saturation index. However, this scheme cannot be applied to the rocks at Bauline because they have experienced Na_2O-enrichment, and alteration has probably also modified K_2O and CaO contents. As well, the feldspar porphyritic nature of rhyolite and feldspar porphyry may have resulted in variations in Na_2O, K_2O and CaO between samples. Therefore, the felsic rocks in this study are classified using the plots of Winchester and Floyd (1977) and Pearce (1996), together with mineral assemblages observed in thin section.

4.3.2. Major element geochemistry

The major element composition of each rock unit is shown on Harker-type variation plots. On plots that show felsic rock data, the major elements are plotted against SiO_2, whereas major element data for mafic-to-intermediate rocks are plotted against Mg# (= MgO/(MgO + FeO*)X100) as a differentiation index.

4.3.3. Trace element geochemistry

Incompatible-immobile trace elements, including Zr, La, Y, Yb, Nb and Th and the REE, are used to characterize and compare each rock unit and identify trends in the data. Trace element data are shown on variation plots against Zr for felsic rocks and Mg# for mafic-to-intermediate rocks. For the mafic-to-intermediate rocks, the concentrations of V, Sc, Ni and Cr are also discussed, since they tend to be compatible-immobile in calc-alkaline rocks, and Sc and V are generally incompatible-immobile in tholeiitic basalts. The felsic rocks in the dataset are plotted on the tectonic discrimination diagram of Pearce *et al.* (1984), which is based on the trace elements Nb and Y. This diagram is not used to conclusively demonstrate the tectonic setting of the granitoid rocks in the study area, but rather to explore correlations between rock units in the dataset and rocks from known tectonic environments.

REE and HFSE data are shown on multi-element diagrams that are normalized to the primitive mantle values of Sun and McDonough (1989). The REE patterns are compared in REE ratio plots, in which La/Yb is a measure of the overall slope of the REE pattern, La/Sm is a measure of LREE-enrichment and Gd/Yb is a measure of HREE-enrichment. The REE ratios are plotted against Nb/Th because several mafic-to-intermediate samples exhibit negative Nb anomalies. Because negative Nb anomalies are associated with magmatism formed by partial melts of subduction-contaminated mantle wedges or with crustal contamination (e.g. Jenner *et al.,* 1991; Swinden *et al.,* 1997), the distribution of data along the Nb/Th axis provides insight into the tectonic setting or crustal contamination of the rocks in the study area. Nb/Th is used to define three compositional fields, following the criteria of Jenner *et al.* (1991) and Swinden *et al.*

(1997). Rocks that have high Nb/Th ratios and do not exhibit negative Nb anomalies plot in the "non-arc" field, and rocks that have low Nb/Th ratios and display well-developed negative Nb anomalies plot in the "arc" field. Rocks that exhibit weakly developed negative Nb anomalies that are within analytical uncertainty plot within the "transitional arc" field. This field also includes rocks in which the lack of a negative Nb anomaly is within analytical uncertainty. The boundaries of these fields, represented by the field of analytical uncertainty surrounding Nb/Th, were determined using the method described in Appendix E.

The data are also plotted on a diagram of Nb/Th vs. Mg#, which highlights occurrences of negative Nb anomalies along with relative degrees of fractionation. Since Th/Ta is another measure of the negative Nb-Ta anomaly, Condie (1997) plotted Th/Ta against La/Yb to determine mafic dyke sources. The data from mafic-to-intermediate rocks are also plotted on a diagram of La/Yb against Th/Ta to allow comparison with compositional fields defined by Condie (1997).

4.4. Whole rock geochemistry of the ca. 625 Ma granodiorite

The geochemical samples from granodiorite include #107, 118, 128, 148 and 171 from Map 1, #68, 70 and 80 from Map 2 and #200 and 202 from Map 3. Sample #118 was collected from the same granodiorite body and less than 1 m away from sample #211, which yielded the U/Pb age of 625 ± 1.4 Ma.

4.4.1. Classification

On the classification diagram of Pearce (1996) (Figure 4.3a), the granodiorite data plot in the andesite/basalt field. On the classification diagram of Winchester and Floyd (1977) (Figure 4.3b), the granodiorite samples form a cluster in the rhyolite field that overlaps slightly with the rhyodacite/dacite field. Based on the classification scheme of LeMaitre (1989) and the proportions of plagioclase, quartz and alkali feldspar observed in thin section, this unit is classified as granodiorite.

4.4.2. Major element geochemistry

The major element compositions of granodiorite are plotted on Harker-type major element variation diagrams (Figure 4.4). Granodiorite exhibits a wide range of CaO, Na_2O and K_2O compositions, and there appears to be a random spread in data on each of these plots. Overall, SiO_2-poor samples that are enriched in MgO, FeO*, TiO_2, Al_2O_3, P_2O_5 and MnO (#200, 202, 80, 118, 68, 70) form a linear trend with SiO_2-enriched samples that are comparatively depleted in MgO, FeO*, TiO_2, Al_2O_3, P_2O_5 and MnO (#148, 128, 107, 171).

4.4.3. Trace element geochemistry

Granodiorite displays a wide compositional range in immobile elements that are typically incompatible, including Zr, Y, Nb, Th, Hf and the REE. When many of these elements are plotted against Zr, the granodiorite data exhibit a linear trend with samples #118 and 128 at low values, #68, 80, 107 and 171 at middle values, and #70, 148, 200 and 202 at high values (Figure 4.5). When plotted on the tectonic discrimination diagram of

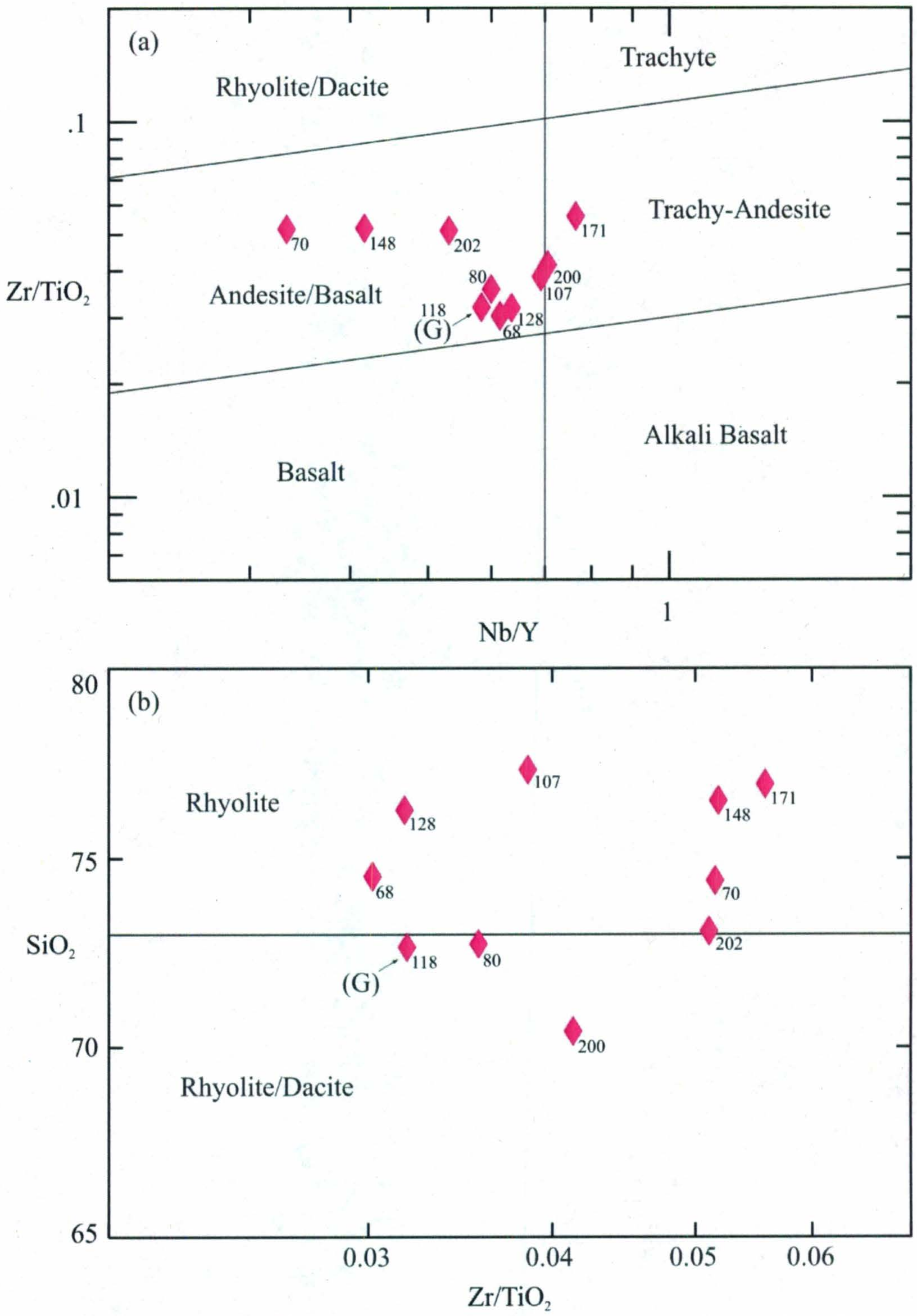

Figure 4.3: Granodiorite data plotted on the classification diagrams of (a) Pearce (1996) and (b) Winchester and Floyd (1977). (G)=U/Pb zircon geochronology sample.

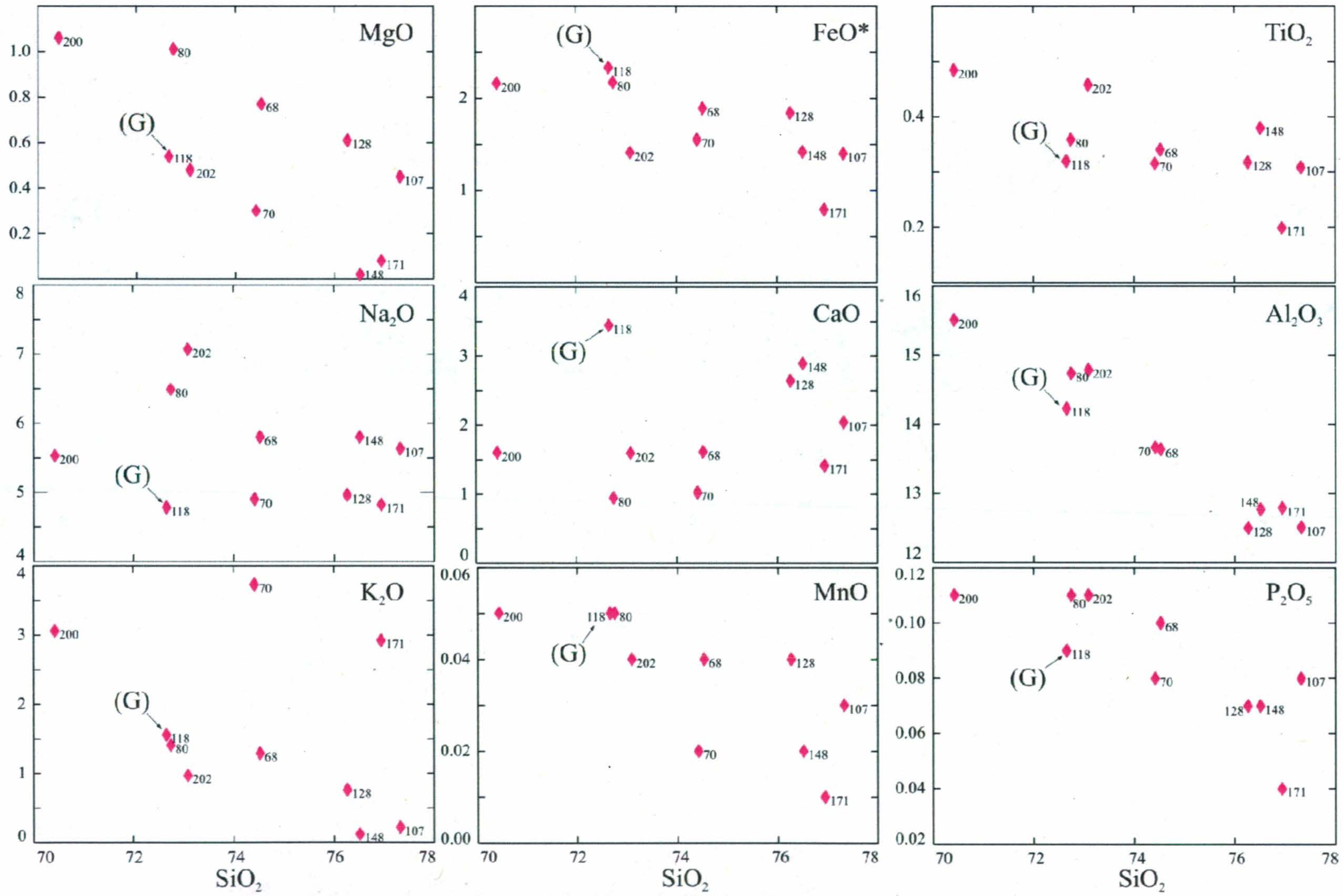

Figure 4.4: Major element data (wt. %) for granodiorite. (G)=U/Pb zircon geochronology sample.

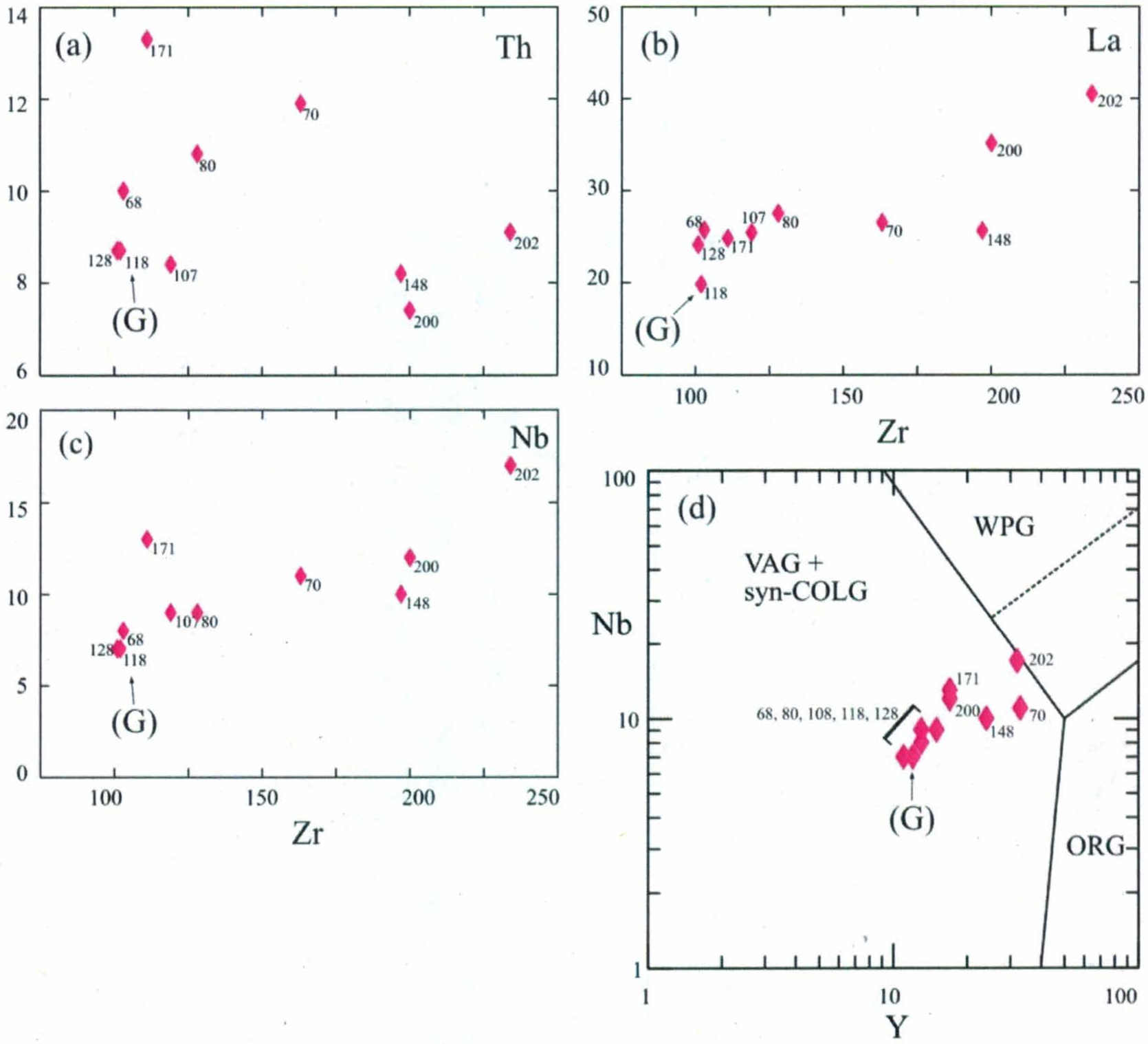

Figure 4.5: Trace element geochemistry of granodiorite. (a) to (c) XY plots of selected trace element data (ppm) against SiO_2 (wt. %) or Zr (ppm). (d) Tectonic discrimination diagram of Pearce *et al.* (1984). WPG=within-plate granite, ORG=ocean-ridge granite, VAG + syn-COLG=volcanic arc and syn-collisional granite. The dotted line is the boundary for the field of ORG from anomalous ridges. (G)=U/Pb zircon geochronology sample.

Pearce *et al.* (1984; Figure 4.5d), the granodiorite data plot in the field of volcanic arc granites.

On extended primitive mantle-normalized REE diagrams (Figure 4.6), the granodiorite samples have steeply sloping REE patterns, indicating enrichment of the LREE relative to the HREE. In addition, all samples have strong negative Nb and Ti anomalies. Relative to the overlapping REE patterns of most samples (#68, 80, 107, 118, 128, 171), samples #70, 148 and 202 are HREE-enriched and sample #200 is LREE-enriched.

4.4.4. Interpretation

Granodiorite appears to represent subduction zone-related magmatism because it exhibits several geochemical characteristics that are typical of volcanic arc granitoid rocks, including enrichment in the LREE relative to the HREE and negative Nb and Ti anomalies. In addition, the granodiorite samples plot in the field of volcanic arc granites on the tectonic discrimination diagram of Pearce *et al.* (1984).

While most of the granodiorite data form a cluster on trace element plots, four samples (#70, 148, 200, 202) typically plot at higher values. This range in incompatible-immobile element data among the granodiorite samples suggests that certain elements (e.g. Zr, La) are behaving compatibly due to the fractionation of trace minerals, such as zircon or monazite. The variability and random distribution of CaO, Na_2O and K_2O contents is attributed to the mobility of these elements during alteration. The linear trends on certain major and trace element plots (Figures 4.4 and 4.5) may represent igneous fractionation, reflecting primary compositional heterogeneity in the granodiorite intrusion

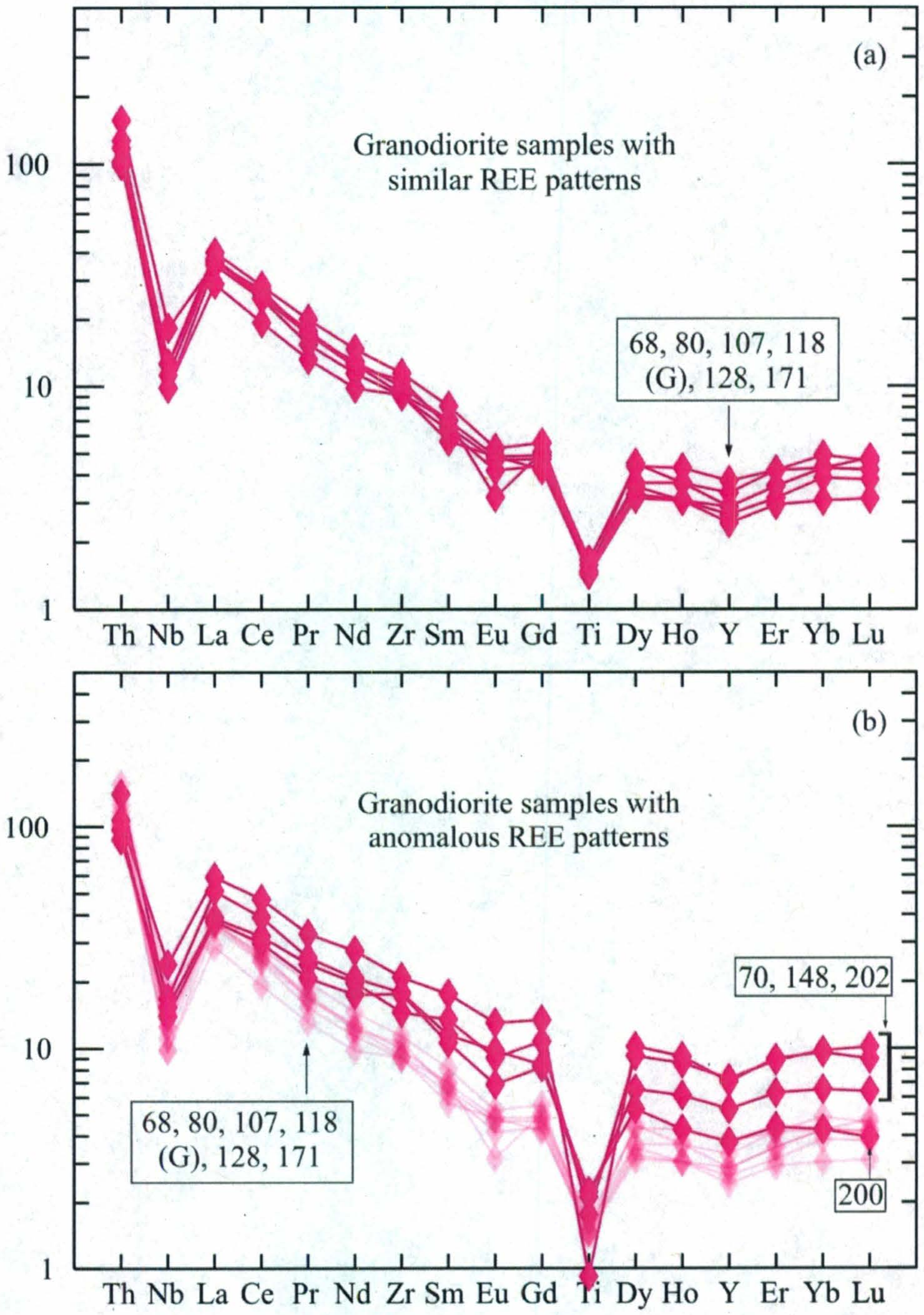

Figure 4.6: Extended REE diagrams for granodiorite, normalized to the primitive mantle values of Sun and McDonough (1989). (a) Samples with overlapping, nearly parallel REE patterns, including U/Pb zircon geochronology sample #118. (b) Samples with HREE-enriched or LREE-enriched REE patterns relative to the samples in (a), which are shown in the background. (G)=U/Pb geochronology sample.

and the sampling of blocks from different parts of the intrusion by magmatic or tectonic processes. Notably, as mentioned in the petrographic descriptions in Chapter 2, samples #148 and 202 are almost fully recrystallized, and although they are interpreted as recrystallized granodiorites, the nature of their protoliths is uncertain and they may represent different felsic rocks that have been strongly deformed.

4.5. Whole rock geochemistry of ca. 580 Ma felsic rocks in the Horse Cove Complex

4.5.1. Feldspar porphyry

The geochemical samples collected from this unit include #112, 117, 139, 177, 182, 193 and 198, all from petrographically indistinguishable feldspar porphyry bodies in Map 1. These samples are petrographically indistinguishable from the dated feldspar porphyry (sample #213), which has a U/Pb age of 580.6 ± 2.0 Ma.

4.5.1.1. Classification

On the classification diagram of Pearce (1996; Figure 4.7a), most of the feldspar porphyry data form a tight cluster in the rhyolite/dacite field. However, two samples (#117, 198) plot in the andesite/basalt field, and one sample (#177) sits on the boundary between the andesite/basalt and basalt fields. On the Zr/TiO_2 vs. SiO_2 diagram (Winchester and Floyd 1977; Figure 4.7b), the feldspar porphyry data lie in the rhyolite field, except for sample #177, which plots in the rhyodacite/dacite field.

4.5.1.2. Major element geochemistry

Most of the feldspar porphyry data form a tight cluster on Harker-type major element variation plots (Figure 4.8), overlapping only with the most SiO_2-rich samples from granodiorite. Sample #117 has slightly lower SiO_2 than the clustered feldspar

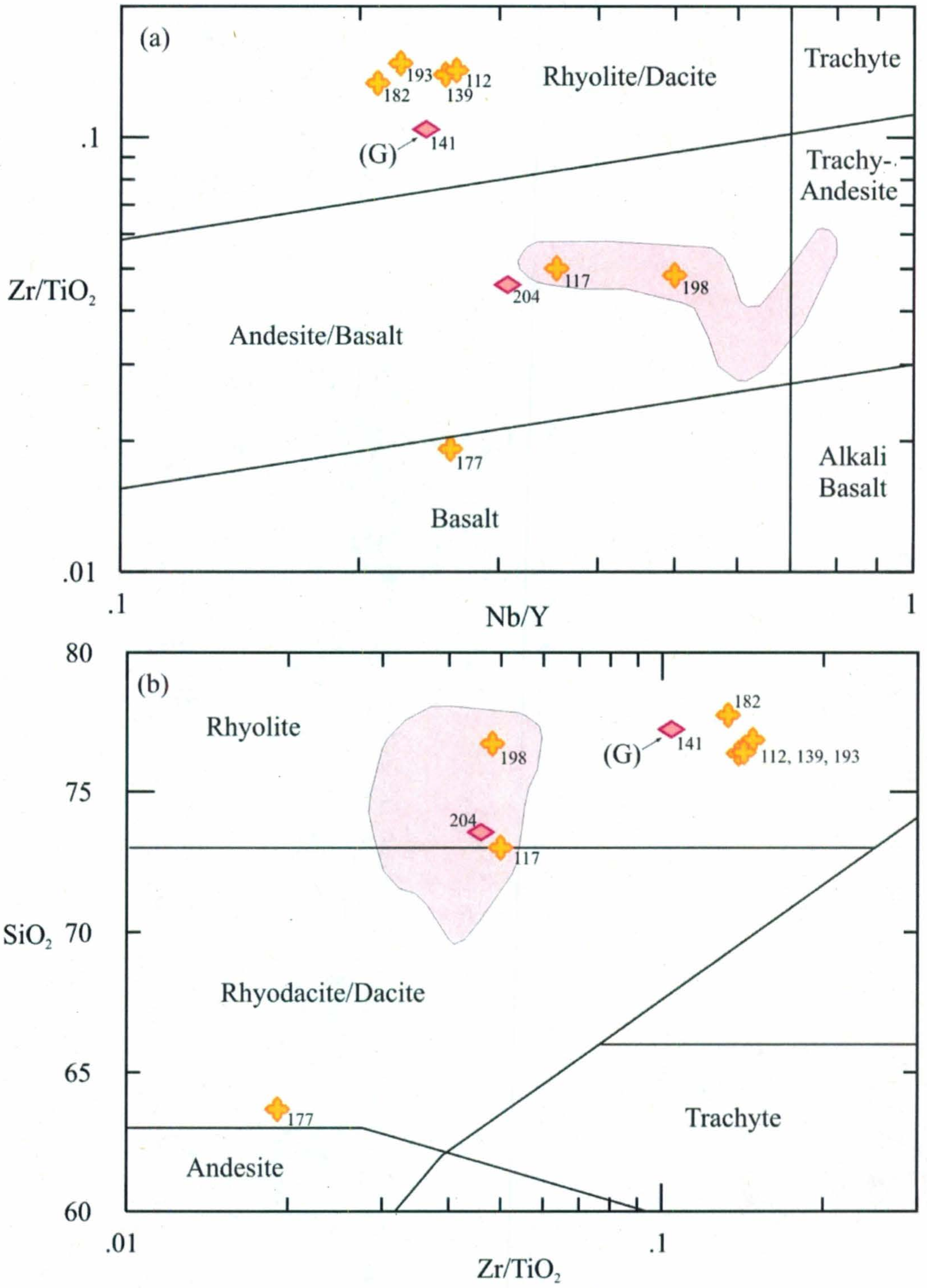

Figure 4.7: Feldspar porphyry and rhyolitic dyke samples plotted on the classification diagrams of (a) Pearce (1996) and (b) Winchester and Floyd (1977). (G)=U/Pb geochronology sample. Symbols are as in Figure 4.1. Pink shading indicates the compositional field of granodiorite.

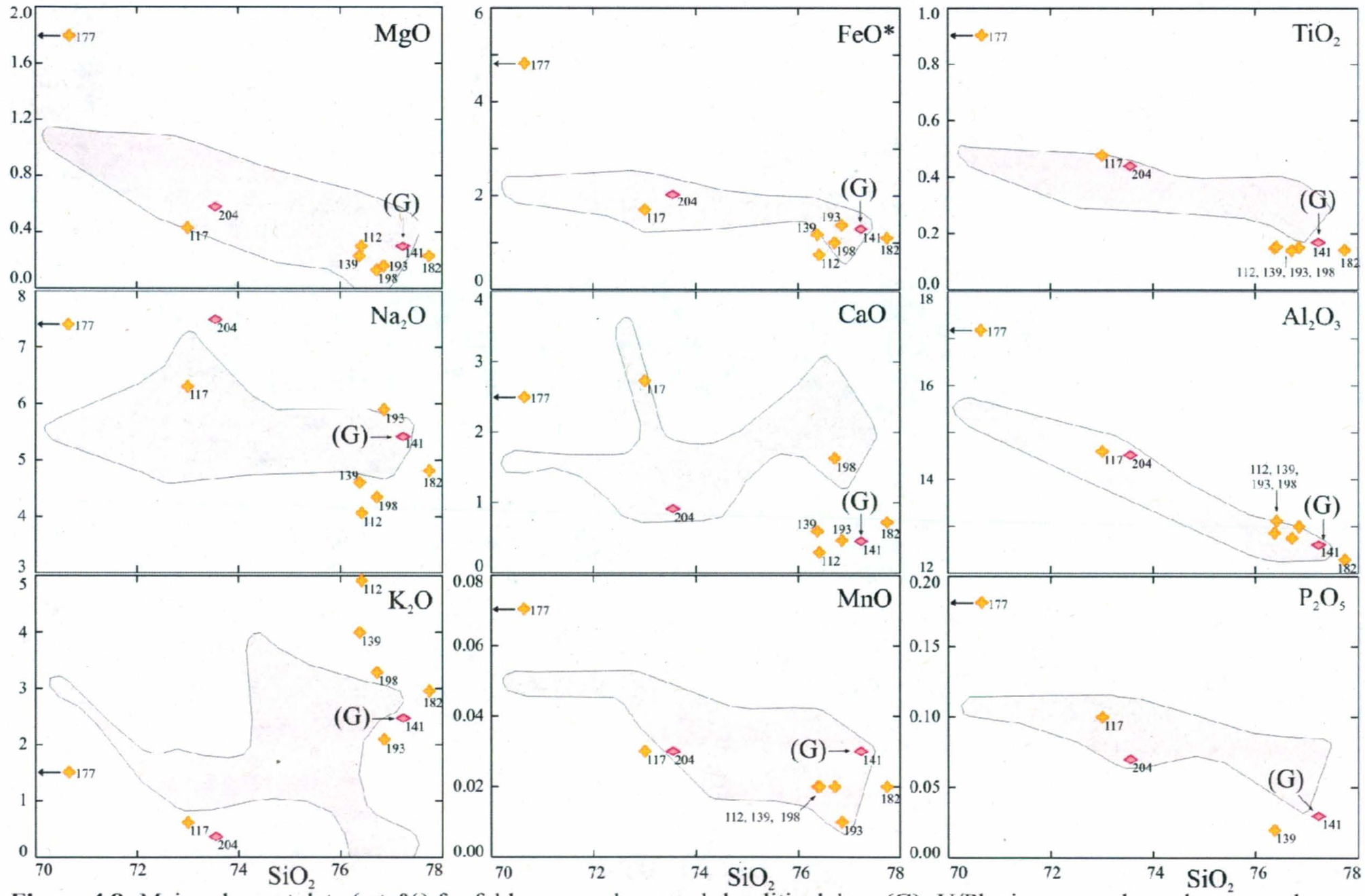

Figure 4.8: Major element data (wt. %) for feldspar porphyry and rhyolitic dykes. (G)=U/Pb zircon geochronology sample. Symbols are as in Figure 4.1. Pink shading indicates the compositional field of granodiorite.

porphyry samples, but plots within the granodiorite compositional field. With only 63.66 wt. % SiO_2, sample #177 is the most SiO_2-poor sample collected from the felsic rocks in the study area, and is more appropriately described as intermediate in composition. The clustered feldspar porphyry samples have lower TiO_2 than the granodiorite samples, and are also depleted in MgO, Na_2O, CaO, Al_2O_3 and MnO compared to most of the granodiorite samples.

4.5.1.3. Trace element geochemistry

On incompatible-immobile element variation diagrams (Figure 4.9), most of the feldspar porphyry samples display low Nb and Th values and high Zr, Y, La and Yb values, rarely overlapping with the granodiorite data. Samples #177 and 198 plot at much lower values than the other feldspar porphyry data, typically in the compositional field defined by the granodiorite samples. The tectonic discrimination diagram of Pearce *et al.* (1984; Figure 4.9d) shows that the Y and Nb compositions of feldspar porphyry overlaps with those of volcanic arc granites.

Feldspar porphyry is LREE-enriched and displays strong negative Nb and Ti anomalies on extended primitive mantle normalized REE plots (Figure 4.10). Most samples (#112, 117, 139, 182, 193) have tightly overlapping REE patterns with negative Eu anomalies. The REE patterns of these samples have shallower slopes than the overlapping, comparatively HREE-depleted REE patterns of the majority of granodiorite samples (#68, 80, 107, 118, 128, 171). One sample (#198) plots below the overlapping REE patterns of other feldspar porphyry samples and is relatively HREE-depleted. The

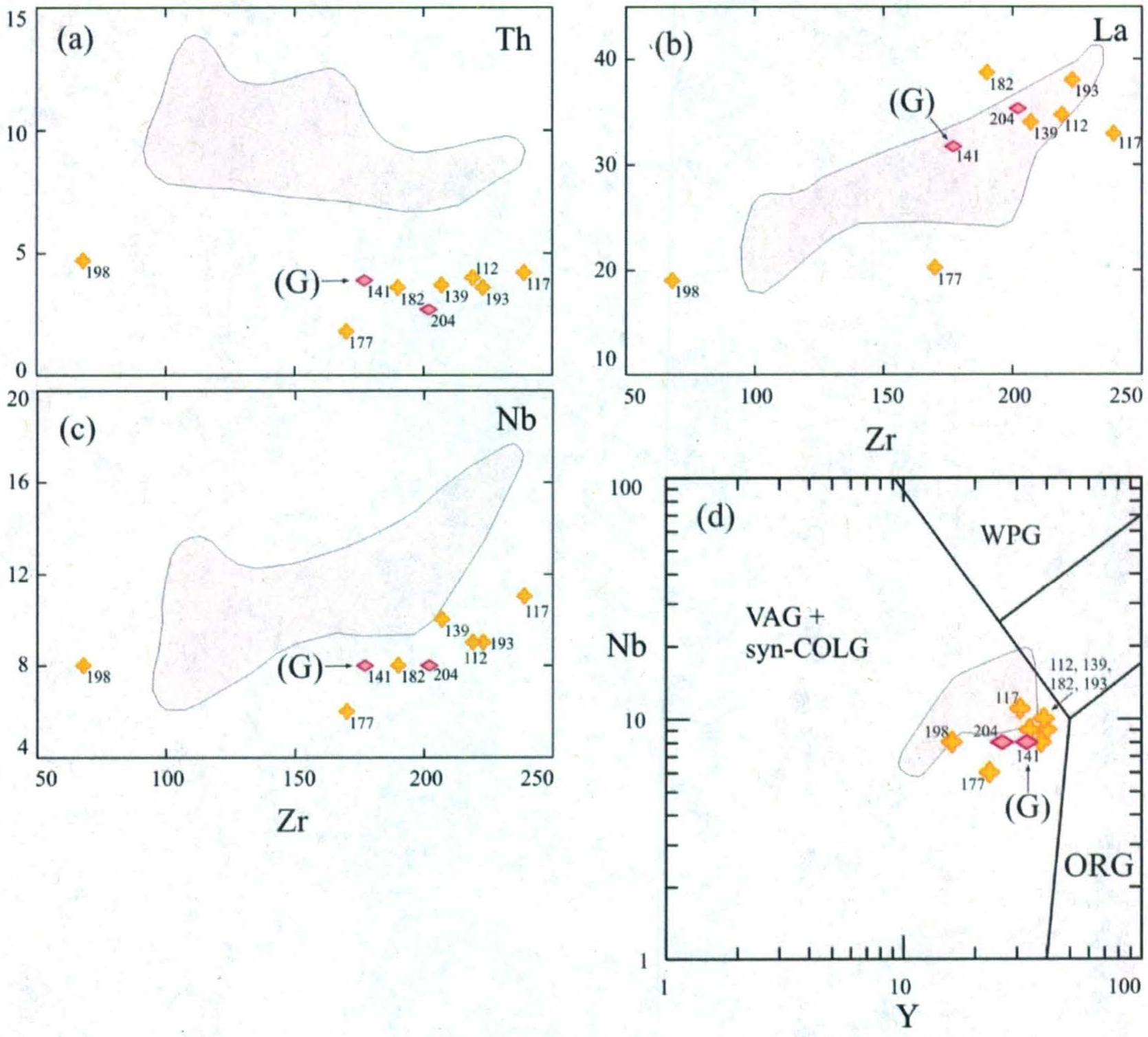

Figure 4.9: Trace element geochemistry of feldspar porphyry and rhyolitic dykes. (a) to (c) XY plots of selected trace element data (ppm) against Zr (ppm). (d) Tectonic discrimination diagram of Pearce *et al.* (1984), with compositional fields as in Figure 4.6. (G)=U/Pb zircon geochronology sample. Pink shading indicates the compositional field of granodiorite.

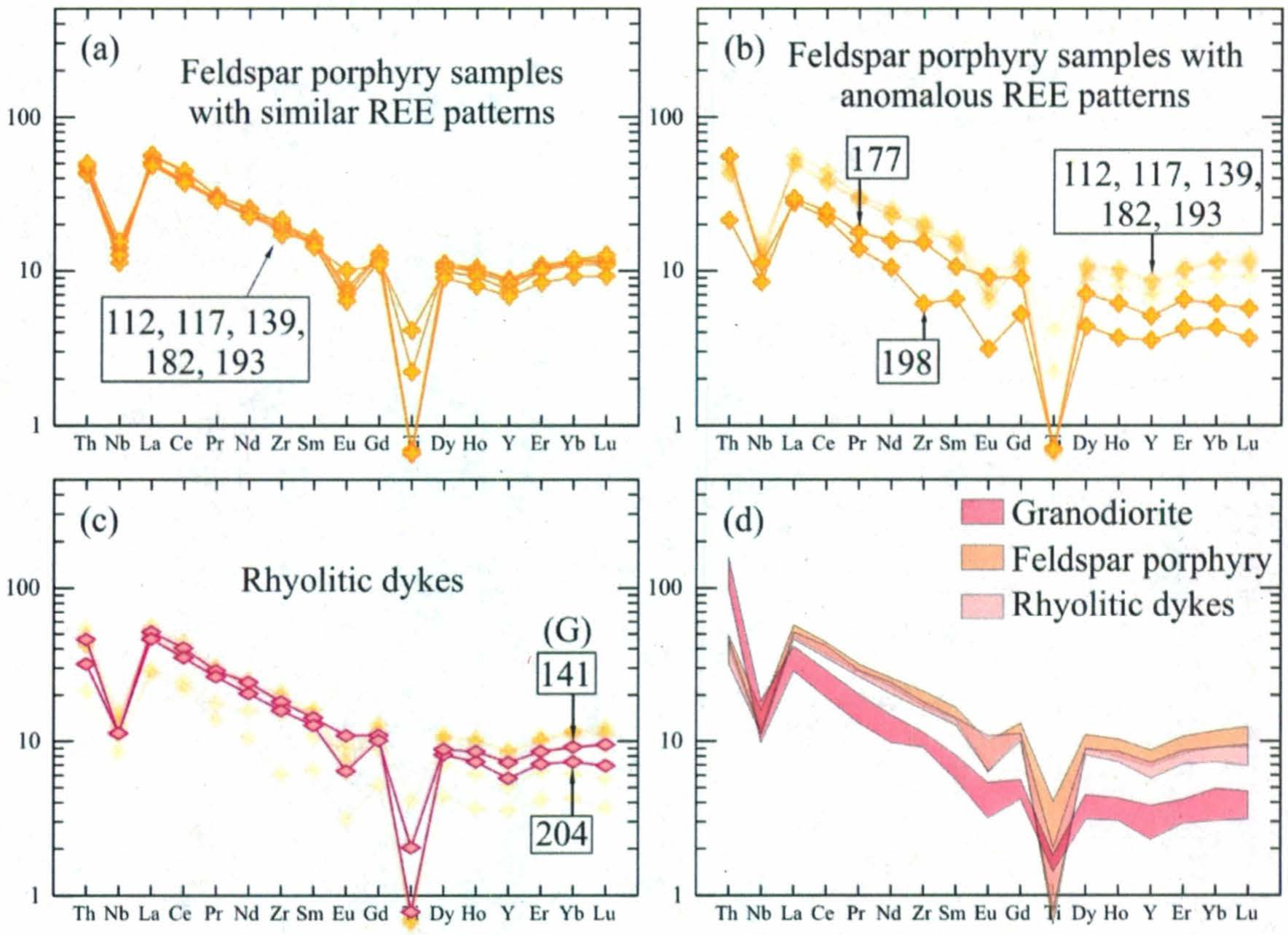

Figure 4.10: Extended REE patterns for feldspar porphyry and rhyolitic dykes, normalized to the primitive mantle values of Sun and McDonough (1989). (a) Feldspar porphyry samples with overlapping, nearly parallel REE patterns. (b) Feldspar porphyry samples with REE patterns that are different from those in (a), which are shown in the background. (c) Extended REE patterns of rhyolitic dykes, with feldspar porphyry REE patterns shown in the background. (G)=U/Pb zircon geochronology sample. (d) A comparison of the extended REE patterns of granodiorite, feldspar porphyry and rhyolitic dykes. For granodiorite and feldspar porphyry, the REE fields do not include samples with anomalous REE patterns.

REE pattern for sample #177 also plots below the overlapping feldspar porphyry REE patterns, displays MREE-enrichment and lacks a Eu anomaly.

4.5.1.4. Interpretation

Because feldspar porphyry plots in the volcanic arc granite field on the diagram of Pearce *et al.* (1984), and is LREE-enriched with negative Nb and Ti anomalies, it appears to represent volcanic arc-related magmatism. The similarities in major and trace element geochemistry of most feldspar porphyry samples (#112, 117, 139, 182, 193) suggest that they are from the same melt. This supports the interpretation, based on mapping and petrography, that the feldspar porphyry bodies in Map 1 are blocks from the same intrusion, separated by subsequent mafic-to-intermediate magmatism.

Variation in Na_2O and K_2O contents among feldspar porphyry samples is attributed to alteration, and may also be partly due to different proportions of feldspar phenocrysts. The relative HREE-depletion of sample #198 may be due to the fractionation of HREE-bearing accessory minerals. Sample #177, however, has significantly different major and trace element geochemistry than the other feldspar porphyry samples. In particular, the low SiO_2-content of sample #177 sets it apart from all the felsic rocks in the study area. In thin section, greenschist-facies metamorphic minerals are slightly more abundant in sample #177 than in other thin sections from feldspar porphyry, but they are otherwise petrographically indistinguishable. Thus, the cause of the anomalous geochemistry of sample #177 remains uncertain.

4.5.2. Rhyolitic dykes

Geochemical samples from rhyolitic dykes include #141 from Map 1 and #204 from the western end of Section B-B'. Sample #141 was collected about 1 m south of geochronology sample #212, and from the same rhyolitic dyke, which has a U/Pb age of 581.7 ± 1.9 Ma.

4.5.2.1. Classification

On the Pearce (1996) diagram (Figure 4.7a), one rhyolitic dyke (#141) plots in the rhyolite/dacite field, whereas the other dyke (#204) lies in the andesite/basalt field. Both dykes plot in the rhyolite field on the SiO_2 vs. Zr/TiO_2 diagram of Winchester and Floyd (1977; Figure 4.7b).

4.5.2.2. Major element geochemistry

The compositional differences between the two rhyolitic dykes are also shown on major element variation diagrams (Figure 4.8), which demonstrate that sample #204 is less concentrated in SiO_2 and enriched in MgO, FeO*, CaO, Na_2O, TiO_2 and P_2O_5 compared to sample #141. The major element geochemistry data of sample #141 generally overlaps with the clustered feldspar porphyry data, whereas sample #204 lies in the broader field defined by the granodiorite samples.

4.5.2.3. Trace element geochemistry

The incompatible-immobile trace element plots in Figure 4.9 show that the rhyolitic dykes have the same Nb content, but sample #141 is enriched in Th and Y and depleted in La and Zr compared to sample #204. Both rhyolitic dyke samples plot close to the trace element compositional field defined by the feldspar porphyry data. On the

tectonic discrimination diagram of Pearce *et al.* (1984; Figure 4.9d), the rhyolitic dykes plot in the volcanic arc granite field, along with feldspar porphyry and granodiorite.

On primitive mantle normalized extended REE plots (Figure 4.10), the REE patterns of the rhyolitic dykes are nearly parallel and overlapping, and well-developed negative Nb and Ti anomalies are exhibited by both dykes. Sample #141 also exhibits a negative Eu anomaly and is slightly HREE-enriched compared to sample #204. The REE patterns of the rhyolitic dykes overlap with the REE patterns of the clustered feldspar porphyry samples except they are slightly HREE-depleted in comparison.

4.5.2.4. Interpretation

The similar trace element geochemistry of the rhyolitic dykes, emphasized by their overlapping REE patterns, suggests that they are petrogenetically related. The enrichment of certain major elements, including FeO* and MgO, in sample #204 relative to sample #141 may be explained by more intense chlorite alteration or by igneous fractionation, as indicated by the slightly higher Mg# of sample #204. Alternatively, sample #204 may have experienced mixing with a mafic melt. This hypothesis is supported by the presence of a mafic component within the rhyolitic dyke from which sample #204 was collected (Plate 2.29e).

4.6. Whole rock geochemistry of ca. 580 Ma mafic-to-intermediate rocks in the Horse Cove Complex

4.6.1. Gabbro

The geochemical samples collected from this unit include #72, 73, 76, 82 and 87 from Map 2.

4.6.1.1. Classification

The gabbro data plot in the basalt field on the classification diagram of Pearce (1996; Figure 4.11a) and in the sub-alkali basalt field on the Zr/TiO_2 vs. SiO_2 diagram (Winchester and Floyd 1977; Figure 4.11b). On the Jensen cation plot (Jensen 1976; Figure 4.12), the gabbro data plot as a cluster in the high-Mg tholeiitic basalt field. The gabbro samples are the only rocks in the dataset that plot in the high-Mg tholeiitic basalt field, apart from two basaltic dykes (#71, 123).

4.6.1.2. Major element geochemistry

The gabbro samples share very similar major element compositions and consistently plot as a cluster on the major element variation plots in Figure 4.13. The gabbro samples have some of the highest Mg#s in the study area, ranging from 43 to 46, and are enriched in MgO, FeO*, MnO and CaO, and depleted in SiO_2 and Na_2O relative to other mafic-to-intermediate rocks in the dataset.

4.6.1.3. Trace element geochemistry

The gabbro data form a tight cluster on incompatible-immobile trace element diagrams (Figure 4.14), except one sample (#73) has a higher Th content (0.6 ppm) compared to the other samples (0.3 ppm). Gabbro has lower Y and Yb contents than many of the mafic-to-intermediate rocks in the study area, and has significantly lower concentrations of Th, Nb, Zr and La. The compositional field defined by the incompatible-immobile trace element data of the gabbro samples coincides with data from only a few other rocks, including certain basaltic dykes (#71, 123), hornblende basaltic dykes (#75, 88) and a basaltic-andesitic dyke (#143). However, gabbro has lower Nb than all these rocks, except for one basaltic-andesitic dyke (#143). There is little

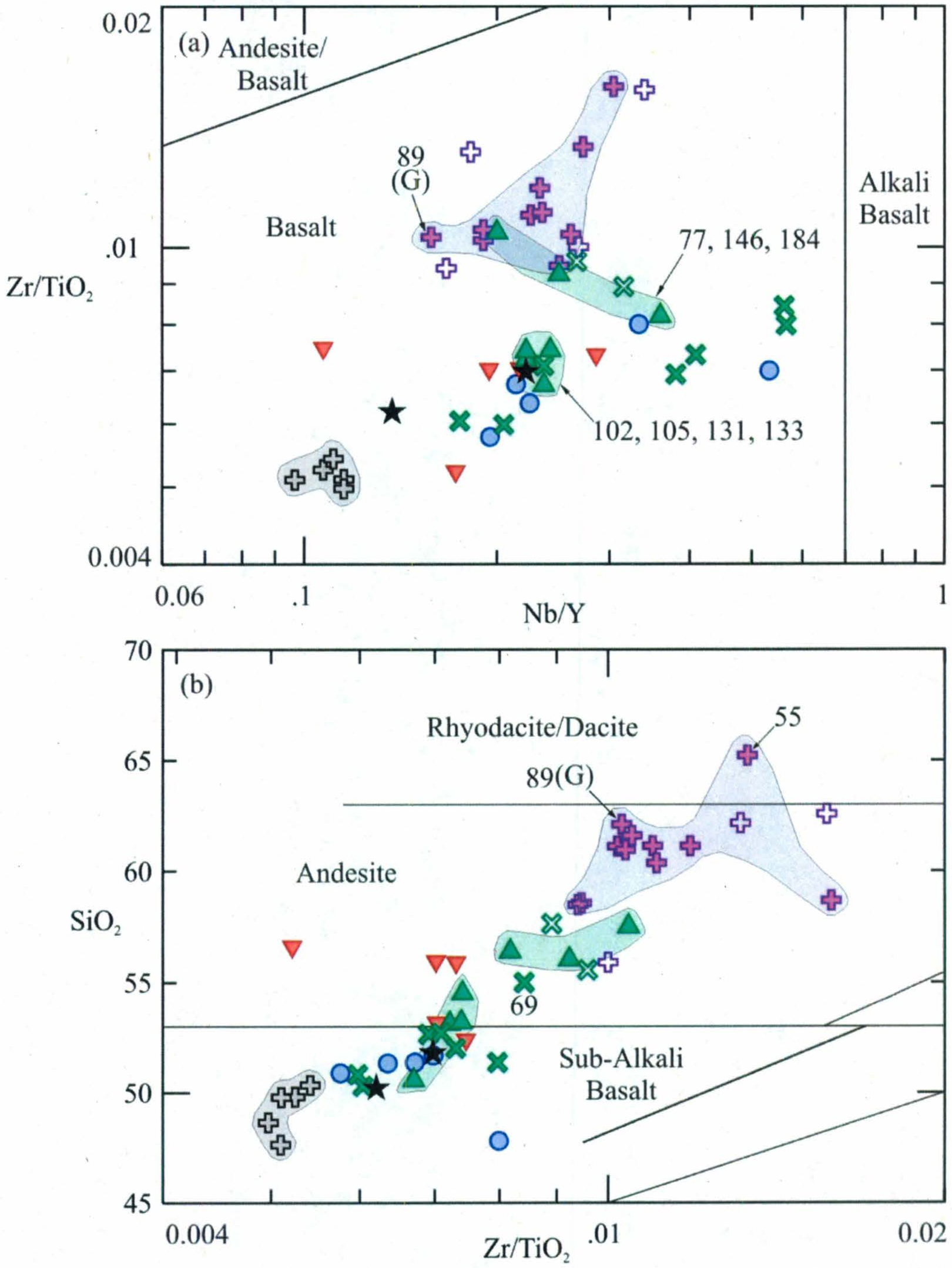

Figure 4.11: Data from mafic-to-intermediate rocks plotted on the classification diagrams of (a) Pearce (1996) and (b) Winchester and Floyd (1977). Symbols are as in Figure 4.1. (G)=U/Pb zircon geochronology sample. The outlined compositional fields of the andesitic dykes (purple) and gabbro (grey) include all data in each of those units, whereas the diorite data (green) form two subgroups, as described in text.

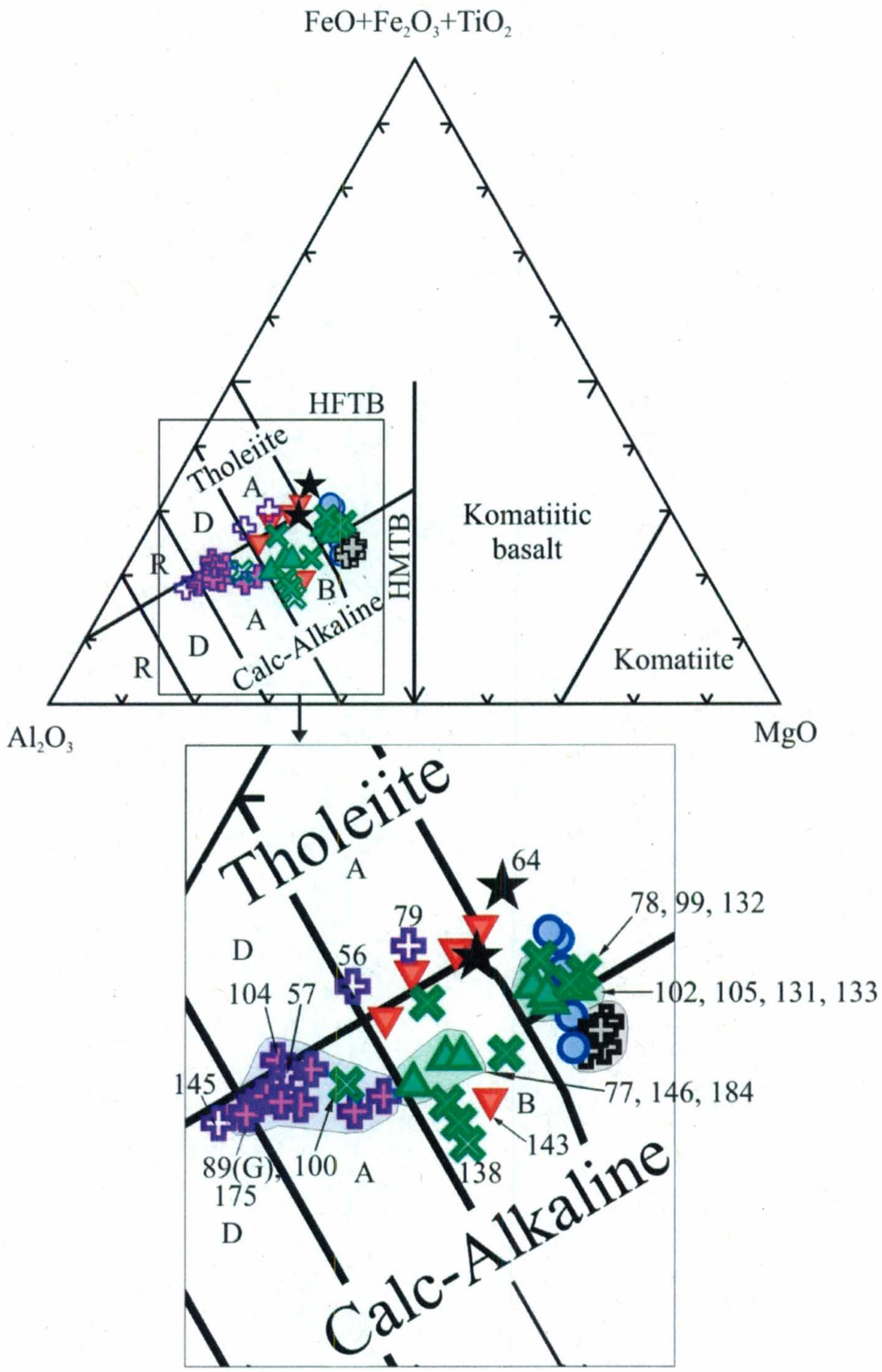

Figure 4.12: Mafic-to-intermediate rocks plotted on the classification diagram of Jensen (1976). HFTB=high-Fe tholeiite basalt; HMTB=high-Mg tholeiite basalt; A=andesite; B=basalt; D=dacite; R=rhyolite. Symbols are as in Figure 4.1.

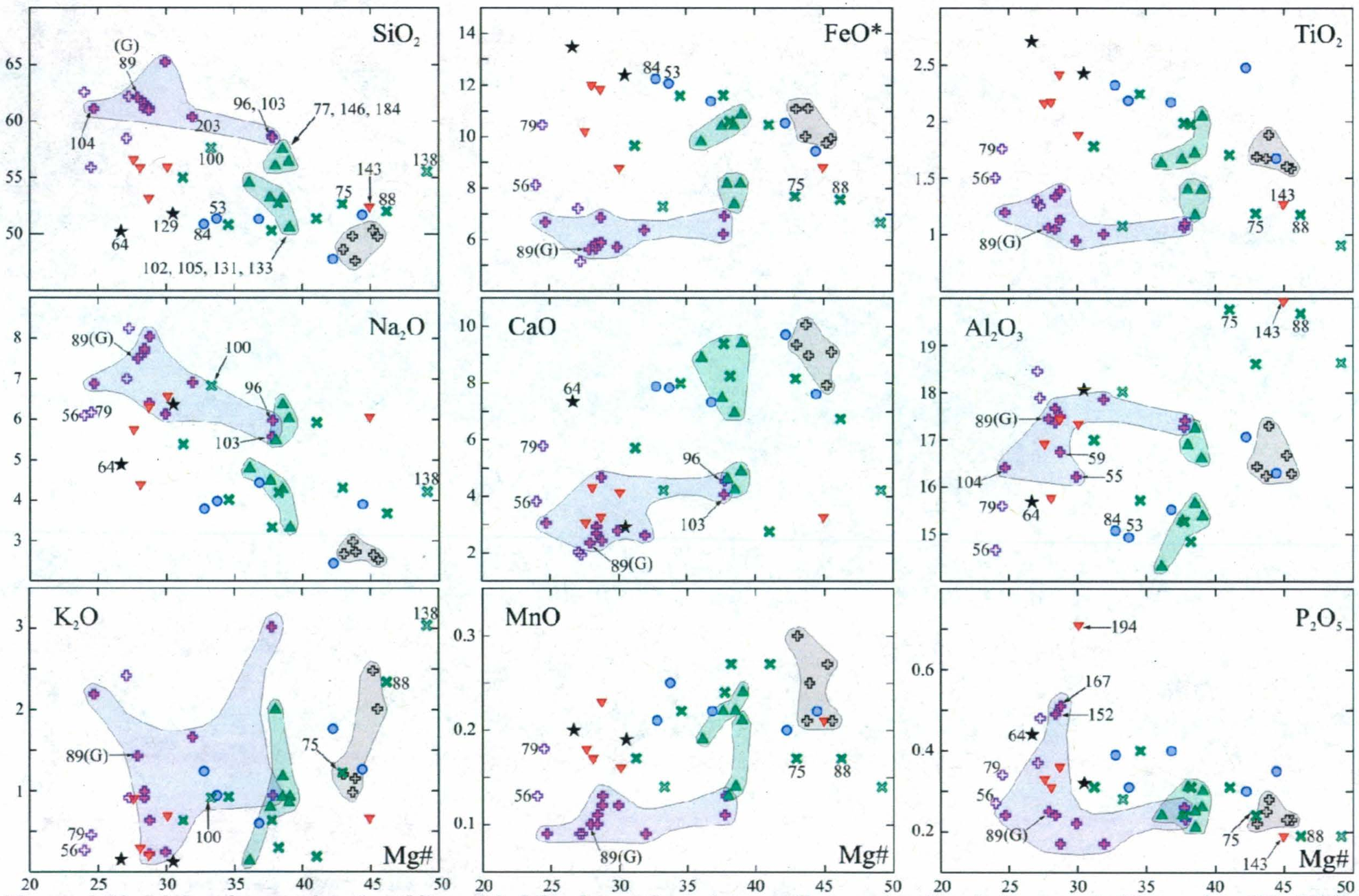

Figure 4.13: Major element data (wt. %) vs. Mg# for the mafic-to-intermediate rocks. Symbols are as in Figure 4.1. (G)=U/Pb geochronology sample.

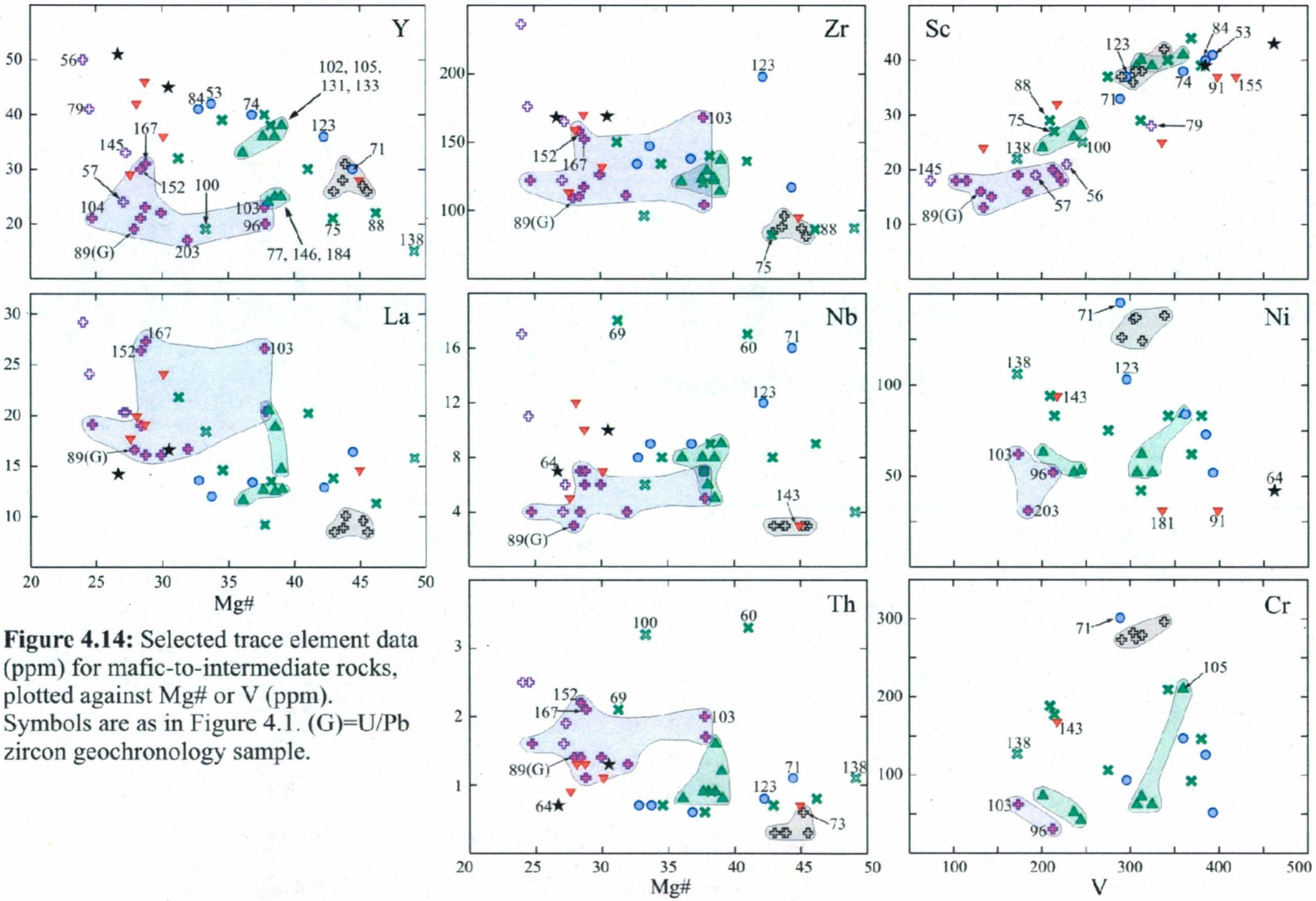

Figure 4.14: Selected trace element data (ppm) for mafic-to-intermediate rocks, plotted against Mg# or V (ppm). Symbols are as in Figure 4.1. (G)=U/Pb zircon geochronology sample.

variation in Sc, V, Ni and Cr among the gabbro data. Sc and V concentrations are higher in gabbro relative to the andesitic dykes, but they are similar to those of the basaltic dykes, some hornblende basaltic dykes (#60, 78, 99, 132) and certain diorite samples (#102, 105, 131, 133). Cr and Ni are more concentrated in gabbro than in all other rocks in the dataset, except for one basaltic dyke (#71).

On primitive mantle normalized multi-element diagrams (Figure 4.15), the gabbro samples have flat REE patterns that are tightly overlapping over all the elements on the diagram except Th. Four out of the five gabbro samples have equal Th contents and lack negative Nb anomalies, although the absence of Nb anomalies is within analytical uncertainty; the fifth sample (#73) displays a strong negative Nb anomaly as a function of its elevated Th content. All five gabbro samples exhibit weak negative Zr and Y anomalies, and all except for one sample (#76) display weak negative Ti anomalies. The flatness of the REE patterns displayed by the gabbro samples is highlighted by their low La/Yb and La/Sm values on the REE ratio diagrams in Figure 4.16. The gabbro data are not shown on the Th/Ta vs. La/Yb diagram in Figure 4.16e because Ta was less than 1.5-times the limit of detection and was removed from the dataset.

4.6.1.4. Interpretation

The tight clustering of gabbro data in the high-Mg tholeiitic basalt field on the Jensen (1976) cation plot indicates that the high Mg-content in gabbro is a signature of its igneous composition and is not due to chlorite alteration. Because gabbro is among the most FeO*-, MgO-, Cr- and Ni-rich rocks in the dataset and exhibits some of the flattest REE patterns, gabbro may be the most primitive rock unit in the study area. However, gabbro has lower Ni and Cr contents than primary magmas, in which Ni and Cr contents

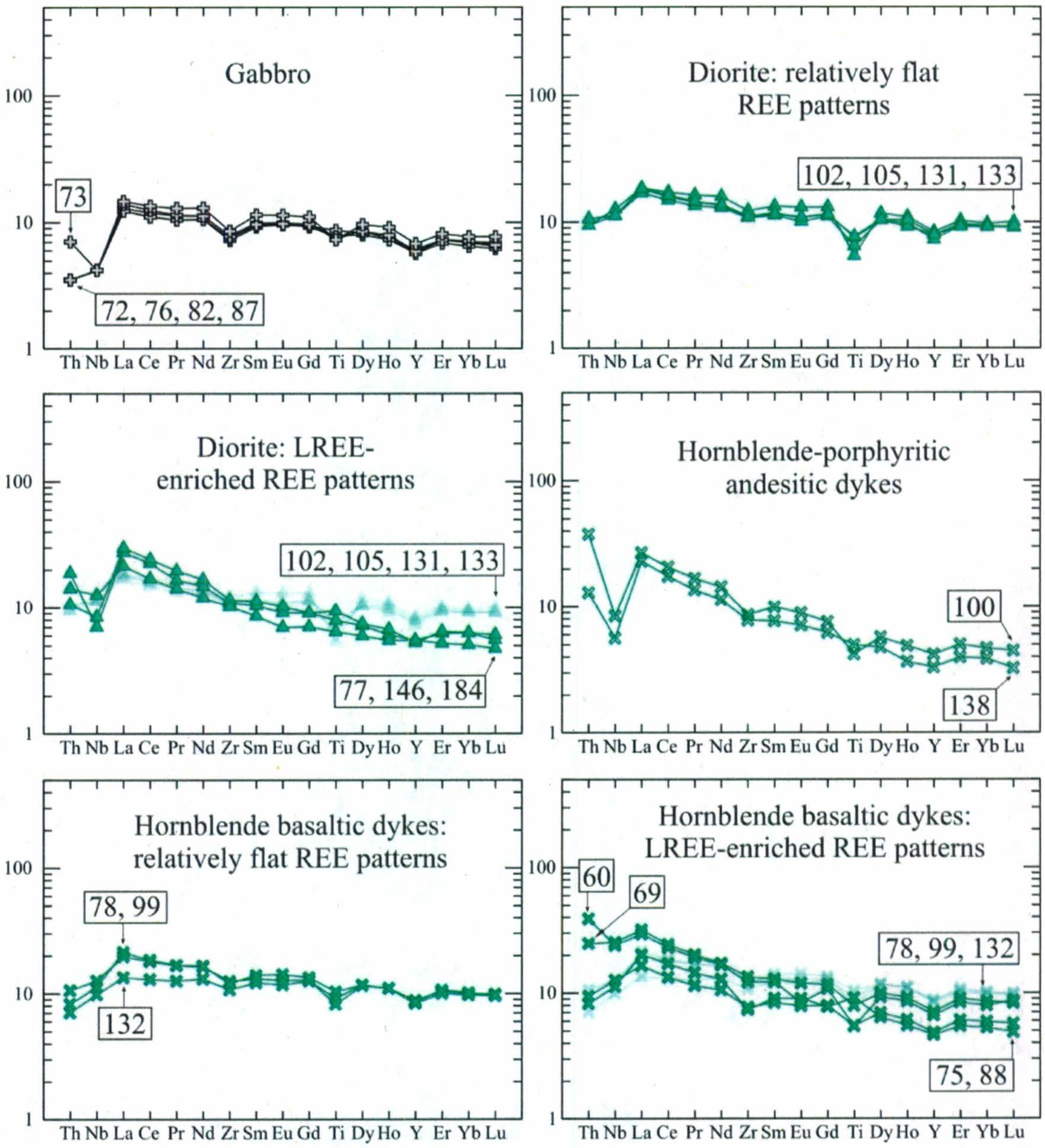

Figure 4.15: Extended REE diagrams for gabbro, diorite, hornblende-porphyritic andesitic dykes and hornblende basaltic dykes. Data are normalized to the primitive mantle values of Sun and McDonough (1989).

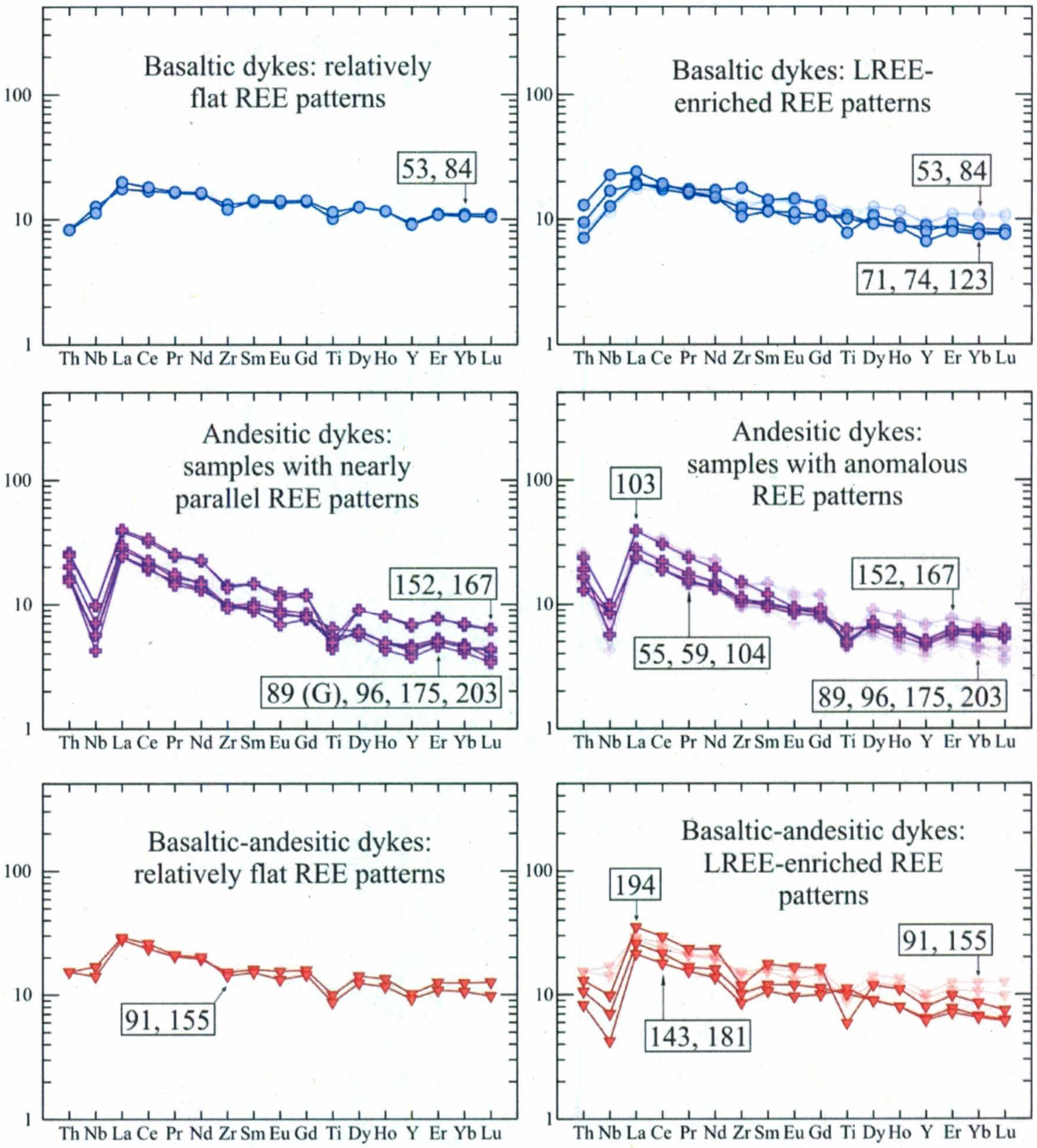

Figure 4.15 (continued): Extended REE patterns for basaltic dykes, andesitic dykes and basaltic-andesitic dykes. The data are normalized to the primitive mantle values of Sun and McDonough (1989). (G)=U/Pb zircon geochronology sample.

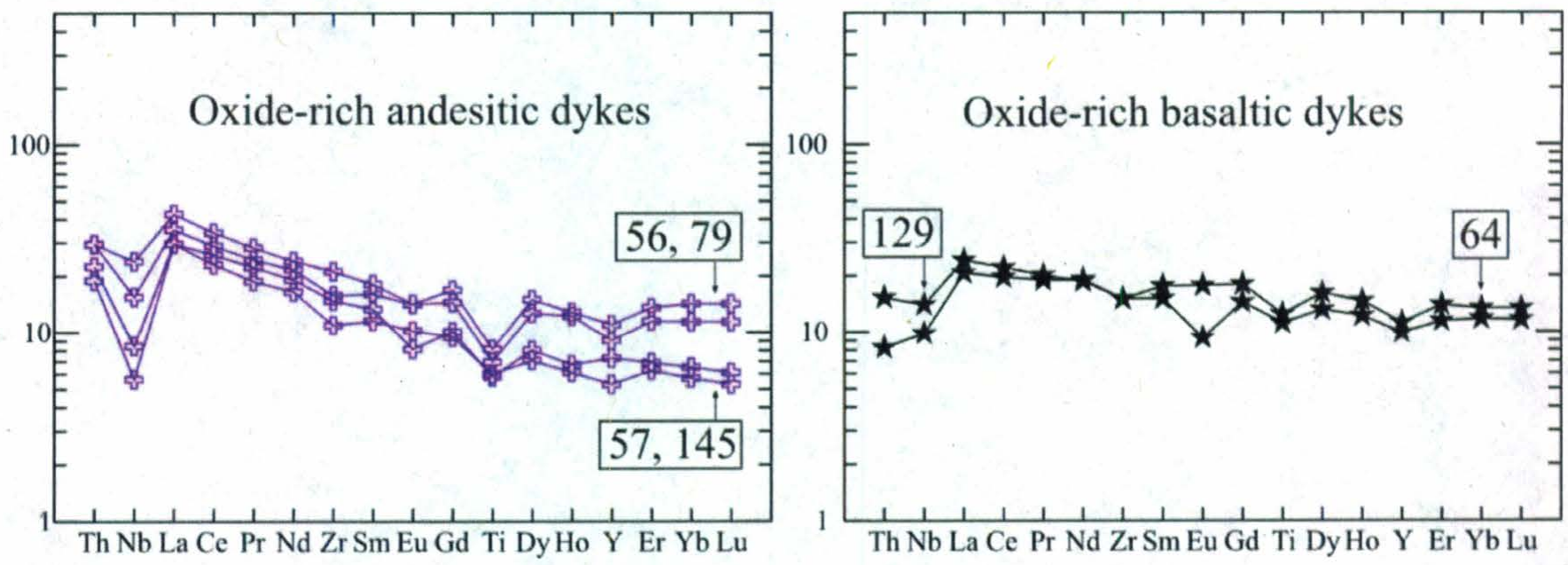

Figure 4.15 (continued): Extended REE diagrams for oxide-rich andesitic dykes and oxide-rich basaltic dykes. The data are normalized to the primitive mantle values of Sun and McDonough (1989).

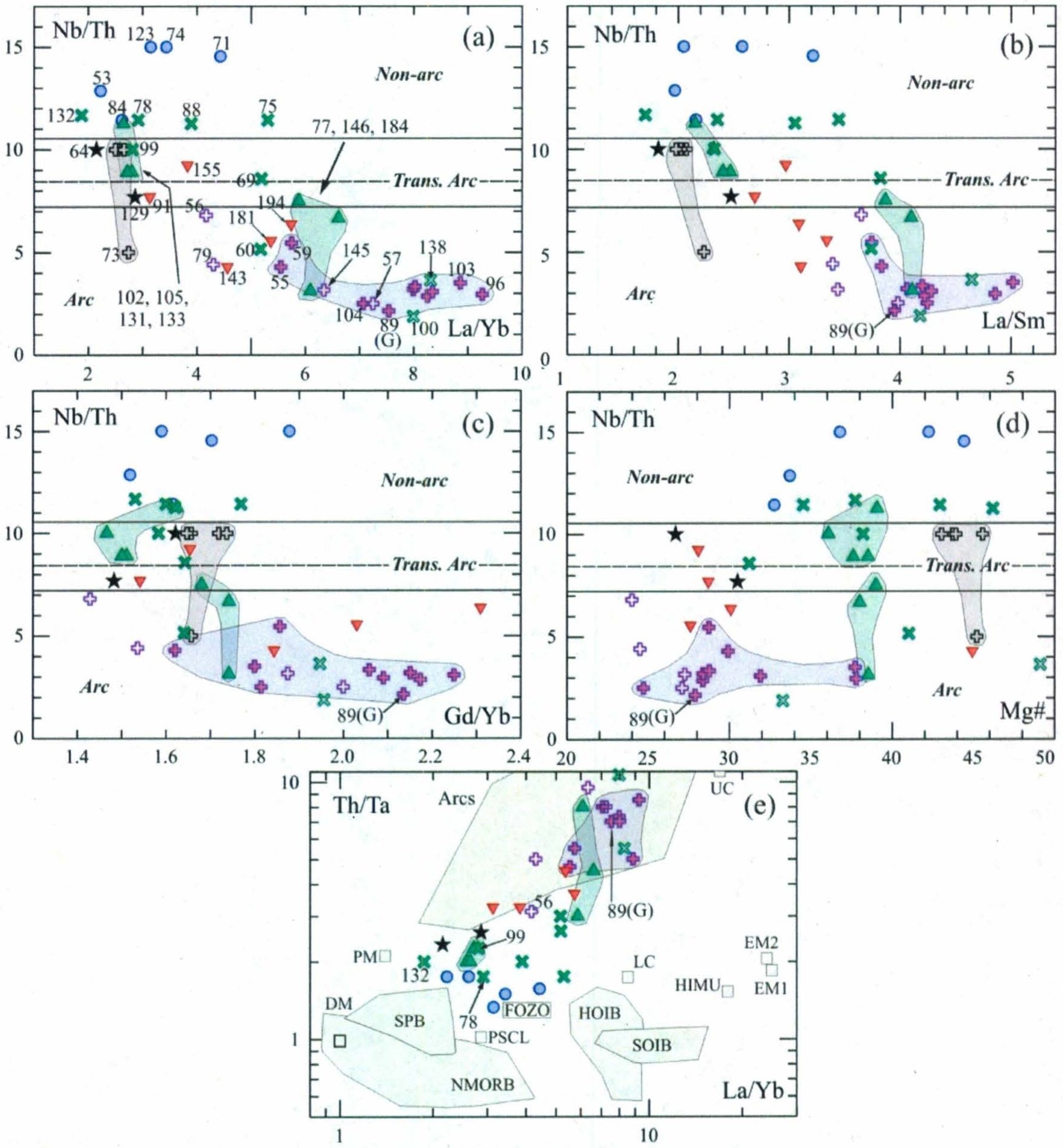

Figure 4.16: Plots of selected trace element ratios in mafic-to-intermediate rocks. Symbols are as in Figure 4.1. (G)=U/Pb zircon geochronology sample. Compositional fields in plots (a) to (d) follow the criteria of Jenner *et al.* (1991): Arc=well-developed negative Nb anomalies; Trans. Arc=weak negative Nb anomalies, within analytical uncertainty; Non-arc=no negative Nb anomalies. Dashed line is the primitive mantle reference line at Nb/Th=8.4 (Sun and McDonough 1989). Shaded areas in plot (e) are compositional fields from Condie (1997): DM=depleted mantle; PM=primitive mantle; PSCL=post-Archean subcontinental lithosphere; LC=lower continental crust; UC=upper continental crust; HIMU=high /Pb mantle source; EM1 & EM2=enriched mantle sources; FOZO=lower mantle plume component; SPB=Ontong-Java submarine plateau basalts; HOIB=Hawaiian oceanic island basalts; SOIB=South Atlantic oceanic island basalts.

are typically greater than 200 ppm and 400 ppm, respectively (Sato, 1977; Hart and Davis, 1978; Kinzler *et al.*, 1990). All the gabbro samples exhibit relatively flat REE patterns and, except for one sample (#73), they lack negative Nb anomalies. The relatively flat REE patterns are similar to those of E-MORBs, suggesting that gabbro was derived from a slightly LREE-enriched mantle source.

Because the major and trace element compositions of the five gabbro samples are otherwise very similar, it was suspected that the Th data for sample #73 was not reliable. However, a second blind analysis of sample #73 also yielded 0.6 ppm Th, and the cause of elevated Th in sample #73 remains unclear. A possible explanation is the presence of a Th-bearing accessory mineral, such as monazite or allanite.

4.6.2. Diorite

The geochemical samples collected from this unit include #102, 105, 131, 133, 146 and 184 from Map 1 and #77 from Map 2.

4.6.2.1. Classification

On the Pearce (1996) classification diagram (Figure 4.11a), diorite plots in the basalt field, whereas on the Zr/TiO_2 vs. SiO_2 diagram (Winchester and Floyd, 1977; Figure 4.11b), the diorite data span the sub-alkaline basalt and andesite fields. On the Jensen cation plot (Jensen, 1976; Figure 4.12), some diorite samples (#77, 146, 184) plot in the calc-alkaline basalt field, whereas others (#105, 102, 131, 133) plot in the high-Fe tholeiitic basalt field.

4.6.2.2. Major element geochemistry

The Mg#s of the diorite samples (36 to 39) are generally higher than those of the andesitic dykes but are lower than those of most mafic rock units in the study area (Figure 4.13). The diorite samples can be divided into two subsets based on major element geochemistry: SiO_2-, Al_2O_3- and Na_2O-rich rocks (#184, 146, 77), and FeO- , TiO_2-, MnO-, CaO- and MgO-rich rocks (#105, 131, 133, 102). These two subsets are indicated in Figure 4.16, except on plots where the diorite data do not plot in two distinct groups (P_2O_5, K_2O).

4.6.2.3. Trace element geochemistry

The diorite data form a broad cluster on incompatible-immobile element variation diagrams in Figure 4.14. However, three samples (#77, 146, 184) have lower Y, Yb, Sc and V contents and are enriched in La relative to the other diorite samples and tend to plot close to the andesitic dyke data. Conversely, the compositional field of the other diorite samples (#102, 105, 131, 133) generally overlaps with the data from mafic rock units. All diorite samples have about the same Ni and Cr contents, except for one sample (#105) that is elevated in Cr.

On primitive mantle-normalized extended REE plots (Figure 4.15), four diorite samples (#102, 105, 131, 133) exhibit tightly-overlapping, relatively flat REE patterns with negative Ti anomalies. In contrast, the REE patterns of the other three samples (#77, 146, 184) have steeper slopes and exhibit negative Nb anomalies, and two of these rocks (#77, 184) also have negative Ti anomalies. The differences in the slope of REE patterns and occurrences of negative Nb anomalies among the diorite samples are emphasized in the trace element ratio plots in Figure 4.16. Notably, the weakly developed negative Nb

anomaly displayed by sample #146, and the absence of negative Nb anomalies in samples #102, 131 and 133, are within analytical uncertainty, and these samples plot in the transitional arc field in Figure 4.16. On the La/Yb vs. Th/Ta diagram (Figure 4.16e), samples #77 and 184 lie in the arc compositional field defined by Condie (1997) and sample #146 plots directly below this field. In contrast, the other diorite samples (#102, 105, 131, 133) have lower Th/Ta and La/Yb values, and plot close to the primitive mantle, submarine plateau basalt and lower mantle plume fields identified by Condie (1997).

4.6.2.4. Interpretation

As discussed in Chapter 2, thin sections from the diorite geochemical samples are petrographically identical except that grain size varies from medium-grained to fine-grained. Diorite may have been emplaced as one continuous intrusion and grain size reduction may be attributed to localized shear zones in the eastern portion of Map 1. However, it is possible that diorite represents two or more intrusions that may or may not be petrogenetically related, and that contacts are covered by vegetation or overwritten by shearing or subsequent magmatism. The latter interpretation is supported by geochemical data, as three samples (#77, 146, 184) are geochemically different from the other samples (#102, 105, 131, 133). The geochemical similarities between samples #77, 146 and 184 imply that they are from the same intrusion, in agreement with interpretations made during field mapping and thin section analysis. Likewise, the geochemical equivalence of samples #102, 105, 131 and 133 suggests that they were collected from a separate diorite intrusion that spans the western portion of Map 1. These samples have E-MORB-like REE patterns, like the gabbro samples, suggestive of a mantle source with minor LREE-

enrichment. It is possible that samples #77, 146 and 184 are not petrogenetically related to samples #102, 105, 131 and 133. Alternatively, all diorite samples may have originated from a similar mantle source, but the melt that formed samples #77, 146 and 184 may have undergone significant assimilation or mixing with a LREE-enriched source in which Th was elevated relative to Nb, such as continental crust or a partial melt of subduction-contaminated mantle.

4.6.3. Hornblende-porphyritic andesitic dykes

Geochemical samples #100 and 138 are from separate hornblende-porphyritic andesitic dykes in Map 1.

4.6.3.1. Classification

The hornblende-porphyritic andesitic dykes plot in the basalt field on the classification diagram of Pearce (1996; Figure 4.11a) and in the andesite field on the SiO_2 vs. Zr/TiO_2 diagram of Winchester and Floyd (1977; Figure 4.11b). On the Jensen (1976) cation classification diagram (Figure 4.12), one dyke (#100) lies in the calc-alkaline andesite field, whereas the other dyke (#138) plots in the calc-alkaline basalt field.

4.6.3.2. Major element geochemistry

As shown by the major element variation diagrams in Figure 4.13, the hornblende-porphyritic andesitic dykes have significantly different Mg#s. One dyke (#100) has a Mg# of 33, and plots close to the andesitic dykes, whereas the other dyke (#138) has a Mg# of 49, which is the highest Mg# in the dataset. The dykes have similar Al_2O_3, FeO, MnO, CaO, TiO_2 and P_2O_5 contents, but one dyke (#100) is enriched in Na_2O and depleted in K_2O relative to the other (#138). Both dykes have lower CaO, FeO, MnO,

TiO_2, P_2O_5 contents and higher SiO_2, Al_2O_3, Na_2O, K_2O contents than most of the mafic rocks in the dataset, and their major element geochemistry is comparable to that of the andesitic dykes.

4.6.3.3. Trace element geochemistry

Incompatible-immobile trace element plots (Figure 4.14) show that the hornblende-porphyritc andesitic dykes have similar concentrations of Zr, Y, Yb, La and Nb, but sample #100 has a much higher Th content than sample #138. In fact, sample #100 is richer in Th than all the mafic-to-intermediate rocks except for one of the hornblende basaltic dykes (#60). The hornblende-porphyritic andesitic dykes generally have lower Y, Yb and Nb concentrations than other mafic-to-intermediate rock units in the dataset, although their La contents are higher than most of the mafic rocks but lower than most of the intermediate rocks. The hornblende-porphyritic andesitic dykes have comparable Sc contents, but sample #100 is enriched in V relative to sample #138. Overall, the Sc and V contents of both dykes are lower than those of the mafic rocks in the study area, and similar to those of the andesitic dykes. Sample #138 has much higher concentrations of Ni and Cr than sample #100, in which Ni was below 1.5 times the limit of detection.

On primitive-mantle normalized extended REE plots (Figure 4.15), the REE patterns of the hornblende-porphyritic andesitic dykes are parallel and nearly overlapping. They exhibit well-developed negative Nb anomalies, which are highlighted in Figures 4.16a-d, and sample #100 displays a negative Ti anomaly. The REE patterns of the dykes are steeply sloped, demonstrating LREE-enrichment and HREE-depletion relative to the flat REE patterns exhibited by several other rocks in the study area, including gabbro and

certain diorite samples. Furthermore, the steeply-sloping REE patterns of the hornblende-porphyritic andesitic dykes are very similar to those of the andesitic dykes. When Th/Ta is plotted against La/Yb (Figure 4.16e), the hornblende-porphyritic andesitic dykes coincide with the arc compositional field identified by Condie (1997).

4.6.3.4. Interpretation

The high Mg# of sample #138 indicates that it has undergone less fractionation than sample #100 and the other mafic-to-intermediate rocks. However, since the hornblende porphyritic andesitic dykes have similar trace element and REE geochemistry, it is possible that they are petrogenetically related, and that sample #100 is more fractionated than #138. The geochemistry of the hornblende-porphyritic andesitic dykes, particularly their steeply-sloping REE patterns and negative Nb anomalies, suggest that they represent arc magmatism or partial melts of the mantle that were contaminated by continental crust.

4.6.4. Hornblende basaltic dykes

Geochemical samples from this unit include #60 from Map 3, #69 and 78 from Map 2, #99 and 132 from Map 1, as well as samples #75 and 88 from feldspar-porphyritic hornblende basaltic dykes in Map 2.

4.6.4.1. Classification

The Pearce (1996) classification diagram (Figure 4.11a) places all the hornblende basaltic dykes in the basalt field. On the SiO_2 vs. Zr/TiO_2 diagram of Winchester and Floyd (1977; Figure 4.11b), the hornblende basaltic dykes form a cluster in the sub-alkali basalt field, except for one dyke (#69), which lies in the andesite field. According to the

classification diagram of Jensen (1976; Figure 4.12), most of the hornblende basaltic dykes are calc-alkaline basaltic rocks, while some of the dykes (#78, 99, 132) lie in the high-Fe tholeiitic field.

4.6.4.2. Major element geochemistry

Major element variation diagrams (Figure 4.13) illustrate the range of Mg#s in the hornblende basaltic dykes, from 31 to 46. Although the hornblende basaltic dykes have similar SiO_2 contents, the wide range of values for other major elements define broad compositional fields that overlap with data from several other rock units. Despite the overall variation in the major element data in this rock unit, two dykes (#75, 88) have similar major element compositions. These two dykes generally plot together in Figure 4.13 and have elevated Mg#'s, Al_2O_3 and K_2O, and lower FeO*, MnO, TiO_2 and P_2O_5 relative to the other hornblende basaltic dykes.

4.6.4.3. Trace element geochemistry

The hornblende basaltic dykes exhibit a range of incompatible-immobile trace element compositions, which overlap with data from several other rock units (Figure 4.14). The hornblende basaltic dykes have a wide array of Y, Yb and La contents but have similar Zr concentrations. Samples #75 and 88 are less concentrated in Y, Yb and Zr than the other samples. The hornblende basaltic dykes have comparable Th and Nb contents, except for samples #60 and 69, which are among the most Th- and Nb-enriched of the mafic-to-intermediate samples. The compositional variety of the hornblende basaltic dykes is also evident on plots of Sc, V, Ni and Cr. On these diagrams, the compositional field defined by the hornblende basaltic dykes coincides with data from

diorite, gabbro and basaltic dykes. Samples #75 and 88 have lower Sc and V values and, as in other geochemical diagrams, plot apart from the other hornblende basaltic dykes.

On primitive-mantle normalized extended REE diagrams (Figure 4.15), samples #75 and 88 have overlapping REE patterns that lack negative Nb anomalies. The extended REE patterns of samples #60 and 69 also overlap with each other, except sample #60 displays a well-developed negative Nb anomaly, whereas the weak negative Nb anomaly exhibited by sample #69 is within analytical uncertainty. Apart from their negative Nb anomalies, the REE patterns of samples #60 and 69 are nearly parallel to those of samples #75 and 88. The REE patterns of samples #78 and 99 nearly overlap with each other, but the relatively flat REE patterns of samples #78, 99 and 132 are LREE-depleted and HREE-enriched relative to the steeply sloping REE patterns of the other hornblende basaltic dykes. Furthermore, the REE patterns of samples #78, 99 and 132 are similar to those exhibited by gabbro and certain diorite samples (#102, 105, 131, 133). The differences in REE behaviour and Nb/Th between the hornblende basaltic dykes are highlighted by the trace element ratio plots in Figure 4.16. On the Th/Ta vs. La/Yb diagram (Figure 4.16e), the hornblende basaltic dyke data form a broad field between several compositional fields defined by Condie (1997), including the fields of arc basalts, submarine plateau basalts, lower mantle plumes and oceanic island basalts. Samples #78, 99 and 132 plot close to the primitive mantle and submarine plateau basalt compositional fields, along with some of the diorite samples (#102, 105, 131, 133).

4.6.4.4. Interpretation

The similar major and trace element compositions and overlapping REE patterns of two hornblende basaltic dykes (#75, 88) suggest that they are from the same melt, in

agreement with field interpretations that they belong to the same rock unit. As well, the geochemical similarities between samples #60 and 69 implies a petrogenetic link between hornblende basaltic dykes in Maps 2 and 3, and the nearly overlapping REE patterns of samples #78 and 99 indicate geochemical similarities between hornblende basaltic dykes in Maps 1 and 2. However, the major and trace element geochemistry, especially the different slopes of REE patterns, demonstrate that the hornblende basaltic dykes are not geochemically equivalent throughout the study area. The trace element data imply that samples #78, 99 and 132 are from a mantle source that has undergone minimal LREE-enrichment, similar to gabbro and certain diorite samples (#102, 105, 131 and 133). The REE patterns of samples #75 and 88 are LREE-enriched but lack negative Nb anomalies, similar to the REE patterns of OIBs. In contrast, the LREE-enrichment and weak-to-strong negative Nb anomalies displayed by samples #60 and 69 imply arc magmatism or crustal contamination. Hence, the hornblende basaltic dykes may represent partial melts of three separate sources or of a common source with a complex mixing history.

4.6.5. Basaltic dykes

Five samples from this unit were selected for geochemical analysis, including #53 from Map 3, #71, 74 and 84 from Map 2 and #123 from Map 1.

4.6.5.1. Classification

The basaltic dykes plot in the basalt field on Pearce (1996) classification diagram (Figure 4.11a) and in the sub-alkali basalt field on the Zr/TiO_2 vs. SiO_2 diagram of Winchester and Floyd (1997; Figure 4.11b). On the Jensen (1976) cation plot (Figure

4.12), the basaltic dyke data form a tight cluster that spans the high-Mg and the high-Fe tholeiitic basalt fields.

4.6.5.2. Major element geochemistry

Major element variation diagrams (Figure 4.13) illustrate that, like the hornblende basaltic dykes, the basaltic dykes have a wide range of Mg#s. The basaltic dykes have similar concentrations of SiO_2, MnO, FeO* and P_2O_5, but exhibit a wide range of Al_2O_3, TiO_2, CaO, Na_2O and K_2O contents. Two of the dykes (#53, 84) have very similar Mg#s and are elevated in FeO* and depleted in Al_2O_3 relative to the other basaltic dykes. As a group, the major element compositions of the basaltic dykes overlap with data from several other rock units but are most similar to the hornblende basaltic dykes.

4.6.5.3. Trace element geochemistry

As shown by incompatible-immobile trace element plots (Figure 4.14), most of the basaltic dykes have similar concentrations of Zr, Y, Yb, Th and Nb. However, two of the dykes (#71, 123) tend to plot apart from the other samples, as they are comparatively depleted in Y, Yb and V and elevated in Nb, Th and Ni. Sample #123 is also enriched in Zr with respect to the other basaltic dyke samples. The basaltic dykes have similar concentrations of Sc, and two of the dykes (#53, 84) have nearly equal Sc and V contents. The basaltic dykes display a range of Cr contents, and sample #71 is the most Cr-enriched sample of all the mafic-to-intermediate rocks in the dataset. As a group, the incompatible-immobile trace element compositions of the basaltic dykes are most similar to those of the hornblende basaltic dykes and some of the diorite samples (#102, 105, 131, 133).

On primitive mantle normalized extended REE plots (Figure 4.15), none of the basaltic dykes exhibit negative Nb anomalies. The relatively flat REE patterns of two of the dykes (#53, 84) overlap almost exactly and are nearly parallel to the flat REE patterns displayed by gabbro and some samples from diorite (#102, 105, 131, 133) and the hornblende basaltic dykes (#78, 99, 132). However, the REE patterns of the other basaltic dykes (#71, 74, 123) do not overlap with each other and are not quite parallel, but they are LREE-enriched compared to samples #53 and 84. Furthermore, the REE patterns of these dykes have similar slopes to certain hornblende basaltic dykes (#75, 88). The differences in LREE-enrichment between the basaltic dykes are emphasized by the REE ratio plots in Figure 4.16. On the Th/Ta vs. La/Yb diagram in Figure 4.16e, the data from the basaltic dykes form a spread between the fields of lower mantle plumes and submarine plateau basalts, as defined by Condie (1997).

4.6.5.4. Interpretation

The overlapping REE patterns of samples #53 and 84 confirm geochemical similarities between basaltic dykes in Maps 2 and 3. However, the non-parallel REE patterns of samples #71, 74 and 123 highlight geochemical differences among the basaltic dykes. The similarity between the relatively flat REE patterns of two of the basaltic dykes (#53, 84) and those displayed by gabbro, and some samples from diorite (#102, 105, 131, 133) and hornblende basaltic dykes (#78, 99, 132) implies that all these rocks share an E-MORB-like source. Conversely, three of the hornblende basaltic dykes (#71, 74, 123) are relatively LREE-enriched and, like particular hornblende basaltic dykes (#75, 88), display OIB-like REE patterns. Therefore, it appears that the basaltic dykes

originated from mantle sources that have undergone different degrees of LREE-enrichment.

4.6.6. Andesitic dykes

Ten geochemical samples were taken from andesitic dykes, including #96, 103, 104, 152, 167 and 175 from Map 1, #55 and 59 from Map 3 and #89 and 203 from Map 2. Samples #89 and 203 were collected from the same andesitic dyke that sample #209 was taken from, which was dated at 578.4 ± 2.3 Ma using U/Pb geochronology. Sample #89 was collected about 2 m west of sample #209, whereas sample #203 was collected about 5 m east of sample #209, where the andesitic dyke locally contains mafic enclaves.

4.6.6.1. Classification

On the classification diagram of Pearce (1996; Figure 4.11a), the andesitic dykes plot in the basalt field. They plot in the andesite field on the SiO_2 vs. Zr/TiO_2 diagram of Winchester and Floyd (1977; Figure 4.11b), except for one dyke (#55), which lies in the rhyodacite/dacite field. On the cation plot of Jensen (1976; Figure 4.12), the andesitic dyke data form a cluster in the calc-alkaline andesite field, although one of the dykes (#104) plots on the boundary with the tholeiitic dacite field and two samples (#89, 175) plot on the boundary with the calc-alkaline dacite field.

4.6.6.2. Major element geochemistry

As demonstrated by major element variation diagrams (Figure 4.13), the andesitic dykes are among the most SiO_2- and Na_2O-rich and CaO-, FeO*-, MgO-, TiO_2-, P_2O_5- and MnO-poor rocks of the mafic-to-intermediate rocks in the dataset. While most andesitic dykes have Mg#s from 28 to 30, one sample (#104) has a much lower Mg# (25),

and three samples (#203, 103, 96) have much higher Mg#s (32, 38, 39, respectively). Four rocks (#89, 152, 167, 175) have nearly equal concentrations of most major elements and form a cluster on major element variation plots, but the other six rocks tend to plot separately. For example, samples #96 and 103, which typically plot together, have higher MgO, CaO and lower Na_2O than the clustered samples. As well, three samples (#55, 59, 104) have lower Al_2O_3 than the other andesitic dykes. As a group, the major element compositions of the andesitic dykes are similar to those of oxide-rich andesitic dykes, basaltic-andesitic dykes and hornblende-porphyritic andesitic dykes.

4.6.6.3. Trace element geochemistry

The andesitic dyke data define wide compositional fields on incompatible-immobile trace element plots (Figure 4.14). Three samples (#103, 152, 167) are enriched in La, Zr and Th relative to the other andesitic dykes, and two of these samples (#152, 167) are enriched in Y and Yb. Generally, the andesitic dykes are enriched in Th, La and depleted in Y, Yb and Nb compared to the mafic rocks in the dataset. Only samples #96, 103 and 203 contain more than 1.5 times the limit of detection (30 ppm) of Ni, and only samples #96 and 103 contain more than 1.5 times the limit of detection (30 ppm) of Cr. The andesitic dykes contain similar concentrations of Sc, but display a range of V concentrations, and they have lower Sc, V, Ni and Cr contents than most of the mafic rocks in the dataset.

On primitive mantle normalized extended REE plots (Figure 4.15), the andesitic dykes exhibit steeply sloping REE patterns with strong negative Nb anomalies and negative Ti anomalies. Most samples from the andesitic dykes (#89, 96, 152, 167, 175, 203) have nearly parallel REE patterns. However, compared to these rocks, the REE

pattern of sample #104 and the overlapping REE patterns of samples #55 and 59 are slightly HREE-enriched, and the REE pattern of sample #103 is LREE-enriched. As shown by the REE ratio plots in Figure 4.16, the REE patterns of the andesitic dykes are more steeply sloped than those of the other mafic-to-intermediate rocks, except for the hornblende-porphyritic andesitic dykes and some of the oxide-rich andesitic dykes. Figure 4.16 also demonstrates that the andesitic dykes have stronger negative Nb anomalies than most of the other mafic-to-intermediate rocks. As well, the Th/Ta vs. La/Yb plot (Figure 4.16e) shows that the andesitic dyke data plot within the compositional field of arc basalts determined by Condie (1997).

4.6.6.4. Interpretation

The close geochemical resemblance between four rocks (#89, 152, 167, 175) from the andesitic dykes indicate that they are probably from the same melt, which supports interpretations made during mapping and thin section analysis. Because samples #96 and 203 have higher Mg#s than these rocks, but parallel REE patterns, they may be from petrogenetically related, less-fractionated melts. Sample #104 appears to be from a less-fractionated melt that is HREE-enriched compared to the other andesitic dykes. The high Mg# and M-HREE-depletion of sample #103 relative to the other andesitic dykes may be related to the presence of clinopyroxene phenocrysts, which are unique to this andesitic dyke. Since the partition coefficients of the M-HREE (Sm to Er) are relatively high in clinopyroxene in andesitic melts, as indicated by Rollinson (1993), M-HREE depletion in sample #103 may be explained by fractionation of clinopyroxene. Two dykes (#55, 59) seem to be from a melt that has a similar degree of fractionation as most of the andesitic dykes, but is LREE-depleted and HREE-enriched. As discussed in Chapter 2, samples

from these two dykes also exhibit petrographic differences from the other andesitic dykes, and could arguably be from an unrelated melt.

The significant LREE-enrichment and well-developed negative Nb and Ti anomalies exhibited by the andesitic dykes indicate that they are probably partial melts of subduction-contaminated mantle or were contaminated by continental crust during ascent. The REE patterns of most of the andesitic dykes, like those of the hornblende-porphyritic andesitic dykes, closely resemble those of calc-alkalic basalts and andesites from subduction zones. The REE patterns of two andesitic dykes (#55, 59) are slightly LREE-depleted compared to those of other andesitic dykes, and resemble REE patterns of IATs.

4.6.7. Basaltic-andesitic dykes

Geochemical samples from this unit comprise #91 from Map 2 and #143, 155, 181 and 194 from Map 1.

4.6.7.1. Classification

The basaltic-andesitic dykes plot in the basalt field on the Pearce (1996) classification diagram (Figure 4.11a) and form a cluster on the Winchester and Floyd (1977) diagram (Figure 4.11b) that spans the boundary between the sub-alkali basalt and andesite fields. On the cation plot of Jensen (1976; Figure 4.12), the data plot along the boundary between the calc-alkaline basalt and tholeiitic andesite fields, except for one dyke (#143), which plots apart from the other samples in the calc-alkaline basalt field.

4.6.7.2. Major element geochemistry

The basaltic-andesitic dykes display a range of major element compositions, as illustrated on major element variation plots in Figure 4.13. For instance, while most of

the basaltic-andesitic dykes have Mg#s between 28 and 30, sample #143 has a Mg# of 45, one of the highest Mg#s in the dataset. While the basaltic-andesitic dykes generally have similar contents of SiO_2, FeO*, MnO, CaO, Na_2O and K_2O, sample #143 is more concentrated in Al_2O_3 and less concentrated in TiO_2 and P_2O_5. As well, sample #194 is more enriched in P_2O_5 than all the rocks in the dataset. The Mg#s of the basaltic-andesitic dykes, apart from sample #143, are comparable to those of the andesitic dykes and the oxide-rich dykes. The major element compositions of the basaltic-andesitic dykes overlap with data from several rock units but are generally mid-range with respect to the mafic-to-intermediate rocks in the dataset.

4.6.7.3. Trace element geochemistry

On incompatible-immobile element plots (Figure 4.14), the basaltic-andesitic dykes exhibit a wide range of compositions, resulting in data fields that overlap with several other units. Three of the dykes (#91, 155, 194) are generally enriched in incompatible-immobile elements with respect to the other samples. As well, two of the dykes (#91, 155) are significantly enriched in V and Sc and depleted in Ni compared to the other three dykes (#143, 181, 194). Only one sample (#143) in this unit has a Cr content above 1.5 times the limit of detection (30 ppm).

On primitive-mantle normalized REE plots (Figure 4.15), the REE patterns of three samples (#143, 181, 194) are nearly parallel to each other, except the REE pattern of one of these samples (#194) displays strong negative Zr and Ti anomalies. As shown by Figures 4.15 and 4.16, these three samples have well-developed negative Nb anomalies. The weak negative Nb anomaly of sample #91, and the absence of a negative Nb anomaly in sample #155, is within analytical uncertainty, placing these rocks in the transitional arc

field in Figure 4.16. The REE patterns of the other two dykes (#91, 155) are also nearly parallel to each other and exhibit negative Zr and Ti anomalies, but are slightly LREE-depleted and HREE-enriched compared to samples #143, 181 and 194. When plotted on the Th/Ta vs. La/Yb diagram (Figure 4.16e), the basaltic-andesitic dyke data lie on the lower edge of the arc basalt field defined by Condie (1997).

4.6.7.4. Interpretation

The nearly overlapping REE patterns of two basaltic-andesitic dykes (#91, 155) imply that they have similar source histories, demonstrating a petrogenetic link between dykes from Maps 1 and 2. As well, a common source for three dykes in Map 1 (#143, 181, 194) is suggested by their similar REE patterns, although the anomalously high Mg# of one of these samples (#143) indicates a lower degree of fractionation than the other samples. The resemblance between the extended REE patterns of samples #143, 181 and 194 and those of IAT suggests that, like IAT, these samples are from a depleted mantle source that was contaminated by fluids from a subduction zone. The relatively flat, E-MORB-like slopes of the extended REE patterns of the other two samples from basaltic-andesitic dykes (#91, 155) suggest that they represent melts of depleted mantle sources that received minor LREE-enrichment. The weak negative Nb anomaly exhibited by sample #91 implies minor contamination by a subducting slab or continental crust.

4.6.8. Oxide-rich basaltic and andesitic dykes

Geochemical samples were collected from four oxide-rich andesitic dykes, including samples #56 and 57 from Map 3, #79 from Map 2 and #145 from Map 1. As

well, geochemical samples were taken from two oxide-rich basaltic dykes: samples #64 from Map 2 and #129 from Map 1.

4.6.8.1. Classification

On the classification diagram of Pearce (1996; Figure 4.11a), the oxide-rich andesitic and basaltic dykes plot in the basalt field, whereas on the Zr/TiO_2 vs. SiO_2 diagram (Winchester and Floyd 1977; Figure 4.11b), the oxide-rich basaltic dykes plot in the sub-alkali basalt field and the oxide-rich andesitic dykes plot in the andesite field. On the Jensen (1976) cation plot (Figure 4.12), one oxide-rich basaltic dyke (#64) plots in the high-Fe tholeiitic basalt field, whereas the other dyke (#129) plots on the boundary between the high-Fe tholeiitic basalt and calc-alkaline basalt fields. When the oxide-rich andesitic dykes are plotted on the Jensen (1976) diagram, two dykes (#56, 79) plot in the tholeiitic andesite field, while the other two dykes (#57, 145) lie in the calc-alkaline andesite and dacite fields, respectively.

4.6.8.2. Major element geochemistry

As shown by major element variation diagrams (Figure 4.13), the oxide-rich dykes have relatively low Mg#s, like the andesitic and basaltic-andesitic dykes. The oxide-rich andesitic dykes have a range of SiO_2-contents that is similar to the andesitic dykes, and they are among the most SiO_2-rich rocks of the mafic-to-intermediate samples. In contrast, with 50.22 to 51.80 wt. % SiO_2, the oxide-rich basaltic dykes have similar SiO_2 contents to the other basaltic rocks in the study area. Among the oxide-rich andesitic dykes, samples #56 and 79) are Al_2O_3-, K_2O-, P_2O_5- and Na_2O-depleted and FeO*-, TiO_2-, CaO and MnO-enriched compared to samples #57 and 145. Furthermore, samples #57 and 145 tend to plot within or close to the compositional field of andesitic

dykes in Figure 4.13. Both samples from oxide-rich basaltic dykes have similar concentrations of many major elements, but sample #64 has lower Al_2O_3 and Na_2O contents and higher CaO and P_2O_5 contents than sample #129.

4.6.8.3. Trace element geochemistry

There is considerable compositional variation in the trace element compositions of the oxide-rich dykes. Incompatible-immobile trace element plots (Figure 4.14) demonstrate that the oxide-rich andesitic dykes display progressively higher concentrations of Zr, Y, Yb, La, Th and Nb from sample #57 through to #145, 56 and 79. In addition, the oxide-rich andesitic dykes display a range of V and Sc contents, increasing from sample #145 through to #57, 56 and 79. None of the oxide-rich andesitic dykes contain more than 30 ppm Ni or Cr.

The oxide-rich basaltic dykes share similar incompatible-immobile trace element compositions, except sample #64 has lower Th and Nb contents than sample #129. In addition, while neither sample contains more than 30 ppm Cr, the Ni content of sample #64 is relatively low, like those of the andesitic dykes, the basaltic-andesitic dykes and diorite.

As shown by primitive mantle normalized REE plots (Figure 4.15), the oxide-rich andesitic dykes exhibit steeply sloping REE patterns with negative Nb and Ti anomalies. The REE patterns of samples #57 and 145 are similar to those of the andesitic dykes, whereas the somewhat concave-upward REE patterns of samples #56 and 79 are flatter and more HREE-enriched than those of samples #57 and 145. In addition, the negative Nb anomalies displayed by samples #56 and 79 are less well-developed (Figure 4.16). On the Th/Ta vs. La/Yb diagram (Figure 4.16e), the oxide-rich andesitic dykes plot in the

arc field, as defined by Condie (1997), except for sample #56, which plots outside the lower boundary of the arc field.

The nearly-parallel REE patterns formed by the oxide-rich basaltic dykes are flatter than those of the oxide-rich andesitic dykes. Sample #129 exhibits a weak negative Nb anomaly that is within analytical uncertainty, and the lack of a negative Nb anomaly in sample #64 is also within analytical uncertainty, placing both samples in the transitional arc field in Figure 4.16. Sample #129 is slightly LREE-enriched and HREE-depleted compared to sample #64, but both samples display relatively flat REE patterns, like those of gabbro. Both oxide-rich basaltic dykes plot just outside the lower boundary of the arc compositional field and next to the primitive mantle field defined by Condie (1997) on the Th/Ta vs. La/Yb diagram (Figure 4.16e).

4.6.8.4. Interpretation

Because samples #56 and 79 are geochemically similar, especially with regard to their REE patterns, the oxide-rich andesitic dykes from Maps 2 and 3 may be petrogenetically linked. Similarly, the geochemical likeness between samples #57 and 145 suggests a petrogenetic relationship between oxide-rich andesitic dykes in Maps 1 and 3. Samples #57 and 145 are geochemically similar to the andesitic dykes in the study area, and their steeply sloping REE patterns imply that they are not from the same melt as samples #56 and 79. Because the oxide-rich andesitic dyke samples display negative Nb anomalies, it is likely that they formed in a subduction zone or that they were contaminated by continental crust during ascent. Because samples #56 and 79 are not as LREE-enriched as samples #57 and 145, they may have received less contamination from continental crust or a subducting slab.

The oxide-rich basaltic dykes share many geochemical similarities, and their relatively flat, slightly LREE-enriched REE patterns suggest an E-MORB-like source. The weak negative Nb anomaly displayed by sample #129 implies minor contamination from a subducting slab or continental crust.

4.7. Nd isotopic data

Because negative Nb anomalies are associated with arc magmatism (e.g. Jenner *et al.* 1991, Swinden *et al.* 1997), many of the rocks in the study area appear to have formed in an arc environment. Partial melts of the subduction-contaminated mantle wedge are enriched in highly incompatible elements, but Nb is depleted relative to Th, possibly because Nb fractionates into rutile at depth (Foley *et al.*, 2000; Rudnick *et al.*, 2000). Alternatively, Nb anomalies may result from contamination during ascent through continental crust that formed in an arc setting. Therefore, the Nb anomalies in the rocks at Bauline do not necessarily indicate formation in a subduction zone. To help resolve this issue, the following seven samples were selected for Nd isotopic analysis: #74 from a basaltic dyke in Map 2, #82 from gabbro in Map 2, #89 from an andesitic dyke in Map 2, #105 and 184 from diorite in Map 1, #181 from a basaltic-andesitic dyke in Map 1 and #141 from the rhyolitic dyke in Map 1. These rocks were selected because their compositional variety, including various degrees of LREE-enrichment and a range of Nb/Th values, is representative of the geochemistry of the HCC.

The Sm and Nd isotopic data and ϵNd values are shown in Table 4.1, and a plot of ϵNd against time is shown in Figure 4.17. Epsilon Nd values were calculated using an age of 580 Ma, and they range from +4.1 to +6.4. These values are all lower than the ϵNd

Table 4.1: Sm and Nd isotopic data for selected samples in the Horse Cove Complex at Bauline.

Sample	Unit	Nd (ppm)	Sm (ppm)	$^{147}Sm/^{144}Nd$	$^{143}Nd/^{144}Nd$	2σ X 10^{-5}	Epsilon Nd (t=0)	Epsilon Nd (t=580 Ma)	T_{DM} (Ma)	T_{DM2} (Ma)
DS-09-74	BD	19.52	5.194	0.1609	0.512825	6	3.6	6.3	653	938
DS-09-82	G	13.42	3.781	0.1704	0.512827	7	3.7	5.6	781	1136
DS-09-89	AD	16.03	3.679	0.1387	0.512629	7	-0.2	4.1	851	1059
DS-09-105	D	18.24	4.96	0.1644	0.512841	7	4.0	6.4	653	955
DS-09-141	RD	25.17	5.081	0.1220	0.512595	7	-0.8	4.7	757	923
DS-09-181	BAD	17.09	4.308	0.1524	0.512699	8	1.2	4.5	865	1121
DS-09-184	D	15.99	3.713	0.1404	0.512670	7	0.6	4.8	787	998

Notes: BD=basaltic dyke, G=gabbro, AD=andesitic dyke, D=diorite, RD=rhyolitic dyke, BAD=basaltic-andesitic dyke; Epsilon Nd values were calculated using the present-day CHUR $^{143}Nd/^{144}Nd$ value of Goldstein *et al.* (1984) and $^{147}Sm/^{144}Nd$ value of Jacobsen and Wasserburg (1980); T_{DM}=model age calculated using the method of DePaolo (1981); T_{DM2}=model age calculated using a linear evolution from the CHUR at 4.55 Ga, with Epsilon Nd=+10 at t=0, using the depleted mantle $^{143}Nd/^{144}Nd$ and $^{147}Sm/^{144}Nd$ values of Peucat *et al.* (1988).

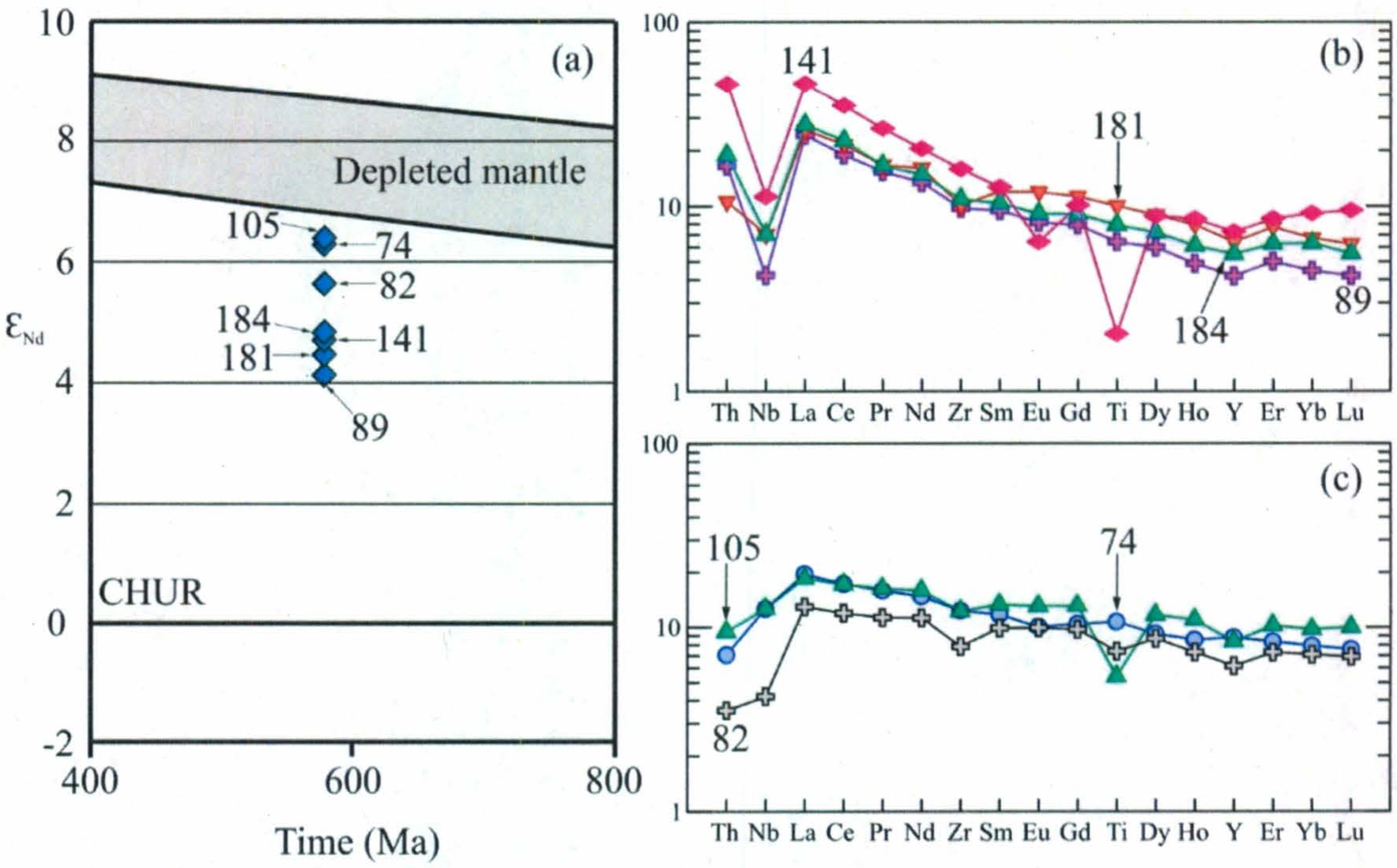

Figure 4.17: (a) Epsilon Nd vs. time plot, showing the seven Horse Cove Complex samples. The shaded area shows the range of depleted mantle values defined by the model of DePaolo (1981) (the lowermost curve) and the linear evolution curve described in Table 4.1. (b) & (c) Extended REE data for samples with Nd isotopic data, normalized to the primitive mantle values of Sun and McDonough (1989).

value of the depleted mantle at 580 Ma (+6.8), calculated using the mantle evolution curve of DePaolo (1981). With εNd=+6.4, one of the diorite samples (#105) has the highest εNd value of all the samples analyzed, and a basaltic dyke (#74) has the second highest εNd value of the seven samples, with εNd=+6.3. However, diorite sample #184, which has a negative Nb anomaly and is LREE-enriched relative to diorite sample #105, has an εNd value of +4.8. Gabbro (#82) has εNd=+5.6, a basaltic-andesitic dyke (#181) has εNd=+4.5 and a rhyolitic dyke (#141) has εNd=+4.7, while the εNd of an andesitic dyke (#89) is +4.1, the lowest εNd value of all the rocks analyzed. All samples with εNd values between +4.1 and +4.8 have significant LREE enrichment and negative Nb anomalies.

4.8. Discussion

4.8.1. Feldspar porphyry and rhyolitic dykes

Both feldspar porphyry and the rhyolitic dykes exhibit geochemical characteristics that are typical of volcanic arc magmatism, including enrichment in the LREE relative to the HREE and negative Nb and Ti anomalies. They also plot in the volcanic arc granite field on the tectonic discrimination diagram of Pearce *et al.* (1984; Figure 4.9d). Because of strong geochemical similarities between feldspar porphyry and the rhyolitic dykes, they are arguably petrogenetically related. This interpretation is reinforced by U/Pb geochronology, which demonstrates that these two rock units overlap in age, within uncertainty.

Although feldspar porphyry and the rhyolitic dykes are HREE-enriched relative to the ca. 625 Ma granodiorite (Figure 4.10d), some feldspar porphyry and rhyolitic dyke

samples plot in the granodiorite compositional field on major and trace element plots. Like feldspar porphyry and the rhyolitic dykes, the ca. 625 Ma granodiorite is interpreted to represent subduction zone-related magmatism. These geochemical similarities, along with the proximity of granodiorite to feldspar porphyry and rhyolitic dykes in the field, raise the question of whether or not the ca. 625 Ma granodiorite is petrogenetically related to the ca. 580 Ma feldspar porphyry and rhyolitic dykes. This question is answered by their notably different Th contents (Figure 4.9a). The granodiorite samples have much higher Th concentrations than the younger felsic rocks, and are enriched in TiO_2 relative to most of the feldspar porphyry and rhyolitic dyke samples (Figure 4.8). Feldspar porphyry and the rhyolitic dykes cannot be petrogenetically related to granodiorite because Th cannot increase with TiO_2 during melt fractionation.

A rhyolitic dyke (#141) has an ϵNd value of +4.7 and a T_{DM} value (DePaolo, 1981) of 757 Ma. The Nd isotopic data suggest that the source of this rhyolitic melt was extracted from the depleted mantle sometime between 757 Ma and 580 Ma but assimilated or mixed with an older, LREE-enriched source. Because sample #141 is LREE-enriched and exhibits a negative Nb anomaly, it probably experienced contamination from continental crust during ascent or from a subducting slab that carried continentally derived sediment. The similar ϵNd values and REE patterns of this rhyolitic dyke (#141), a basaltic-andesitic dyke (#181) and a diorite sample (#184) suggest that these three rocks share similar source regions and may represent products of melts related by fractionation. Hence, feldspar porphyry and other rhyolitic dykes may have evolved

from similar sources as many of the mafic-to-intermediate rocks in the study area, and it is possible that they are related by fractionation.

4.8.2. Mafic-to-intermediate rocks

4.8.2.1. Distinction between mapped rock units and geochemical groups

Many of the mafic-to-intermediate rock units defined by mapping and petrography exhibit geochemical variations between samples, especially with respect to REE patterns and negative Nb anomalies. In addition, similarities exist between the trace element compositions of samples from different rock units. The mafic-to-intermediate rocks are separated into six groups according to the slope of their REE patterns, measured by La/Yb, and the presence or absence of a negative Nb anomaly (Figures 4.18 and 4.19).

4.8.2.2. Group 1: E-MORB-like REE-patterns

This group includes a diorite sample (#105), two hornblende basaltic dykes (#78, 132) and two basaltic dykes (#53, 84). The rocks in this group have Mg#s that are greater than 33, indicating a low degree of fractionation with respect to many samples in the dataset. The samples in this group plot in the non-arc field in Figure 4.19a and close to the primitive mantle field defined by Condie (1997) in Figure 4.19b. The samples in this group display relatively flat REE patterns with La/Yb ratios that are less than 2.9. The REE patterns in this group closely resemble the REE patterns displayed by E-MORB (Figure 4.20), which are relatively flat and lack negative Nb anomalies, but exhibit

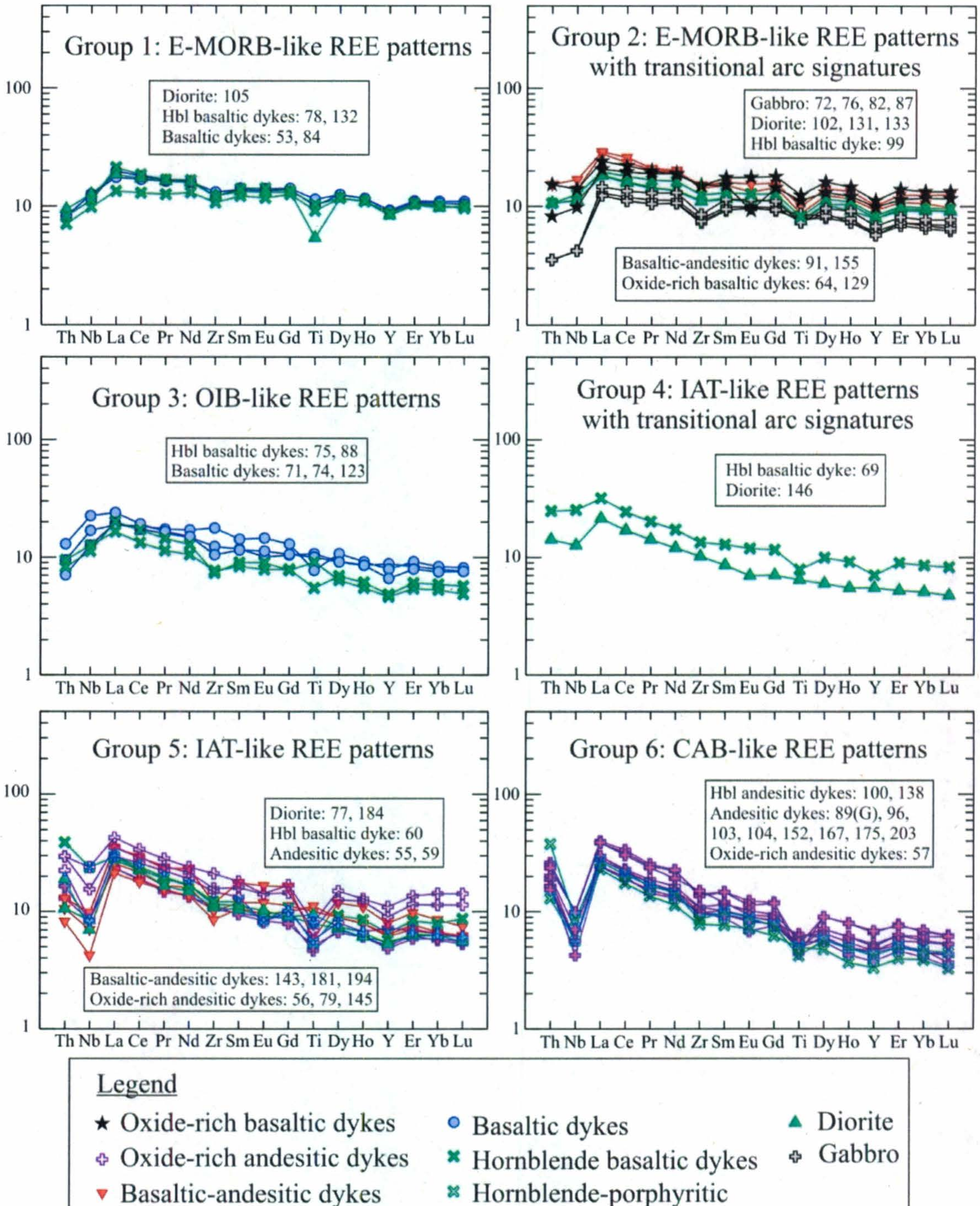

Figure 4.18: Extended REE diagrams showing the mafic-to-intermediate rocks in the study area divided into six groups according to La/Yb and the presence or absence of a negative Nb anomaly. The data are normalized to the primitive mantle values of Sun and McDonough (1989). (G)=U/Pb zircon geochronology sample.

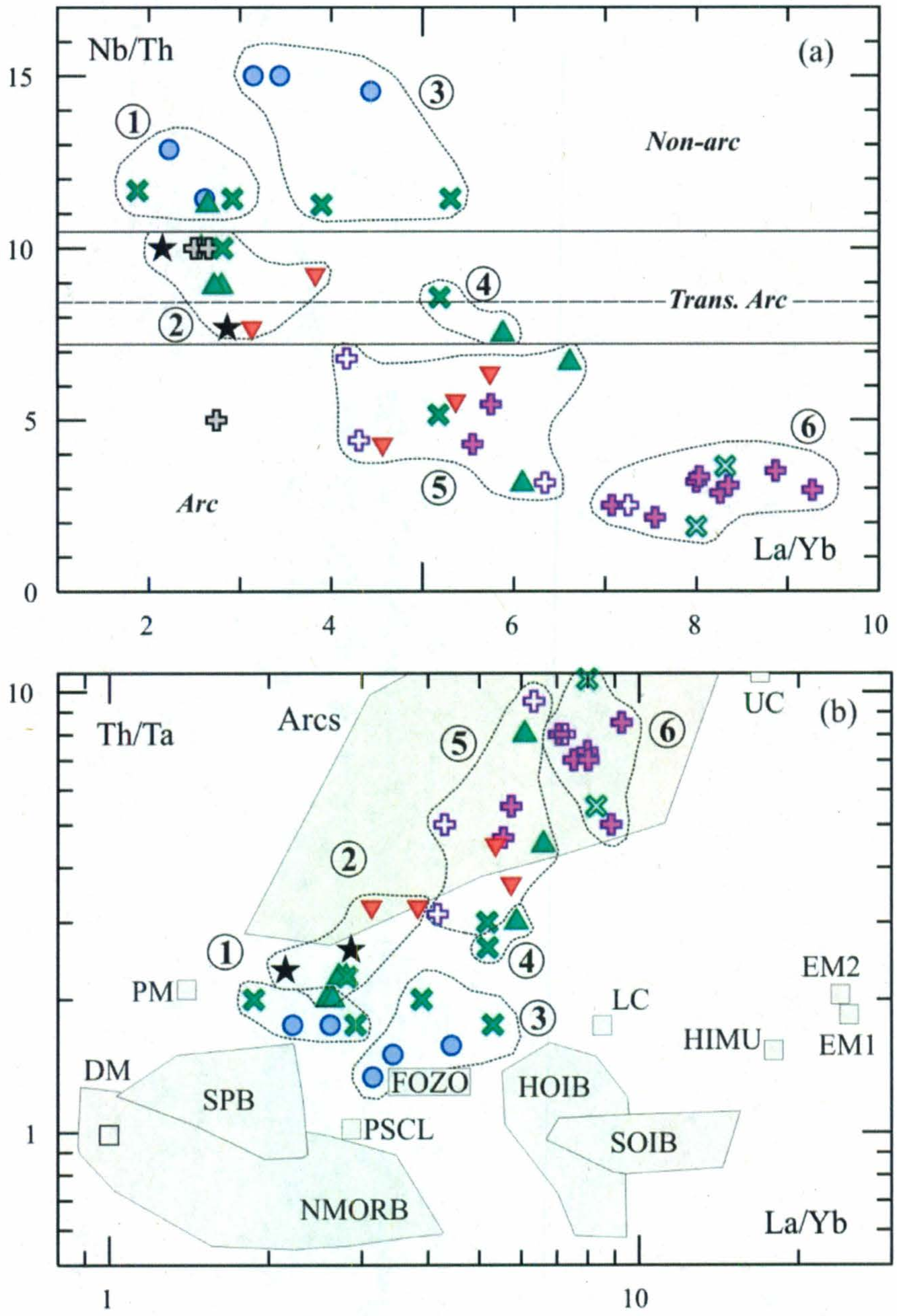

Figure 4.19: Plots of selected trace element ratios in mafic-to-intermediate rocks. Symbols are as in Figure 4.1. (a) Nb/Th - La/Yb plot, with compositional fields defined according to the criteria used by Jenner *et al.* (1991) and Swinden *et al.* (1997), as in Figure 4.16. (b) Th/Ta - La/Yb plot, with compositional fields (grey) defined by Condie (1997), as in Figure 4.16. Dotted lines enclose data from samples that have similar REE patterns and Nb/Th ratios, as shown in Figure 4.18: 1) E-MORB-like REE patterns; 2) E-MORB-like REE patterns with transitional arc signatures; 3) OIB-like REE patterns; 4) IAT-like REE patterns with transitional arc signatures; 5) IAT-like REE patterns; 6) CAB-like REE patterns.

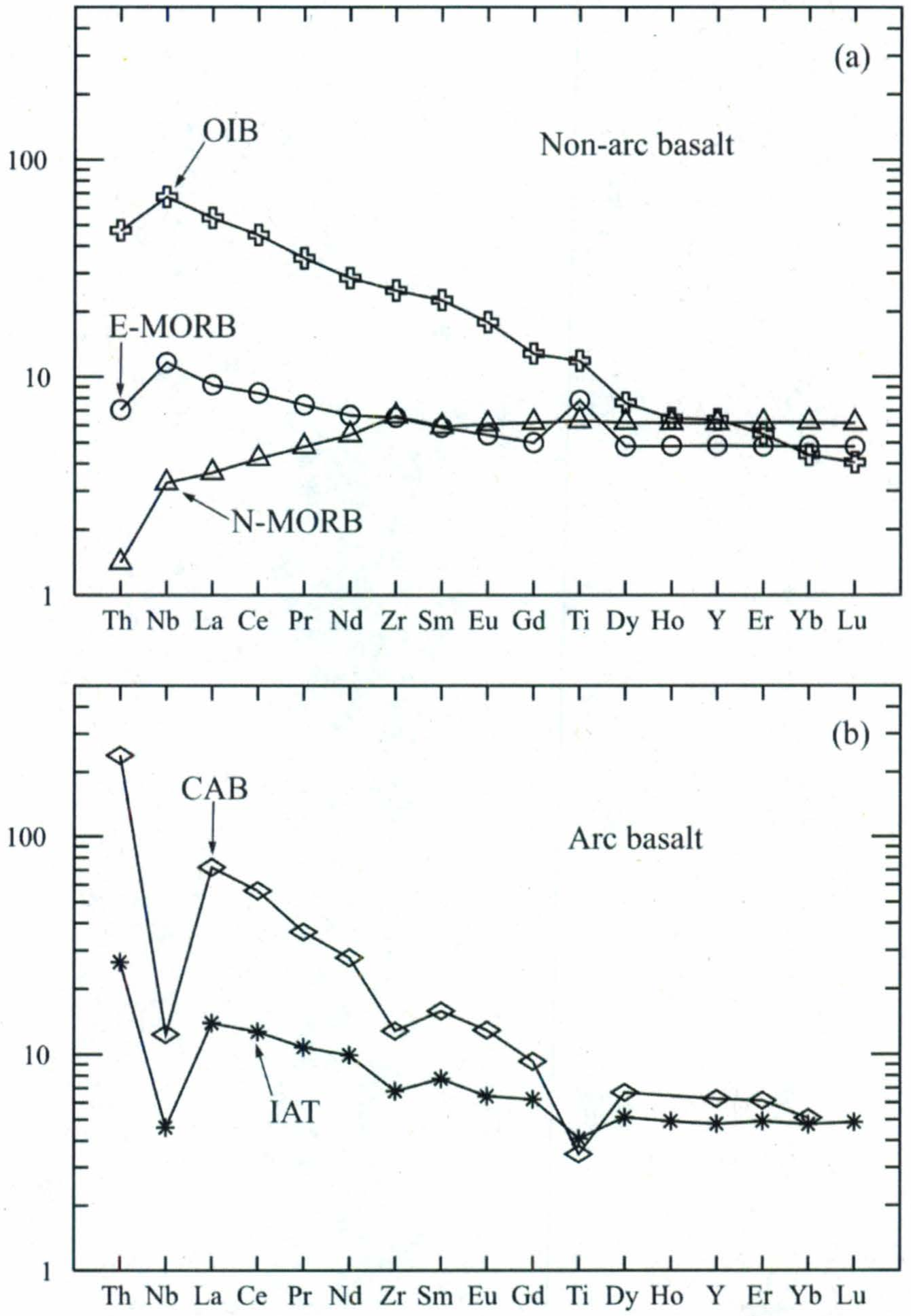

Figure 4.20: Examples of extended REE plots for arc and non-arc rocks. (a) non-arc basalt, including N-MORB, E-MORB and OIB (Sun and McDonough, 1989). (b) arc basalt, including CAB (Stolz *et al.,* 1990) and IAT (Shinjo *et al.,* 1999). All data are normalized to the primitive mantle values of Sun and McDonough (1989).

enrichment in the LREE compared to N-MORB. This similarity to E-MORB geochemistry suggests that, like E-MORB, the rocks in this group represent magmatism from segments of spreading ridges in ocean basins or back arc basins that were affected by mantle upwelling.

The εNd value of diorite sample #105 (+6.4) is close to that of the depleted mantle at 580 Ma (+6.8), according to the mantle evolution curve of DePaolo (1981). Its T_{DM} (DePaolo, 1981) value of 653 Ma is close to the estimated crystallization age that was used to calculate εNd (580 Ma). Thus, the Nd isotopic data suggest that this dioritic melt had a depleted mantle source and did not mix with an older source. Together, the high εNd value, relatively flat REE pattern and lack of a negative Nb anomaly render crustal contamination unlikely, and imply that sample #105 represents magmatism from the depleted mantle.

4.8.2.3. Group 2: E-MORB-like REE patterns with transitional arc signatures

The rocks in this group have relatively flat REE patterns that are similar to those of E-MORB, except for weak negative Nb anomalies, which are within analytical uncertainty. Some rocks in this group do not exhibit negative Nb anomalies, but the lack of a negative Nb anomaly is within analytical uncertainty. Therefore, the rocks in this group plot in the transitional arc field in Figure 4.19a. The rocks in this group include gabbro (except for sample #73, due to its anomalously high Th content), oxide-rich basaltic dykes (#64, 129), one hornblende basaltic dyke (#99), two basaltic-andesitic dykes (#91, 155) and several diorite samples (102, 131, 133). This group has similar La/Yb ratios (2.1 to 3.8) and Mg#s (27 to 46) to the rocks in Group 1. The relatively flat, slightly LREE-enriched REE patterns of these samples resemble REE patterns of E-

MORB. However, the weak negative Nb anomalies displayed by two dykes (#91, 129) suggest that they represent N-MORB or E-MORB-type sources that have undergone minor contamination from a subducting slab in an arc environment or from continental crust during ascent.

Since the εNd value of gabbro sample #82 (+5.6) is lower than those of sample #105 and the DePaolo (1981) depleted mantle at 580 Ma (+6.8), this gabbroic melt may have undergone mixing with an older, LREE-enriched source after being extracted from the depleted mantle. However, since the REE pattern of sample #82 is only slightly LREE-enriched and lacks a negative Nb anomaly, it probably did not undergo significant mixing with a crustal source.

4.8.2.4. Group 3: OIB-like REE patterns

This group is characterized by LREE-enriched REE patterns without negative Nb anomalies. The rocks in this group include two hornblende basaltic dykes (#75, 88) and several basaltic dykes (#71, 74, 123). These rocks plot in the non-arc field in Figure 4.19a and next to the lower mantle plume field in Figure 4.19b. The La/Yb ratios in this group range from 3.1 to 5.3. In addition, with Mg#s ranging from 37 to 46, the samples in this group have undergone a degree of fractionation that is comparable to the samples in Group 1. The REE patterns exhibited by this group are similar to those of OIBs (Figure 4.20), which implies that, like OIBs, the rocks in this group had mantle sources that were enriched in incompatible elements.

The εNd value of one basaltic dyke (#74; +6.3) is similar to those of diorite sample #105 (+6.4) and the depleted mantle at 580 Ma (+6.8), according to the mantle evolution curve of DePaolo (1981). This implies that this basaltic melt was extracted

from the depleted mantle shortly before crystallization and did not mix with an older source. Therefore, samples #74 and 105 both appear to represent magmatism from the depleted mantle, although sample #74 appears to have undergone more LREE-enrichment due to mantle upwelling.

4.8.2.5. Group 4: IAT-like REE patterns with transitional arc signatures

This group consists of only two samples: a hornblende basaltic dyke (#69) and a diorite sample (#146). These rocks are characterized by weak negative Nb anomalies and LREE-enriched REE patterns with slopes intermediate between the relatively flat REE patterns of Groups 1 and 2 and the steeply sloping REE patterns of Group 6. As shown by Figure 4.19a, both rocks have La/Yb ratios of 5.3 and 5.8, and they plot in the transitional arc field. In Figure 4.19b, Group 4 plots next to the arc basalt field. Sample #69 has a Mg# of 31, lower than the Mg#s of most other mafic rocks in the dataset, and sample #146 has a Mg# of 39, comparable to other diorite samples. The REE patterns of these samples resemble REE patterns of IATs (Figure 4.20), although they do not exhibit the depletion in the most incompatible elements (La, Ce, Pr) that is characteristic of some IATs (e.g. Swinden *et al.* 1997), and their negative Nb anomalies are not well-developed. It is likely that the rocks in this group, like IATs, represent N-MORB or E-MORB-type sources that have been contaminated by fluid or melt from a subducting slab or by continental crust during ascent. Because these rocks are not as enriched in incompatible elements as the rocks in Group 6, and do not display well-developed negative Nb anomalies, like the rocks in Groups 5 and 6, they appear to have received less crustal or subduction-related contamination.

4.8.2.6. Group 5: IAT-like REE patterns

The rocks in this group a hornblende basaltic dyke (#60), three basaltic-andesitic dykes (#143, 181, 194), two diorite samples (#77, 184), two andesitic dykes (#55, 59) and three oxide-rich andesitic dykes (#56, 79, 145). These rocks share well-developed negative Nb anomalies and, like Group 4, have LREE-enriched REE patterns with slopes intermediate between the REE patterns of Groups 1 and 2 and those of Group 6. They have La/Yb values that range from 4.2 to 6.6, plot in the arc field in Figure 4.19a and have a wide range of Mg#s (24 to 45). The rocks in this group plot within or along the edge of the arc field defined by Condie (1997) in Figure 4.19b and they exhibit REE patterns that are comparable to those of IATs (Figure 4.20). Like IATs, the rocks in this group may have originated from mantle sources that were contaminated in a subduction zone or during ascent through continental crust.

The ϵNd values of a basaltic-andesitic dyke (#181) and diorite (#184) from this group are +4.5 and +4.8, respectively, which are intermediate between the low ϵNd value of an andesitic dyke (#89; +4.1) and the high ϵNd value of the other diorite sample (#105; +6.4), which is thought to represent magmatism from the depleted mantle. With T_{DM} values (DePaolo, 1981) of 865 Ma and 787 Ma, respectively, these samples may have mixed with older sources. The Nd isotopic data, together with the LREE-enrichment and negative Nb anomalies displayed by these samples, suggest that they represent mantle sources that have been contaminated by continental crust or by a subducting slab. As mentioned above, the similar ϵNd and T_{DM} values of these rocks and a rhyolitic dyke (#141) indicate that all three rocks may have had similar mixed sources.

4.8.2.7. Group 6: CAB-like REE patterns

The rocks in this group are distinguished by steeply sloped, LREE-enriched REE patterns and well-developed negative Nb anomalies and most of the samples also display negative Ti anomalies. This group includes eight andesitic dykes (#89, 96, 103, 104, 152, 167, 175, 203), two hornblende-porphyritic andesitic dykes (#100, 138), and and oxide-rich andesitic dyke (#57). The rocks in this group plot in the arc field in Figure 4.19 and have high La/Yb values (7.1 to 9.3) and relatively low Mg#s (less than 33), except for samples #96, 103 and 138, which have higher Mg#s and represent less fractionated melts. There is a strong resemblance between the REE patterns exhibited by the rocks in this group and those of calc-alkalic basalts and andesites (CABs) (Figure 4.20). Likewise, samples in this group probably represent partial melting of subduction-contaminated mantle sources or mantle sources that have been significantly contaminated by continental crust during ascent.

The low ϵNd value of +4.1 for sample #89 and its T_{DM} value (851 Ma), together with a LREE-enriched REE pattern with a strong negative Nb anomaly, imply that the melt that formed this andesitic dyke mixed with an older, LREE-enriched source, such as continental crust. This is plausible, especially given the presence of inherited zircon in fraction Z3 of geochronology sample #209, which was collected from the same andesitic dyke as sample #89. However, the andesitic melt may have collected older zircon through stoping of minor amounts of crustal material, and crustal contamination during ascent may not have been significant. Instead, the relatively low ϵNd value and old T_{DM} value of the andesitic dyke may be due to contamination by continentally derived sediments in a subduction zone.

4.8.2.8. Geochemistry of mafic-to-intermediate rocks in the HCC: A summary

An important outcome of the geochemical data is that, in several cases, samples collected from a given rock unit in the HCC do not appear to be co-magmatic or co-genetic, despite similarities in lithology and petrography. For example, the samples collected from diorite form two geochemically distinct groups that may represent two unrelated intrusions: four samples from the east side of Map 1 appear to have E-MORB-like sources, whereas three samples from Map 2 and the west side of Map 1 are LREE-enriched and have negative Nb anomalies. As well, samples collected from basaltic dykes, hornblende basaltic dykes, basaltic-andesitic dykes and oxide-rich andesitic dykes exhibit variable geochemistry.

Nevertheless, samples collected from some rock units are geochemically similar and appear to be co-magmatic. For example, data from all samples of gabbro form a cluster on major and trace element variation diagrams, and exhibit overlapping REE patterns. As well, most of the andesitic dyke samples (#89, 96, 152, 167, 175, 203) have similar major and trace element geochemistry and parallel REE patterns, indicating that many andesitic dykes in Maps 1 and 2 are probably from the same liquid batch.

Another outcome of the trace element and Nd isotopic data is that some samples share geochemical similarities, and potential petrogenetic relationships, with samples collected from other rock units. For example, there are numerous samples from different rock units that exhibit relatively flat, E-MORB-like REE patterns (Groups 1 and 2). Most of these samples do not exhibit negative Nb anomalies, but some samples exhibit very weakly developed negative Nb anomalies that are within analytical uncertainty. Several rocks from Groups 1 and 2 not only appear to share similar, E-MORB-like sources, but

also have similar major and trace element geochemistry. For example, some diorite samples (#102, 105, 131, 133) and hornblende basaltic dykes (#78, 99, 132) plot close together on major and trace element variation diagrams. This suggests that the dykes may be offshoots from the diorite intrusion. Relative to other rocks in Groups 1 and 2, gabbro samples have the highest Mg#s and are elevated in Al_2O_3 and depleted in FeO*, TiO_2 and several incompatible elements (Y, Zr, La, Nb, Th). Therefore, gabbro may represent a more primitive melt that is related by fractionation. Some basaltic dykes (#53, 84) and oxide-rich basaltic dykes (#64, 129) have lower Mg#s and are elevated in Y, Nb, Zr, Th and V compared to other samples with E-MORB-like REE patterns. Therefore, they may represent more evolved melts that are related by fractionation. The basaltic-andesitic dykes (#91, 155) in Group 2 are slightly LREE-enriched relative to the other rocks in Groups 1 and 2, and may not be related by fractionation. Even if the rocks in Groups 1 and 2 are from melts that are not co-magmatic, they all appear to have depleted mantle sources that have undergone minor LREE-enrichment, and they represent a suite of rocks in the HCC with E-MORB-like geochemistry. This interpretation is supported by the high εNd values of gabbro (#82; +5.6) and diorite (#105; +6.4), which are close to that of contemporaneous depleted mantle (+6.8; DePaolo, 1981).

In addition to numerous rocks that exhibit E-MORB-like geochemistry, there are many dykes of andesitic composition in the study area that exhibit pronounced LREE-enrichment and negative Nb anomalies and also have similar major and trace element compositions. These are the rocks of Group 6 and one from Group 5 (#145). The hornblende-porphyritic andesitic dykes and many of the andesitic dykes (#89, 96, 152, 167, 175, 203) exhibit parallel extended REE patterns and have very similar major and

trace element compositions, suggesting that they are co-magmatic and may be related by fractionation. The anomalously high Mg# of sample #138 implies that it has undergone less fractionation than the other samples. Relative to this group, the other andesitic dykes (#55, 59, 103, 104) and the oxide-rich andesitic dykes (#57, 145) exhibit minor enrichment or depletion in the HREE or LREE, indicating different petrogenetic histories. Nevertheless, as a group, the andesitic dykes, the hornblende-porphyritic andesitic dykes and some of the oxide-rich andesitic dykes (#57, 145) all exhibit similar, LREE-enriched REE patterns with well-developed negative Nb anomalies, and have similar major and trace element geochemistry. Therefore, these rocks appear to represent a suite of calc-alkaline andesites that share similar, subduction- or continental crust-contaminated mantle sources. This theory is supported by the relatively low εNd value of sample #89 (+4.1).

Several rocks in the dataset exhibit REE patterns with slopes that are intermediate between those of the E-MORB-like samples and those of calc-alkaline andesites. These rocks appear to represent melts from depleted mantle sources that have undergone LREE-enrichment via mantle upwelling or various degrees of mixing or assimilation with continental crust or subduction-contaminated mantle. Rocks in Group 3, which display OIB-like REE patterns, generally plot with rocks that have E-MORB-like REE patterns on major and selected trace element variation diagrams. Compared to rocks with E-MORB-like REE patterns, the rocks in Group 3 exhibit enriched LREE relative to the HREE, which suggests that they represent melts of depleted mantle sources that received LREE-enrichment. This interpretation is supported by Nd isotopic data for sample #74, which has an εNd value of +6.3, very close to the εNd of contemporaneous depleted mantle (+6.8). Rocks in Group 4 and 5 are LREE-enriched and exhibit weak to strong

negative Nb anomalies, but their REE patterns are not as steeply sloped as those of Group 6. These rocks appear to represent melts of the depleted mantle that have mixed with or assimilated continental crust or partial melts of a subduction-contaminated mantle wedge, but to a lesser extent than the suite of calc-alkaline andesites. As a result, these rocks exhibit IAT-like REE patterns. The similar εNd values of samples #181 and 184 (+4.5 and +4.8, respectively) suggest that these rocks share similar mixed sources.

4.9. Geochemical implications for the tectonic setting of the Horse Cove Complex

As shown by field relationships and U/Pb geochronology, granodiorite is either the *in situ* host rock for subsequent magmatism in the HCC or represents blocks that were transported tectonically or magmatically from an older intrusion. Geochemical data illustrate that granodiorite is probably a volcanic arc-related intrusion but its age links it to an older magmatic cycle. It is not related to the ca. 580 Ma rocks in the HCC.

As discussed in Chapter 3, the younger rocks in the study area are bracketed between the U/Pb ages of feldspar porphyry at 580.6 ± 2.0 Ma and an andesitic dyke at 578.4 ± 2.3 Ma. Cross-cutting relationships show that these rocks follow an overall progression from rocks with E-MORB-like signatures, including gabbro and some of the diorite samples, to rocks with volcanic arc geochemical signatures, such as the andesitic dykes. However, there are some notable exceptions to this general trend. For example, feldspar porphyry exhibits volcanic arc geochemical signatures and hosts many dykes in the study area, and may also be older than gabbro, diorite and dykes that have E-MORB- or OIB-like REE patterns. Furthermore, an E-MORB-like hornblende-basaltic dyke in Map 2 (#78) cross-cuts LREE-enriched diorite (#77) and an oxide-rich andesitic dyke

(#79) that have negative Nb anomalies. In addition, basaltic-andesitic dykes with E-MORB-like REE patterns (#91, 155) cross-cut andesitic dykes that have arc signatures (#89, 138).

The paleo-tectonic environment of the HCC was one where melts from the depleted mantle and melts that were contaminated by continental crust or by subduction processes were emplaced side-by-side and closely spaced in time. A possible tectonic setting for the HCC is a back-arc basin, in which melts may have been extracted from the depleted mantle through rifting in the older, arc crust. Mantle upwelling may have provided LREE-enrichment to melts from the depleted mantle, giving many of the rocks in the study area E-MORB-like and OIB-like REE patterns. Partial melts of the subduction-contaminated mantle wedge may have produced LREE-enriched magmas with depleted Nb relative to Th, ultimately producing the multitude of rocks in the study area with arc and transitional-arc signatures. Neodymium isotopic data from some of these rocks suggest that partial melts of the subduction-contaminated mantle wedge pooled to produce one magma that fractionated to produce rocks of different compositions. Although it is possible that the melts that formed the HCC acquired their transitional arc and arc signatures solely from partial melts of the subduction-contaminated mantle wedge, they may have received negative Nb anomalies and additional LREE-enrichment by assimilating continental crust during ascent through the rifted back-arc basin.

Alternatively, the arc signatures displayed by many of the rocks may have been acquired solely via contamination of mantle-derived melts during ascent through continental crust. Intracontinental rifting may have tapped partial melts of the depleted

mantle, resulting in rocks with E-MORB-like REE patterns and high εNd values. Some melts may have assimilated continental crust during their ascent, resulting in εNd values ranging from +4.1 to +4.8, negative Nb anomalies and LREE-enrichment. Some rocks, including those with εNd values from +4.5 to +4.8, may have originated from the same crustally contaminated magma, which fractionated to produce rocks of different compositions. Other rocks, including the andesitic dyke with εNd = +4.1, appear to have undergone more extensive crustal contamination, or have been contaminated by crust with a different composition, than rocks with higher εNd values (+4.5 to +4.8) and less LREE-enrichment. It is also possible that the LREE-enriched rocks with negative Nb anomalies and εNd values ranging from +4.1 to +4.8 were sourced from a part of the mantle that was affected by an ancient subduction zone, and that this old, deep arc mantle was accessed by mantle upwelling during intracontinental rifting.

4.10. Geochemical comparison of the rocks in this study with selected rocks on the NE Avalon Peninsula

4.10.1. The granodiorite at Bauline and ca. 620 Ma felsic plutonic rocks

Felsic plutonic rocks on the NE Avalon Peninsula include the Holyrood Intrusive Suite (HIS), which is located predominantly in the central portion of the Holyrood Horst, and the White Hills Intrusive Suite (WHIS), which occurs on the eastern margin of the Holyrood Horst. Due to their geochemical similarities and overlapping U/Pb zircon ages, the WHIS is interpreted to be cogenetic with the principal granite phases of the HIS in the Holyrood Horst (Sparkes, 2005). Based on whole rock geochemistry and field relationships, HIS granite from west of the Topsail Fault has been correlated to granite

from east of the Topsail Fault (Sparkes, 2006; Sparkes *et al.,* 2007). Furthermore, pink, white and green-weathering granite occurs locally near Bauline, and correlates to the HIS (Sparkes, 2006). According to previous studies (e.g. King, 1990; Sparkes, 2005; Sparkes *et al.,* 2007), the HIS rocks were emplaced in the volcano-plutonic arc system that was active at about 620 Ma in the region of the Holyrood Horst.

The 625 ± 1.4 Ma U/Pb zircon age of the granodiorite in the study area overlaps, within uncertainties, with established U/Pb zircon ages of rocks in the HIS, including the 622.5 ± 1.3 Ma pink, white and green granite dated by Sparkes (2005; modified after O'Brien *et al.,* 2001) and the 622 ± 2 Ma Butler's Pond Porphyry dated by Sparkes *et al.* (2002). The U/Pb zircon ages of WHIS monzonite (623.5 ± 3.5 Ma; Sparkes, 2005) and quartz-feldspar porphyry (625 ± 2.5 Ma; Sparkes, 2005) also overlap, within uncertainties, with the age of the granodiorite at Bauline. Lithological similarities, together with overlapping U/Pb zircon ages, imply a co-genetic relationship between the HIS, WHIS and the granodiorite at Bauline.

Many whole-rock geochemical samples were collected from the HIS and WHIS during mapping studies carried out separately by S. O'Brien and G. Sparkes of the Geological Survey of Newfoundland and Labrador. The major and trace element concentrations of the HIS and WHIS samples were measured using the ICP-ES technique at the geochemical lab at the Geological Survey of Newfoundland and Labrador (Sparkes, 2005; Sparkes *et al.,* 2007). Forty seven samples were analysed from the HIS granite and three samples were analysed from HIS granodiorite intrusions that are interpreted to be co-genetic with the HIS granite but are not related through typical chemical fractionation

(Sparkes *et al.*, 2007). Seven quartz-feldspar porphyry samples and twenty-five granite samples were analysed from the WHIS.

On the classification plot of Winchester and Floyd (1977), data from the WHIS, HIS and the granodiorite from Bauline plot mostly in the rhyolite field, although some samples from each unit plot in the rhyodacite/dacite field. Major element XY plots (Figure 4.21a-c) show that the Bauline granodiorite has major element compositions that are similar to the HIS granite and WHIS, except the Bauline granodiorite is comparatively enriched in Na_2O, TiO_2 and CaO, and depleted in K_2O. Relative to the HIS granodiorite, the Bauline granodiorite is significantly enriched in SiO_2 and Na_2O and depleted in MgO, Al_2O_3, FeO, K_2O, TiO_2 and P_2O_5. The Bauline granodiorite and the HIS and WHIS data define broad, overlapping compositional fields on trace element XY plots and generally have similar Zr, La, Y (Figure 4.21d) and Nb contents. The rocks from the Bauline granodiorite, the HIS and WHIS exhibit similar enrichment in the LILE relative to the HFSE and they all plot in the volcanic arc granite field on the tectonic discrimination diagram of Pearce *et al.* (1984; Figure 4.22a). The steeply sloping extended REE patterns of three samples of HIS granite and three samples of WHIS granite (Sparkes, 2005) overlap with and are nearly parallel to the extended REE patterns of most of the granodiorite samples from Bauline (Figure 4.22b).

Enrichment in the LILE and LREE relative to the HFSE and HREE, together with Y and Nb compositions that are similar to those of the volcanic arc granites of Pearce *et al.* (1984), suggests that the Bauline granodiorite and HIS and WHIS were all derived from a volcanic arc setting. Nevertheless, some differences in major and trace element geochemistry suggest that they may not be co-magmatic. Because the Bauline

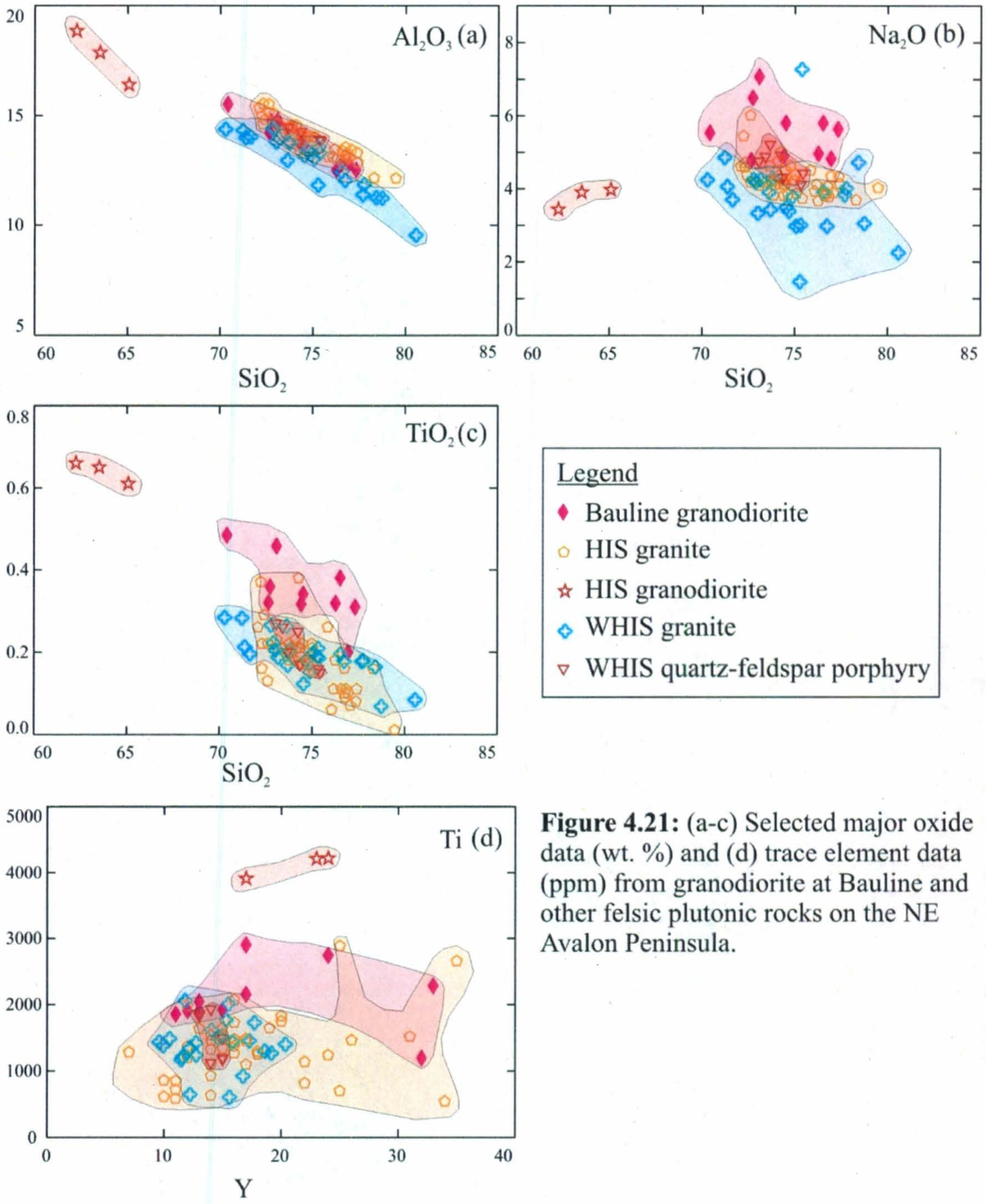

Figure 4.21: (a-c) Selected major oxide data (wt. %) and (d) trace element data (ppm) from granodiorite at Bauline and other felsic plutonic rocks on the NE Avalon Peninsula.

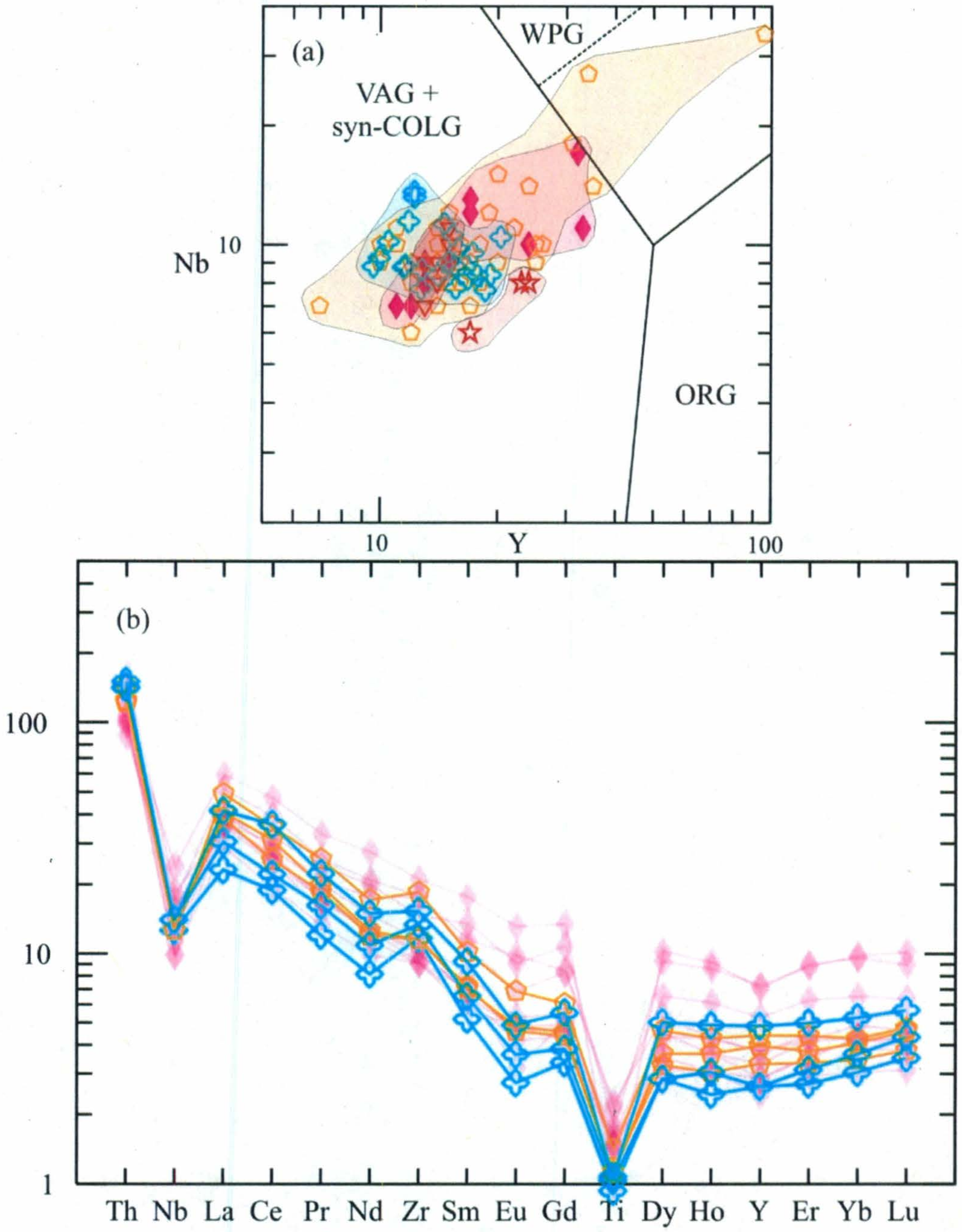

Figure 4.22: (a) Data from the granodiorite at Bauline and other felsic plutonic rocks on the NE Avalon Peninsula plotted on the tectonic discrimination diagram of Pearce *et al.* (1984). WPG=within-plate granites, ORG=ocean-ridge granites, VAG=volcanic-arc granites, syn-COLG=syn-collisional granites. The dotted line is the boundary for the field of ORG from anomalous ridges; (b) Extended REE patterns for three samples from the HIS granite and three samples from the WHIS granite, normalized to the primitive mantle values of Sun and McDonough (1989). REE patterns of the granodiorite from Bauline are shown in the background. Symbols are as in Figure 4.21.

granodiorite has a higher Ti content than the HIS granite and the WHIS rocks, and a lower Ti content than the HIS granodiorite, but has a similar Y content, the Bauline granodiorite does not appear to be related to the HIS and WHIS rocks through typical chemical fractionation. This interpretation is supported by XY plots of immobile-compatible elements, on which the Bauline granodiorite data do not lie on a fractionation line with data from the HIS and WHIS. Like the HIS granodiorite, the Bauline granodiorite may represent an intrusion that is co-genetic with the HIS and WHIS, and may be related to the same ca. 620 Ma volcanic arc as the HIS and WHIS. However, it appears to be from a separate source or has undergone a different geochemical history.

4.10.2. HCC rhyolitic dykes, HCC feldspar porphyry and post-620 Ma felsic rocks

On the NE Avalon Peninsula, several felsic magmatic rocks have been mapped by G. Sparkes and S. O'Brien of the Geological Survey of Newfoundland and Labrador. These include flow-banded rhyolite at Cape St. Francis and in the Manuels Volcanic Suite (MVS) and the White Mountain Volcanic Suite (WMVS). As well, feldspar porphyry intrudes mafic volcanic and marine sedimentary rocks in the Wych Hazel Pond Complex (WHPC). In addition to being lithologically similar, some of these rocks have U/Pb ages that overlap, within uncertainties, with those of the 580.6 ± 2.0 Ma feldspar porphyry and the 581.7 ± 1.9 Ma rhyolitic dyke mapped at Bauline. For instance, the Fowler's Road Porphyry in the WHPC was dated at 585 ± 5 Ma (Sparkes, 2005) and the Farmer's Field Rhyolite in the MVS was dated as 584 ± 1 Ma (Sparkes *et al.*, 2005). In the WMVS,

there is no age data for rhyolite, but a welded ash-flow tuff was dated at 616 ± 2 Ma (Sparkes, 2005).

Whole rock geochemical data from several of these felsic rocks are presented and described in Sparkes (2005) and Sparkes *et al.* (2007). The data were measured using the ICP-ES technique at the geochemical laboratory of the Geological Survey of Newfoundland and Labrador. Geochemical samples include: 12 samples from feldspar porphyry in the WHPC; 22 samples from rhyolite in the WMVS; 24 samples from rhyolite in the MVS; and 8 samples from rhyolite near Cape St. Francis. Extended REE data exist for only 3 samples of flow-banded rhyolite from the WMVS, collected along the eastern margin of the Holyrood Horst near Manuels, south of Bauline. Extended REE data for 3 felsic rocks collected from the Cripple Cove area near Cape St. Francis were provided by J. Hanchar from the Department of Earth Sciences, Memorial University of Newfoundland, and were measured at Actlabs using the fusion dissolution ICP-AES technique for major elements and the fusion dissolution ICP-MS method for trace elements. Samples from Cripple Cove include a dacitic dyke, a flow-banded rhyolite and an associated ash-flow tuff.

Most of the rhyolite and feldspar porphyry data from the HCC, WMVS, MVS, WHPC and the Cape St. Francis area plot in the rhyolite field on the Zr/TiO_2 vs. SiO_2 plot of Winchester and Floyd (1977), although some samples from each unit plot in the rhyodacite/dacite field. Similarities in major element chemistry between rhyolite and feldspar porphyry from Bauline and from elsewhere in the NE Avalon region are shown by their overlapping compositional fields on major element XY plots. These data fields are generally broad, but on plots of SiO_2 against immobile major elements, including

Al_2O_3 and TiO_2, the data field of each unit defines a linear igneous differentiation trend that overlaps with similar trends defined by the other units.

Although there is significant variation among the trace element compositions of samples from each of the rhyolite and feldspar porphyry units, both the rhyolite and feldspar porphyry samples from the NE Avalon region and those collected from the Bauline area generally exhibit enrichment in the LILE relative to the HFSE. On the Y vs. Nb tectonic discrimination plot of Pearce *et al.* (1984; Figure 4.23a), samples from feldspar porphyry in the WHPC, as well as rhyolite samples from Cape St. Francis and the WMVS and MVS, plot predominantly in the volcanic arc and syn-collisional granite field, similar to the rhyolitic dykes and feldspar porphyry from Bauline.

The sample collected from a dacitic dyke in Cripple Cove has an extended REE pattern that is parallel to and overlaps with the REE patterns of the rhyolitic dykes at Bauline (Figure 4.23b). In addition, two rhyolite samples from the WMVS have extended REE patterns that overlap with and are nearly parallel to those of feldspar porphyry and rhyolitic dykes from Bauline, as well as the dacitic dyke from Cripple Cove. All these samples have well-developed negative Nb anomalies and are enriched in the LREE relative to the HREE.

Due to the broad major and trace element data fields exhibited by feldspar porphyry and rhyolitic dykes in the NE Avalon region, and the limited extended REE data, geochemical trends and similarities are not easily identified. For rocks collected outside of Bauline, the range in major and trace element compositions among samples in each unit may be a result of low sampling density spread over a 25 km long area, both east and west of the Topsail Fault. Furthermore, variations in major element

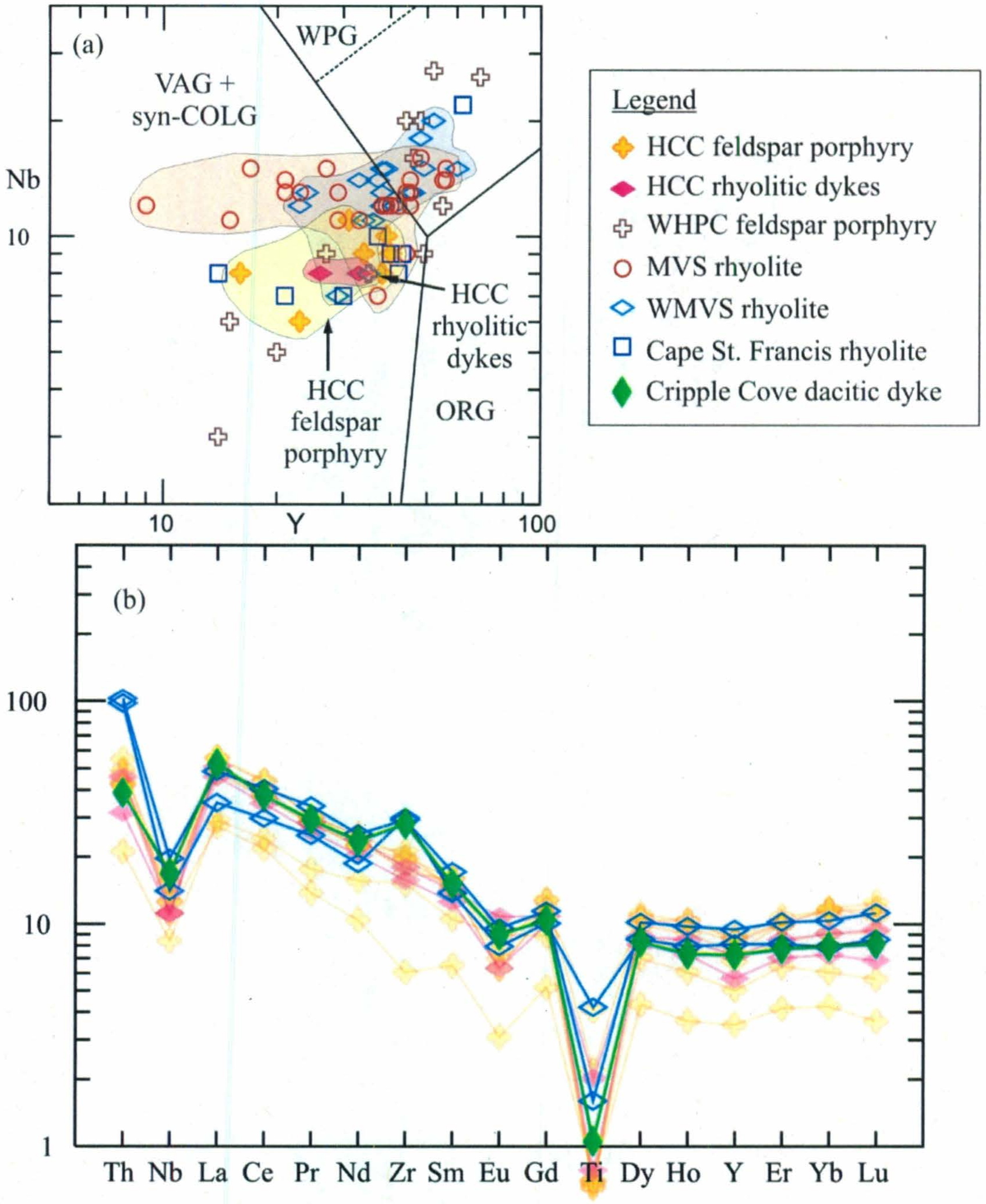

Figure 4.23: (a) Data from the HCC feldspar porphyry, HCC rhyolitic dykes and selected felsic rocks on the NE Avalon Peninsula plotted on the tectonic discrimination diagram of Pearce *et al.* (1984). Compositional fields are as in Figure 4.22a. (b) Extended REE patterns of two samples from the WMVS flow-banded rhyolite and one sample from a dacitic dyke from Cripple Cove. REE patterns of the HCC feldspar porphyry and rhyolitic dykes are shown in the background. Data are normalized to the primitive mantle values of Sun and McDonough (1989).

compositions may be due to the effects of alteration or, in the case of feldspar porphyry and feldspar-porphyritic rhyolite samples, as a result of different abundances and compositions of feldspar phenocrysts. Differences in immobile trace element data may be attributed to the fractionation of accessory minerals, such as zircon, that incorporate trace elements that are otherwise incompatible.

Nevertheless, enrichment in the LILE relative to the HFSE, together with the Y vs. Nb plot of Pearce *et al.* (1984), suggests that rhyolite and feldspar porphyry in the Bauline area and elsewhere in the NE Avalon region formed in a volcanic arc setting. For rocks with extended REE data, this interpretation is supported by enrichment in the LREE relative to the HREE and strong negative Nb anomalies. In addition, since the rhyolitic dykes and feldspar porphyry from Bauline exhibit REE patterns that overlap with and are nearly parallel to those of dacite from Cripple Cove and the WMVS, they may share the same arc-related source. Since a welded ash-flow tuff from the WMVS was dated at 616 ± 2 Ma (Sparkes, 2005), the WMVS rhyolite may also be as much as 38.2 Ma older than the rhyolitic dyke at Bauline. Therefore, rhyolite and feldspar porphyry on the NE Avalon Peninsula appear to share similar arc-related sources over a distance of about 35 km, and over a period of about 40 Ma.

This hypothesis supports interpretations made in previous studies regarding felsic volcanic rocks on the NE Avalon Peninsula. For instance, felsic volcanic rocks throughout the NE Avalon region range in age from 730 to 580 Ma and yet they display similar geochemistry, including LILE-enriched trace element patterns that suggest prolonged magmatism from volcanic arc source regions (Sparkes, 2005; Sparkes *et al.*, 2007). It is important to note, however, that even though the felsic volcanic rocks are

geochemically similar to the arc-related HIS, geochronology and field relationships indicate that the HIS does not represent the magmatic roots of the MVS, although it may be coeval and co-magmatic with the WMVS (Sparkes *et al.*, 2005). In addition, the WHPC feldspar porphyry is geochemically unrelated to the HIS quartz-feldspar porphyry, although some feldspar porphyry intrusions display arc-related signatures (Sparkes *et al.*, 2005). Similarly, as discussed above, the rhyolitic dykes and feldspar porphyry in the HCC are not co-magmatic or co-genetic with the granodiorite at Bauline.

4.10.3. Mafic-to-intermediate rocks in the HCC and on the NE Avalon Peninsula

As mentioned in Chapter 1, several mafic-to-intermediate rocks were mapped along the east coast of Conception Bay by G. Sparkes of the Geological Survey of Newfoundland and Labrador. On both sides of the Topsail Fault, the WHPC includes epidote-rich basalt and younger, hematite-rich pillowed basalt, and the dyke swarm in the HCC is predominantly hosted by the mafic volcanic rocks of the WHPC (Sparkes, 2006). The Herring Cove Diorite (HCD) intrudes epidote-rich basalt and siliciclastic sedimentary rocks of the WHPC east of the Topsail Fault, and it locally hosts mafic-to-felsic dykes associated with the HCC (Sparkes, 2006). The NE Avalon region also includes gabbroic intrusions, known as the Beaver Hat Intrusive Suite (BHIS), which represent the youngest known intrusive event in the region. Sparkes *et al.* (2007) interpreted that the HCD and BHIS were co-genetic and share an arc-related source, similar to the older HIS (Sparkes *et al.*, 2007). Mafic-to-intermediate dykes also occur in abundance along the east coast of Conception Bay in the dyke swarm that characterizes the HCC (Sparkes, 2006).

Whole rock geochemical data from several mafic-to-intermediate rocks on the NE Avalon Peninsula are described and interpreted in Sparkes *et al.* (2007). Major and trace element concentrations were analyzed using the ICP-ES in the geochemical laboratory at the Geological Survey of Newfoundland and Labrador. Geochemical samples include: 12 epidote-rich basalt samples and 4 hematite-rich basalt samples from the WHPC; 3 HCD samples; 6 BHIS samples; and 17 mafic-to-intermediate dykes. The lack of extended REE data limits the correlations that may be drawn between these samples and the mafic-to-intermediate rocks at Bauline. Instead of the La/Yb ratio that was used to characterize the mafic-to-intermediate rocks in the study area, La/Y is used as a measure of enrichment of the LREE relative to the HREE.

4.10.3.1. The WHPC hematite-rich basalt

The WHPC hematite-rich basalt shares some geochemical similarities with gabbro in the HCC at Bauline. Both units are high-Mg tholeiites according to the classification plot of Jensen (1976; Figure 4.24), and both units have low La/Y ratios (Figure 4.25a). Hence, the WHPC hematite-rich basalt has low enrichment of the LREE relative to the HREE and therefore, like the HCC gabbro, has E-MORB-like geochemistry. As well, unlike any other rocks in the HCC, the gabbro from Bauline and the hematite-rich basalt in the WHPC plot in the MORB/volcanic arc basalt field on the Zr vs. Zr/Y plot of Pearce and Norry (1979; Figure 4.25b). Furthermore, the hematite-rich basalt and HCC gabbro share low SiO_2 contents, high Mg#s and elevated Cr and Ni contents relative to the mafic-to-intermediate rocks in the study area, which indicates a low degree of fractionation. Thus, the gabbro that was mapped as the host rock to the dyke swarm in Map 2 at Bauline may be co-genetic with the WHPC hematite-rich mafic rocks that were mapped on a

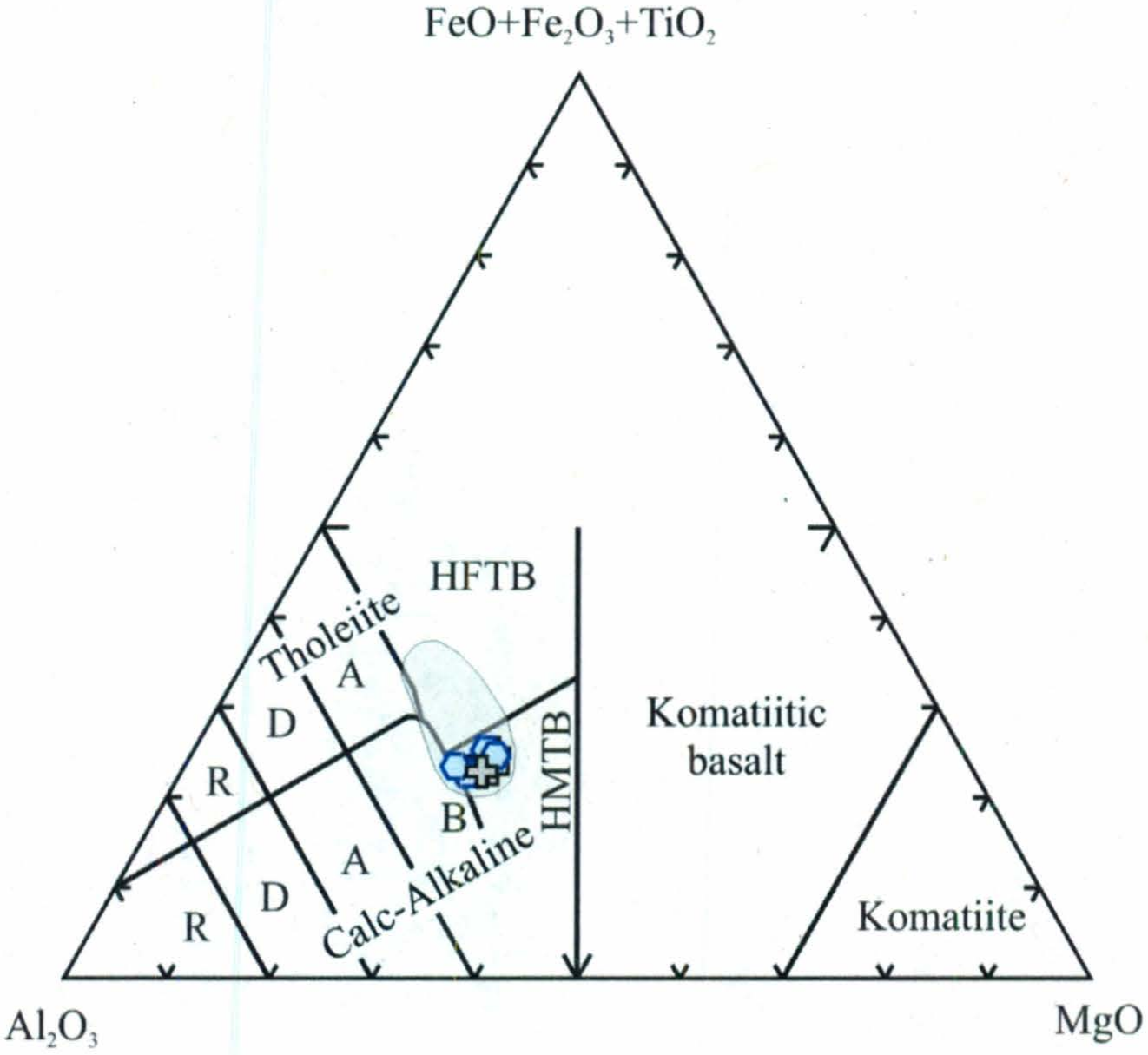

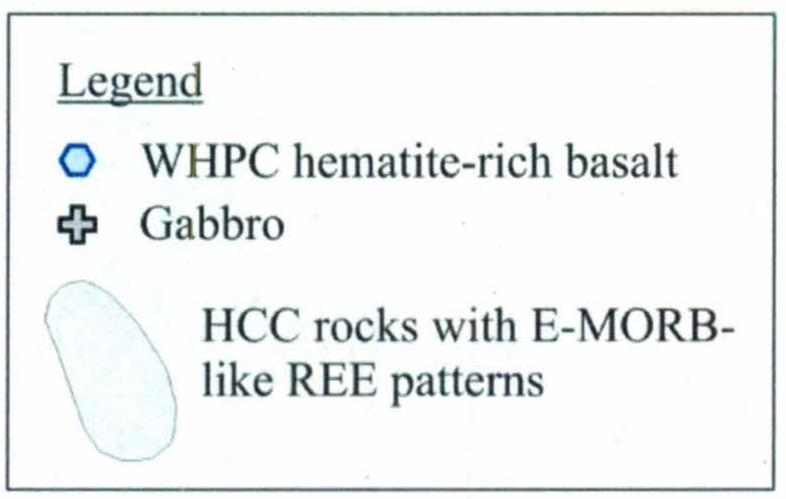

Figure 4.24: Classification plot of Jensen (1976), showing data from the WHPC hematite-rich basalt and the HCC gabbro. HFTB=high-Fe tholeiite basalt; HMTB=high-Mg tholeiite basalt; A=andesite; B=basalt; D=dacite; R=rhyolite.

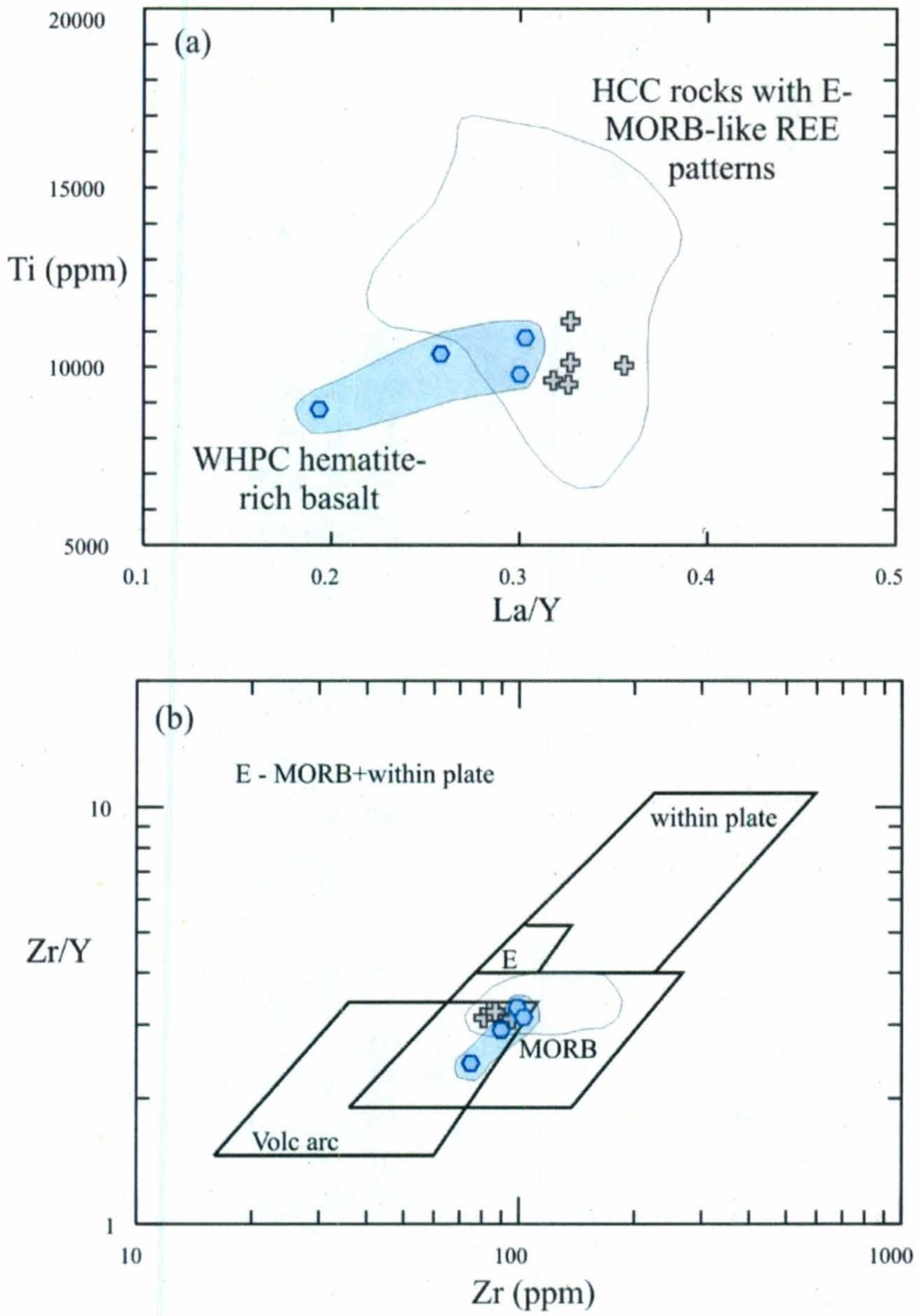

Figure 4.25: Data from the WHPC hematite-rich basalt and the HCC gabbro plotted on (a) a diagram of Ti against La/Y, and (b) the Zr/Y-Zr discrimination diagram for basalts of Pearce and Norry (1979). Volc arc=volcanic-arc basalts, within-plate=within-plate basalts, E=MORB and within-plate basalts. Symbols are as in Figure 4.24.

regional scale by G. Sparkes along the east coast of Conception Bay. Furthermore, since pillow structures are present in the WHPC hematite-rich basalt (Sparkes, 2006), the gabbro at Bauline may be volcanic. However, the lack of such features in the study area suggests that the gabbro at Bauline is a shallow-level intrusion, such as a volcanic sill.

As discussed above, some samples from diorite, basaltic dykes and hornblende basaltic dykes in the HCC at Bauline have E-MORB-like REE patterns, similar to gabbro. Therefore, these rocks may also be genetically related to the hematite-rich basalt in the WHPC. Furthermore, the dykes may represent feeder conduits to the hematite-rich basalt in the WHPC, as suggested by Sparkes *et al.* (2007).

4.10.3.2. The HCD, BHIS and WHPC epidote-rich basalt

On the classification diagram of Jensen (1976; Figure 4.26), datasets from the WHPC epidote-rich basalt, the HCD and the BHIS each form broad clusters that overlap with each other and span several compositional fields, including the calc-alkaline andesite and basalt, tholeiitic andesite and high-Mg and -Fe tholeiite basalt fields. Rocks units in the HCC that form similar data fields on the Jensen (1976) cation plot include diorite, basaltic-andesitic dykes and hornblende basaltic dykes. The epidote-rich basalt in the WHPC, the HCD and the BHIS exhibit La/Y values that are mid-range between the low La/Y values of the hematite-rich basalt and the HCC gabbro, and the high La/Y values of the HCC andesitic dykes (Figure 4.27a). The La/Y values of the epidote-rich basalt, the HCD and the BHIS are similar to those of several dykes in the HCC, including the basaltic-andesitic dykes and some of the oxide-rich andesitic dykes and hornblende-basaltic dykes. On the Zr vs. Zr/Y plot of Pearce and Norry (1979; Figure 4.27b), the WHPC epidote-rich basalt, HCD and BHIS plot mostly in the MORB/within-plate basalt

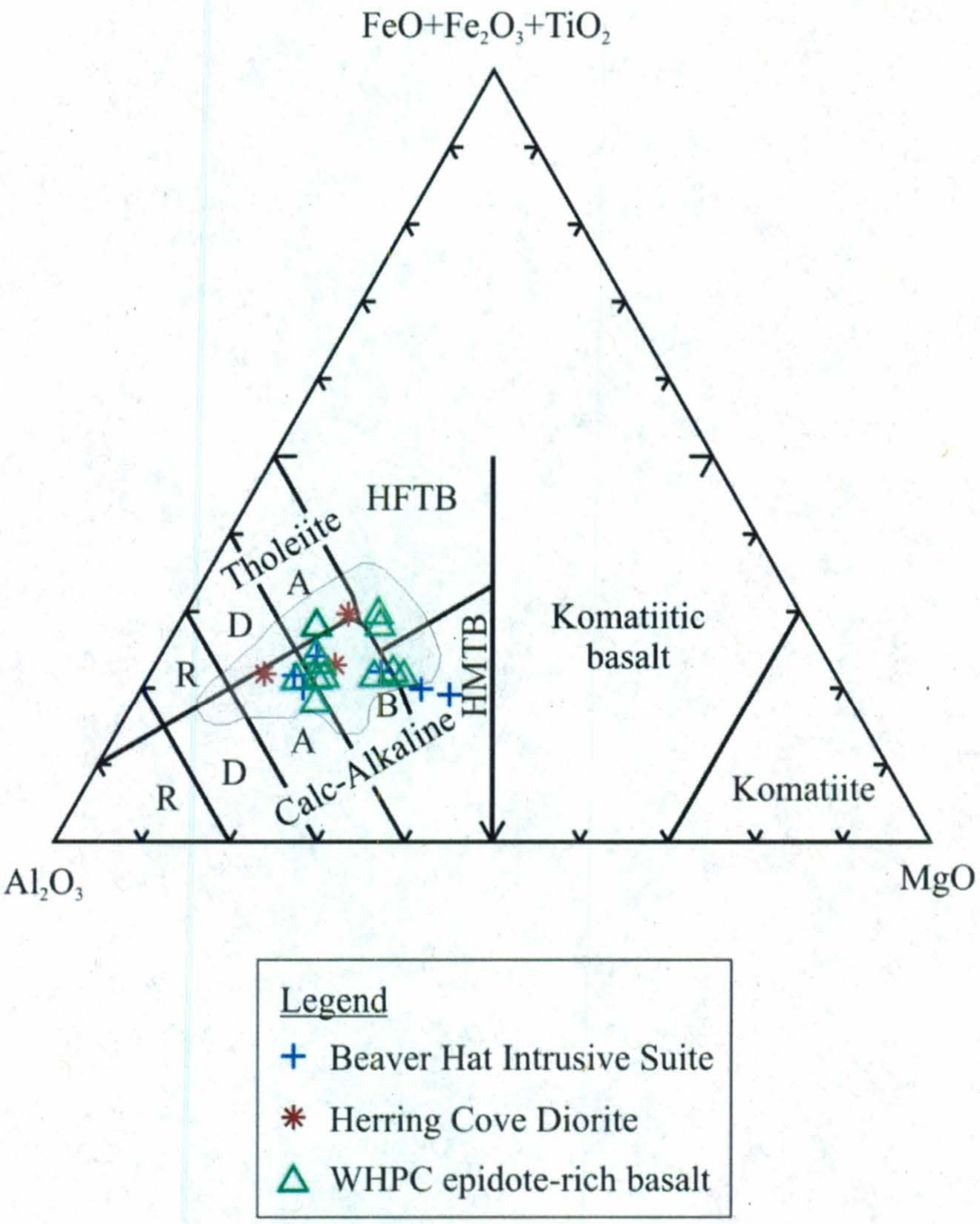

Figure 4.26: Data from the HCD, BHIS and the WHPC epidote-rich basalt plotted on the classification plot of Jensen (1976), with compositional fields as in Figure 4.24: Light grey shading indicates the compositional field of the mafic-to-intermediate rocks from the HCC at Bauline.

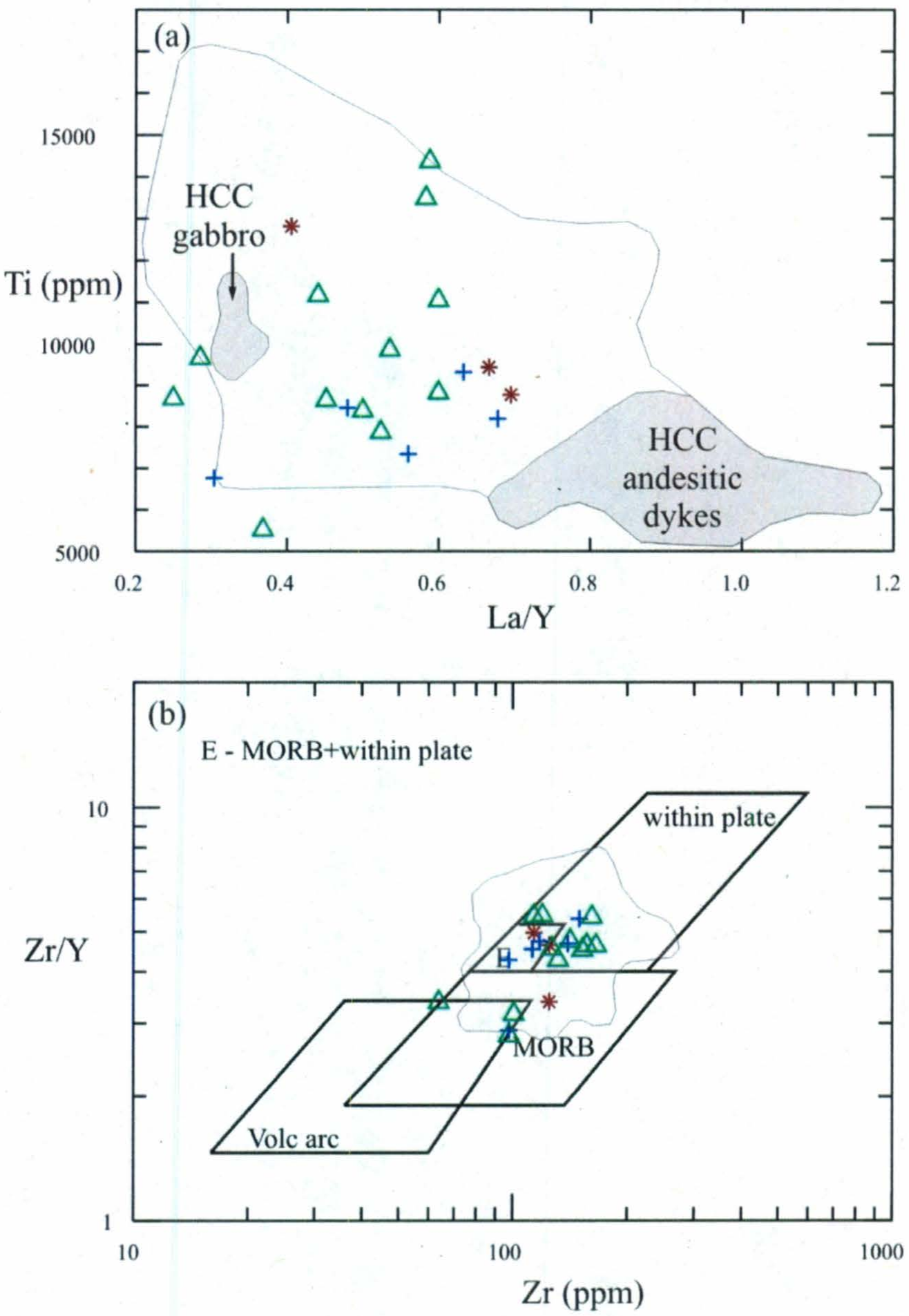

Figure 4.27: Data from the HCD, BHIS and the WHPC epidote-rich basalt plotted on (a) a diagram of Ti against La/Y, and (b) the Zr/Y-Zr discrimination diagram for basalts of Pearce and Norry (1979), with compositional fields as in Figure 4.25b. Symbols are as in Figure 4.26. Light grey shading indicates the compositional field of the mafic-to-intermediate rocks in the HCC at Bauline.

field, along with some of the diorite samples and hornblende basaltic, andesitic and oxide-rich andesitic dykes in the HCC at Bauline.

The epidote-rich basalt in the WHPC, the HCD and the BHIS are each characterized by small sample sets that define broad data fields. While these datasets overlap with data from several units in the HCC, none of them appears to exhibit a trend or similarities with any one rock unit in particular. Out of all the rocks in the HCC, the major and trace element compositions of the WHPC epidote-rich basalt, the HCD and the BHIS seem to be most similar to those of mafic-to-intermediate dykes that have either OIB-like REE patterns or LREE-enriched REE patterns with arc or transitional arc signatures. Therefore, they may be from related or similar melts that formed in an OIB, arc or transitional arc setting or were contaminated by continental crust.

As with the hematite-rich basalt in the WHPC, geochemical similarities between the epidote-rich basalt and the mafic dykes along the east coast of Conception Bay led Sparkes (2007) to suggest that at least some of the dykes may represent feeder conduits to the epidote-rich basalt in the WHPC. Hence, at least some of the mafic-to-intermediate dykes in the HCC at Bauline may represent feeder conduits to higher-level intrusions and/or volcanic rocks with similar compositions, which may include the HCD, the BHIS and mafic volcanic rocks in the WHPC.

The relationship between the diorite that hosts the dykes in the HCC at Bauline and the HCD and BHIS remains uncertain. Since the data from each of these units are characterized by a large spread of values among a small set of samples, and because no extended REE data exists for the HCD and BHIS, geochemical trends and similarities between the units are unclear.

4.10.3.3. Mafic-to-intermediate dykes

The mafic-to-intermediate dykes sampled along the east coast of Conception Bay were divided into three groups by Sparkes *et al.* (2007), based on major element geochemistry: Group 1 has $Al_2O_3/(CaO + Na_2O + K_2O) > 1$; Group 2 has relatively high SiO_2 contents, and Group 3 has $Al_2O_3/(CaO + Na_2O + K_2O) < 1$. In general, the La/Y values of Groups 1 and 2 coincide with those of several dykes from the HCC, including the basaltic-andesitic and hornblende basaltic dykes, as well as La/Y values of the WHPC epidote-rich basalt, the HCD and the BHIS. Like these rocks, the mafic-to-intermediate dykes in Groups 1 and 2 plot in the calc-alkaline andesite and basalt fields and high-Mg tholeiite fields on the Jensen (1976) cation plot. On the Zr vs. Zr/Y plot of Pearce and Norry (1979), the mafic-to-intermediate dykes in Groups 1 and 2 plot in the MORB and within-plate basalt fields, and their data fields overlap closely with those of diorite and the hornblende basaltic and basaltic dykes from the HCC at Bauline. These similarities in major and trace element geochemistry support a correlation between mafic-to-intermediate dykes mapped at Bauline and those mapped elsewhere on the NE Avalon Peninsula.

The dykes in Group 3 form two distinct groups on the Jensen (1976) classification diagram (Figure 4.28): some of the samples in this group have high $MgO + TiO_2 + FeO^*$ and plot in the tholeiitic andesite and high-Fe tholeiitic basalt fields, whereas the other samples in Group 3 have high Al_2O_3 and span the calc-alkaline dacite and andesite fields, along with andesitic dykes from the HCC. Geochemical differences among the samples in Group 3 are also illustrated by La/Y ratios. The tholeiitic rocks in Group 3 have relatively low La/Y ratios, like the dykes in Groups 1 and 2, whereas the calc-alkaline

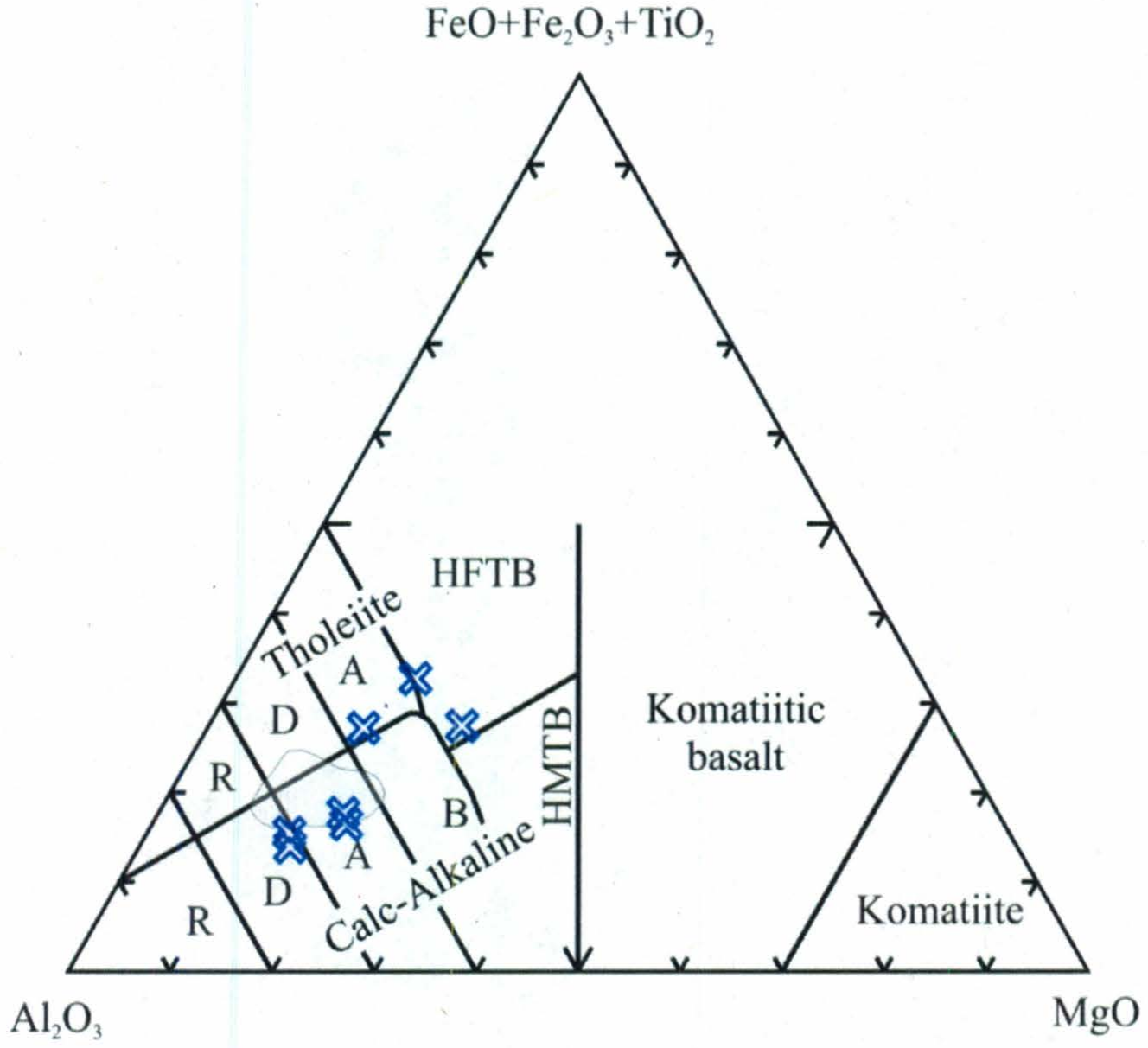

Figure 4.28: The classification diagram of Jensen (1976), showing data from mafic-to-intermediate dykes (denoted "Group 3" by G. Sparkes; blue x's) along the eastern margin of the Holyrood Horst and the east coast of Conception Bay. Compositional fields as in Figure 4.24. Light grey shading indicates the compositional field of andesitic dykes from the HCC at Bauline.

andesitic and basaltic rocks have high La/Y values that are similar to those of the andesitic dykes in the HCC at Bauline (Figure 4.29a). As well, like the andesitic dykes in the HCC at Bauline, the calc-alkaline dykes in Group 3 have elevated Zr/Y and Zr values, causing them to plot within and above the within-plate basalt field on the tectonic discrimination diagram of Pearce and Norry (1979; Figure 4.29b).

The calc-alkaline andesitic and basaltic dykes in Group 3 were collected by G. Sparkes near the eastern margin of the Holyrood Horst and on the east coast of Conception Bay, south of Bauline near Portugal Cove. The geochemical similarities between these dykes and the andesitic dykes at Bauline suggest that andesitic dykes with arc-related or crustally-contaminated sources may have been emplaced on a regional scale on the NE Avalon Peninsula, both east and west of the Topsail Fault.

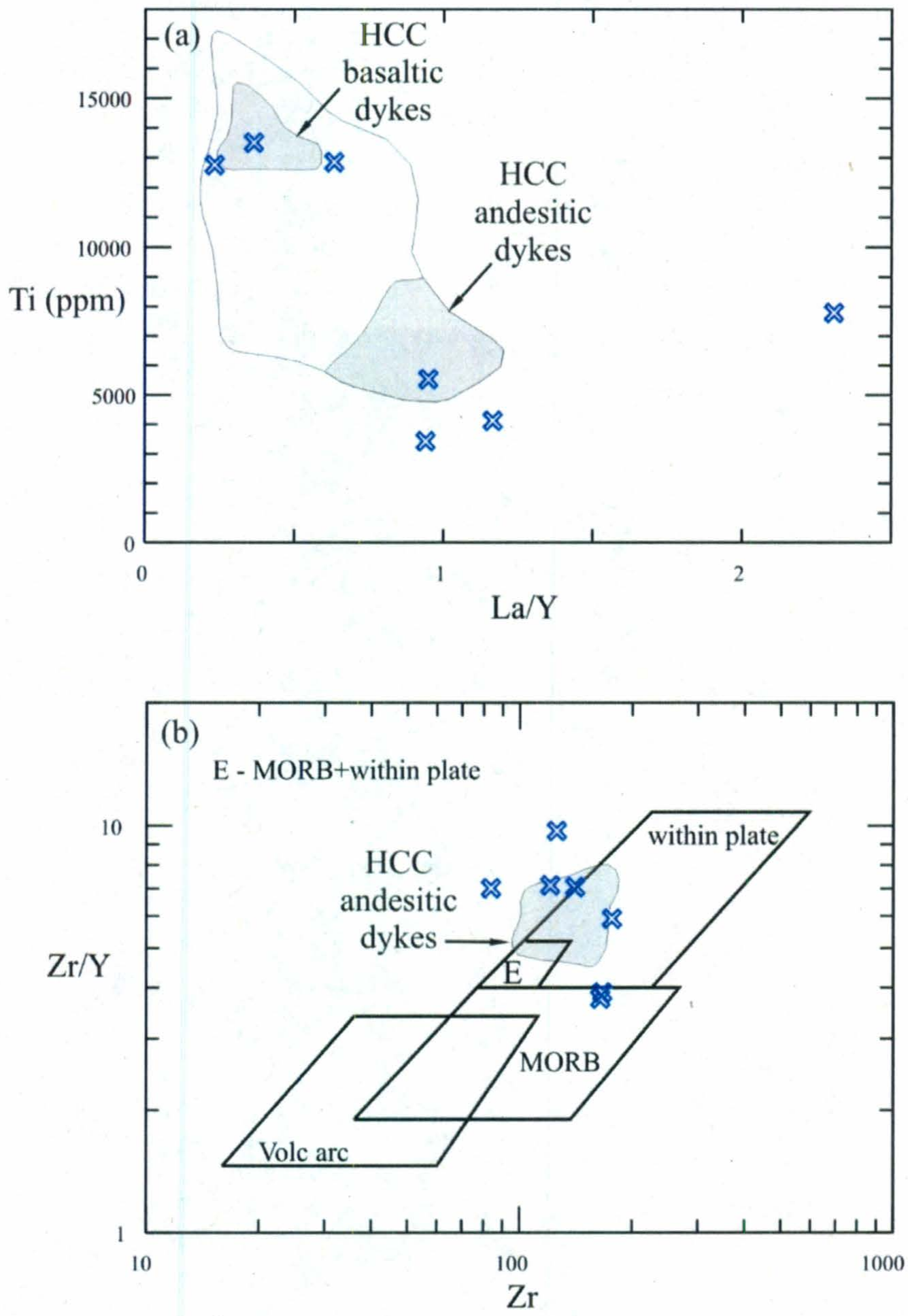

Figure 4.29: Data from the mafic-to-intermediate dykes represented in Figure 4.28 plotted on (a) a diagram of La/Y against Ti, and (b) the tectonic discrimination diagram of Pearce and Norry (1979), with compositional fields as in Figure 4.25b. Symbols are as in Figure 4.28. Light grey shading indicates the compositional field of the mafic-to-intermediate rocks in the HCC at Bauline.

DISCUSSION AND CONCLUSIONS

5.1. Overview of key findings

5.1.1. Host rocks to the Horse Cove Complex

Detailed mapping has shown that the geology of the Bauline area consists of a swarm of mafic-to-felsic dykes hosted by granodiorite, feldspar porphyry, diorite and gabbro. Field relationships indicate that granodiorite is the oldest unit in the study area and this is confirmed with a U/Pb zircon age of 625 ± 1.4 Ma, about 40 Ma older than the other rocks in this study. This new work has demonstrated that granodiorite at Bauline is correlative with felsic plutonic rocks of the Holyrood Intrusive Suite (HIS), and it is therefore not included in the Horse Cove Complex (HCC).

Sparkes (2006) defined the HCC as a composite unit that consists of a swarm of mafic-to-felsic dykes and their host rocks. Sparkes (2006) showed that, in most areas, the dykes are hosted by submarine mafic volcanic rocks of the Wych Hazel Pond Complex (WHPC) and, along the northern part of the east coast of Conception Bay, including the Bauline area, by the Herring Cove Diorite (HCD). Mapping in the Bauline area in this study has shown that, in addition to granodiorite and feldspar porphyry, host rocks to the dyke swarm include gabbro and diorite. These rocks are lithologically similar to the mafic volcanic rocks in the WHPC and the HCD, and they also share some geochemical similarities. However, direct correlations with the WHPC and HCD are restricted by the limited geochemical dataset that is currently available for these units. Therefore, gabbro and diorite, along with feldspar porphyry and the dyke swarm, are included in the HCC.

5.1.2. Geology of the Horse Cove Complex

5.1.2.1. Main rock units

The HCC is divided into ten rock units based on mapping and petrography. Three of these units are the host rocks to the dyke swarm, including feldspar porphyry, gabbro and diorite. The dyke swarm is divided into seven rock units, including one unit that consists of rhyolitic dykes and six units that represent mafic-to-intermediate dykes. The dykes occur in similar abundances throughout the study area. Diorite is the most extensive rock unit, whereas feldspar porphyry is limited to the northeastern portion of the map area and gabbro is present only in Map 2.

5.1.2.2. Relative ages and U/Pb geochronology

Three samples of the HCC were dated using U/Pb zircon geochronology, including: an andesitic dyke that cross-cuts several mafic dykes in Map 2; feldspar porphyry that hosts the dyke swarm in Map 1; and a rhyolitic dyke that cross-cuts feldspar porphyry in Map 1. The best estimate for the age of magmatism in the HCC is constrained by the 578.4 ± 2.3 Ma age of the andesitic dyke and the 580.6 ± 2.0 Ma age of feldspar porphyry. Thus, the majority of magmatism in the HCC occurred over a period of, at most, about 6.5 Ma, between about 582.6 and 576.1 Ma.

Although cross-cutting relationships and pristine chilled margins are exposed in many places, the order of intrusive events in the HCC between 582.6 and 576.1 Ma is complicated due to the episodic emplacement of the dyke swarm. Field relationships show that feldspar porphyry, gabbro and diorite are the host rocks to the dyke swarm, along with granodiorite that is correlated with the HIS. Although the relative ages of gabbro and diorite remain uncertain, feldspar porphyry appears to be older than diorite.

In general, the hornblende basaltic dykes and basaltic dykes are the oldest dykes in the dyke swarm, and the andesitic and rhyolitic dykes are the youngest magmatic events in the HCC. However, andesitic dykes are locally cross-cut by oxide-rich and basaltic-andesitic dykes, although the majority of dykes in these units are older than the andesitic dykes. Therefore, many of the lithologically distinct rock units that comprise the dyke swarm were emplaced episodically and broadly overlap in time.

5.1.2.3. Whole rock geochemistry

Feldspar porphyry and the rhyolitic dykes have overlapping, LREE-enriched REE patterns with negative Nb anomalies and volcanic arc affinities, suggesting that feldspar porphyry and rhyolitic dykes are petrogenetically related, in agreement with their lithological and petrographical similarities and their overlapping U/Pb zircon ages.

For several mafic-to-intermediate rock units mapped in the HCC, many samples are not petrogenetically related, despite their petrographical similarities. For instance, the samples collected from gabbro have similar major and trace element geochemistry, whereas the samples collected from diorite form two geochemically distinct groups. In addition, while most samples collected from the andesitic dykes are petrogenetically related, some samples are comparatively enriched or depleted in the HREE or LREE.

The mafic-to-intermediate rocks in the HCC form six geochemical groups, regardless of lithology, petrography and age relationships, including: (1) E-MORB-like REE patterns; (2) E-MORB-like REE patterns with transitional arc signatures; (3) OIB-like REE patterns; (4) IAT-like REE patterns with transitional arc signatures; (5) IAT-like REE patterns; (6) CAB-like REE patterns. There is an overall temporal progression from rocks with E-MORB-like REE patterns (Group 1) to rocks with CAB-like REE patterns

(Group 6). However, exceptions exist due to the episodic and broadly coeval emplacement of different rock units in the dyke swarm.

5.1.2.4. Nd isotopic data

Seven samples collected from the HCC yield $\varepsilon_{Nd(t=580\ Ma)}$ values from +4.1 to +6.4. The two rocks with the highest ε_{Nd} values have relatively flat REE patterns that lack negative Nb anomalies, including a diorite sample (#105) with an E-MORB-like REE pattern (+6.4) and a basaltic dyke (#74) with an OIB-like REE pattern (+6.3). Since the ε_{Nd} values of these rocks are similar to the ε_{Nd} value of contemporaneous depleted mantle (DePaolo, 1981), they represent magmatism from the depleted mantle that has undergone minor LREE-enrichment via mantle upwelling. A gabbro sample (#82) with an E-MORB-like REE pattern has an ε_{Nd} value of +5.6, which is slightly less than the ε_{Nd} value of coeval depleted mantle (DePaolo, 1981). Since this sample does not exhibit a negative Nb anomaly or pronounced LREE-enrichment, it was probably not significantly contaminated by a subducting slab in an arc environment or by continental crust. It appears to have received LREE-enrichment from an enriched mantle source.

Four rocks have similar ε_{Nd} values ranging from +4.1 to +4.8, suggesting that they share similar source characteristics. These rocks include an andesitic dyke (#89) with a CAB-like REE pattern (+4.1), a basaltic-andesitic dyke (#181) and a diorite sample (#184) with IAT-like REE patterns (+4.5 and +4.8, respectively) and a rhyolitic dyke (#141; +4.7). These rocks represent magmatism that was contaminated by either a subducting slab in an arc environment or by continental crust during ascent.

5.2. Tectonic setting of the Horse Cove Complex

Field relationships, U/Pb ages, whole rock geochemistry and Nd isotopic data suggest that the HCC formed from melts derived from the depleted mantle together with melts that were contaminated by subduction in an arc environment or during ascent through continental crust, and that these melts were emplaced closely in time and space. Therefore, the paleo-tectonic environment of the HCC may be a back-arc basin or a rifted arc sequence, where melts from the depleted mantle were accessed through rifting in older, arc crust. These melts may have received LREE-enrichment from upwelling of the back-arc asthenopheric mantle, resulting in juvenile compositions and E-MORB-like REE patterns. LREE-enriched melts with negative Nb anomalies may have been produced from partial melts of the subduction-contaminated mantle wedge, and/or from ancient arc-contaminated mantle at depth. It is possible that these melts received additional contamination from continental crust during ascent.

An alternate paleo-tectonic setting for the HCC may be an intracontinental rift. In this scenario, melts extracted from the depleted mantle may have been slightly LREE-enriched by rift-induced mantle upwelling, and ascended through the rifted crust without undergoing contamination. Other melts extracted from the depleted mantle may have achieved more significant LREE-enrichment and negative Nb anomalies by assimilating or mixing with partial melts of continental crust during ascent. Alternatively, arc signatures may have been acquired from ancient arc mantle at depth that was tapped by mantle upwelling during rifting.

There are limited Nd isotopic data from the NE Avalon Peninsula and the nature of basement rocks remains enigmatic, together with the source of the ca. 1380 Ma

inherited zircon component in sample #209. A recent Nd isotopic study of selected samples from the NE Avalon Peninsula has been conducted by G. Dunning, Memorial University, and G. Sparkes, Geological Survey of Newfoundland and Labrador. Two samples from the HIS, from west and east of the Topsail Fault, have εNd values of +2.6 and +2.9 at 620 Ma and a sample from the Hawke Hills Tuff in the Holyrood Horst has an εNd value of +2.7 at 730 Ma (G. Sparkes, personal communication, 2011). Therefore, since the HCC is hosted by a ca. 620 Ma granodiorite that is correlated to the HIS, and because the HIS is intrusive into the Hawke Hills Tuff volcanic sequence, it is possible that the εNd values of some of the HCC rocks have been lowered from primitive mantle εNd values through assimilation of the HIS and/or Hawke Hills Tuff. Furthermore, since the HIS and Hawke Hills Tuff are interpreted to represent volcanic arc magmatism (Sparkes, 2005; Sparkes *et al.,* 2007), some rocks in the HCC may have acquired negative Nb anomalies and LREE-enrichment by assimilating HIS host rocks and/or Hawke Hills Tuff-equivalent volcanic rocks at depth.

Given the current tectonic interpretation of the Avalon Zone in Newfoundland, it is more likely that the HCC was emplaced in an environment of back-arc or arc rifting, rather than in a non-arc-related, intracontinental rift setting. Because subduction beneath the Gondwanan margin resulted in extensive arc-related magmatism during 650-550 Ma in the Avalon Terrane (Nance and Murphy, 1994, 1996; Thompson *et al.,* 2007), arc-related magmatism is probable in the Avalon Peninsula at about 580 Ma. As well, magmatism in the HCC may overlap in age with a volcanic arc-related sequence of calc-alkaline mafic to felsic volcanic rocks in the ca. 590-565 Ma Marystown Group on the Burin Peninsula (O'Brien *et al.*, 1990, 1996, 1999). In addition, the HCC is pre-dated by

several volcano-plutonic arc magmatic events that have been documented in the Avalon Zone in Newfoundland. These include the predominantly mafic rocks of the ca. 760 Ma Burin Group, which represent the oldest known subduction-related magmatism in the Avalon Zone (Krogh *et al.,* 1988; Murphy *et al.,* 2008). Closer to the HCC, arc magmatism is recorded by the ca. 730 Ma felsic porphyries and volcanic rocks in the Holyrood Horst, including the 729 ± 7 Ma Hawke Hill Tuff (Israel, 1998; O'Brien *et al.,* 2001). Also in the region of the Holyrood Horst, the HIS, WHIS and associated volcanic rocks represent a ca. 640-606 Ma volcano-plutonic arc magmatic event (Sparkes, 2005; Sparkes *et al.,* 2007). It is possible that there was an active subduction zone at ca. 580 Ma, resulting in widespread magmatism in the present-day NE Avalon Peninsula, recorded by the Manuels Volcanic Suite (MVS), Wych Hazel Pond Complex (WHPC) and HCC. The melts that formed the HCC may have ascended through rifted arc or back-arc crust adjacent to an active subduction zone, and they may represent the "last gasp" of subduction zone related magmatism in the NE Avalon region.

Furthermore, there is no reliable evidence of significant crustal contamination. Out of the four geochronology samples in the HCC, inherited zircon components were encountered only in sample #209. Inheritance in sample #209 occurred in only one of three fractions, and the other two fractions are concordant at ca. 578 Ma. Zircon inheritance may be due to assimilation of minor crustal material during stoping, and may not be indicative of the significant crustal contamination required to induce the low ε_{Nd} value and arc geochemical signatures exhibited by this andesitic dyke (sample #89). Moreover, several other U/Pb geochronology studies on the NE Avalon Peninsula found no inherited zircon (Krogh *et al.,* 1988; Sparkes *et al.,* 2002; O'Brien *et al.,* 2001;

Sparkes, 2005). Most notably, in the work of Sparkes (2005), no inherited zircon components were encountered during U/Pb age determinations of nine units on the eastern margin of the Holyrood Horst. Several of these units overlap in age, within uncertainties, with magmatism in the HCC. The lack of inherited zircon components in U/Pb samples from the NE Avalon Peninsula may be due, at least in part, to selectivity during the U/Pb dating process. Only a small proportion of zircon grains were analyzed from each sample, and these were selected from the clearest, most euhedral grains to minimize occurrences of inherited cores. Nevertheless, the rarity of inherited zircon in the geochronology samples from the NE Avalon region implies an insignificant amount of assimilation or mixing with an older crustal source.

5.3. Correlations with the geology of the NE Avalon Peninsula

5.3.1. Host rocks to the Horse Cove Complex

Because the 625 ± 1.4 Ma U/Pb age of the granodiorite in the Bauline area overlaps, within uncertainties, with U/Pb ages of the HIS granite and quartz-feldspar porphyry in the region of the Holyrood Horst, and they have similar chemistry, this granodiorite is correlated with the HIS plutons. This provides the first evidence of HIS-aged rocks east of the Topsail Fault, and supports the correlation drawn by Sparkes (2006) between granitoid rocks on the NE Avalon Peninsula north of the Topsail Fault with those of the HIS. Both the granodiorite at Bauline and the HIS granitoid rocks appear to represent volcanic arc plutons that were emplaced in arc system that was active at about 620 Ma in the region of the Holyrood Horst, as described by King (1990), Sparkes (2005) and Sparkes *et al.* (2007). This correlation between granodiorite and the

HIS rocks from 25 km further south indicates that ca. 620 Ma volcanic arc-related plutonism occurred regionally along the east coast of Conception Bay, or that the original HIS batholith has been tectonically separated.

5.3.2. The Horse Cove Complex

The U/Pb ages of the HCC feldspar porphyry, rhyolitic and andesitic dykes overlap in time, within uncertainties, with U/Pb ages of several felsic units on the eastern margin of the Holyrood Horst, including ash-flow tuffs in the WHPC and MVS and feldspar porphyry in the WHPC, and with a a dacitic dyke at Cripple Cove. As well, the HCC rhyolitic dyke overlaps in age, within uncertainties, with rhyolite in the MVS. Magmatism in the HCC also coincides with the 585 to 580.5 Ma high-sulphidation style alteration system and the 584 ± 4 Ma-and-younger low-sulphidation alteration system (Sparkes, 2005), both associated with gold deposition in the eastern Avalon high-alumina belt.

The feldspar porphyry and rhyolitic dykes in the HCC share geochemical similarities with rhyolite from Cape St. Francis, a ca. 580 Ma dacitic dyke from Cripple Cove, and with ca. 580 Ma rhyolite (MVS) and feldspar porphyry (WHPC) on the eastern margin of the Holyrood Horst. Like the HCC feldspar porphyry and rhyolitic dykes, these rocks plot in the volcanic arc granite field of Pearce *et al.* (1984) and exhibit geochemical signatures that are typical of volcanic arc rocks, including enrichment in the LILE relative to the HFSE, and rocks with extended REE data display negative Nb anomalies and LREE-enrichment. Therefore, ca. 580 Ma felsic magmatism that exhibits

volcanic arc geochemistry appears to have been emplaced over a distance of at least 35 km, north to south, on the NE Avalon Peninsula.

There are also geochemical similarities between the mafic-to-intermediate rocks in the HCC at Bauline and elsewhere in the NE Avalon region. For example, the HCC gabbro and the WHPC hematite-rich basalt (Sparkes, 2006) are both high-Mg tholeiitic basalts with low La/Y values. Since the HCC gabbro displays E-MORB-like REE geochemistry, the WHPC hematite-rich basalt may similarly have an E-MORB-like source. Thus, E-MORB-like basalts may occur regionally along the east coast of Conception Bay. Of all the mafic-to-intermediate rocks in the HCC, the WHPC epidote-rich basalt, HCD and Beaver Hat Intrusive Suite (BHIS) appear to be most geochemically similar to mafic-to-intermediate dykes that have either OIB-like REE patterns or LREE-enriched REE patterns with arc or transitional arc signatures. This implies that they are from similar or related melts, and perhaps some of the mafic-to-intermediate dykes in the HCC represent feeder conduits to the WHPC epidote-rich basalt, HCD or BHIS, as suggested by Sparkes *et al.* (2007). In addition, the andesitic dykes in the HCC at Bauline share geochemical traits, including high La/Y values, with some calc-alkaline andesitic and basaltic dykes that were sampled elsewhere on the east coast of Conception Bay and from the eastern margin of the Holyrood Horst. This implies that andesitic and basaltic dykes with arc-related or crustally-contaminated sources were emplaced on a regional scale on the NE Avalon Peninsula, both east and west of the Topsail Fault.

At the youngest limit of uncertainty on the 578.4 ± 2.3 Ma U/Pb age, the HCC andesitic dyke represents the youngest dated magmatic event on the NE Avalon Peninsula. However, the BHIS probably represents even younger magmatism, since it

intrudes folded strata of the Mannings Hill Member in the Drook Formation of the Conception Group near Cape St. Francis (Sparkes, 2006). The best estimate of the older age limit of the Mannings Hill Member is ca. 580 Ma, the age of the Gaskiers tuff near the base of the Conception Group in St. Mary's Bay (Bowring *et al.,* 2003). The younger age limit of the Mannings Hill Member is ca. 565 Ma, the age of a tuff bed in the overlying Mistaken Point Formation (G. Dunning, unpubished data, 1988; Benus, 1988). The age of this tuff bed also provides the older age limit of the St. John's and Signal Hill groups, which lie stratigraphically above the Mistaken Point Formation. Given that folding of the Mannings Hill Member presumably occurred during the same late Neoproterozoic regional deformation event that created large-scale folds in the Signal Hill and St. John's groups, the BHIS may be younger than ca. 565 Ma. Therefore, the BHIS, which exhibits volcanic arc-related geochemistry (Sparkes *et al.,* 2007), appears to represent volcanic arc-related magmatism that is younger than the HCC andesitic dyke.

In summary, magmatism in the HCC, between about 582.6 and 576.1 Ma, is contemporaneous with felsic magmatism that occurred along the eastern margin of the Holyrood Horst and in the Cape St. Francis area. Geochemical traits suggest that, like the HCC feldspar porphyry and andesitic dykes, these felsic rocks represent volcanic arc-related magmatism. As well, certain mafic-to-intermediate rocks in the HCC exhibit geochemical similarities with those elsewhere along the east coast of Conception Bay, including a range of compositions that are comparable to the E-MORB-like, transitional arc and CAB-like rocks in the HCC. Thus, ca. 580 Ma volcanic arc-related magmatism appears to have occurred on a regional scale, trending SW-NE from the eastern margin of the Holyrood Horst to Bauline and farther north to Cape St. Francis.

Beginning at ca. 582 Ma, the marine sedimentary and mafic volcanic rocks of the WHPC were deposited in a basinal environment in an extensional setting (Sparkes, 2005, 2006). The volcanic rocks in the WHPC display both E-MORB-like and transitional arc basalt geochemistry (Sparkes *et al.*, 2007), and presumably represent an early stage of the arc-rift- or back-arc basin-related magmatism of the HCC during about 582.6 to 576.1 Ma. Deep marine sedimentation is recorded by the turbiditic siliciclastic rocks of the Conception Group, deposited during ca. 580-565 Ma, which overlie the late Neoproterozoic volcanic and plutonic rocks. The subsequent deposition of the deltaic St. John's Group and molasse-like Signal Hill Group marks the transition from an extensional tectonic setting to a compressional environment during the late Neoproterozoic. Interbeds of tuff and ash signify intermittent volcanism that continued throughout the deposition of the Conception, St. John's, and Signal Hill groups. By the beginning of the Cambrian, the tectonic environment stabilized and platformal siliciclastic strata were deposited over the Neoproterozoic succession.

It is noteworthy that U/Pb ages of ca. 580 Ma magmatism in the HCC, MVS and WHPC overlap, within uncertainties, with the ca. 580 Ma age of the Gaskiers tillite, dated by Bowring *et al.* (2003). The interpreted back-arc basin setting – or alternative intracontinental rift environment – of the HCC and felsic rocks in the MVS and WHPC is at odds with the quiet deep marine environment in which the Gaskiers tillite was simultaneously deposited. The Gaskiers Formation, which lies near the base of the Conception Group, consists of turbidites interbedded with glacial diamictites, deposited in a submarine fan or slope setting (Bowring *et al.*, 2003). The ash bracketing the Gaskiers tillite, dated at ca. 580 Ma, was collected from St. Mary's Bay, approximately 100 km

south of the HCC. It is uncertain whether this distance is sufficient to account for such different tectonic/depositional environments, or if these rocks were juxtaposed during subsequent regional deformation.

On the southern Avalon Peninsula, the Gaskiers Formation is overlain by the Drook Formation in the Conception Group. The age of the Drook Formation in this area is constrained by the ca. 580 Ma Gaskiers tillite (Bowring *et al.,* 2003) and a tuff in the Mistaken Point Formation, dated at 565 ± 3 Ma (G. Dunning, unpublished data; Benus, 1988). As well, a tuff bed near the top of the Drook Formation near Mistaken Point was dated at ca. 575 Ma (J. Ramezani, unpublished data, 2005; G. Dunning, personal communication). On the NE Avalon Peninsula, the Drook Formation represents the basal strata of the Conception Group, and overlies the volcano-plutonic package that occurs along the east coast of Conception Bay, including the HCC. Since there are no U/Pb ages for tuff interbeds in the Conception, St. John's and Signal Hill groups on the northern Avalon Peninsula, the only age constraints for these rocks are those of correlative strata on the southern Avalon Peninsula. Therefore, the Drook Formation, which currently lies in close proximity to the volcano-plutonic succession on the NE Avalon Peninsula, may have been deposited as early as 580 Ma. In this case, the close proximity of siliciclastic rocks deposited in a deep marine environment with potentially contemporaneous, subduction-zone related volcanic and plutonic rocks suggests that these rocks may have been further away from each other at the time of their formation, and that they have been structurally juxtaposed to their present-day positions. Alternatively, the basal strata of the Conception Group on the NE Avalon Peninsula may be considerably younger than 580

Ma, perhaps allowing sufficient time for the transition from a back-arc basin adjacent to an active subduction zone to a deep marine basin.

5.4. Tectonic importance of the HCC in the Avalon Zone in Newfoundland

While magmatism occurred in the HCC during about 582.6 to 576.1 Ma, magmatic events were also taking place elsewhere in the Avalon Zone in Newfoundland. The geology of the Avalon Zone is summarized schematically in Figure 5.1, and lithological descriptions and data that provide age control for the main rock packages are provided in Appendix G. As shown by this diagram, magmatism in the Avalon Zone at ca. 580 Ma was preceded by widespread plutonism, volcanism and sedimentation in subduction zone related environments during ca. 640-606 Ma. These events include the volcano-plutonic arc complex recorded by the HIS, WHIS and associated volcanic rocks and minor marine siliciclastic rocks on the Avalon Peninsula; the volcano-sedimentary successions of the Love Cove and Connecting Point Groups in the Burin Peninsula – Bonavista Bay area; and the volcano-sedimentary and plutonic rocks of the Connaigre Bay Group and Simmons Brook Intrusive Suite on the Connaigre Peninsula.

On the Avalon Peninsula, the ca. 582 Ma basinal volcano-sedimentary rocks of the WHPC were intruded by the mafic-to-felsic intrusions of the HCC from about 582.6 to 576.1 Ma. This lithologic assemblage is broadly echoed by contemporaneous rock packages elsewhere in the Avalon Zone and in Avalon-aged rocks in Newfoundland, including the volcanic rocks of the Marystown Group and younger mafic-to-felsic intrusions on the Burin Peninsula, and the volcano-sedimentary Whittle Hill Sandstone –

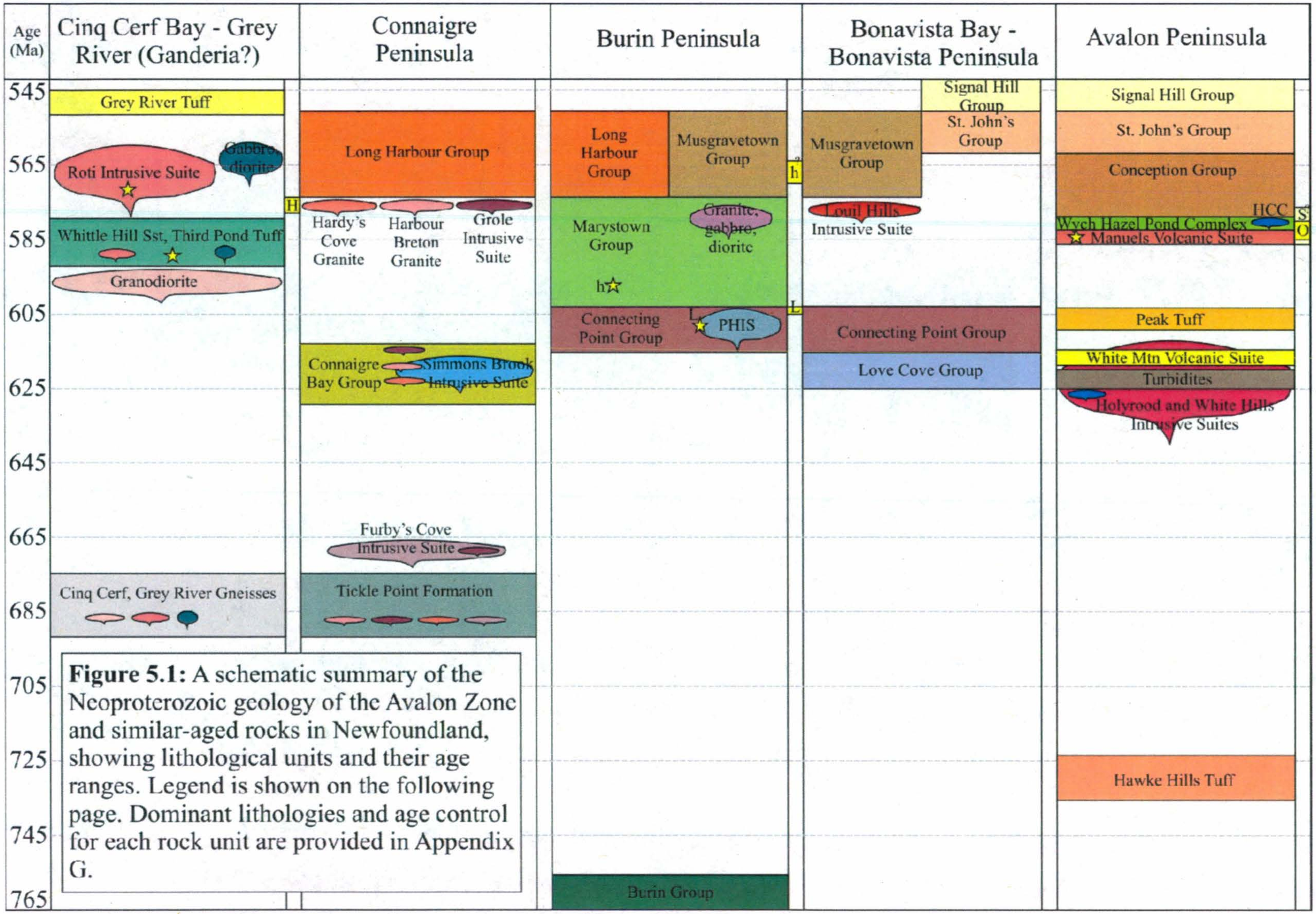

Figure 5.1: A schematic summary of the Neoproterozoic geology of the Avalon Zone and similar-aged rocks in Newfoundland, showing lithological units and their age ranges. Legend is shown on the following page. Dominant lithologies and age control for each rock unit are provided in Appendix G.

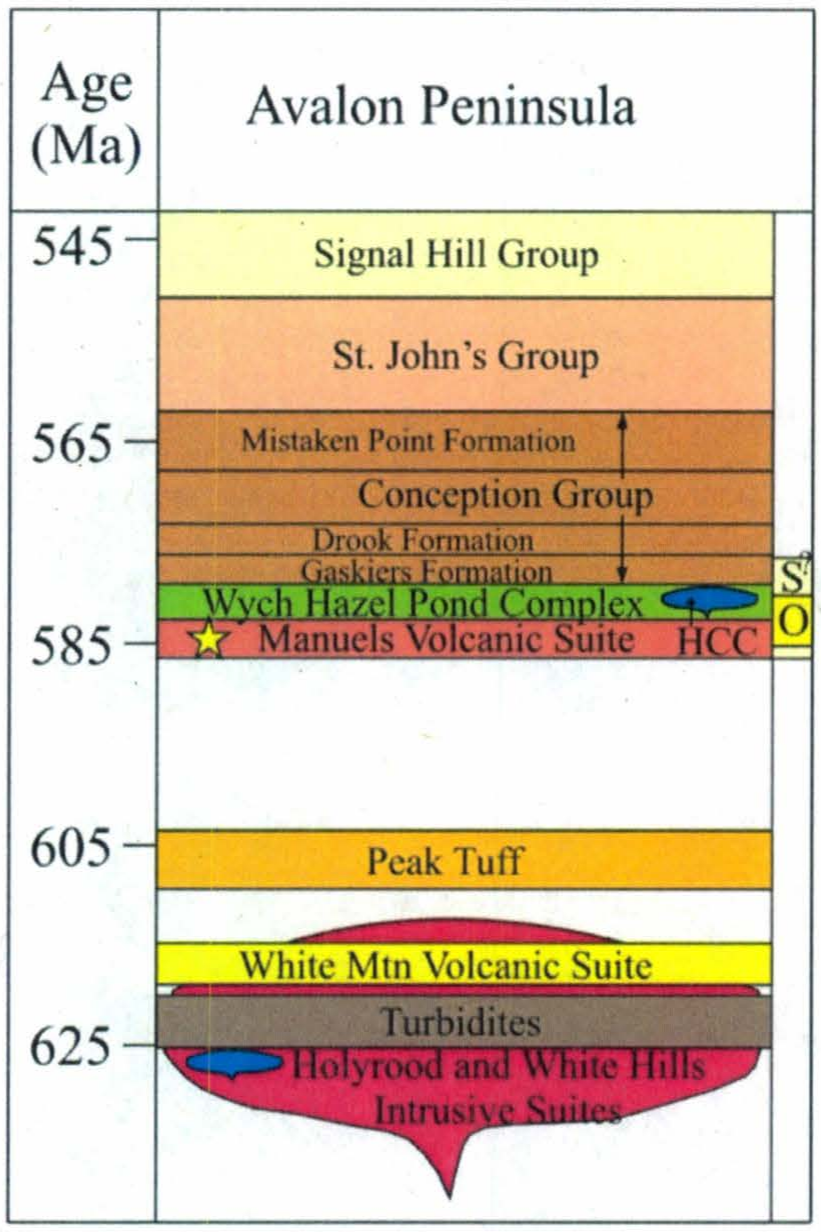

Legend:

Sedimentary or volcanic rocks or a volcano-sedimentary sequence. Top and bottom indicate approximate age range.

Intrusive rocks. Top and bottom indicate approximate age range.

Age range of low-sulphidation-style or high-sulphidation-style alteration system. H=Hope Brook Mine; h=Hickey's Pond and Stewart prospects; L=Lodestar prospect; O=Oval Pit Mine; S=Steep Nap Prospect.

Indicates epithermal alteration system hosted by .

Indicates intrusive relationship of into .

Figure 5.1 (continued): Schematic representation of post-645 Ma Neoproterozoic geology of the Avalon Peninsula in the Avalon Zone, Newfoundland.

Third Pond Tuff succession and felsic Roti Intrusive Suite in the Hermitage Flexure basement inlier.

Magmatism in the HCC between about 582.6 and 576.1 Ma overlaps in time with the age range of the Marystown Group on the Burin Peninsula. The Marystown Group includes volcanic arc rocks that were deposited during ca. 590-565 Ma (O'Brien *et al.,* 1999). The Marystown Group consists of greenschist-facies subaerial volcanic rocks, ranging in composition from basalt to rhyolite and exhibiting calc-alkaline and tholeiitic chemistries, overlain by volcaniclastic rocks and an upper sequence of continental, alkaline basalt and rhyolite (O'Brien *et al.,* 1990, 1996, 1999). Limited age control in the Marystown Group is provided by a ca. 572 Ma pyroclastic rock, host to the Hickey's Pond epithermal gold deposit (Ketchum, unpublished data, 1998, in O'Brien *et al.,* 1999), by a 568 ± 5 Ma rhyolite at the base of the overlying Long Harbour Group (Tucker, unpublished data, O'Brien *et al.,* 1984), and by a 610 ± 1 Ma tuff from the middle of the underlying Connecting Point Group (G. Dunning, unpublished data, in Dec *et al.,* 1992). The Marystown Group was intruded by numerous, co-eval, high-level intrusions of granite, diorite and gabbro, including the Swift Current, Cape Roger and Burin Knee Granites, during ca. 570-580 Ma (O'Brien *et al.,* 1984, 1999). Although there are limited U/Pb ages in the Marystown Group, and no ca. 580 Ma rocks have yet been found, arc-related magmatic events in the Marystown Group and HCC may overlap in time.

Also contemporaneous with magmatism in the HCC is the volcano-sedimentary succession of the Whittle Hill Sandstone and overlying Third Pond Tuff in the basement inlier south of the Hermitage Flexure in the Cinq Cerf Bay area. This basement inlier has been correlated with the Avalon Terrane (Dunning and O'Brien, 1989), but some workers

have more recently correlated it with Ganderia (e.g. Hibbard *et al.,* 2007; Lin *et al.,* 2007). The conglomerate, sandstone and turbidites of the Whittle Hill Sandstone are overlain by submarine mafic and felsic tuffs of the Third Pond Tuff (Dubé *et al.,* 1998). Age control is provided by tuffs dated at 583 +7/-3 Ma and 585 ± 5 Ma, which host the Hope Brook epithermal gold deposit (Dubé *et al.,* 1998). A granodiorite that intrudes the Cinq Cerf Gneiss was dated at 584 +7/-6 Ma, coeval with the Whittle Hill Sandstone – Third Pond Tuff succession (Valverde-Vaquero *et al.,* 2006). The Whittle Hill Sandstone – Third Pond Tuff succession is intruded by calc-alkaline granodiorite, tonalite and quartz-feldspar porphyry intrusions of the Roti Intrusive Suite, which are constrained in age by a 578 ± 10 Ma granodiorite (Krogh *et al.,* 1988) and a 563 ± 4 Ma tonalite (Dunning and O'Brien, 1989). A more precise older age limit is provided by a quartz-feldspar porphyry intrusion, dated at 576 ± 2 Ma (Dubé *et al.,* 1998). This age, and ages of tuffs from the Whittle Hill Sandstone – Third Pond Tuff succession, overlaps with the age of magmatism in the HCC, within uncertainties. The Whittle Hill Sandstone – Third Pond Tuff succession and Cinq Cerf Gneiss are also intruded by mafic and intermediate intrusions that range in age from ca. 570-552 Ma (Dubé *et al.,* 1998; Valverde-Vaquero *et al.,* 2006).

Together with the Marystown Group on the Burin Peninsula, and possibly the Whittle Hill Sandstone – Third Pond Tuff and Roti Intrusive Suite in the Cinq Cerf Bay area, the HCC and associated ca. 580 Ma magmatism on the Avalon Peninsula may represent the last pulse of subduction zone related magmatism during the Neoproterozoic in the Avalon Zone in Newfoundland, prior to the emplacement of continental, alkaline intrusions, such as the Louil Hills Intrusive Suite, and the volcano-sedimentary

successions of the Long Harbour, Musgravetown, Conception, St. John's and Signal Hill groups.

5.5. Conclusions

1) Granodiorite in the Bauline area is correlative with the felsic plutonic rocks of the Holyrood and White Hills Intrusive Suites, and is therefore not included in the Horse Cove Complex. This correlation confirms the occurrence of Holyrood or White Hills Intrusive Suite rocks further north of their previously known distribution, and east of the Topsail Fault.

2) After the emplacement of ca. 625 Ma granodiorite, there was a gap in magmatism in the study area of about 40 Ma, until the emplacement of the Horse Cove Complex. Magmatism in the Horse Cove Complex occurred between about 582.6 and 576.1 Ma.

3) The Horse Cove Complex is a composite unit, composed of shallow-level intrusions of feldspar porphyry, gabbro and diorite, which host a swarm of mafic-to-felsic dykes. The dykes are dominantly basaltic to andesitic in composition, and rhyolitic dykes are rare.

4) Feldspar porphyry and rhyolitic dykes appear to be petrogenetically related and demonstrate volcanic arc geochemistry.

5) The mafic-to-intermediate rocks in the study area are divided into six geochemically distinct groups based on REE patterns and Nb/Th ratios. The rocks in these groups cover a range of compositions, from rocks with E-MORB geochemical signatures to calc-alkaline andesites and basalts with well-developed negative Nb anomalies. Cross-cutting

relationships indicate that these rocks follow an overall progression from rocks with E-MORB-like geochemistry to rocks with arc signatures. However, there are exceptions to this general trend due to the episodic emplacement of the dyke swarm and the broadly coeval nature of several mafic-to-intermediate rock units.

6) The most likely tectonic setting for the Horse Cove Complex is a back-arc basin because: (1) in a back-arc basin, melts from the depleted mantle and melts that were contaminated by subduction processes and/or continental crust can be emplaced side-by-side and closely spaced in time, as they were in the Horse Cove Complex; (2) the rarity of inherited zircon components in geochronology samples from the Horse Cove Complex and correlative rocks on the NE Avalon Peninsula suggests insignificant assimilation of continental crust, rendering it unlikely that arc signatures in the Horse Cove Complex were acquired solely via crustal contamination; and (3) in the context of the current tectonic interpretation of the Avalon Zone in Newfoundland, an active subduction zone on the NE Avalon Peninsula at ca. 580 Ma is plausible.

7) The Horse Cove Complex appears to represent the last period of Neoproterozoic subduction zone related magmatism on the NE Avalon Peninsula. Magmatism in the Horse Cove Complex may be contemporaneous with the deposition of basal strata in the Conception Group, but subsequent sedimentation marks the transition from the back-arc basin environment of the Horse Cove Complex to the deep marine setting of the Conception Group, followed by basinal-deltaic sedimentation in the St. John's Group and molasse-like deposits in the Signal Hill Group.

REFERENCES

Bea, F. 1996. Residence of REE, Y, Th and U in granites and crustal protoliths; implications for the chemistry of crustal melts. Journal of Petrology, vol.37, no.3, 521-552.

Bell, R. 1892. Alexander Murray, F.G.S., F.R.S.C., C.M.G. The Canadian Record of Science, vol.5, no.2, 77-96.

Benus, A. P. 1988. Sedimentological context of a deep-water Ediacaran fauna (Mistaken Point, Avalon zone, eastern Newfoundland). *In*: Trace fossils, small shelly fossils and the Precambrian-Cambrian boundary. *Edited by*: Landing, E., *et al.* New York State Museum and Geological Survey Bulletin, vol.463, 8-9.

Blackwood, R. F. and Kennedy, M. J. 1975. The Dover Fault; western boundary of the Avalon Zone in northeastern Newfoundland. Canadian Journal of Earth Sciences, vol.12, no.2, 320-325.

Bowring, S. A., Myrow, P. M., Landing, E., Ramezani, J., Condon, D., and Hoffmann, K. H. 2003. Geochronological constraints on Neoproterozoic glaciations and the rise of metazoans. Abstracts with Programs - Geological Society of America, vol.35, no.6, 516.

Boyce, W. D. and Hayes, J. P. 1991. Middle Cambrian trilobites from Topsail Head, Avalon Peninsula. Current Research - Newfoundland and Labrador Department of Natural Resources, Geological Survey, Report 91-1, 83-84.

Buddington, A. F. 1916. Pyrophyllitization, pinitization and silicification of rocks around Conception Bay, Newfoundland. Journal of Geology, vol.24, 130-152.

Calon, T. 2005. Late Precambrian sedimentation and related orogenesis of the Avalon Peninsula, eastern Avalon Zone, Newfoundland. Field Trip Guidebook, St. John's 2005 AUGC Annual Meeting, 35 pages.

Condie, K. C. 1997. Sources of Proterozoic mafic dyke swarms; constraints from Th/Ta and La/Yb ratios. Precambrian Research, vol.81, no.1-2, 3-14.

Cooper, M. 2011. An integrated mapping, petrographic, geochemical and U/Pb study of main rock units at Cripple Cove, Newfoundland. Unpublished thesis, Memorial University of Newfoundland.

Dalziel, I. W. D. 1997. Neoproterozoic-Paleozoic geography and tectonics; review, hypothesis, environmental speculation. Geological Society of America Bulletin, vol.109, no.1, 16-42.

Dec, T., O'Brien, S. J. and Knight, I. 1992. Late Precambrian volcaniclastic deposits of the Avalonian Eastport Basin (Newfoundland Appalachians); petrofacies, detrital clinopyroxene geochemistry and palaeotectonic implications. Precambrian Research, vol.59, no. 3-4, 243-262.

DePaolo, D. J. 1981. Neodymium isotopes in the Colorado Front Range and crust-mantle evolution in the Proterozoic. Nature, vol. 291, no. 5812, 193-196.

Dunning, G. R. and O'Brien, S. J. 1989. Late Proterozoic-early Paleozoic crust in the Hermitage Flexure, Newfoundland Appalachians; U/Pb ages and tectonic significance. Geology, vol. 17, no. 6, 548-551.

Evans, D. T. W., Kean, B. F. and Dunning, G. R. 1990. Geological studies, Victoria Lake Group, central Newfoundland. Current Research - Newfoundland and Labrador Department of Natural Resources, Geological Survey, Report 90-1, 131-144.

Foley, S. F., Barth, M. G. and Jenner, G. A. 2000. Rutile/melt partition coefficients for trace elements and an assessment of the influence of rutile on the trace element characteristics of subduction zone magmas. Geochimica et Cosmochimica Acta, vol.64, no.5, 933-938.

Frost, B. R., Barnes, C. G., Collins, W. J., Arculus, R. J., Ellis, D. J. and Frost, C. D. 2001. A geochemical classification for granitic rocks. Journal of Petrology, vol. 42, no. 11, 2033-2048.

Goldstein, S. L., O'Nions, R. K. and Hamilton, P. J. 1984. A Sm-Nd isotopic study of atmospheric dusts and particulates from major river systems. Earth and Planetary Science Letters, vol. 70, no. 2, 221-236.

Greenough, J. D. and Papezik,V. S. 1985. Petrology and geochemistry of Cambrian volcanic rocks from the Avalon Peninsula, Newfoundland. Canadian Journal of Earth Sciences, vol. 22, no. 11, 1594-1601.

Hart, S. R. and Davis, K. E. 1978. Nickel partitioning between olivine and silicate melt. Earth and Planetary Science Letters, vol. 40, no. 2, 203-219.

Hibbard, J. P., van Staal, C. R. and Miller, B. V. 2007. Links among Carolinia, Avalonia, and Ganderia in the Appalachian peri-Gondwanan realm. Special Paper - Geological Society of America, vol. 433, 291-311.

Hoffman, P. F. 1991. Did the breakout of Laurentia turn Gondwanaland inside-out? Science, vol. 252, 1409-1412.

Howley, J. P. Geological map of Newfoundland: Scale 1 inch to 17 miles, reprinted 1925.

Hsu, E. Y. C. 1975. Pouch Cove-St. John's, Map 7836. Newfoundland and Labrador Department of Natural Resources, Mineral Development Division.

Hughes, C. J. and Brueckner, W. D. 1971. Late Precambrian rocks of eastern Avalon Peninsula, Newfoundland; a volcanic island complex. Canadian Journal of Earth Sciences, vol. 8, no. 8, 899-915.

Hughes, C. J. 1973. Late Precambrian volcanic rocks of Avalon, Newfoundland; a spilite/keratophyre province; recognition and implications. Canadian Journal of Earth Sciences, vol. 10, no. 2, 272-282.

Hussey, E. M. 1979. The stratigraphy, structure and petrochemistry of the Clode Sound map area, northwestern Avalon Zone, Newfoundland. Unpublished M. Sc. thesis, Memorial Univerity of Newfoundland, 312 pages.

Hutchinson, R. D. 1953. Geology of Harbour Grace map area, Newfoundland. Memoir - Geological Survey of Canada, vol. 275, 43 pages.

Hutchinson, R. D. 1962. Cambrian stratigraphy and trilobite faunas of southeastern Newfoundland. Bulletin - Geological Survey of Canada, 156 pages.

Israel, S. 1998. Geochronological, structural and stratigraphic investigation of a Precambrian unconformity between the Harbour Main Group and Conception Group, east coast Holyrood Bay, Avalon Peninsula, Newfoundland. Unpublished B. Sc. thesis, Memorial University of Newfoundland, 78 pages.

Jacobsen, S. B. and Wasserburg, G. J. 1980. Sm-Nd isotopic evolution of chondrites. Earth and Planetary Science Letters, vol.50, no.1, 139-155.

Jaffey, A. H., Flynn, K. F., Glendenin, L. E., Bentley, W. C. and Essling, A. M. 1971. Precision measurement of half-lives and specific activities of 235U and 238U. Phys. Rev., vol.4, 1889.

Jenner, G. A., Dunning, G. R., Malpas, J., Brown, M. and Brace, T. 1991. Bay of Islands and Little Port complexes, revisited; age, geochemical and isotopic evidence confirm suprasubduction-zone origin. Canadian Journal of Earth Sciences, vol.28, no.10, 1635-1652.

Jenner,G. A., Dunning,G. R., Malpas,J., Brown,M. and Brace,T. 1991. Bay of islands and little port complexes, revisited; age, geochemical and isotopic evidence confirm suprasubduction-zone origin.Canadian Journal of Earth Sciences = Revue Canadienne des Sciences de la Terre; Canadian Journal of Earth Sciences = Revue Canadienne des Sciences de la Terre, Ottawa, ON, Canada, vol.28, no.10, 1635-1652.

Jensen, L. S. 1976. A new cation plot for classifying subalkalic volcanic rocks. Ontario Geological Survey, Miscellaneous Paper, Issue 66.

Jukes, J. B. 1843. General report of the Geological Survey of Newfoundland during the years 1839 and 1840. John Murray, London, 160 pages.

King, A. F. 1990. Geology of the St. John's area. Newfoundland and Labrador Department of Natural Resources, Geological Survey, Report 90-2, 93 pages.

King, A. F. 1988. Geology of the Avalon Peninsula, Newfoundland (parts of 1K, 1L, 1M, 1N and 2C). Newfoundland and Labrador Department of Natural Resources, Mineral Development Division, Map 88-01.

Kinzler, R. J., Grove, T. L. and Recca, S. I. 1990. An experimental study on the effect of temperature and melt composition on the partitioning of nickel between olivine and silicate melt. Geochimica et Cosmochimica Acta, vol.54, no.5, 1255-1265.

Krogh, T. E. 1973. A low-contamination method for hydrothermal decomposition of zircon and extraction of U and Pb for isotopic age determinations. Geochimica et Cosmochimica Acta, vol.37, no.3, 485-494.

Krogh, T. E., Strong, D. F., O'Brien, S. J. and Papezik, V. S. 1988. Precise U-Pb zircon dates from the Avalon Terrane in Newfoundland. Canadian Journal of Earth Sciences, vol.25, no.3, 442-453.

Landing, E. 2 005. Early Paleozoic Avalon-Gondwana unity; an obituary; response to 'Palaeontological evidence bearing on global Ordovician-Silurian continental reconstructions'; discussion. Earth-Science Reviews, vol.69, no.1-2, 169-175.

Le Bas, M. J., Le Maitre, R. W., Streckeisen, A. and Zanettin, B. A. 1986. Chemical classification of volcanic rocks based on the total alkali-silica diagram. Journal of Petrology, vol.27, no.3, 745-750.

Le Maitre, R. W. [editor], Bateman, P., Dudek, A., Keller, J., Lemeyre, J., Le Bas, M. J., Sabine, P. A., Schmid, R., Sorensen, H., Streckeisen, A., Wooley, A. R. and Zanettin, B. 1989. A classification of igneous rocks and glossary of terms. Oxford, United Kingdom, 193 pages.

Lin, S., Davis, D. W., Barr, S. M., van Staal, C. R., Chen, Y. and Constantin, M. 2007. U-Pb geochronological constraints on the evolution of the Aspy Terrane, Cape Breton Island; implications for relationships between Aspy and Bras d'Or Terranes and Ganderia in the Canadian Appalachians. American Journal of Science, vol.307, no.2, 371-398.

Mattinson, J. M. 2005. Zircon U/Pb chemical abrasion (CA-TIMS) method; combined annealing and multi-step partial dissolution analysis for improved precision and accuracy of zircon ages. Chemical Geology, vol. 220, 47-66.

McCartney, W. D. 1969. Geology of the Avalon Peninsula, southeast Newfoundland. Memoir - American Association of Petroleum Geologists, vol.12, 115-129.

McCartney, W. D. 1967. Whitbourne map-area, Newfoundland. Memoir - Geological Survey of Canada, 132 pages.

Miller, H. G. 1983. A geophysical interpretation of the geology of Conception Bay, Newfoundland. Canadian Journal of Earth Sciences, vol.20, no.9, 1421-1433.

Murphy, J. B., McCausland, P. J. A., O'Brien, S. J., Pisarevsky, S. and Hamilton, M. A. 2008. Age, geochemistry and Sm/Nd isotopic signature of the 0.76 Ga Burin Group; compositional equivalent of Avalonian basement? Precambrian Research, vol. 165, 37-48.

Murphy, J. B. and Nance, R. D. 1989. Model for the evolution of the Avalonian-Cadomian Belt. Geology, vol.17, no.8, 735-738.

Murray, A. 1869. The economic value of a Geological Survey. John Lovell, Montreal, 20 pages.

Murray, A. and Howley, J. P. 1881. Report of the Geological Survey of Newfoundland 1864-1880. Stanford, London.

Nance, R. D. and Murphy, J. B. 1996. Basement isotopic signatures and Neoproterozoic paleogeography of Avalonian-Cadomian and related terranes in the Circum-North Atlantic. Special Paper - Geological Society of America, vol.304, 333-346.

Nance, R. D. and Murphy, J. B. 1994. Contrasting basement isotopic signatures and the palinspastic restoration of peripheral orogens; example from the Neoproterozoic Avalonian-Cadomian Belt. Geology, vol.22, no.7, 617-620.

Nesse,W. D. 2000. Introduction to mineralogy. Oxford University Press, Inc., 442 pages.

O'Brien, S. J. 1993. A preliminary account of geological investigations in the Clode Sound-Goose Bay region, Bonavista Bay, Newfoundland (NTS 2C/5 NW and 2D/8 NE). Current Research - Newfoundland and Labrador Department of Natural Resources, Geological Survey, 293-309.

O'Brien, S. J., O'Driscoll, C. F., Greene, B. A. and Tucker, R. D. 1995. Pre-Carboniferous geology of the Connaigre Peninsula and the adjacent coast of Fortune Bay, Southern Newfoundland. Current Research - Newfoundland and Labrador Department of Natural Resources, Geological Survey, Report 95-1, 267-297.

O'Brien, S. J., Tucker, R. D. and O'Driscoll, C. F. 1994. Neoproterozoic basement-cover relationships and the tectono-magmatic record of the Avalon Zone on the Hermitage Peninsula and environs, Newfoundland: New perspectives in the Appalachian-Caledonian Orogen. Geological Association of Canada Nuna Conference, Program and Abstracts, 21-22.

O'Brien, B. H., O'Brien, S. J. and Dunning, G. R. 1991. Silurian cover, late Precambrian-Early Ordovician basement, and the chronology of Silurian orogenesis in the Hermitage Flexure (Newfoundland Appalachians). American Journal of Science, vol.291, no.8, 760-799.

O'Brien, B. H., O'Brien, S. J., Dunning, G. R. and Tucker, R. D. 1993. Episodic reactivation of a late Precambrian mylonite zone on the Gondwanan margin of the Appalachians, southern Newfoundland. Tectonics, vol.12, no.4, 1043-1055.

O'Brien, B. H. 1988. Relationships of phyllite, schist and gneiss in the La Poile Bay-Roti Bay area (parts of 110/9 and 110/16), southwestern Newfoundland. Current Research – Newfoundland and Labrador Department of Natural Resources, Mineral Development Division, Report.88-1, 109-125.

O'Brien, B. H. 1987. The lithostratigraphy and structure of the Grand Bruit-Cinq Cerf area (parts of NTS areas 11O/9 and 11O/16), southwestern Newfoundland. Current Research - Newfoundland and Labrador Department of Natural Resources, Mineral Development Division, Report 87-1, 311-334.

O'Brien, B., Swinden, H. S., Dunning, G. R., Williams, S. H. and O'Brien, F. H. C. 1997. A peri-Gondwanan arc-back arc complex in Iapetus; Early-Mid Ordovician evolution of the Exploits Group, Newfoundland. American Journal of Science, vol.297, no.2, 220-272.

O'Brien, S. J. 2002. A note on Neoproterozoic gold, early Paleozoic copper and basement-cover relationships on the margins of the Holyrood Horst, southeastern Newfoundland. Current Research – Newfoundland and Labrador Department of Natural Resources, Geological Survey, Report 02-1, 219-227,

O'Brien,S. J., Dube,B. and O'Driscoll, C. F. 1999. High-sulphidation, epithermal-style hydrothermal systems in late Neoproterozoic Avalonian rocks on the Burin Peninsula, Newfoundland; implications for gold exploration. Current Research – Newfoundland and Labrador Department of Natural Resources, Geological Survey, Report 99-1, 275-296.

O'Brien, S. J., Dube, B., O'Driscoll, C. F. and Mills, J. 1998. Geological setting of gold mineralization and related hydrothermal alteration in late Neoproterozoic (post-640 ma) Avalonian rocks of Newfoundland, with a review of coeval gold deposits elsewhere in the Appalachian Avalonian belt. Current Research – Newfoundland and Labrador Department of Natural Resources, Geological Survey, Report 98-1, 93-124.

O'Brien, S. J., Dunning, G. R., Dube, B., O'Driscoll, C. F., Sparkes, B., Israel, S. and Ketchum, J. 2001. New insights into the Neoproterozoic geology of the central Avalon Peninsula (parts of NTS map areas 1N/6, 1N/7 and 1N/3), eastern Newfoundland. Current Research – Newfoundland and Labrador Department of Natural Resources, Geological Survey, Report 01-1, 169-189.

O'Brien, S. J., Dunning, G. R., Knight, I. and Dec, T. 1989. Late Precambrian geology of the north shore of Bonavista Bay (Clode Sound to Lockers Bay). Report of Activities – Newfoundland and Labrador Department of Natural Resources, Geological Survey, 49-50.

O'Brien, S. J., King, A. F. and O'Driscoll, C. F. 1997. Late Neoproterozoic geology of the central Avalon Peninsula, Newfoundland, with an overview of mineralization and hydrothermal alteration. Current Research - Newfoundland and Labrador Department of Natural Resources, Geological Survey, Report 97-1, 257-282.

O'Brien, S. J., Nunn, G. A. G., Dickson, W. L. and Tuach, J. 1984. Geology of Terrenceville (IM/10) and Gisborne lake (IM/15) map areas, southeast Newfoundland. Report of Activities - Newfoundland and Labrador Department of Natural Resources, Mineral Development Division, Report 84-4, 54 pages.

O'Brien, S. J., O'Brien, B. H., Dunning, G. R. and Tucker, R. D. 1996. Late Neoproterozoic Avalonian and related peri-Gondwanan rocks of the Newfoundland Appalachians. Special Paper - Geological Society of America, vol.304, 9-28.

O'Brien, S. J., O'Driscoll, C. F. and Tucker, R. D. 1992. A reinterpretation of the geology of parts of the Hermitage Peninsula, southwestern Avalon Zone, Newfoundland. Current Research - Newfoundland and Labrador Department of Natural Resources, Geological Survey, Report 92-1, 185-194.

O'Brien, S. J., Strong, D. F. and King, A. F. 1990. The Avalon Zone type area; southeastern Newfoundland Appalachians. Chapman and Hall : New York, NY, United States, 29 pages.

O'Brien, S. J., Wardle, R. J. and King, A. F. 1983. The Avalon Zone; a pan-African Terrane in the Appalachian Orogen of Canada. Geological Journal, vol.18, no.3, 195-222.

O'Nions, R. K., Hamilton, P. J. and Evensen, N. M. 1977. Variations in 143Nd/144Nd and 87Sr/86Sr ratios in oceanic basalts. Earth and Planetary Science Letters, vol.34, no.1, 13-22.

Papezik, V. S. 1970. Petrochemistry of volcanic rocks of the Harbour Main Group, Avalon Peninsula, Newfoundland. Canadian Journal of Earth Sciences, vol.7, no.6, 1485-1498.

Papezik, V. S. 1969. Late Precambrian ignimbrites on the Avalon Peninsula, Newfoundland. Canadian Journal of Earth Sciences, vol.6, no.6, 1405-1414.

Pearce, J. A. and Norry, M. J. 1979. Petrogenetic implications of Ti, Zr, Y, and Nb variations in volcanic rocks. Contributions to Mineralogy and Petrology, vol.69, no.1, 33-47.

Pearce, J. A. 1996. A user's guide to basalt discrimination diagrams. Short Course Notes - Geological Association of Canada, vol.12, 79-113.

Pearce, J. A., Harris, N. B. W. and Tindle, A. G. 1984. Trace element discrimination diagrams for the tectonic interpretation of granitic rocks. Journal of Petrology, vol.25, no.4, 956-983.

Peucat, J. J., Vidal, P., Bernard-Griffiths, J. and Condie, K. C. 1988. Sr, Nd, and Pb isotopic systematics in the Archean low- to high-grade transition zone of southern India; syn-accretion vs. post-accretion granulites. Journal of Geology, vol.97, no.5, 537-550.

Pisarevsky, S. A., Murphy, J. B., Cawood, P. A. and Collins, A. S. 2008. Late Neoproterozoic and Early Cambrian palaeogeography; models and problems. Geological Society Special Publications, vol.294, 9-31.

Pisarevsky, S. A., Wingate, M. T. D., Powell, C. M., Johnson, S. and Evans, D. A. D. 2003. Models of Rodinia assembly and fragmentation. Geological Society Special Publications, vol.206, 35-55.

Rollinson, H. R. 1993. Using geochemical data; evaluation, presentation, interpretation. Harlow, United Kingdom, 352 pages.

Rose, E. R. 1952. Torbay map-area, Newfoundland. Memoir - Geological Survey of Canada, 64 pages.

Rudnick, R. L., Barth, M., Horn, I., McDonough, W. F. 2000. Rutile-bearing refractory eclogites; missing link between continents and depleted mantle. Science, vol.287, no.5451, 278-281.

Sato, H. 1977. Nickel content of basaltic magmas; identification of primary magmas and a measure of the degree of olivine fractionation. Lithos, vol. 19, 113-120.

Sears,W. A. 1990. A geochemical, petrographic, and metallogenic analysis of volcanogenic sulphide deposition within the Connaigre Bay Group, Hermitage Peninsula, southern Newfoundland. Unpublished thesis, Memorial University of Newfoundland.

Shinjo, R., Chung, S., Kato,Y. and Kimura, M. 1999. Geochemical and Sr-Nd isotopic characteristics of volcanic rocks from the Okinawa trough and Ryukyu arc; implications for the evolution of a young, intracontinental back arc basin. Journal of Geophysical Research, vol. 104, 10591-10608.

Smith, R. S. 1987. Structural evolution of the Portugal Cove area, northeastern Avalon Zone, Newfoundland. Unpublished B. Sc. thesis, Memorial University of Newfoundland, 113 pages.

Sparkes, G. W. 2006. Late Neoproterozoic geology of the east coast of Conception Bay, Newfoundland Avalon Zone. Current Research - Newfoundland and Labrador Department of Natural Resources, Geological Survey, Report 06-1, 265-279.

Sparkes, G. W. 2005. The geological setting, geochemistry and geochronology of host rocks to high- and low-sulphidation style epithermal systems of the Eastern Avalon High-Alumina Belt, eastern Avalon Zone, Newfoundland. Unpublished M. Sc. thesis, Memorial University of Newfoundland, 313 pages.

Sparkes, G. W., O'Brien, S. J. and Dunning, G. R. 2007. Preliminary notes on some geochemical characteristics of plutonic and volcanic suites in the region between Manuels and Cape St. Francis, Avalon Peninsula, Newfoundland. Current Research - Newfoundland and Labrador Department of Natural Resources, Geological Survey, Report 07-1, 179-195.

Sparkes, G. W., O'Brien, S. J. and Dunning, G. R. 2004. The setting and timing of epithermal alteration and gold mineralization in the eastern Avalon Zone: An update.

Report of Activities - Newfoundland and Labrador Department of Natural Resources, Geological Survey, 24-26.

Sparkes, G. W., O'Brien, S. J., Dunning, G. R. and Dubé, B. 2005. U-Pb geochronological constraints on the timing of magmatism, epithermal alteration and low-sulphidation gold mineralization, eastern Avalon Zone, Newfoundland. Current Research - Newfoundland and Labrador Department of Natural Resources, Geological Survey, Report 05-1, 115-130.

Sparkes, B. A., O'Brien, S. J., Wilson, M. R. and Dunning, G. R. 2002. The geological setting, geochemistry and age of Late Proterozoic intrusive rocks at the Butlers Pond Cu-Au prospect (NTS 1N/3), Avalon Peninsula, Newfoundland. Current Research - Newfoundland and Labrador Department of Natural Resources, Geological Survey, Report 02-1, 245-264.

Stacey, J. S. and Kramers, J. D. 1975. Approximation of terrestrial lead isotope evolution by a two-stage model. Earth and Planetary Science Letters, vol.26, no.2, 207-221.

Stolz, A. J., Varne, R., Davies, G. R., Wheller, G. E. and Foden, J. D. 1990. Magma source components in an arc-continent collision zone; the Flores-Lembata sector, Sunda arc, Indonesia. Contributions to Mineralogy and Petrology, vol.105, no.5, 585-601.

Streckeisen, A. 1976. To each plutonic rock its proper name. Earth-Science Reviews, vol.12, no.1, 1-33.

Strong, D. F. and Dostal, J. 1980. Dynamic melting of Proterozoic upper mantle; evidence from rare earth elements in oceanic crust of eastern Newfoundland. Contributions to Mineralogy and Petrology, vol.72, no.2, 165-173.

Strong, D. F., O'Brien, S. J., Taylor, S. W., Strong, P. G. and Wilton, D. H. 1978. Aborted Proterozoic rifting in eastern Newfoundland. Canadian Journal of Earth Sciences, vol.15, no.1, 117-131.

Sun, S. S. and McDonough, W. F. 1989. Chemical and isotopic systematics of oceanic basalts; implications for mantle composition and processes. Geological Society Special Publications, vol.42, 313-345.

Swinden, H. S. and Hunt,P. A. 1991. A U-Pb zircon age from the Connaigre Bay Group, southwestern Avalon Zone, Newfoundland; implications for regional correlations and metallogenesis, *in* Radiogenic age and isotopic studies, Report 4, Geological Survey of Canada, Paper 90-2, 3-10.

Tanaka, T., Togashi, S., Kamioka, H., Amakawa, H., Kagami, H., Hamamoto, T., Yuhara, M., Orihashi, Y., Yoneda, S., Shimizu, H., Kunimaru, T., Takahashi, K., Yanagi, T., Nakano, T., Fujimaki, H., Shinjo, R., Asahara, Y., Tanimizu, M. and Dragusanu, C. 2000. JNdi-1; a neodymium isotopic reference in consistency with LaJolla neodymium. Chemical Geology, vol. 168, no. 3-4, 279-281.

Taylor, S. 1976. Geology of Marystown map sheet (E/2), Burin Peninsula, southeastern Newfoundland. Unpublished M. Sc. thesis, Memorial University of Newfoundland, 165 pages.

Theokritoff, G. 1979. Early Cambrian provincialism and biogeographic boundaries in the North Atlantic region. Lethaia, vol.12, 281-295.

Thompson, M. D., Grunow, A. M. and Ramezani, J. 2007. Late Neoproterozoic paleogeography of the southeastern New England Avalon Zone; insights from U-Pb geochronology and paleomagnetism. Geological Society of America Bulletin, vol.119, no.5-6, 681-696.

Valverde-Vaquero, P., Dunning, G. R. and O'Brien, S. J. 2006. Polycyclic evolution of the late Neoproterozoic basement in the Hermitage Flexure region (southwest Newfoundland Appalachians); new evidence from the Cinq-Cerf Gneiss. Precambrian Research, vol. 148, 1-18.

van Staal, C. R., Dewey, J. F., Mac Niocaill, C. and McKerrow, W. S. 1998. The Cambrian-Silurian tectonic evolution of the northern Appalachians and British Caledonides; history of a complex, west and southwest Pacific-type segment of Iapetus. Geological Society Special Publications, vol.143, 199-242.

Walcott, C. D. 1900. Random, a pre-Cambrian upper Algonkian terrane. Geological Society of America Bulletin, vol.11, 3-5.

Williams, H. 1979. Appalachian orogen in Canada. Canadian Journal of Earth Sciences, vol.16, no.3, 792-807.

Williams, H. 1971. Geology of Belleoram Map-Area, Newfoundland (1M/11). Paper - Geological Survey of Canada, vol.70-65, 39 pages.

Williams, H. and King, A. F. 1979. Trepassey map area, Newfoundland. Memoir - Geological Survey of Canada, no. 389, 24 pages.

Williams, H. 1964. The Appalachians in Northeastern Newfoundland; a two-sided symmetrical system. American Journal of Science, vol.262, no.10, 1137-1158.

Williams, H., Kennedy, M. J. and Neale, E. R. W. 1970. The Hermitage Flexure, the Cabot Fault, and the disappearance of the Newfoundland central mobile belt. Geological Society of America Bulletin, vol.81, no.5, 1563-1567.

Wilson, J. T. 1966. Did the Atlantic close and then re-open? Nature, vol.211, no.5050, 676-681.

Winchester, J. A. and Floyd, P. A. 1977. Geochemical discrimination of different magma series and their differentiation products using immobile elements. Chemical Geology, vol.20, no.4, 325-343.

Winchester, J. A. and Floyd, P. A. 1977. Geochemical discrimination of different magma series and their differentiation products using immobile elements. Chemical Geology, vol.20, no.4, 325-343.

Wingate, M. T. D. and Giddings, J. W. 2000. Age and palaeomagnetism of the Mundine Well dyke swarm, Western Australia; implications for an Australia-Laurentia connection at 755 ma. Precambrian Research, vol.100, no.1-3, 335-357.

APPENDIX A: THIN SECTION DESCRIPTIONS

The petrography of 117 samples from the study area are summarized in Tables A-1 to A-12, below. The tables include modal abundances, grain sizes and descriptions of vein-filling minerals, foliations and textures.

Notes for Tables A-1 through A-12: t.s.=thin section, phenos=phenocrysts, μm=micrometers, min=minimum, max=maximum, ave=average, mins=minerals, gm=groundmass, fb=flow banding, xtl=crystal, f.gr.=fine-grained, c.gr.=coarse-grained, b/w=between, w/=with, surr'd=surrounded, conc'd=concentrated. Vein-filling minerals are not included in modal abundances. Grain sizes of groundmass minerals refer to plagioclase and other igneous minerals in the groundmass. No minimum grain size is estimated for the groundmass, since the minimum grain size for all groundmass minerals is <50 μm. For thin sections in which no maximum grain size is given, maximum grain size of groundmass minerals is <50 μm.

Table A-1: Mineralogy and petrography of **granodiorite** thin sections.

Sample	Sample location	Mineralogy													Grain Size (μm)			
		Porphyroclasts (% t.s.)			Groundmass (% t.s.)									Accessory minerals	Porphyroclasts		Groundmass	
		Pl	Kfs	Qtz	Pl	Qtz	Kfs	Hbl	Epi	Act	Chl	Opq	Carb		Min-Max	Ave	Max	Ave
DS-09-13	Section A-A'				50	41	5		2		1	1					900	300
DS-09-27	Section A-A'				35	46	7		4		4	3	1	Ser, Act			2000	300
DS-09-33	Section A-A'				32	43	6	2	7		6	3	1	Ser, Ttn			2000	300
DS-09-36	Section B-B'				23	50	19		5	1	2			Opq, Ser			450	150
DS-09-42	Section C-C'				41	48	4		3		2	2		Ser			2000	300
DS-09-44	Section C-C'				41	48	4		3		2	2		Ser, Ttn			2000	300
DS-09-62	Section B-B'				12	65	12		10			1					1800	350
DS-09-68	Map 2	13	7	7	30	37		1	2		2	1			500-10000	2000		<50
DS-09-70	Map 2				36	36	20		3		2	3		Ttn			1000	500
DS-09-80	Map 2	7	2	4	41	40			2		2	2		Ttn	250-2500	1000		<50
DS-09-107	Map 1	14	2	2	39	39			1	1	1	1			250-2000	1000		<50
DS-09-118	Map 1	15	7	10	30	31			1	2	2	2		Hbl	500-10000	2000		<50
DS-09-128	Map 1	15	5	4	30	38			2	2	3	1			500-10000	2000		<50
DS-09-148	Map 1	5			35	30	15		10			5		Ap	500-5000	1000	200	50
DS-09-171	Map 1				25	50	25		3			2					2000	700
DS-09-199	Section B-B'	15	5		38	38			1		2	1			250-2500	2000		<50
DS-09-200	Map 3				36	30	15		5		7	7		Ser			2000	300
DS-09-202	Map 3				26	45	17		5		4	3		Opq, Ser			450	150

Table A-1 (continued): Mineralogy and petrography of **granodiorite** thin sections.

Sample	Veins		Foliation defined by:	Comments
	Vein-filling minerals	% t.s.		
DS-09-13	Epi	50		
DS-09-27	Epi (±Qtz)	25		
DS-09-33	Epi (±Carb±Qtz)	50		
DS-09-36	Epi	20		More f.gr. than other granodiorite samples, and equigranular: granulated, rextlized; exsolution: perthite, flame-textured mesoperthite (in ~25% Fsp grains)
DS-09-42				Exsolution in Kfs (perthite)
DS-09-44	Qtz±Epi	1		Exsolution in Kfs (perthite)
DS-09-62	Epi+Qtz	20		
DS-09-68	Epi±Chl±Opq	10	Gm mins, Qtz ribbons	Qtz porphyroclasts are stretched into partially rextlized ribbons up to 1 cm long; Fsp porphyroclasts and Qtz ribbons are offset by Epi±Chl-filled fractures; gm is intergrown, nearly microxtline Qtz+Pl: granulated, rextlized
DS-09-70	Epi+Opq	5		Qtz+Fsp xtls are commonly fractured; nearly microxtline Qtz+Fsp occurs in vein-like networks (~30% t.s.) b/w areas of larger xtls
DS-09-80	Epi, Opq	2	Gm mins, Fsp porphyroclasts	Deformed granodiorite: Fsp and Qtz grains surr'd by granulated gm
DS-09-107	Epi+Opq	10	Qtz ribbons, gm mins	Epi forms elongate aggregates (up to 2 mm long; <1% t.s) in the shape of bladed xtls: pseudomorphing another mineral?; some Qtz grains are stetched into ribbons; some Pl grains have diffuse boundaries: resorption by matrix?; some Fsp clasts are euhedral: was originally a porphyritic rock, not granodiorite?
DS-09-118	Epi	7	Qtz ribbons, some Epi veins, gm mins	Qtz porphyroclasts are stretched into partially rextlized ribbons up to 1 cm long; Fsp porphyroclasts and Qtz ribbons are offset by Epi±Chl-filled fractures; gm is intergrown, nearly microxtline Qtz+Fsp: granulated, rextlized
DS-09-128	Epi	3	Qtz ribbons, some Epi veins, gm mins	Qtz porphyroclasts are stretched into partially rextlized ribbons up to 1 cm long; Fsp porphyroclasts and Qtz ribbons are offset by Epi±Chl-filled fractures; gm is intergrown, nearly microxtline Qtz+Pl: granulated, rextlized
DS-09-148	Epi	15		Gm is ~equigranular, mostly subhedral xtls with some euhedral xtls forming triple-junctions: rextlized; many Pl phenos have diffuse boundaries, suggesting resorption by gm; all Pl phenos contain tiny round Qtz (+Fsp?) xtls
DS-09-171	Epi+Opq	50		Fsp+Qtz xtls are hydrothermally brecciated within veins; Kfs displays perthitic texture, mesoperthitic in some grains
DS-09-199	Epi, Qtz	2	Gm mins, Fsp porphyroclasts	
DS-09-200				
DS-09-202	Epi	5		Very similar to #36; similar mins to #200, but much more f.gr (granulated); exsolution in Kfs: perthite, flame-textured mesoperthite

Table A-2: Mineralogy and petrography of **feldspar porphyry** thin sections.

Sample	Sample location	Mineralogy									Grain Size (μm)			
		Phenos (% t.s.)		Groundmass (% t.s.)						Accessory minerals	Phenocrysts		Groundmass	
		Pl	Kfs	Pl	Qtz	Epi	Act	Chl	Opq		Min-Max	Ave	Max	Ave
DS-09-01B	Section A-A'	3	2	45	30	15			5		500-1000	700		<50
DS-09-07	Section A-A'	5	4	37	34	7	3	5	5	Ser	250-2000	1000		<50
DS-09-11	Section A-A'	4	4	35	33	10	4		10		200-1000	500		<50
DS-09-37	Section B-B'	4	4	44	25	15	1	4	3	Ser	200-1500	700	75	<50
DS-09-61	Section B-B'	2	2	50	37	4		3	2		200-1000	700	100	75
DS-09-98	Map 1	4	3	46	42	2		1	2		500-4000	1000	250	150
DS-09-112	Map 1	2	2	49	42	2		1	2		500-4000	1000	250	100
DS-09-117	Map 1	4	4	46	30	10	2	2	2		500-2000	1000	250	200
DS-09-134	Map 1	2	2	49	42	2		1	2		500-4000	1000	250	100
DS-09-139	Map 1	2	2	49	42	2		1	2		500-4000	1000	250	150
DS-09-164	Map 1	2	2	47	40	3		2	4		500-4000	1000		<50
DS-09-177	Map 1	2	2	47	40	3		2	4	Hbl	500-4000	1000		<50
DS-09-178	Map 1	2	2	49	42	2		1	2		500-4000	1000	250	150
DS-09-182	Map 1	2	2	49	42	2		1	2		500-4000	1000	250	150
DS-09-191	Section B-B'			46	45	4		2	3				500	250
DS-09-193	Map 1	2	2	49	42	2		1	2		500-4000	1000	250	150
DS-09-198	Map 1			45	40	10		2	3				500	250

Table A-2 (continued): Mineralogy and petrography of **feldspar porphyry** thin sections.

Sample	Veins		Foliation defined by:	Comments
	Vein-filling minerals	% t.s.		
DS-09-01B	Epi	25		~1/3 phenos (~4% of t.s.) have been replaced by Epi aggregates
DS-09-07	Qtz	1		Some Fsp phenos are fragmental; some phenos replaced by Epi aggregates (~2% t.s.)
DS-09-11	Epi+Opq	1	Opq, gm Pl	All Fsp phenos partially (10-90%) replaced by Epi aggregates; contact w/Hbl basaltic dyke: parallel to foliation, no chilled margin
DS-09-37	Epi	30	Pl	All Fsp phenos partially (30-50%) replaced by Epi; some fully replaced: Epi aggregates (±Chl) pseudomorphing Pl (~2% t.s.)
DS-09-61				
DS-09-98	Opq±Epi	2		
DS-09-112	Opq±Epi	1		
DS-09-117	Epi±Opq	15	Chl+Act+Epi in gm	Fsp phenos locally occur in clusters of up to 6 xtls; Epi forms aggregates replacing Fsp phenos: some Fsp phenos (~1% t.s.) fully replaced by Epi
DS-09-134	Opq±Epi	2	gm mins	
DS-09-139	Opq±Epi	1		
DS-09-164	Opq+Epi	2		
DS-09-177	Opq+Epi	2		Rare Hbl xtls are subhedral, tabular-shaped, ~250-1000 μm, ave.~500 μm
DS-09-178	Qtz, Opq+Epi	4		
DS-09-182	Epi+Opq, Qtz±Chl	2		
DS-09-191	Epi	2		Epi forms ~0.5 mm, tabular-shaped aggegates: probably pseudomorphing Fsp phenos (~2% t.s.)
DS-09-193	Epi+Opq	1		
DS-09-198	Epi	1		Epi forms ~0.5 mm, tabular-shaped aggregates: probably pseudormorphing Fsp phenos (~7% t.s.)

Table A-3: Mineralogy and petrography of **gabbro** thin sections.

Sample	Sample location	Mineralogy									Grain Size (μm)			
		Phenos (% t.s.)	Groundmass (% t.s.)							Accessory minerals	Phenocrysts		Groundmass	
		Pl	Pl	Hbl	Epi	Act	Chl	Opq	Cpx		Min-Max	Ave	Max	Ave
DS-09-72	Map 2		38	21	8	12	14	7					1500	700
DS-09-73	Map 2	3	23		17	25	12	17	3	Ser	1500-4000	2000	400	250
DS-09-76	Map 2	3	23		17	25	12	17	3	Ser	1500-4000	2000	400	250
DS-09-82	Map 2		27	7	8	30	8	8	12				2500	1000
DS-09-85	Map 2		27	7	8	30	8	8	12				2500	1000

Sample	Veins		Foliation defined by:	Comments
	Vein-filling minerals	% t.s.		
DS-09-72	Epi	30		Hbl is partially replaced by Act+Chl, but twinning still preserved in some grains; large Hbl/Act grains envelop Pl laths: is this Cpx replaced by Hbl/Act?
DS-09-73	Qtz±Carb, Epi+Opq	2	Opq, Act±Chl aggregates, Chl aggregates	Intensely altered; anhedral Cpx remnants surr'd by Act+Chl (partial replacement of Cpx by greenschist mins); some Act aggregates pseudomorphing Hbl?; Chl is conc'd in large (up to 2 mm) clots ± Epi
DS-09-76	Qtz±Epi	1		Intensely altered; anhedral Cpx remnants surr'd by Act+Chl (partial replacement of Cpx by greenschist mins); some Act aggregates pseudomorphing Hbl?; Chl is conc'd in large (up to 2 mm) clots ± euhedral Epi
DS-09-82	Epi+Carb, Qtz	2		Hbl and Cpx are both partially replaced by Act+Chl; Cpx partially encloses Pl laths: sub-ophitic texture
DS-09-85				Hbl and Cpx are both partially replaced by Act+Chl

Table A-4: Mineralogy and petrography of **diorite** thin sections.

Sample	Sample location	Mineralogy								Grain Size (μm)			
		Phenos (% t.s.)	Groundmass (% t.s.)							Phenocrysts		Groundmass	
		Pl	Pl	Hbl	Epi	Act	Chl	Ttn	Opq	Accessory minerals	Min-Max	Ave	Max	Ave
DS-09-19	Section A-A'		45	30	7	5	3	5	5	Ap			1000	500
DS-09-23	Section A-A'	2	55		13	13	12		5	Ser	200-600	450	500	300
DS-09-26	Section A-A'		50	25	7	5	3	5	5	Ap			800	400
DS-09-39	Section B-B'		33	25	8	18	14		2	Ttn			900	500
DS-09-52	Section C-C'		55		10	13	15		7	Carb			1800	700
DS-09-77	Map 2		55	11	3	12	14		5				2000	1000
DS-09-102	Map 1		40	20	6	20	8		6				2000	1000
DS-09-105	Map 1		38	19	8	14	14		7	Ser			2000	1000
DS-09-131	Map 1		38	10	7	30	10		5				2000	1000
DS-09-133	Map 1		40	20	6	20	8		6	Ser			2000	1000
DS-09-135	Map 1		38	10	7	30	10		5				2000	1000
DS-09-146	Map 1		40	20	6	20	8		6	Ser			1000	700
DS-09-160	Map 1		38	10	7	30	10		5				2000	1000
DS-09-170	Map 1		40	20	6	20	8		6	Ser			1000	700
DS-09-184	Map 1	2	38	20	6	20	8		6	Ser	1000-2000	1500	1000	700
DS-09-187	Map 1	2	38	20	6	20	8		6	Ser	1000-2000	1500	1000	700

Table A-4 (continued): Mineralogy and petrography of **diorite** thin sections.

Sample	Veins		Foliation defined by:	Comments
	Vein-filling minerals	% t.s.		
DS-09-19				Several angular, tabular-shaped Epi aggregates (~4% t.s.) pseudomorphing another mineral; Act (± Chl) seems to have partially replaced Hbl
DS-09-23				
DS-09-26	Epi±Qtz±Chl± Carb, Chl±Qtz	5		
DS-09-39	Epi	30		~50% of original Hbl appears to have been replaced by Act±Chl
DS-09-52	Epi+Chl+Act	1		
DS-09-77				Hbl mostly replaced by Act+Chl; contains one subhedral, blocky, ~5 mm long Pl phenocryst
DS-09-102	Epi	2		Contains one ~2 mm long, subhedral, blocky Pl phenocryst; Hbl is partially replaced by Act+Chl; Hbl appears to fill spaces b/w groundmass Pl laths; Epi forms lath-shaped aggregates up to 2.5 mm long: pseudomorphing another mineral?
DS-09-105	Epi	2	Opq	Intensely altered; Hbl partially replaced by Act+Chl
DS-09-131	Epi	1	Opq, Hbl/Act	
DS-09-133	Epi	1		
DS-09-135	Epi	<1		
DS-09-146	Epi±Opq	<1	Opq±Chl±Hbl /Act	Opq aggregates (up to 1 mm wide) surr'd by Epi occur near veins
DS-09-160	Epi	5	Opq, Hbl/Act	
DS-09-170	Epi+Chl	<1		
DS-09-184	Epi, Opq	1		
DS-09-187				

Table A-5: Mineralogy and petrography of **hornblende-porphyritic andesitic dyke** thin sections.

Sample	Sample location	Mineralogy										Grain Size (μm)			
		Phenos (% t.s.)		Groundmass (% t.s.)							Accessory minerals	Phenocrysts		Groundmass	
		Pl	Hbl	Pl	Qtz	Epi	Act	Chl	Ttn	Opq		Min-Max	Ave	Max	Ave
DS-09-100	Map 1	7	12	33	25	5	6	6	1	5		200-2500	750	150	100
DS-09-138	Map 1	12	7	50		5	10	9		7	Ser	400-3000	1000	600	250

Sample	Veins		Foliation defined by:	Comments
	Vein-filling minerals	% t.s.		
DS-09-100	Epi±Opq	<1	Hbl phenos, Act+Chl+Epi aggregates in gm	Hbl occurs as subhedral to euhedral, strongly brown-to-dark brown pleochroic xtls; many Hbl grains are twinned; some have zoning defined by Opq needles exsolved at xtl edges
DS-09-138	Epi	<1	Act+Chl+Opq+Epi in gm	Hbl is partially replaced by Act+Chl; Chl+Epi form irregularly-shaped aggregates up to 1 mm long

Table A-6: Mineralogy and petrography of **hornblende basaltic dyke** thin sections.

Sample	Sample location	Mineralogy										Grain Size (μm)			
		Phenos (% t.s.)	Groundmass (% t.s.)								Accessory minerals	Phenocrysts		Groundmass	
		Pl	Pl	Qtz	Hbl	Epi	Act	Chl	Ttn	Opq	Carb		Min-Max	Ave	Max	Ave
DS-09-11	Section A-A'		45		15	12	15	10		3						<50
DS-09-12	Section A-A'	4	50	1	9	3	9	17	3	4		Se, Ap	450-1800	650	250	150
DS-09-18	Section A-A'		38	1	12	3	12	24	3	7					250	100
DS-09-31	Section A-A'		50		15	3	12	14		6					150	75
DS-09-34	Section B-B'		15	15	10	25	13	12	10						150	75
DS-09-40	Section C-C'	3	45	3	9	9	9	8		8	6	Ser	200-1000	400	300	200
DS-09-60	Map 3		45		5	15		25		10					100	75
DS-09-63	Map 2	3	40		13	7	12	13		12			200-700	450	150	75
DS-09-67	Map 2		50		15	3	14	8		10					1000	250
DS-09-69	Map 2		50		15	3	14	8		10					1000	250
DS-09-75	Map 2	12	27	1	10	10	21	10		9		Ser	700-6000	2000	1000	300
DS-09-78	Map 2		41		13	4	14	8		20					500	250
DS-09-88	Map 2	12	35	1	8	8	19	8		9		Ser	700-6000	2000	1000	300
DS-09-99	Map 1		50		13	3	16	8		10					1000	250
DS-09-132	Map 1		41		13	4	14	8		20		Ser			500	250
DS-09-188	Map 1		44		12	10	12	10		12					700	500

Table A-6 (continued): Mineralogy and petrography of **hornblende basaltic dyke** thin sections.

Sample	Veins		Foliation defined by:	Comments
	Vein-filling minerals	% t.s.		
DS-09-11	Epi+Opq	1	Act, Chl, Pl, Act-rich/poor layering	Lath-shaped Epi aggregates (~2% t.s.); large (up to 600 μm) Chl xtls (~2% t.s.) elongate parallel to foliation; contact w/ feldspar porphyry: parallel to foliation, no chilled margin
DS-09-12	Epi±Qtz	2		
DS-09-18	Epi±Qtz±Chl	3	Pl, Act, Chl, Act-rich/poor layering	
DS-09-31	Epi (±Opqs±Carb)	4	All mins	GmPl appears brecciated
DS-09-34				
DS-09-40				Chl+Epi+Carb seem to be replacing Hbl
DS-09-60	Epi	20		
DS-09-63				
DS-09-67	Epi	<1		Hbl is partially replaced by Act+Chl
DS-09-69	Epi, Chl	2	Opq, Act+Hbl+Chl aggregates	Hbl is partially replaced by Act+Chl
DS-09-75	Qtz+Pl	<1		Intensely altered; Hbl is partially replaced by Act+Chl; Chl forms aggregates (up to 2 mm) with Epi±Act
DS-09-78	Qtz+Chl	15	Act+Chl+Opq+Epi in gm	
DS-09-88	Epi	1	Pl phenos, Act+Chl+Opq in gm	Intensely altered; Hbl is partially replaced by Act+Chl; Chl forms aggregates (up to 2 mm) with Epi±Act
DS-09-99	Epi±Opq	3	Act+Chl+Opq in gm	
DS-09-132	Epi	3		Contains one ~5 mm long, subhedral, blocky Pl pheno
DS-09-188				

Table A-7: Mineralogy and petrography of **basaltic dyke** thin sections.

Sample	Sample location	Mineralogy										Grain Size (μm)			
		Phenos (% t.s.)	Groundmass (% t.s.)								Accessory minerals	Phenocrysts		Groundmass	
		Pl	Pl	Qtz	Epi	Act	Chl	Ttn	Opq	Cpx	Scp		Min-Max	Ave	Max	Ave
DS-09-20	Section A-A'		30		10	24	24	3	7	2		Carb			200	100
DS-09-53	Map 3		30	2	7	30	16		10	5					700	250
DS-09-71	Map 2	1	55		5	14	12		5	8		Carb	2000-5000	2500	2000	700
DS-09-74	Map 2		40		4	25	8		20	3					500	250
DS-09-84	Map 2	2	38		4	25	8		20	3			2000-5000	2500	400	250
DS-09-123	Map 1		40	3	3	4	6		5	30	9				1200	250

Sample	Veins		Foliation defined by:	Comments
	Vein-filling minerals	% t.s.		
DS-09-20				Intensely altered (abundant greenschist facies minerals); Cpx grains surr'd & partially replaced by Chl & Act
DS-09-53				Cpx xtls seem to be "skeletons" of xtls surr'd by Act; large (~300 μm) Act xtls often surround pieces of Cpx
DS-09-71				Anhedral Cpx remnants are surr'd by Act+Chl: partial replacement of Cpx by greenschist minerals
DS-09-74	Epi	<1		Anhedral Cpx remnants are surr'd by Act+Chl: partial replacement of Cpx by greenschist minerals; Chl forms ~500 μm clots with euhedral Epi
DS-09-84			Act+Chl+Opq +Epi in gm	
DS-09-123			Chl aggregates	Anhedral Cpx partially encloses Pl laths: sub-ophitic texture; Cpx exhibits strong pinkish-brown-to-lt-pinkish-brown pleochroism; very little replacement of Cpx by Act+Chl; Chl forms ~700 μm long, tabular-shaped aggregates (±Epi) that comprise ~3% t.s.: pseudomorphing another mineral?; Pl is partially replaced by Scp

Table A-8: Mineralogy and petrography of **andesitic dyke** thin sections.

Sample	Sample location	Mineralogy										Grain Size (μm)			
		Phenos (% t.s.)		Groundmass (% t.s.)							Accessory minerals	Phenocrysts		Groundmass	
		Pl	Cpx	Pl	Qtz	Hbl	Epi	Act	Chl	Opq		Min-Max	Ave	Max	Ave
DS-09-21	Section A-A'			55			15	5	15	10				250	100
DS-09-35	Section B-B'	2		60	2		10		20	6	Scr	75-450	150		<50
DS-09-55	Map 3	1		50	15		12	8	8	6		150-450	150	100	<50
DS-09-55B	Map 3	1		40	22		14	8	12	3		150-450	150	100	<50
DS-09-59	Map 3	1		40	16		16	10	14	3		150-450	150	100	<50
DS-09-89	Map 2	4		64		1	6	7	10	8		500-2000	1000	700	500
DS-09-96	Map 1	2		58			8	10	12	10		500-2000	1000	700	500
DS-09-103	Map 1	6	4	52			10	10	10	8		250-2000	1000	500	250
DS-09-104	Map 1	2		76			3	6	4	9		500-2000	1000	1000	500
DS-09-152	Map 1	1		60			10	10	10	9		250-500	500	500	250
DS-09-165	Map 1	4		64		1	6	7	10	8		500-2000	1000	700	500
DS-09-167	Map 1	2		64			7	8	11	8		500-2000	1000	700	500
DS-09-175	Map 1	4		64		1	6	7	10	8		500-2000	1000	700	500
DS-09-203	Map 2	5		59			7	10	10	9		500-2000	1000	700	500

Table A-8 (continued): Mineralogy and petrography of **andesitic dyke** thin sections.

Sample	Veins		Foliation defined by:	Comments
	Vein-filling minerals	% t.s.		
DS-09-21			Pl, Act, Chl	
DS-09-35	Epi+Opq	10		Pheno-shaped Epi aggregates (~0.5% t.s.) pseudomorphing Pl
DS-09-55	Qtz+Epi	40		
DS-09-55B			Gm Pl, felsic bands	Several felsic bands (Pl+Qtz-rich, Chl-Epi-Act-poor) ~300 μm thick, parallel to each other; pockets of Qtz pseudomorphing Pl phenos (~2% t.s.); several large (~1000 μm) Epi+Qtz±Chl±Opq aggregates in or adjacent to felsic bands
DS-09-59	Epi	1	Gm Pl	Very similar to #55B, but greenschist mins are more abundant, and no felsic bands
DS-09-89	Carb+Qtz	1		
DS-09-96			Gm Pl+Chl+Act	
DS-09-103			Gm Pl	Cpx phenos are subhedral tabular xtls partially replaced by Act+Chl; some Cpx grains are twinned; Epi forms irregularly-shaped aggregates up to 500 μm long
DS-09-104	Epi, Qtz	<1	Gm Pl+Act	
DS-09-152	Qtz+Chl	10	Gm Chl+Act	
DS-09-165	Epi+Chl	<1	Gm Pl, Chl+Act+Epi	
DS-09-167	Epi, Qtz+Chl	3	Gm Pl, Chl+Act+Epi	
DS-09-175				
DS-09-203	Epi	<1		

Table A-9: Mineralogy and petrography of **basaltic-andesitic dyke** thin sections.

Sample	Sample location	Mineralogy								Grain Size (μm)			
		Phenos (% t.s.)	Groundmass (% t.s.)						Accessory minerals	Phenocrysts		Groundmass	
		Pl	Pl	Qtz	Epi	Act	Chl	Opq		Min-Max	Ave	Max	Ave
DS-09-28	Section A-A'		35		17		30	18					<50
DS-09-38	Section B-B'	4	50		4	12	22	8		150-1500	450	200	75
DS-09-43	Section C-C'	30	30		4		30	6	Ser	400-3600	1800	150	100
DS-09-91	Map 2		43		14	2	16	25	Hbl			400	250
DS-09-143	Map 1		53			10	30	7				1000	400
DS-09-155	Map 1		40	12	11	10	12	15	Ser			2000	1000
DS-09-181	Map 1		51	1	10	10	18	10				700	500
DS-09-194	Map 1		60	2	6	8	16	8				700	500

Sample	Veins		Foliation defined by:	Comments
	Vein-filling minerals	% t.s.		
DS-09-28			All mins, Pl-rich/Chl+Opq-rich layering	Rare large (25X450 μm) Chl clots elongate parallel to foliation; large (100X450 μm) xtl-shaped (angular, tabular) Epi aggregates (~1% t.s.) pseudomorphing another min; chilled margin against granodiorite (which makes up ~50% t.s.)
DS-09-38	Epi+Opq±Chl	4	All mins, veins	Partial replacement of Pl phenos by Chl+Act+Opq±Epi, conc'd at xtl cores; Epi pseudomorphing Pl (<1% t.s.); gm Pl appears fragmental
DS-09-43	Epi	1	Pl phenos, clots of Chl+Opqs, gm Pl, veins	Abundant Chl inclusions in Pl phenos, and filling fractures in Pl phenos
DS-09-91	Opq	1		Contains <1% Pl phenos: ~700 μm, subhedral, blocky xtls; contains one ~500 μm, subhedral Hbl crystal, mostly replaced by Chl
DS-09-143	Epi+Opq	65		Pl grains are hydrothermally brecciated
DS-09-155	Epi, Qtz, Opq	2		~1 mm long, subhedral, blocky Pl phenos comprise <1% t.s.; gm Pl occurs as very elongate subhedral laths, with length often 15X width; Opq form elongate rectangular or rod-shaped aggregates (~250 μm) w/leucoxene: altered ilmeno-magnetites
DS-09-181	Qtz, Epi+Opq	1		Subhedral, blocky, up to 1 mm long Pl phenos comprise <1% t.s.
DS-09-194	Epi+Carb	1		

Table A-10: Mineralogy and petrography of **oxide-rich andesitic dyke** thin sections.

Sample	Sample location	Mineralogy										Grain Size (μm)			
		Phenos (% t.s.)		Groundmass (% t.s.)							Accessory minerals	Phenocrysts		Groundmass	
		Pl	Qtz	Pl	Qtz	Hbl	Epi	Act	Chl	Opq		Min-Max	Ave	Max	Ave
DS-09-50	Section C-C'	1		30	15		10		29	15	Ser	150-400	300	75	75
DS-09-56	Map 3	2	6	11	11		20		25	25		<50-800	200		<50
DS-09-57	Map 3	5		45	15		9		14	12		75-700	300	100	75
DS-09-79	Map 2	1		27	5	3	15	17	12	20		250-1000	400	250	100
DS-09-145	Map 1			39	12		10	6	16	17				250	100

Sample	Veins		Foliation defined by:	Comments
	Vein-filling minerals	% t.s.		
DS-09-50	Qtz±Carb	20	All mins	Subtle chilled margin in dyke against feldspar porphyry; foliation parallel to contact
DS-09-56			Pl & Qtz phenos, clots of Opq+Chl, clotted Opq/disseminated Opq layering	Phenos: Qtz (~50 μm) smaller than Pl (250 μm); one large (3300 X 450 μm) Opq+Chl+Epi aggregate (lithic frag?), elongate parallel to foliation; foliation is cut by a second foliation defined by ribbons of Act
DS-09-57			Gm Pl	Pl phenos tend to occur in clusters (up to 20 xtls); large (up to 100 μm) Chl clots & Opq xtls occur adjacent to Pl phenos
DS-09-79	Epi	<1		Opq occur as chains of tiny, euhedral xtls: igneous magnetite?; compositional banding (~3 mm thick) defined by different %'s of Opq: flow banding?
DS-09-145			Gm minerals, Qtz aggregates	~250 μm long, euhedral, blocky Pl phenos comprise <1% t.s.; Qtz is conc'd in aggregates, up to 5 mm long, elongate parallel to foliation

Table A-11: Mineralogy and petrography of **oxide-rich basaltic dyke** thin sections.

Sample	Sample location	Mineralogy								Grain Size (μm)			
		Phenos (% t.s.)	Groundmass (% t.s.)						Accessory minerals	Phenocrysts		Groundmass	
		Pl	Pl	Qtz	Epi	Act	Chl	Opq		Min-Max	Ave	Max	Ave
DS-09-08	Section A-A'	5	29	10	16		26	14	Ser	250-1000	500		<50
DS-09-29	Section A-A'	4	35		16		29	16	Carb	50-1800	100		<50
DS-09-47	Section C-C'		36		15		35	14					<50
DS-09-51	Section C-C'		20		5		10	65					<50
DS-09-64	Map 2		25		12	20	18	25					<50
DS-09-129	Map 1		42	2	10	6	20	20				250	100
DS-09-174	Map 1	1	38	2	9	10	10	30		400-1000	700	350	100

Sample	Veins		Foliation defined by:	Comments
	Vein-filling minerals	% t.s.		
DS-09-08	Epi+Opq	1		Some Qtz & Pl phenos replaced by Epi aggregates (~2% t.s.); round vescicles (~4% t.s.) rimmed by Epi xtls
DS-09-29			All mins, Chl-rich/poor layering	Large (~100 μm) xtl-shaped (tabular, round) Epi aggregates (~2% t.s.) pseudomorphing another min
DS-09-47	Epi±Opq	2		Opq form large (up to 300 μm) clots conc'd in an area of the t.s. w/rusty-orange staining & abundant, thin, Opq-filled veins
DS-09-51				Very rich in Opq: very few visible Pl laths; some Epi forms round aggregates w/Chl at centre: Epi+Chl filled vescicles?
DS-09-64	Epi+Chl	2	All mins, Chl aggregates	Flow (?) foliation also defined by Opq-rich patches throughout gm; Chl is conc'd in tabular-shaped aggregates elongate parallel to foliation: pseudomorphing Pl phenocrysts?
DS-09-129	Opq	4		Qtz occurs as round 50-250 μm xtls, and also forms aggregates w/Chl±Epi
DS-09-174	Epi, Qtz+Chl, Carb	1	Pl, Opqs, Chl–Act+Epi in gm	Contains one ~400 μm, twinned, euhedral Hbl phenocryst

Table A-12: Mineralogy and petrography of **rhyolitic dyke** thin sections.

Sample	Sample location	Mineralogy											Grain Size (μm)			
		Phenos (% t.s.)				Groundmass (% t.s.)						Accessory minerals	Phenocrysts		Groundmass	
		Pl	Qtz	Opq	Hbl	Pl	Qtz	Epi	Chl	Opq	Carb		Min-Max	Ave	Max	Ave
DS-09-05	Section A-A'	15				45	30	5	3	2		Ser	500-2000	1000		<50
DS-09-48	Section C-C'	3				41	47	2	3	3	1	Ser, Ap	200-900	450	200	<50
DS-09-50	Section C-C'	5				39	43	3	4	4	2	Ser	200-900	450	200	<50
DS-09-141	Map 1	3	3			44	44	2	2	2			250-1000	500		<50
DS-09-142	Map 1	3	3			44	44	2	2	2			250-1000	500		<50
DS-09-204	Section B-B'	2	1	1	1	35	30	5	10	15			500-4000	700		<50

Sample	Veins		Foliation defined by:	Comments
	Vein-filling minerals	% t.s.		
DS-09-05				Some Pl phenos are fragmental; ~10-15% Pl phenos partially replaced by Epi aggregates
DS-09-48			Pl phenos, Qtz patches	~17% of total Qtz (~7% t.s.) forms irregular patches (100-200 μm) of 1 or more anhedral xtls, elongate parallel to foliation: late SiO2-rich melt pockets?; Carb occurs as large (~300 μm) xtls surr'd by smaller anhedral Carb grains; Carb seems to have fully replaced some Pl phenos (only ~1% t.s.)
DS-09-50			Pl phenos, Qtz patches, Qtz+Fsp-rich/Chl-rich patches	~8% total Qtz (~3% t.s.) forms irregular patches (100-200 μm) of 1 or more anhedral xtls, elongate parallel to foliation: late SiO2-rich melt pockets?; Carb occurs as large (~300 μm) xtls surr'd by smaller anhedral Carb grains: Carb seems to have fully replaced some Pl phenos (only ~2% t.s.); no visible chilled margin in feldspar porphyry at contact w/oxide-rich andesitic dyke; foliation parallel to contact
DS-09-141	Epi	3	Qtz aggregates, gm mins	Qtz forms elongate aggregates up to 500X2500 μm; oval-shaped patches of Fsp enclose tiny Fsp laths in groundmass: Fsp patches probably result of devitrification; common orientation of Qtz aggregates and gm minerals could be due to igneous flow
DS-09-142	Epi	<1	Qtz aggregates, gm mins, fb	~1 mm to 1 cm-thick flow bands are composed of Fsp-rich bands alternating with Chl+Opq-rich bands
DS-09-204			All mins	Subtle flow bands are defined by different proportions of Opq minerals (+Chl?); fb seems to be discontinuous but bands are ~1mm to 1 cm-wide; all mins are aligned parallel to fb

APPENDIX B: U/PB GEOCHRONOLOGY METHODS

About 20 kg of rock was collected for each geochronology sample. The sample was washed and then crushed in a jaw-crusher and powdered in a disk mill. About 100 to 200 ml of heavy minerals were separated from the powder using a Wilfley table. The heavy mineral concentrate was then immersed in methylene iodide to separate the lowest density minerals from the highest density minerals. This heavy mineral concentrate was passed through a Frantz magnetic separator to remove magnetic minerals, leaving only the least magnetic minerals, including the highest quality zircons. The least magnetic, highest density mineral fraction was sorted under the microscope, using tweezers, to separate out the clearest, most euhedral zircon crystals.

The highest quality zircon crystals were chemically abraded, following the chemical abrasion technique developed by Mattinson (2005), to remove radiation-damaged parts of the zircon crystals and thereby reduce discordance due to Pb loss. The zircon crystals were heated for 36 hours at 900°C to anneal radiation damage in the zircon lattice, and were then loaded in TEFLON bombs with concentrated HF and heated for 6-8 hours at 200°C. The etched zircon fractions were washed with distilled HNO_3 and doubly distilled H_2O and then rinsed with acetone. They were then loaded into Krogh-type TEFLON dissolution bombs with a mixed $^{205}Pb/^{235}U$ tracer, along with about 15 drops of distilled HF and 1 drop of HNO_3. The sealed bombs were placed in an oven at 200°C for 5 days to fully dissolve the zircon crystals. Ion exchange chemistry was completed following the methods of Krogh (1973), except with miniaturized ion exchange columns

and one tenth of the reagent volumes. After ion exchange chemistry, Pb and U were collected in clean beakers with one drop of ultrapure H_3PO_3 per sample.

The Pb and U isotopic compositions of each sample were measured using the Finnigan MAT 262V thermal ionization mass spectrometer in the Department of Earth Sciences at Memorial University of Newfoundland. Each sample was loaded on an outgassed single Re filament with dilute H_3PO_4 and silica gel. Because all samples were too small to measure using Faraday cups, all Pb and U compositions were measured by peak jumping on the ion counting secondary electron multiplier (SEM). For each sample, several datasets were measured between 1400°C to 1550°C for Pb and 1550°C to 1640°C for U. A mean value for each ratio was calculated using the best datasets.

The measured ratios were corrected for Pb fractionation (0.1% amu), U fractionation (0.03% amu) and laboratory procedure blanks (Pb = 2 pg, U = 0.3 pg). The two-stage model of Stacey and Kramers (1975) was used to calculate the composition of common Pb above the laboratory blank and the decay constants of Jaffey *et al.* (1971) were used in the calculation of U/Pb ages. Two sigma uncertainties on isotopic ratios and ages were calculated using an unpublished program, and ISOPLOT was used to calculate the weighted averages of the $^{206}Pb/^{238}U$ ages at the 95% confidence interval.

APPENDIX C: LITHOGEOCHEMICAL SAMPLE PREPARATION AND METHODS OF ANALYSIS

Sixty-six samples were prepared for geochemical analysis at the rock preparation facilities at Memorial University, along with blind duplicates and triplicates of two samples (#59 and 128). Each sample was broken using a titanium carbide splitter and unweathered pieces were selected and reduced to chip-size. The chip samples were pulverized to powder using an agate disk-mill. The rock powders were sent to Actlabs, where they were mixed with a flux of lithium metaborate and lithium tetraborate and then fused in an induction furnace. The molten sample was added to a solution of 5% HNO_3 and mixed for about 30 minutes, until dissolution was complete. The samples were analysed at Actlabs, using an inductively coupled plasma emission spectrometer (ICP-ES) for major elements and selected trace elements (Sc, Be, V, Ba, Sr, Y, Zr), and an inductively coupled plasma mass spectrometer (ICP-MS) for trace elements. Included with each sample batch were three blanks and five controls. One duplicate sample was analyzed for every fifteen samples, and the machine was recalibrated every 40 samples.

APPENDIX D: LITHOGEOCHEMICAL DATA

Table D-1 (following pages): Major and trace element concentrations for 66 samples, representing each of the rock units in the study area. The prefix "DS-09-" applies to all sample numbers. Major elements in weight percent, trace elements in ppm; recalculated volatile free. Unit=rock unit as defined in text: Gr=granodiorite, FP=feldspar porphyry, G=gabbro, D=diorite, HAD=hornblende-porphyritic andesitic dykes, HBD=hornblende basaltic dykes, BD=basaltic dykes, AD=andesitic dykes, BAD=basaltic-andesitic dykes, OAD=oxide-rich andesitic dykes, OBD=oxide-rich basaltic dykes, RD=rhyolitic dykes. UTM projection=Zone 22, NAD 27 for Canada. All UTM coordinates have been extracted from registered base maps. LOD=limit of detection. Ti is calculated from measured TiO_2. LOI=loss on ignition. Mg#=(MgO/(MgO + FeO*))X100.

Unit		Gr	Gr	Gr	Gr	Gr	Gr	Gr	Gr
Sample	LOD	**68**	**70**	**80**	**107**	**118**	**128**	**148**	**171**
Easting		362141	362136	362399	362450	362450	362464	362485	362498
Northing		5286677	5286680	5287009	5287153	5287134	5287145	5287150	5287130
SiO_2	0.01	74.52	74.41	72.74	77.32	72.65	76.26	76.51	76.94
Al_2O_3	0.01	13.64	13.67	14.74	12.51	14.23	12.50	12.77	12.79
FeO	0.01	1.89	1.55	2.17	1.40	2.33	1.84	1.42	0.79
MnO	0.001	0.04	0.02	0.05	0.03	0.05	0.04	0.02	0.01
MgO	0.01	0.77	0.30	1.01	0.45	0.54	0.61	0.02	0.08
CaO	0.01	1.61	1.02	0.94	2.04	3.44	2.64	2.89	1.41
Na_2O	0.01	5.80	4.90	6.49	5.63	4.78	4.96	5.80	4.82
K_2O	0.01	1.29	3.73	1.41	0.22	1.56	0.76	0.12	2.92
TiO_2	0.001	0.341	0.316	0.359	0.309	0.320	0.318	0.380	0.199
P_2O_5	0.01	0.10	0.08	0.11	0.08	0.09	0.07	0.07	0.04
LOI		0.64	0.40	0.75	0.65	0.89	0.73	0.56	0.36
Total		99.78	99.55	100.40	100.10	99.60	100.28	99.86	99.99
Mg#		28.88	16.40	31.65	24.51	18.76	25.00	1.40	9.27
Sc	1	5	7	5	4	5	5	6	3
Be	1	-	-	-	-	-	-	-	-
V	5	42	18	33	33	54	53	49	21
Ba	3	490	1114	673	123	524	196	44	492
Sr	2	171	145	176	243	415	329	280	202
Y	2	13	33	15	13	12	11	24	17
Zr	4	103	163	128	119	102	101	197	111
Cr	20	-	-	-	-	-	-	-	-
Co	1	4	2	4	3	2	3	-	-
Ni	20	-	-	-	-	-	-	-	-
Cu	10	-	-	-	-	-	20	-	-
Zn	30	-	-	-	-	-	-	-	-
Ga	1	12	13	15	11	17	13	17	11
Ge	1	-	-	-	-	2	2	2	2
As	5	-	-	-	-	-	-	-	-
Rb	2	9	28	11	-	18	6	-	53
Nb	1	8	11	9	9	7	7	10	13
Mo	2	-	-	-	-	-	-	-	-

Unit		Gr	Gr	Gr	Gr	Gr	Gr	Gr	Gr
Sample	LOD	**68**	**70**	**80**	**107**	**118**	**128**	**148**	**171**
Easting		362141	362136	362399	362450	362450	362464	362485	362498
Northing		5286677	5286680	5287009	5287153	5287134	5287145	5287150	5287130
Ag	0.5	-	-	-	-	-	-	-	-
In	0.2	-	-	-	-	-	-	-	-
Sn	1	2	3	2	2	-	2	4	-
Sb	0.5	-	-	-	0.8	1.0	1.5	1.1	1.0
Cs	0.5	-	-	-	-	-	-	-	-
La	0.1	25.7	26.5	27.5	25.4	19.8	24.1	25.6	24.8
Ce	0.1	46.4	56.9	50.3	44.7	34.4	44.0	53.0	48.3
Pr	0.05	4.88	6.61	5.51	4.72	3.64	4.25	5.73	4.65
Nd	0.1	16.9	26.7	19.8	16.5	13.2	15.4	23.6	17.4
Sm	0.1	3.1	6.0	3.6	2.9	2.5	2.8	4.7	3.1
Eu	0.05	0.81	1.52	0.88	0.78	0.81	0.70	1.15	0.53
Gd	0.1	2.9	6.4	3.3	2.8	2.5	2.6	4.9	3.0
Tb	0.1	0.4	1.1	0.5	0.4	0.4	0.4	0.8	0.5
Dy	0.1	2.7	6.8	3.3	2.6	2.4	2.3	4.8	3.2
Ho	0.1	0.6	1.4	0.6	0.5	0.5	0.5	1.0	0.7
Er	0.1	1.7	4.2	2.0	1.7	1.5	1.4	3.0	2.0
Tm	0.05	0.29	0.67	0.30	0.28	0.25	0.22	0.47	0.34
Yb	0.1	2.1	4.8	2.1	2.1	1.9	1.5	3.2	2.4
Lu	0.04	0.31	0.75	0.35	0.31	0.28	0.23	0.47	0.34
Hf	0.2	3.4	4.8	3.9	3.8	3.4	3.4	6.4	4.3
Ta	0.1	0.6	1.0	0.7	0.7	0.5	0.5	0.5	0.9
W	1	2	-	-	-	-	2	2	-
Tl	0.1	-	-	-	-	-	-	-	-
Pb	5	-	-	-	-	11	-	-	-
Bi	0.4	-	-	-	-	-	-	-	-
Th	0.1	10.0	11.9	10.8	8.4	8.7	8.7	8.2	13.3
U	0.1	2.4	4.0	3.0	2.3	2.4	2.1	2.4	2.9
Ti		2042	2279	1918	1896	1907	1854	2743	2152
Eu/Eu*		0.80	0.75	0.77	0.82	0.97	0.78	0.72	0.53
Ti/Ti*		0.36	0.18	0.29	0.35	0.39	0.38	0.28	0.35
La/Yb		12.1	5.5	13.0	12.0	10.3	15.6	7.9	10.3
Nb/Th		0.8	0.9	0.8	1.1	0.8	0.8	1.2	1.0

Unit		Gr	Gr	FP	FP	FP	FP	FP
Sample	LOD	**200**	**202**	**112**	**117**	**139**	**177**	**182**
Easting		362143	362136	362442	362456	362473	362483	362512
Northing		5286676	5286680	5287144	5287172	5287142	5287120	5287107
SiO_2	0.01	70.42	73.08	76.41	73.00	76.37	63.66	77.74
Al_2O_3	0.01	15.51	14.79	13.12	14.60	12.86	17.14	12.29
FeO	0.01	2.16	1.41	0.74	1.70	1.17	4.90	1.10
MnO	0.001	0.05	0.04	0.02	0.03	0.02	0.07	0.02
MgO	0.01	1.06	0.48	0.30	0.43	0.23	1.78	0.23
CaO	0.01	1.60	1.59	0.29	2.73	0.59	2.49	0.72
Na_2O	0.01	5.53	7.07	4.06	6.31	4.60	7.38	4.81
K_2O	0.01	3.06	0.97	4.91	0.62	3.99	1.52	2.95
TiO_2	0.001	0.484	0.458	0.154	0.478	0.149	0.888	0.143
P_2O_5	0.01	0.11	0.11	-	0.10	0.02	0.18	-
LOI		0.92	0.55	0.52	0.77	0.29	1.08	0.45
Total		99.71	99.47	99.22	99.55	100.90	99.59	99.60
Mg#		32.78	25.21	29.16	20.06	16.33	26.59	17.44
Sc	1	7	9	5	5	5	14	5
Be	1	2	2	-	-	-	-	-
V	5	39	26	-	37	-	125	-
Ba	3	1205	356	1293	223	1083	557	740
Sr	2	272	207	100	341	156	265	150
Y	2	17	32	34	31	39	23	38
Zr	4	200	234	219	239	207	170	190
Cr	20	-	-	-	-	-	-	-
Co	1	8	3	-	2	-	12	-
Ni	20	-	-	-	-	-	-	-
Cu	10	-	-	-	20	-	20	-
Zn	30	-	-	-	-	-	51	-
Ga	1	15	13	15	18	15	18	14
Ge	1	2	-	-	2	-	-	-
As	5	-	-	-	-	-	-	-
Rb	2	40	9	61	5	38	15	34
Nb	1	12	17	9	11	10	6	8
Mo	2	-	-	-	-	-	-	-

Unit		Gr	Gr	FP	FP	FP	FP	FP
Sample	LOD	**200**	**202**	**112**	**117**	**139**	**177**	**182**
Easting		362143	362136	362442	362456	362473	362483	362512
Northing		5286676	5286680	5287144	5287172	5287142	5287120	5287107
Ag	0.5	-	0.9	-	0.9	-	-	-
In	0.2	-	-	-	-	-	-	-
Sn	1	3	2	3	3	3	3	3
Sb	0.5	1.2	1.1	-	-	-	1.0	-
Cs	0.5	0.9	-	-	-	-	-	-
La	0.1	35.1	40.5	34.7	32.9	34.0	20.2	38.7
Ce	0.1	69.3	83.6	68.5	65.7	66.6	43.3	79.1
Pr	0.05	7.08	9.04	8.08	7.84	7.92	4.87	8.39
Nd	0.1	28.0	37.1	30.8	30.3	30.3	21.2	33.7
Sm	0.1	5.1	7.8	6.6	6.3	6.5	4.7	7.1
Eu	0.05	1.64	2.19	1.07	1.68	1.06	1.52	1.18
Gd	0.1	5.0	8.0	6.9	6.5	7.0	5.3	7.6
Tb	0.1	0.7	1.2	1.2	1.1	1.2	0.8	1.2
Dy	0.1	3.9	7.5	7.3	6.6	7.7	5.2	7.9
Ho	0.1	0.7	1.5	1.5	1.3	1.7	1.0	1.6
Er	0.1	2.1	4.3	4.8	4.0	4.9	3.1	4.8
Tm	0.05	0.33	0.69	0.79	0.62	0.79	0.45	0.82
Yb	0.1	2.1	4.7	5.8	4.5	5.7	3.0	5.4
Lu	0.04	0.29	0.66	0.93	0.68	0.87	0.42	0.80
Hf	0.2	6.3	7.5	7.6	7.4	7.2	5.3	6.8
Ta	0.1	0.8	1.3	0.6	0.6	0.6	0.2	0.5
W	1	2	-	-	-	-	-	-
Tl	0.1	-	-	0.2	-	-	-	-
Pb	5	12	10	-	-	-	-	-
Bi	0.4	-	-	-	-	-	-	-
Th	0.1	7.4	9.1	4.0	4.2	3.7	1.8	3.6
U	0.1	1.9	2.5	0.9	1.0	0.8	0.4	0.8
Ti		2901	1192	5322	860	846	907	895
Eu/Eu*		0.99	0.84	0.48	0.80	0.48	0.93	0.49
Ti/Ti*		0.33	0.08	0.38	0.07	0.06	0.09	0.06
La/Yb		16.5	8.7	6.0	7.4	6.0	6.8	7.2
Nb/Th		1.6	1.9	2.3	2.7	2.7	3.3	2.2

Unit		FP	FP	G	G	G	G	G	D
Sample	LOD	**193**	**198**	**72**	**73**	**76**	**82**	**87**	**77**
Easting		362517	362528	362389	362387	362389	362400	362400	362391
Northing		5287091	5287103	5287007	5287007	5287010	5287013	5287017	5287011
SiO_2	0.01	76.85	76.71	47.64	50.35	48.65	49.81	49.79	56.01
Al_2O_3	0.01	13.00	12.75	17.30	16.68	16.44	16.24	16.29	16.89
FeO	0.01	1.37	1.00	11.10	9.76	11.09	10.02	9.94	8.16
MnO	0.001	0.01	0.02	0.25	0.27	0.30	0.21	0.21	0.13
MgO	0.01	0.16	0.13	8.69	8.05	8.38	7.78	8.32	5.00
CaO	0.01	0.46	1.63	8.98	7.93	9.36	10.06	9.10	4.61
Na_2O	0.01	5.90	4.34	2.72	2.65	2.67	2.97	2.53	5.48
K_2O	0.01	2.09	3.28	1.15	2.48	1.20	0.98	2.01	2.00
TiO_2	0.001	0.151	0.141	1.882	1.605	1.689	1.675	1.586	1.396
P_2O_5	0.01	-	-	0.28	0.23	0.22	0.25	0.23	0.31
LOI		0.25	0.37	3.31	3.06	2.93	2.43	2.86	1.95
Total		100.80	100.40	98.98	99.23	99.15	100.40	99.51	98.78
Mg#		10.41	11.52	43.90	45.20	43.03	43.71	45.55	38.01
Sc	1	5	3	42	37	38	38	36	26
Be	1	2	-	-	-	-	-	-	-
V	5	-	21	339	291	307	314	304	236
Ba	3	570	1080	531	1022	541	415	671	797
Sr	2	106	242	437	308	411	404	368	292
Y	2	40	16	31	27	26	28	26	24
Zr	4	223	68	96	87	84	88	81	129
Cr	20	-	-	296	273	274	279	282	52
Co	1	-	-	52	46	44	47	51	32
Ni	20	-	-	138	126	137	124	136	52
Cu	10	-	-	32	84	116	93	94	42
Zn	30	-	-	180	200	179	124	136	115
Ga	1	16	14	22	19	20	20	19	18
Ge	1	-	-	2	2	2	2	2	-
As	5	-	-	-	-	-	-	-	-
Rb	2	23	31	23	50	26	24	50	19
Nb	1	9	8	3	3	3	3	3	6
Mo	2	-	-	-	-	-	-	-	-

Unit		FP	FP	G	G	G	G	G	D
Sample	LOD	**193**	**198**	**72**	**73**	**76**	**82**	**87**	**77**
Easting		362517	362528	362389	362387	362389	362400	362400	362391
Northing		5287091	5287103	5287007	5287007	5287010	5287013	5287017	5287011
Ag	0.5	0.8	-	-	-	-	-	-	-
In	0.2	-	-	-	-	-	-	-	-
Sn	1	3	2	2	2	3	2	2	2
Sb	0.5	1.2	0.9	1.3	1.2	0.9	-	1.2	0.9
Cs	0.5	-	-	-	-	-	-	-	-
La	0.1	38.0	19.0	10.1	9.6	8.5	8.9	8.5	20.5
Ce	0.1	77.9	38.8	24.0	22.3	19.8	21.3	19.8	43.1
Pr	0.05	8.43	3.81	3.58	3.17	2.90	3.12	2.89	5.43
Nd	0.1	34.2	14.1	17.6	15.2	14.4	15.2	14.3	22.6
Sm	0.1	7.2	2.9	5.1	4.3	4.2	4.4	4.1	5.0
Eu	0.05	1.29	0.52	1.92	1.64	1.61	1.67	1.64	1.71
Gd	0.1	7.7	3.1	6.6	5.8	5.6	5.8	5.5	5.4
Tb	0.1	1.3	0.5	1.2	0.9	0.9	1.0	0.9	0.8
Dy	0.1	8.2	3.2	7.1	6.3	6.1	6.4	5.9	5.5
Ho	0.1	1.7	0.6	1.5	1.3	1.3	1.2	1.2	1.1
Er	0.1	5.2	2.0	3.9	3.5	3.5	3.5	3.3	3.1
Tm	0.05	0.88	0.32	0.58	0.52	0.51	0.52	0.48	0.47
Yb	0.1	5.7	2.1	3.8	3.5	3.4	3.5	3.2	3.1
Lu	0.04	0.83	0.27	0.57	0.49	0.48	0.51	0.46	0.45
Hf	0.2	7.5	2.8	3.2	2.8	2.6	2.9	2.6	3.8
Ta	0.1	0.6	0.7	-	-	-	-	-	0.2
W	1	-	-	2	-	-	-	-	-
Tl	0.1	-	-	-	-	-	-	-	-
Pb	5	-	12	12	9	13	-	-	-
Bi	0.4	-	-	-	-	-	-	-	-
Th	0.1	3.6	4.7	0.3	0.6	0.3	0.3	0.3	0.9
U	0.1	0.8	1.4	-	-	-	-	-	0.2
Ti		2863	924	9506	10042	11279	9621	10123	12248
Eu/Eu*		0.53	0.53	1.02	1.01	1.02	1.01	1.06	1.00
Ti/Ti*		0.18	0.15	0.71	0.85	0.98	0.80	0.90	1.13
La/Yb		6.7	9.0	2.6	2.8	2.5	2.5	2.6	6.6
Nb/Th		2.5	1.7	10.0	5.0	10.0	10.0	10.0	6.7

Unit		D	D	D	D	D	D	HAD
Sample	LOD	**102**	**105**	**131**	**133**	**146**	**184**	**100**
Easting		362452	362448	362457	362460	362482	362500	362449
Northing		5287176	5287155	5287133	5287156	5287144	5287103	5287171
SiO_2	0.01	54.50	50.56	53.11	53.18	56.37	57.49	57.62
Al_2O_3	0.01	14.32	15.38	15.65	15.29	16.61	17.24	18.02
FeO	0.01	9.79	10.86	10.41	10.40	8.17	7.37	7.28
MnO	0.001	0.19	0.24	0.22	0.22	0.21	0.14	0.14
MgO	0.01	5.53	6.97	6.52	6.27	5.23	4.62	3.63
CaO	0.01	8.88	9.40	6.94	7.47	4.88	4.22	4.21
Na_2O	0.01	4.78	3.32	4.26	4.48	6.01	6.36	6.83
K_2O	0.01	0.13	0.92	0.92	0.79	0.85	1.17	0.91
TiO_2	0.001	1.632	2.043	1.717	1.663	1.393	1.169	1.077
P_2O_5	0.01	0.24	0.30	0.25	0.24	0.26	0.21	0.28
LOI		1.71	2.45	2.56	2.17	2.38	2.11	1.62
Total		99.18	98.78	100.60	100.10	98.34	98.75	99.30
Mg#		36.09	39.07	38.52	37.61	39.00	38.54	33.29
Sc	1	39	41	40	39	28	24	25
Be	1	-	-	-	-	-	-	-
V	5	325	360	313	308	244	201	246
Ba	3	67	684	716	562	473	575	576
Sr	2	342	396	318	302	233	276	341
Y	2	33	38	36	36	25	25	19
Zr	4	121	137	124	123	114	122	96
Cr	20	62	210	72	62	42	73	-
Co	1	33	43	38	41	29	28	14
Ni	20	52	84	62	52	53	63	-
Cu	10	21	63	31	41	42	52	21
Zn	30	124	126	155	114	137	104	72
Ga	1	20	20	19	19	17	17	19
Ge	1	3	2	2	2	-	-	-
As	5	-	-	-	-	-	-	-
Rb	2	-	16	12	8	8	13	14
Nb	1	8	9	8	8	9	5	6
Mo	2	-	-	-	-	-	-	-

Unit		D	D	D	D	D	D	HAD
Sample	LOD	**102**	**105**	**131**	**133**	**146**	**184**	**100**
Easting		362452	362448	362457	362460	362482	362500	362449
Northing		5287176	5287155	5287133	5287156	5287144	5287103	5287171
Ag	0.5	-	-	-	-	-	-	-
In	0.2	-	-	-	-	-	-	-
Sn	1	2	2	2	2	-	2	2
Sb	0.5	1.1	0.9	1.1	0.9	-	0.9	1.0
Cs	0.5	-	-	-	-	-	-	-
La	0.1	11.6	12.7	12.5	12.6	14.7	18.9	18.4
Ce	0.1	26.4	30.5	28.2	28.7	30.2	40.1	36.7
Pr	0.05	3.69	4.49	3.94	4.00	3.90	4.57	4.62
Nd	0.1	17.5	21.4	18.5	18.2	16.2	20.0	19.4
Sm	0.1	5.0	5.9	5.2	5.1	3.8	4.6	4.4
Eu	0.05	1.69	2.19	1.82	1.83	1.17	1.53	1.49
Gd	0.1	6.6	7.8	6.9	6.8	4.2	5.4	4.5
Tb	0.1	1.1	1.4	1.2	1.2	0.7	0.8	0.7
Dy	0.1	7.6	8.6	7.6	7.7	4.4	5.3	4.2
Ho	0.1	1.6	1.8	1.5	1.7	0.9	1.0	0.8
Er	0.1	4.5	4.9	4.6	4.4	2.5	3.0	2.4
Tm	0.05	0.65	0.74	0.67	0.67	0.39	0.47	0.35
Yb	0.1	4.5	4.8	4.6	4.5	2.5	3.1	2.3
Lu	0.04	0.67	0.74	0.67	0.68	0.35	0.41	0.33
Hf	0.2	3.7	4.1	3.8	3.8	3.0	4.0	3.0
Ta	0.1	0.4	0.4	0.4	0.4	0.4	0.2	0.3
W	1	-	-	-	-	-	-	-
Tl	0.1	-	-	-	-	-	-	-
Pb	5	-	-	-	-	-	-	-
Bi	0.4	-	-	-	-	-	-	-
Th	0.1	0.8	0.8	0.9	0.9	1.2	1.6	3.2
U	0.1	-	-	-	-	0.3	0.2	0.9
Ti		8365	7009	9785	9970	8351	10290	5439
Eu/Eu*		0.90	0.99	0.93	0.95	0.89	0.94	1.00
Ti/Ti*		0.60	0.44	0.68	0.70	0.98	0.97	0.63
La/Yb		2.6	2.6	2.7	2.8	5.8	6.0	8.1
Nb/Th		10.0	11.3	8.9	8.9	8.2	3.3	1.9

Unit		HAD	HBD	HBD	HBD	HBD	HBD	HBD	HBD
Sample	LOD	**138**	**60**	**69**	**75**	**78**	**88**	**99**	**132**
Easting		362472	362141	362143	362388	362396	362404	362445	362461
Northing		5287145	5286677	5286676	5287011	5287010	5287018	5287167	5287154
SiO_2	0.01	55.54	51.36	54.98	52.65	50.82	52.01	52.72	50.29
Al_2O_3	0.01	18.64	19.76	17.00	18.61	15.72	19.68	14.85	15.27
FeO	0.01	6.66	10.46	9.65	7.68	11.58	7.56	10.59	11.60
MnO	0.001	0.14	0.27	0.17	0.17	0.22	0.17	0.27	0.24
MgO	0.01	6.44	7.28	4.38	5.78	6.11	6.49	6.55	7.03
CaO	0.01	4.22	2.75	5.71	8.16	7.99	6.74	8.25	9.39
Na_2O	0.01	4.21	5.92	5.38	4.31	4.01	3.67	4.19	3.33
K_2O	0.01	3.04	0.18	0.63	1.22	0.92	2.34	0.29	0.63
TiO_2	0.001	0.907	1.706	1.781	1.186	2.242	1.176	1.974	1.986
P_2O_5	0.01	0.19	0.31	0.31	0.24	0.40	0.19	0.31	0.24
LOI		3.11	4.05	2.05	2.51	2.47	2.95	2.40	2.20
Total		98.60	99.03	99.19	99.45	99.76	99.49	99.36	100.90
Mg#		49.13	41.04	31.22	42.94	34.55	46.19	38.22	37.74
Sc	1	22	37	29	27	39	29	40	44
Be	1	-	-	-	-	-	-	-	-
V	5	172	275	312	214	380	209	343	369
Ba	3	2989	54	519	955	386	1169	232	329
Sr	2	406	140	353	577	369	378	368	261
Y	2	15	30	32	21	39	22	38	40
Zr	4	87	136	150	82	134	86	140	120
Cr	20	127	106	-	177	146	188	209	92
Co	1	31	43	34	33	43	37	41	45
Ni	20	106	75	42	83	83	94	83	62
Cu	10	42	32	42	52	52	42	73	72
Zn	30	84	256	125	114	115	167	136	113
Ga	1	18	27	21	19	23	18	19	20
Ge	1	-	-	2	2	2	-	2	2
As	5	-	-	-	-	-	-	-	-
Rb	2	26	-	7	20	12	41	3	11
Nb	1	4	17	18	8	8	9	9	7
Mo	2	-	-	-	-	-	-	-	-

Unit		HAD	HBD	HBD	HBD	HBD	HBD	HBD	HBD
Sample	LOD	**138**	**60**	**69**	**75**	**78**	**88**	**99**	**132**
Easting		362472	362141	362143	362388	362396	362404	362445	362461
Northing		5287145	5286677	5286676	5287011	5287010	5287018	5287167	5287154
Ag	0.5	-	-	-	-	-	-	-	-
In	0.2	-	-	-	-	-	-	-	-
Sn	1	-	3	3	2	3	2	3	3
Sb	0.5	1.4	0.9	1.0	-	0.9	-	1.0	0.9
Cs	0.5	-	-	-	-	-	-	-	-
La	0.1	15.8	20.2	21.8	13.8	14.6	11.3	13.5	9.2
Ce	0.1	31.0	40.7	43.3	30.3	32.8	23.6	32.0	23.0
Pr	0.05	3.75	5.27	5.55	3.98	4.63	3.14	4.61	3.47
Nd	0.1	15.3	22.6	23.2	17.3	22.4	14.2	22.0	17.6
Sm	0.1	3.4	5.4	5.7	4.0	6.2	3.7	5.8	5.4
Eu	0.05	1.19	1.40	2.00	1.51	2.38	1.32	2.14	1.97
Gd	0.1	3.7	6.4	6.9	4.6	8.0	4.7	7.6	7.5
Tb	0.1	0.6	1.1	1.1	0.7	1.4	0.8	1.4	1.3
Dy	0.1	3.5	6.8	7.3	4.7	8.6	5.1	8.5	8.6
Ho	0.1	0.6	1.4	1.5	0.9	1.8	1.0	1.8	1.8
Er	0.1	1.9	4.0	4.3	2.6	5.1	2.9	4.8	5.0
Tm	0.05	0.28	0.59	0.61	0.40	0.75	0.44	0.71	0.75
Yb	0.1	1.9	3.9	4.2	2.6	5.0	2.9	4.8	4.9
Lu	0.04	0.24	0.64	0.61	0.36	0.71	0.42	0.71	0.73
Hf	0.2	2.6	3.9	4.5	2.5	4.1	2.7	4.3	3.8
Ta	0.1	0.2	1.1	0.8	0.4	0.4	0.4	0.4	0.3
W	1	-	-	-	-	-	-	-	-
Tl	0.1	-	-	-	-	-	-	-	-
Pb	5	-	-	-	-	-	-	-	-
Bi	0.4	-	-	-	-	-	-	-	-
Th	0.1	1.1	3.3	2.1	0.7	0.7	0.8	0.9	0.6
U	0.1	-	0.6	0.4	-	-	-	-	-
Ti		6458	7049	10227	11832	13440	7108	10677	11907
Eu/Eu*		1.03	0.72	0.97	1.08	1.03	0.97	0.98	0.95
Ti/Ti*		0.91	0.54	0.73	1.30	0.82	0.74	0.68	0.75
La/Yb		8.3	5.1	5.3	5.3	2.9	3.9	2.8	1.9
Nb/Th		4.0	5.2	8.5	11.4	11.4	11.3	10.0	11.7

Unit		BD	BD	BD	BD	BD	AD	AD	AD
Sample	LOD	**53**	**71**	**74**	**84**	**123**	**55**	**59**	**89**
Easting		362145	362388	362390	362402	362452	362140	362144	362403
Northing		5286680	5287006	5287008	5287015	5287143	5286676	5286681	5287011
SiO_2	0.01	51.37	51.68	51.33	50.88	47.80	65.20	60.93	62.08
Al_2O_3	0.01	14.94	16.31	15.53	15.08	17.07	16.22	16.75	17.45
FeO	0.01	12.07	9.44	11.38	12.24	10.54	5.70	6.85	5.61
MnO	0.001	0.25	0.22	0.22	0.21	0.20	0.12	0.12	0.10
MgO	0.01	6.14	7.54	6.62	5.96	7.71	2.43	2.76	2.17
CaO	0.01	7.83	7.62	7.33	7.88	9.71	2.78	4.67	2.35
Na_2O	0.01	3.98	3.90	4.43	3.79	2.44	6.13	6.39	7.50
K_2O	0.01	0.94	1.26	0.59	1.24	1.76	0.24	0.22	1.43
TiO_2	0.001	2.187	1.675	2.170	2.323	2.477	0.945	1.128	1.059
P_2O_5	0.01	0.31	0.35	0.40	0.39	0.30	0.22	0.17	0.25
LOI		1.99	2.75	2.61	2.12	2.57	1.91	1.63	1.16
Total		100.10	100.00	98.93	98.83	100.60	100.70	100.03	99.92
Mg#		33.71	44.41	36.79	32.76	42.24	29.92	28.73	27.89
Sc	1	41	33	38	40	37	13	19	16
Be	1	-	-	-	-	-	-	-	-
V	5	393	289	360	385	296	134	218	131
Ba	3	603	1040	273	726	367	78	59	481
Sr	2	296	331	320	309	296	250	405	233
Y	2	42	30	40	41	36	22	23	19
Zr	4	147	117	138	134	198	126	117	109
Cr	20	52	301	147	126	93	-	-	-
Co	1	45	44	42	46	51	10	17	16
Ni	20	52	145	84	73	103	-	-	-
Cu	10	62	94	32	52	52	-	72	20
Zn	30	134	177	116	136	103	102	82	71
Ga	1	21	19	18	21	22	21	24	19
Ge	1	2	2	-	2	2	-	3	-
As	5	-	-	-	-	-	-	-	-
Rb	2	15	16	7	16	53	3	-	9
Nb	1	9	16	9	8	12	6	6	3
Mo	2	-	-	-	-	-	-	-	-

Unit		BD	BD	BD	BD	BD	AD	AD	AD
Sample	LOD	**53**	**71**	**74**	**84**	**123**	**55**	**59**	**89**
Easting		362145	362388	362390	362402	362452	362140	362144	362403
Northing		5286680	5287006	5287008	5287015	5287143	5286676	5286681	5287011
Ag	0.5	-	-	-	-	-	-	-	-
In	0.2	-	-	-	-	-	-	-	-
Sn	1	3	2	2	3	4	-	2	2
Sb	0.5	-	0.9	-	-	0.9	0.9	1.2	0.8
Cs	0.5	-	-	-	-	-	-	-	-
La	0.1	12.0	16.4	13.4	13.6	12.9	16.1	16.1	16.6
Ce	0.1	29.9	34.1	30.7	32.0	32.6	33.3	33.7	33.6
Pr	0.05	4.48	4.55	4.38	4.57	4.77	4.27	4.07	4.23
Nd	0.1	21.5	20.2	19.9	22.0	23.0	18.0	18.3	18.1
Sm	0.1	6.1	5.1	5.2	6.3	6.3	4.2	4.3	4.2
Eu	0.05	2.26	1.89	1.69	2.36	2.44	1.40	1.52	1.37
Gd	0.1	8.2	6.3	6.2	8.4	7.7	4.7	5.2	4.7
Tb	0.1	1.4	1.0	1.2	1.5	1.3	0.8	0.8	0.7
Dy	0.1	9.2	6.7	6.8	9.2	7.9	4.9	5.2	4.4
Ho	0.1	1.9	1.4	1.4	1.9	1.5	1.0	1.0	0.8
Er	0.1	5.3	3.8	4.0	5.2	4.4	2.8	3.0	2.4
Tm	0.05	0.80	0.56	0.60	0.79	0.63	0.43	0.43	0.36
Yb	0.1	5.4	3.7	3.9	5.2	4.1	2.9	2.8	2.2
Lu	0.04	0.81	0.56	0.56	0.77	0.60	0.41	0.39	0.31
Hf	0.2	4.3	3.4	3.9	4.2	5.2	3.9	3.7	3.4
Ta	0.1	0.4	0.7	0.4	0.4	0.6	0.3	0.2	0.2
W	1	-	-	-	-	-	2	2	-
Tl	0.1	-	-	-	-	0.2	-	-	-
Pb	5	-	-	-	-	-	-	14	-
Bi	0.4	-	-	-	-	-	-	-	-
Th	0.1	0.7	1.1	0.6	0.7	0.8	1.4	1.1	1.4
U	0.1	-	0.2	0.2	-	-	0.4	0.2	0.3
Ti		13109	13008	13921	14850	10040	6580	6021	8306
Eu/Eu*		0.98	1.02	0.92	0.99	1.07	0.96	0.98	0.94
Ti/Ti*		0.77	1.02	1.09	0.86	0.65	0.70	0.59	0.92
La/Yb		2.2	4.4	3.4	2.6	3.1	5.6	5.8	7.4
Nb/Th		12.9	13.6	15.0	11.4	15.0	4.3	5.5	2.1

Unit		AD	AD	AD	AD	AD	AD	AD	BAD
Sample	LOD	**96**	**103**	**104**	**152**	**167**	**175**	**203**	**91**
Easting		362409	362449	362450	362493	362500	362488	362143	362410
Northing		5287017	5287166	5287162	5287141	5287140	5287122	5286676	5287016
SiO_2	0.01	58.55	58.66	61.10	61.11	61.12	61.58	60.35	53.17
Al_2O_3	0.01	17.42	17.27	16.42	17.37	17.50	17.67	17.86	17.44
FeO	0.01	6.91	6.21	6.66	5.85	5.88	5.64	6.35	11.85
MnO	0.001	0.13	0.11	0.09	0.11	0.13	0.10	0.09	0.23
MgO	0.01	4.20	3.76	2.19	2.32	2.38	2.23	2.98	4.77
CaO	0.01	4.54	4.07	3.05	2.69	2.43	2.92	2.62	3.27
Na_2O	0.01	5.97	5.57	6.88	7.74	8.04	7.66	6.91	6.30
K_2O	0.01	0.94	3.02	2.19	0.99	0.63	0.91	1.66	0.20
TiO_2	0.001	1.098	1.060	1.196	1.333	1.386	1.046	1.004	2.417
P_2O_5	0.01	0.23	0.26	0.24	0.49	0.51	0.24	0.17	0.36
LOI		2.49	1.56	0.60	1.37	1.47	1.36	1.50	2.88
Total		98.98	98.45	98.32	99.12	100.20	99.16	100.30	99.53
Mg#		37.80	37.73	24.71	28.38	28.77	28.37	31.92	28.70
Sc	1	20	19	18	18	18	15	16	37
Be	1	-	-	-	-	-	-	-	-
V	5	212	173	222	103	115	143	184	398
Ba	3	373	1316	933	624	362	353	872	97
Sr	2	380	320	212	267	209	318	325	151
Y	2	20	23	21	30	31	21	17	46
Zr	4	104	168	122	158	152	110	111	170
Cr	20	31	62		-	-	-	-	-
Co	1	28	25	14	12	14	17	22	34
Ni	20	52	62		-	-	-	31	31
Cu	10	52	73	-	-	-	21	20	262
Zn	30	84	83	62	82	61	82	82	210
Ga	1	22	20	19	23	20	21	18	24
Ge	1	2	-	-	-	-	-	-	2
As	5	-	-	-	-	-	-	-	-
Rb	2	9	22	13	10	6	8	13	-
Nb	1	5	7	4	7	7	4	4	10
Mo	2	-	-	-	-	-	-	-	-

Unit		AD	AD	AD	AD	AD	AD	AD	BAD
Sample	LOD	**96**	**103**	**104**	**152**	**167**	**175**	**203**	**91**
Easting		362409	362449	362450	362493	362500	362488	362143	362410
Northing		5287017	5287166	5287162	5287141	5287140	5287122	5286676	5287016
Ag	0.5	-	-	-	-	-	-	-	-
In	0.2	-	-	-	-	-	-	-	-
Sn	1	2	2	2	3	2	2	2	5
Sb	0.5	0.9	1.0	-	1.0	1.1	1.2	1.1	-
Cs	0.5	-	-	-	-	-	-	-	-
La	0.1	20.4	26.6	19.1	26.4	27.3	19.0	16.7	19.1
Ce	0.1	39.7	53.8	38.9	56.4	59.6	39.0	35.3	41.7
Pr	0.05	4.83	6.52	4.83	6.72	6.97	4.49	3.95	5.64
Nd	0.1	19.6	25.8	20.2	30.1	30.5	20.4	17.6	26.1
Sm	0.1	4.2	5.3	4.5	6.5	6.5	4.5	3.9	7.1
Eu	0.05	1.43	1.57	1.53	2.07	1.89	1.51	1.14	2.59
Gd	0.1	4.6	5.4	4.9	7.1	7.0	5.0	4.5	9.4
Tb	0.1	0.7	0.8	0.8	1.1	1.1	0.7	0.7	1.7
Dy	0.1	4.4	5.2	4.8	6.6	6.6	4.5	4.1	10.4
Ho	0.1	0.8	1.0	0.9	1.3	1.3	0.8	0.7	2.2
Er	0.1	2.4	3.0	2.7	3.7	3.6	2.5	2.2	6.0
Tm	0.05	0.36	0.46	0.40	0.53	0.52	0.37	0.35	0.89
Yb	0.1	2.2	3.0	2.7	3.3	3.4	2.3	2.0	6.1
Lu	0.04	0.32	0.45	0.39	0.46	0.46	0.27	0.25	0.93
Hf	0.2	3.2	4.8	3.7	5.1	5.1	3.6	3.6	5.3
Ta	0.1	0.2	0.4	0.2	0.3	0.3	-	-	0.4
W	1	-	-	-	-	-	-	-	-
Tl	0.1	-	-	-	-	-	-	-	-
Pb	5	-	-	-	-	-	-	-	-
Bi	0.4	-	-	-	-	-	-	-	-
Th	0.1	1.7	2.0	1.6	2.2	2.1	1.4	1.3	1.3
U	0.1	0.3	0.4	0.3	0.4	0.4	0.3	0.2	0.2
Ti		6354	6345	7993	5666	6759	6272	7167	12965
Eu/Eu*		0.99	0.89	0.98	0.93	0.85	0.97	0.84	0.97
Ti/Ti*		0.71	0.61	0.83	0.42	0.50	0.66	0.84	0.67
La/Yb		9.3	8.8	7.1	8.0	8.1	8.4	8.2	3.1
Nb/Th		3.1	3.7	2.5	3.3	3.3	2.9	3.1	8.3

Unit		BAD	BAD	BAD	BAD	OAD	OAD	OAD	OAD
Sample	LOD	**143**	**155**	**181**	**194**	**56**	**57**	**79**	**145**
Easting		362478	362465	362517	362519	362140	362147	362397	362478
Northing		5287146	5287135	5287108	5287098	5286682	5286673	5287012	5287141
SiO_2	0.01	52.40	55.89	56.61	55.95	62.56	58.47	55.88	62.15
Al_2O_3	0.01	19.94	15.77	16.92	17.34	14.67	18.46	15.60	17.89
FeO	0.01	8.82	12.00	10.21	8.78	8.12	7.20	10.45	5.14
MnO	0.001	0.21	0.17	0.18	0.16	0.13	0.09	0.18	0.09
MgO	0.01	7.19	4.68	3.89	3.78	2.56	2.67	3.39	1.93
CaO	0.01	3.27	4.32	3.06	4.13	3.82	2.03	5.78	1.93
Na_2O	0.01	6.05	4.39	5.75	6.57	6.09	7.00	6.17	8.24
K_2O	0.01	0.66	0.29	0.90	0.69	0.26	2.42	0.45	0.91
TiO_2	0.001	1.272	2.173	2.163	1.880	1.503	1.297	1.759	1.255
P_2O_5	0.01	0.19	0.31	0.33	0.71	0.27	0.37	0.34	0.48
LOI		4.12	3.03	2.73	2.83	1.25	1.69	1.24	1.79
Total		100.60	99.96	99.72	100.40	100.50	99.74	99.14	98.39
Mg#		44.93	28.07	27.59	30.08	24.00	27.08	24.49	27.25
Sc	1	32	37	25	24	21	19	28	18
Be	1	2	-	-	-	-	-	-	-
V	5	217	419	336	134	228	193	324	74
Ba	3	277	130	397	387	101	985	172	444
Sr	2	334	225	190	186	186	139	324	99
Y	2	28	42	29	36	50	24	41	33
Zr	4	95	159	113	132	236	122	176	165
Cr	20	168	-	-	-	-	-	-	-
Co	1	36	39	29	17	23	23	31	8
Ni	20	94	-	31	-	-	-	-	-
Cu	10	63	52	42	21	-	62	21	-
Zn	30	168	84	125	114	92	134	124	115
Ga	1	26	23	20	20	21	22	23	17
Ge	1	2	2	-	-	2	-	2	-
As	5	-	-	-	-	-	-	-	-
Rb	2	10	3	9	7	3	22	-	7
Nb	1	3	12	5	7	17	4	11	6
Mo	2	-	-	-	-	-	-	-	-

Unit		BAD	BAD	BAD	BAD	OAD	OAD	OAD	OAD
Sample	LOD	**143**	**155**	**181**	**194**	**56**	**57**	**79**	**145**
Easting		362478	362465	362517	362519	362140	362147	362397	362478
Northing		5287146	5287135	5287108	5287098	5286682	5286673	5287012	5287141
Ag	0.5	-	-	-	-	0.9	-	-	-
In	0.2	-	-	-	-	-	-	-	-
Sn	1	2	3	2	2	4	2	4	2
Sb	0.5	0.9	1.0	1.1	1.1	1.0	-	1.4	-
Cs	0.5	-	-	-	-	-	-	-	-
La	0.1	14.6	19.9	17.7	24.1	29.2	20.3	24.1	20.3
Ce	0.1	31.7	46.1	38.3	52.3	60.3	40.8	51.3	46.0
Pr	0.05	4.23	5.77	4.59	6.43	7.78	5.16	6.71	6.12
Nd	0.1	18.4	27.2	21.6	31.4	32.3	22.2	29.1	25.7
Sm	0.1	4.7	6.7	5.3	7.8	8.0	5.1	7.1	5.9
Eu	0.05	1.61	2.22	2.00	2.79	2.38	1.71	2.37	1.36
Gd	0.1	5.9	8.6	6.7	9.7	10.0	5.6	8.6	6.0
Tb	0.1	0.9	1.5	1.0	1.4	1.7	0.8	1.4	1.0
Dy	0.1	6.5	9.1	6.6	8.7	11.0	5.2	9.3	5.9
Ho	0.1	1.3	1.9	1.3	1.8	2.1	1.0	2.0	1.1
Er	0.1	3.4	5.2	3.7	4.7	6.5	3.0	5.5	3.3
Tm	0.05	0.48	0.83	0.53	0.67	1.01	0.43	0.82	0.49
Yb	0.1	3.2	5.2	3.3	4.2	7.0	2.8	5.6	3.2
Lu	0.04	0.45	0.72	0.46	0.55	1.05	0.39	0.84	0.45
Hf	0.2	2.9	5.1	3.8	4.1	7.3	3.6	5.6	4.6
Ta	0.1	-	0.4	0.2	0.3	0.8	0.2	0.5	0.2
W	1	-	-	2	-	2	-	3	3
Tl	0.1	-	-	-	-	-	-	-	-
Pb	5	-	-	-	-	11	-	-	11
Bi	0.4	-	-	-	-	-	-	-	-
Th	0.1	0.7	1.3	0.9	1.1	2.5	1.6	2.5	1.9
U	0.1	0.2	0.2	-	-	0.6	0.3	0.3	0.5
Ti		14488	11271	13023	7626	10542	7777	9008	7521
Eu/Eu*		0.94	0.90	1.03	0.98	0.81	0.97	0.93	0.69
Ti/Ti*		1.19	0.65	1.00	0.42	0.51	0.73	0.51	0.64
La/Yb		4.5	3.8	5.3	5.7	4.2	7.3	4.3	6.3
Nb/Th		4.3	9.2	5.6	6.4	6.8	2.5	4.6	3.3

Unit		OBD	OBD	RD	RD
Sample	LOD	**64**	**129**	**141**	**204**
Easting		362144	362463	362479	362136
Northing		5286681	5287141	5287141	5286680
SiO_2	0.01	50.22	51.80	77.23	73.55
Al_2O_3	0.01	15.69	18.06	12.61	14.52
FeO	0.01	13.47	12.39	1.29	2.02
MnO	0.001	0.20	0.19	0.03	0.03
MgO	0.01	4.90	5.44	0.30	0.58
CaO	0.01	7.34	2.91	0.45	0.91
Na_2O	0.01	4.88	6.36	5.42	7.50
K_2O	0.01	0.15	0.12	2.47	0.37
TiO_2	0.001	2.705	2.423	0.170	0.440
P_2O_5	0.01	0.44	0.32	0.03	0.07
LOI		2.50	2.90	0.39	0.34
Total		99.15	99.87	100.00	99.55
Mg#		26.68	30.50	18.91	22.20
Sc	1	43	39	3	5
Be	1	-	-	-	-
V	5	462	385	-	9
Ba	3	87	58	563	353
Sr	2	332	91	84	140
Y	2	51	45	33	26
Zr	4	168	169	177	202
Cr	20	-	-	-	-
Co	1	56	33	-	-
Ni	20	42	-	-	-
Cu	10	105	31	-	20
Zn	30	158	115	-	-
Ga	1	27	22	14	14
Ge	1	3	-	-	-
As	5	-	-	-	-
Rb	2	-	-	32	4
Nb	1	7	10	8	8
Mo	2	-	-	-	-

Unit		OBD	OBD	RD	RD
Sample	LOD	**64**	**129**	**141**	**204**
Easting		362144	362463	362479	362136
Northing		5286681	5287141	5287141	5286680
Ag	0.5	-	-	-	-
In	0.2	-	-	-	-
Sn	1	3	3	4	3
Sb	0.5	1.1	-	0.8	1.1
Cs	0.5	-	-	-	-
La	0.1	14.2	16.6	31.7	35.3
Ce	0.1	34.9	39.3	62.2	71.9
Pr	0.05	5.23	5.53	7.23	7.93
Nd	0.1	25.7	25.2	27.5	32.6
Sm	0.1	7.8	6.7	5.6	6.3
Eu	0.05	2.97	1.56	1.07	1.82
Gd	0.1	10.7	8.6	6.0	6.5
Tb	0.1	1.9	1.6	1.0	1.0
Dy	0.1	11.9	9.7	6.5	6.0
Ho	0.1	2.4	2.0	1.4	1.2
Er	0.1	6.7	5.5	4.1	3.4
Tm	0.05	1.01	0.86	0.64	0.52
Yb	0.1	6.6	5.8	4.5	3.6
Lu	0.04	0.99	0.86	0.70	0.51
Hf	0.2	5.4	5.3	5.9	6.1
Ta	0.1	0.3	0.5	0.5	0.4
W	1	-	-	-	-
Tl	0.1	-	-	-	-
Pb	5	-	-	-	-
Bi	0.4	-	-	-	-
Th	0.1	0.7	1.3	3.9	2.7
U	0.1	-	0.2	0.9	0.5
Ti		16214	14521	2640	1018
Eu/Eu*		1.00	0.63	0.56	0.87
Ti/Ti*		0.73	0.81	0.21	0.08
La/Yb		2.1	2.9	7.0	9.7
Nb/Th		10.0	8.3	2.1	3.0

APPENDIX E: LITHOGEOCHEMISTRY DATA QUALITY

E.1. Standard and duplicate/triplicate analyses

Table E-1: Major element concentrations in standard reference materials included with the samples in this study during lithium metaborate/tetraborate ICP analysis at Actlabs. Meas=measured value, Cert=certified value, %RD=percent relative difference. %RD=[(μ_i – STD_i)/STD_i]*100, where μ_i = mean value of element *i*, STD_i = certified value of element *i* in the standard reference material.

Analyte Symbol	SiO2	Al2O3	Fe2O3(T)	MnO	MgO	CaO	Na2O	K2O	TiO2	P2O5
Unit Symbol	%	%	%	%	%	%	%	%	%	%
Detection Limit	0.01	0.01	0.01	0.001	0.01	0.01	0.01	0.01	0.001	0.01
NIST 694 Meas	11.38	1.97	0.77	0.013	0.35	43.68	0.9	0.58	0.12	30.26
NIST 694 Cert	11.2	1.8	0.79	0.0116	0.33	43.6	0.86	0.51	0.11	30.2
%RD	1.61	9.44	-2.53	12.07	6.06	0.18	4.65	13.73	9.09	0.20
DNC-1 Meas	47.24	18.8	9.94	0.149	10.02	11.33	1.89	0.23	0.499	0.04
DNC-1 Cert	47	18.3	9.93	0.149	10.1	11.3	1.87	0.234	0.48	0.09
%RD	0.51	2.73	0.10	0.00	-0.79	0.27	1.07	-1.71	3.96	-55.56
GBW 07113 Meas	73.04	12.86	3.18	0.141	0.14	0.57	2.43	5.37	0.283	0.02
GBW 07113 Cert	72.8	13	3.21	0.14	0.16	0.59	2.57	5.43	0.3	0.05
%RD	0.33	-1.08	-0.93	0.71	-12.50	-3.39	-5.45	-1.10	-5.67	-60.00
W-2a Meas	52.81	15.55	10.69	0.165	6.21	10.8	2.23	0.64	1.08	0.11
W-2a Cert	52.4	15.4	10.7	0.163	6.37	10.9	2.14	0.626	1.06	0.13
%RD	0.78	0.97	-0.09	1.23	-2.51	-0.92	4.21	2.24	1.89	-15.38
SY-4 Meas	49.68	21.16	6.21	0.106	0.49	7.84	7.07	1.7	0.292	0.1
SY-4 Cert	49.9	20.69	6.21	0.108	0.54	8.05	7.1	1.66	0.287	0.131
%RD	-0.44	2.27	0.00	-1.85	-9.26	-2.61	-0.42	2.41	1.74	-23.66
BIR-1a Meas	47.72	15.53	11.21	0.172	9.48	13.33	1.77	0.02	0.97	< 0.01
BIR-1a Cert	47.8	15.4	11.3	0.171	9.68	13.2	1.75	0.03	0.96	0.05
%RD	-0.17	0.84	-0.80	0.58	-2.07	0.98	1.14	-33.33	1.04	

Table E-2 (following pages): Trace element concentrations in standard reference materials included with the samples in this study during lithium metaborate/tetraborate ICP analysis at Actlabs. Meas=measured value, Cert=certified value, %RD=percent relative difference. %RD=[(μ_i – STD_i)/STD_i]*100, where μ_i = mean value of element *i*, STD_i = certified value of element *i* in the standard reference material.

Analyte Symbol	Sc	Be	V	Ba	Sr	Y	Zr	Cr	Co	Ni	Cu	Zn	Ga	Ge	As	Rb	Nb
Unit Symbol	ppm	ppm	ppm	ppm	ppm	ppm	ppm	ppm	ppm	ppm	ppm	ppm	ppm	ppm	ppm	ppm	ppm
Detection Limit	1	1	5	3	2	2	4	20	1	20	10	30	1	1	5	2	1
WMG-1 Meas								740	197	2430	5910	110	9		15		5
WMG-1 Cert								770	200	2700	5900	110	10.3		7		6
%RD								-3.90	-1.50	-10.00	0.17	0.00	-12.62		114.29		-16.67
NIST 694 Meas			1716														
NIST 694 Cert			1740														
%RD			-1.38														
DNC-1 Meas	31	< 1	155	109	146	16	38	270	59	260	110	70	14	2	< 5	3	2
DNC-1 Cert	31	1	148	114	145	18	41	285	54.7	247	96	66	15	1.3	0.2	4.5	3
%RD	0.00		4.73	-4.39	0.69	-11.11	-7.32	-5.26	7.86	5.26	14.58	6.06	-6.67	53.85		-33.33	-33.33
GBW 07113 Meas	5	4	< 5	505	41	46	403										
GBW 07113 Cert	5	4	5	506	43	43	403										
%RD	0.00	0.00		-0.20	-4.65	6.98	0.00										
GXR-2 Meas								40	9	< 20	80	530	34		24	78	11
GXR-2 Cert								36	8.6	21	76	530	37		25	78	11
%RD								11.11	4.65		5.26	0.00	-8.11		-4.00	0.00	0.00
MAG-1 (Depleted) Meas								90	21	40	30	130	22		8	145	14
MAG-1 (Depleted) Cert								97	20.4	53	30	130	20.4		9.2	149	12
%RD								-7.22	2.94	-24.53	0.00	0.00	7.84		-13.04	-2.68	16.67
W-2a Meas	35	< 1	284	181	199	20	91	80	42	70	110	80	16	2	< 5	18	8
W-2a Cert	36	1.3	262	182	190	24	94	92	43	70	110	80	17	1	1.2	21	7.9
%RD	-2.78		8.40	-0.55	4.74	-16.67	-3.19	-13.04	-2.33	0.00	0.00	0.00	-5.88	100.00		-14.29	1.27
SY-4 Meas	1	3	5	358	1223	119	583										
SY-4 Cert	1.1	2.6	8	340	1191	119	517										
%RD	-9.09	15.38	-37.50	5.29	2.69	0.00	12.77										

Analyte Symbol	Mo	Ag	In	Sn	Sb	Cs	La	Ce	Pr	Nd	Sm	Eu	Gd	Tb	Dy	Ho	Er
Unit Symbol	ppm	ppm	ppm	ppm	ppm	ppm	ppm	ppm	ppm	ppm	ppm	ppm	ppm	ppm	ppm	ppm	ppm
Detection Limit	2	0.5	0.2	1	0.5	0.5	0.1	0.1	0.05	0.1	0.1	0.05	0.1	0.1	0.1	0.1	0.1
WMG-1 Meas	< 2	1.6		4	3.2	< 0.5	8.6	16.7		9.3	2.3	0.7		0.4	2.7	0.5	
WMG-1 Cert	1.4	2.7		2.2	1.8	0.48	8.2	16		9	2.3	0.82		0.3	2.8	0.5	
%RD		-40.74		81.82	77.78		4.88	4.38		3.33	0.00	-14.63		33.33	-3.57	0.00	
NIST 694 Meas																	
NIST 694 Cert																	
%RD																	
DNC-1 Meas	< 2	< 0.5			1.1	< 0.5	4	8.4	1.07	4.9	1.4	0.59	2.2	0.4	3.1	0.7	2
DNC-1 Cert	0.7	0.027			0.96	0.34	3.8	10.6	1.3	4.9	1.38	0.59	2	0.41	2.7	0.62	2
%RD					14.58		5.26	-20.75	-17.69	0.00	1.45	0.00	10.00	-2.44	14.81	12.90	0.00
GBW 07113 Meas																	
GBW 07113 Cert																	
%RD																	
GXR-2 Meas	< 2	16.6	< 0.2	4	54.7	5.3	27.6	51.9		20.2	3.7	0.75	3.4	0.5	3.2		
GXR-2 Cert	2.1	17	0.252	1.7	49	5.2	25.6	51.4		19	3.5	0.81	3.3	0.48	3.3		
%RD		-2.35		135.29	11.63	1.92	7.81	0.97		6.32	5.71	-7.41	3.03	4.17	-3.03		
MAG-1 (Depleted) Meas	< 2	0.7	< 0.2	7	< 0.5	8.6	44	85.3	9.88	37	7.2	1.47	6.3	1	5.5	1	2.9
MAG-1 (Depleted) Cert	1.6	0.08	0.18	3.6	0.96	8.6	43	88	9.3	38	7.5	1.6	5.8	0.96	5.2	1.02	3
%RD		775.00		94.44		0.00	2.33	-3.07	6.24	-2.63	-4.00	-8.13	8.62	4.17	5.77	-1.96	-3.33
W-2a Meas	< 2	< 0.5			1.1	0.8	11.1	22.7		12.6	3.2	1.08		0.6	4.1	0.8	2.3
W-2a Cert	0.6	0.046			0.79	0.99	10	23		13	3.3	1		0.63	3.6	0.76	2.5
%RD					39.24	-19.19	11.00	-1.30		-3.08	-3.03	8.00		-4.76	13.89	5.26	-8.00
SY-4 Meas																	
SY-4 Cert																	
%RD																	

Analyte Symbol	Tm	Yb	Lu	Hf	Ta	W	Tl	Pb	Bi	Th	U
Unit Symbol	ppm	ppm	ppm	ppm	ppm	ppm	ppm	ppm	ppm	ppm	ppm
Detection Limit	0.05	0.1	0.04	0.2	0.1	1	0.1	5	0.4	0.1	0.1
WMG-1 Meas	0.17	1.4	0.16	1.5	0.2	< 1		13		1.2	0.6
WMG-1 Cert	0.2	1.3	0.21	1.3	0.5	1.3		15		1.1	0.65
%RD	-15.00	7.69	-23.81	15.38	-60.00			-13.33		9.09	-7.69
NIST 694 Meas											
NIST 694 Cert											
%RD											
DNC-1 Meas	0.28	2.2	0.3	1	< 0.1	< 1	< 0.1	6	< 0.4	0.2	< 0.1
DNC-1 Cert	0.38	2.01	0.32	1.01	0.098	0.2	0.026	6.3	0.02	0.2	0.1
%RD	-26.32	9.45	-6.25	-0.99				-4.76		0.00	
GBW 07113 Meas											
GBW 07113 Cert											
%RD											
GXR-2 Meas	0.25	2	0.27	6.3	0.7	3	0.6	690	< 0.4	8.4	2.8
GXR-2 Cert	0.3	2.04	0.27	8.3	0.9	1.9	1.03	690	0.69	8.8	2.9
%RD	-16.67	-1.96	0.00	-24.10	-22.22	57.89	-41.75	0.00		-4.55	-3.45
MAG-1 (Depleted) Meas	0.4	2.8	0.4	3.3	1	< 1	0.2	27	< 0.4	11.5	2.7
MAG-1 (Depleted) Cert	0.43	2.6	0.4	3.7	1.1	1.4	0.59	24	0.34	11.9	2.7
%RD	-6.98	7.69	0.00	-10.81	-9.09		-66.10	12.50		-3.36	0.00
W-2a Meas	0.3	2.2	0.28	2.4	0.4	< 1	< 0.1	8	< 0.4	2.2	0.4
W-2a Cert	0.38	2.1	0.33	2.6	0.5	0.3	0.2	9.3	0.03	2.4	0.53
%RD	-21.05	4.76	-15.15	-7.69	-20.00			-13.98		-8.33	-24.53
SY-4 Meas											
SY-4 Cert											
%RD											

Analyte Symbol	Sc	Be	V	Ba	Sr	Y	Zr	Cr	Co	Ni	Cu	Zn	Ga	Ge	As	Rb	Nb
Unit Symbol	ppm	ppm	ppm	ppm	ppm	ppm	ppm	ppm	ppm	ppm	ppm	ppm	ppm	ppm	ppm	ppm	ppm
Detection Limit	1	1	5	3	2	2	4	20	1	20	10	30	1	1	5	2	1
CTA-AC-1 Meas									< 1		70	< 30					
CTA-AC-1 Cert									2.72		54	38					
%RD											29.63						
BIR-1a Meas	43	< 1	346	8	109	14	15	370	52	160	130	70	15	2	< 5	< 2	< 1
BIR-1a Cert	44	0.58	313	7	108	16	16	382	51.4	166	126	71	16	1.5	0.44	0.25	0.6
%RD	-2.27		10.54	14.29	0.93	-12.50	-6.25	-3.14	1.17	-3.61	3.17	-1.41	-6.25	33.33			
NCS DC86312 Meas																	
NCS DC86312 Cert																	
%RD																	
NCS DC70014 Meas									25	70	2590	7050	24		1520		1
NCS DC70014 Cert									26.2	70.9	2600	7400	25.2		7900		46.9
%RD									-4.58	-1.27	-0.38	-4.73	-4.76		-80.76		-97.87
NCS DC70009 (GBW07241) Meas								30	3	< 20	980	110	16	11	71	507	
NCS DC70009 (GBW07241) Cert								30	3.7	2.8	960	100	16.5	11.2	69.9	500	
%RD								0.00	-18.92		2.08	10.00	-3.03	-1.79	1.57	1.40	
OREAS 100a (Fusion) Meas									17		180						
OREAS 100a (Fusion) Cert									18.1		169						
%RD									-6.08		6.51						
OREAS 101a (Fusion) Meas									48		450						
OREAS 101a (Fusion) Cert									48.8		434						
%RD									-1.64		3.69						
JR-1 Meas								< 20	< 1	< 20	< 10	30	16	3	18	249	15
JR-1 Cert								2.83	0.83	1.67	2.68	30.6	16.1	1.88	16.3	257	15.2
%RD												-1.96	-0.62	59.57	10.43	-3.11	-1.32

Analyte Symbol	Mo	Ag	In	Sn	Sb	Cs	La	Ce	Pr	Nd	Sm	Eu	Gd	Tb	Dy	Ho	Er
Unit Symbol	ppm	ppm	ppm	ppm	ppm	ppm	ppm	ppm	ppm	ppm	ppm	ppm	ppm	ppm	ppm	ppm	ppm
Detection Limit	2	0.5	0.2	1	0.5	0.5	0.1	0.1	0.05	0.1	0.1	0.05	0.1	0.1	0.1	0.1	0.1
CTA-AC-1 Meas							> 2000	> 3000		1130	166	49.6	141	16.6			
CTA-AC-1 Cert							2176	3326		1087	162	46.7	124	13.9			
%RD										3.96	2.47	6.21	13.71	19.42			
BIR-1a Meas	< 2	< 0.5		2	0.7	< 0.5	1	2.7	0.43	2.6	1.1	0.53	2	0.4	2.8	0.6	1.8
BIR-1a Cert	0.5	0.036		0.65	0.58	0.005	0.62	1.95	0.38	2.5	1.1	0.54	1.85	0.36	2.5	0.57	1.7
%RD				207.69	20.69		61.29	38.46	13.16	4.00	0.00	-1.85	8.11	11.11	12.00	5.26	5.88
NCS DC86312 Meas																	
NCS DC86312 Cert																	
%RD																	
NCS DC70014 Meas	> 100	17.1		> 1000	180		46.3	84.2	9.93	37.7	7.7	1.74	7.8	1.2	7	1.3	3.7
NCS DC70014 Cert	270	16.7		44700	180		45.3	87	10.8	39.9	8	1.8	7.4	1.1	6.7	1.3	3.5
%RD		2.40			0.00		2.21	-3.22	-8.06	-5.51	-3.75	-3.33	5.41	9.09	4.48	0.00	5.71
NCS DC70009 (GBW07241) Meas	> 100	2	1.3	> 1000	4.1	44.2	25.6	60.7	7.93	32.4	12.6	0.05	16.7	3.7	23.8	4.9	14.5
NCS DC70009 (GBW07241) Cert	980	1.8	1.3	1700	3.1	41	23.7	60.3	7.9	32.9	12.5	0.16	14.8	3.3	20.7	4.5	13.4
%RD		11.11	0.00		32.26	7.80	8.02	0.66	0.38	-1.52	0.80	-68.75	12.84	12.12	14.98	8.89	8.21
OREAS 100a (Fusion) Meas	24						277	465	46.2	152	24.3	3.99	23.3	4	25.4	5.5	16
OREAS 100a (Fusion) Cert	24.1						260	463	47.1	152	23.6	3.71	23.6	3.8	23.2	4.81	14.9
%RD	-0.41						6.54	0.43	-1.91	0.00	2.97	7.55	-1.27	5.26	9.48	14.35	7.38
OREAS 101a (Fusion) Meas	21						861	1400	129	394	50.5	8.73	40.2	6.1	35.4	7.3	21.1
OREAS 101a (Fusion) Cert	21.9						816	1396	134	403	48.8	8.06	43.4	5.92	33.3	6.46	19.5
%RD	-4.11						5.51	0.29	-3.73	-2.23	3.48	8.31	-7.37	3.04	6.31	13.00	8.21
JR-1 Meas	3	< 0.5	< 0.2	5	1.7	20.7	21.8	47.9	5.92	23.5	5.8	0.23	6.1	1.1	7.1	1.5	4.4
JR-1 Cert	3.25	0.031	0.028	2.86	1.19	20.8	19.7	47.2	5.58	23.3	6.03	0.3	5.06	1.01	5.69	1.11	3.61
%RD	-7.69			74.83	42.86	-0.48	10.66	1.48	6.09	0.86	-3.81	-23.33	20.55	8.91	24.78	35.14	21.88

Analyte Symbol	Tm	Yb	Lu	Hf	Ta	W	Tl	Pb	Bi	Th	U
Unit Symbol	ppm	ppm	ppm	ppm	ppm	ppm	ppm	ppm	ppm	ppm	ppm
Detection Limit	0.05	0.1	0.04	0.2	0.1	1	0.1	5	0.4	0.1	0.1
CTA-AC-1 Meas		12.3	1.33	1.7	2.9					22.9	4.1
CTA-AC-1 Cert		11.4	1.08	1.13	2.65					21.8	4.4
%RD		7.89	23.15	50.44	9.43					5.05	-6.82
BIR-1a Meas	0.25	1.8	0.25	0.6	< 0.1	< 1	< 0.1	< 5	< 0.4	0.3	< 0.1
BIR-1a Cert	0.26	1.65	0.26	0.6	0.04	0.07	0.01	3	0.02	0.03	0.01
%RD	-3.85	9.09	-3.85	0.00						900.00	
NCS DC86312 Meas										31.4	
NCS DC86312 Cert										23.6	
%RD										33.05	
NCS DC70014 Meas	0.53	3.7	0.54		0.3	205		> 10000	448		
NCS DC70014 Cert	0.57	3.3	0.5		16.2	680		27200	80.3		
%RD	-7.02	12.12	8.00		-98.15	-69.85			457.91		
NCS DC70009 (GBW07241) Meas	2.62	18.3	2.8			2350	2.1	63	680	28.5	
NCS DC70009 (GBW07241) Cert	2.2	14.9	2.4			2200	1.8	81.2	680	28.3	
%RD	19.09	22.82	16.67			6.82	16.67	-22.41	0.00	0.71	
OREAS 100a (Fusion) Meas	2.59	16.9	2.59							49.9	137
OREAS 100a (Fusion) Cert	2.31	14.9	2.26							51.6	135
%RD	12.12	13.42	14.60							-3.29	1.48
OREAS 101a (Fusion) Meas	3.22	20.2	3.03					74		34.5	417
OREAS 101a (Fusion) Cert	2.9	17.5	2.66					19		36.6	422
%RD	11.03	15.43	13.91					289.47		-5.74	-1.18
JR-1 Meas	0.71	5.3	0.8	4.7	1.6	2	1.2	21	1.4	25.9	9.1
JR-1 Cert	0.67	4.55	0.71	4.51	1.86	1.59	1.56	19.3	0.56	26.7	8.88
%RD	5.97	16.48	12.68	4.21	-13.98	25.79	-23.08	8.81	150.00	-3.00	2.48

Table E-3: Major element concentrations in duplicate/triplicate samples analyzed by the lithium metaborate/tetraborate ICP technique at Actlabs. Orig=original sample, Dup=duplicate sample, Trip=triplicate sample, %RSD=percent relative standard deviation. %RSD=(s_i/μ_i)*100, where s_i=standard deviation of the mean of the original and duplicate/triplicate analyses for element i, μ_i=mean value of element i over the original and duplicate/triplicate analyses.

Analyte Symbol	SiO2	Al2O3	Fe2O3(T)	MnO	MgO	CaO	Na2O	K2O	TiO2	P2O5	LOI	Total
Unit Symbol	%	%	%	%	%	%	%	%	%	%	%	%
Detection Limit	0.01	0.01	0.01	0.001	0.01	0.01	0.01	0.01	0.001	0.01		0.01
DS-09-75 Orig	50.52	17.93	8.21	0.162	5.54	7.83	4.13	1.16	1.137	0.23	2.51	99.36
DS-09-75 Dup	50.69	17.84	8.22	0.162	5.57	7.86	4.14	1.18	1.143	0.23	2.51	99.54
%RSD	0.24	0.36	0.09	0.00	0.38	0.27	0.17	1.21	0.37	0.00	0.00	0.13
DS-09-104 Orig	59.25	15.92	7.17	0.083	2.11	2.96	6.66	2.11	1.158	0.23	0.6	98.25
DS-09-104 Dup	59.31	15.94	7.19	0.083	2.12	2.97	6.68	2.12	1.162	0.22	0.6	98.39
%RSD	0.07	0.09	0.20	0.00	0.33	0.24	0.21	0.33	0.24	3.14	0.00	0.10
DS-09-202 Orig	72.42	14.58	1.55	0.037	0.47	1.57	7.03	0.97	0.452	0.11	0.55	99.75
DS-09-202 Dup	71.94	14.64	1.54	0.036	0.46	1.56	6.92	0.96	0.452	0.11	0.55	99.18
%RSD	0.47	0.29	0.46	1.94	1.52	0.45	1.12	0.73	0.00	0.00	0.00	0.41
DS-09-59 Orig	59.44	16.22	7.33	0.121	2.71	4.58	6.22	0.21	1.094	0.19	1.72	99.83
DS-09-205 Dup	59.36	16.39	7.51	0.123	2.69	4.6	6.2	0.21	1.103	0.16	1.59	99.95
DS-09-206 Trip	59.68	16.45	7.46	0.121	2.69	4.51	6.3	0.21	1.106	0.16	1.58	100.3
%RSD	0.28	0.73	1.25	0.95	0.43	1.04	0.85	0.00	0.57	10.19	4.79	0.24
DS-09-128 Orig	75.09	12.51	2.08	0.037	0.62	2.7	4.83	0.74	0.322	0.09	0.71	99.73
DS-09-207 Dup	75.96	12.43	2.02	0.036	0.61	2.59	4.99	0.77	0.315	0.06	0.69	100.5
DS-09-208 Trip	76.17	12.3	2	0.036	0.6	2.58	4.96	0.76	0.311	0.06	0.8	100.6
%RSD	0.76	0.85	2.05	1.59	1.64	2.54	1.73	2.02	1.76	24.74	7.99	0.47

Table E-4 (following pages): Trace element concentrations in duplicate/triplicate samples analyzed by the lithium metaborate/tetraborate ICP technique at Actlabs. Orig=original sample, Dup=duplicate sample, Trip=triplicate sample, %RSD=percent relative standard deviation. %RSD=(s_i/μ_i)*100, where s_i=standard deviation of the mean of the original and duplicate/triplicate analyses for element i, μ_i=mean value of element i over the original and duplicate/triplicate analyses.

Analyte Symbol	Sc	Be	V	Ba	Sr	Y	Zr	Cr	Co	Ni	Cu	Zn	Ga	Ge	As	Rb	Nb	Mo	Ag	In	Sn	Sb
Unit Symbol	ppm	ppm	ppm	ppm	ppm	ppm	ppm	ppm	ppm	ppm	ppm	ppm	ppm	ppm	ppm	ppm	ppm	ppm	ppm	ppm	ppm	ppm
Detection Limit	1	1	5	3	2	2	4	20	1	20	10	30	1	1	5	2	1	2	0.5	0.2	1	0.5
DS-09-75 Orig	26	1	204	917	555	20	79	170	32	80	50	110	18	2	< 5	19	8	< 2	< 0.5	< 0.2	2	0.8
DS-09-75 Dup	26	1	207	920	555	20	79	170	32	80	60	110	18	2	< 5	19	8	< 2	< 0.5	< 0.2	2	0.7
%RSD	0.00	0.00	1.03	0.23	0.00	0.00	0.00	0.00	0.00	0.00	12.86	0.00	0.00	0.00		0.00	0.00				0.00	9.43
DS-09-104 Orig	17	1	214	900	206	20	116	< 20	14	20	10	60	18	1	< 5	13	4	< 2	< 0.5	< 0.2	2	0.6
DS-09-104 Dup	17	1	216	909	206	20	119	< 20	15	20	10	60	18	1	< 5	13	5	< 2	< 0.5	< 0.2	2	0.8
%RSD	0.00	0.00	0.66	0.70	0.00	0.00	1.81		4.88	0.00	0.00	0.00	0.00	0.00		0.00	15.71				0.00	20.20
DS-09-146 Orig								40	28	60	40	130	16	1	< 5	8	9	< 2	< 0.5	< 0.2	< 1	< 0.5
DS-09-146 Dup								40	29	50	40	130	16	1	< 5	8	9	< 2	< 0.5	< 0.2	1	< 0.5
%RSD								0.00	2.48	12.86	0.00	0.00	0.00	0.00		0.00	0.00					
DS-09-202 Orig	9	2	27	354	206	31	235	< 20	3	< 20	< 10	< 30	13	1	< 5	8	18	< 2	0.9	< 0.2	2	1
DS-09-202 Dup	8	2	26	349	202	33	227	< 20	3	< 20	< 10	< 30	13	1	< 5	9	16	< 2	0.9	< 0.2	2	1.1
%RSD	8.32	0.00	2.67	1.01	1.39	4.42	2.45		0.00				0.00	0.00		8.32	8.32		0.00		0.00	6.73
DS-09-59 Orig	18	1	213	57	394	22	111	< 20	17	< 20	70	80	25	3	< 5	< 2	6	< 2	< 0.5	< 0.2	2	0.9
DS-09-205 Dup	19	< 1	213	58	395	22	114	< 20	16	20	60	80	22	3	< 5	2	6	< 2	< 0.5	< 0.2	1	1.3
DS-09-206 Trip	19	< 1	214	58	396	22	117	< 20	17	20	80	80	23	3	< 5	2	6	< 2	< 0.5	< 0.2	2	1.4
%RSD	3.09		0.27	1.00	0.25	0.00	2.63		3.46	0.00	14.29	0.00	6.55	0.00		0.00	0.00				34.64	22.05
DS-09-128 Orig	5	< 1	52	196	322	12	97	< 20	2	< 20	20	< 30	14	2	< 5	5	7	< 2	< 0.5	< 0.2	2	0.8
DS-09-207 Dup	5	< 1	55	196	328	11	100	< 20	3	< 20	< 10	< 30	13	2	< 5	6	6	< 2	< 0.5	< 0.2	2	1.6
DS-09-208 Trip	5	< 1	52	192	329	11	104	< 20	3	< 20	< 10	< 30	13	2	< 5	6	8	< 2	< 0.5	< 0.2	2	2.1
%RSD	0.00		3.27	1.19	1.16	5.09	3.50		21.65				4.33	0.00		10.19	14.29				0.00	43.72

Analyte Symbol	Cs	La	Ce	Pr	Nd	Sm	Eu	Gd	Tb	Dy	Ho	Er	Tm	Yb	Lu	Hf	Ta	W	Tl	Pb	Bi	Th	U
Unit Symbol	ppm	ppm	ppm	ppm	ppm	ppm	ppm	ppm	ppm	ppm	ppm	ppm	ppm	ppm	ppm	ppm	ppm	ppm	ppm	ppm	ppm	ppm	ppm
Detection Limit	0.5	0.1	0.1	0.05	0.1	0.1	0.05	0.1	0.1	0.1	0.1	0.1	0.05	0.1	0.04	0.2	0.1	1	0.1	5	0.4	0.1	0.1
DS-09-75 Orig	< 0.5	13.8	30.3	3.98	17.1	3.9	1.47	4.4	0.7	4.6	0.9	2.6	0.38	2.5	0.35	2.4	0.4	1	< 0.1	5	< 0.4	0.7	0.1
DS-09-75 Dup	< 0.5	12.8	27.9	3.67	16.2	3.7	1.43	4.4	0.7	4.5	0.9	2.5	0.37	2.5	0.35	2.3	0.3	< 1	< 0.1	< 5	< 0.4	0.7	< 0.1
%RSD		5.32	5.83	5.73	3.82	3.72	1.95	0.00	0.00	1.55	0.00	2.77	1.89	0.00	0.00	3.01	20.20					0.00	
DS-09-104 Orig	< 0.5	18.5	37.6	4.66	19.6	4.4	1.5	4.8	0.8	4.7	0.9	2.6	0.4	2.6	0.38	3.6	0.2	< 1	< 0.1	< 5	< 0.4	1.6	0.3
DS-09-104 Dup	< 0.5	18.4	37.7	4.72	19.7	4.4	1.46	4.8	0.7	4.6	0.9	2.6	0.39	2.6	0.38	3.6	0.2	< 1	< 0.1	< 5	< 0.4	1.6	0.3
%RSD		0.38	0.19	0.90	0.36	0.00	1.91	0.00	9.43	1.52	0.00	0.00	1.79	0.00	0.00	0.00	0.00					0.00	0.00
DS-09-146 Orig	< 0.5	13.8	28.5	3.68	15.4	3.7	1.11	4	0.7	4.1	0.9	2.4	0.37	2.4	0.33	2.9	0.4	1	< 0.1	< 5	< 0.4	1.1	0.3
DS-09-146 Dup	< 0.5	14.1	28.9	3.73	15.4	3.6	1.12	4	0.7	4.2	0.9	2.5	0.37	2.5	0.34	3	0.4	< 1	< 0.1	< 5	< 0.4	1.1	0.3
%RSD		1.52	0.99	0.95	0.00	1.94	0.63	0.00	0.00	1.70	0.00	2.89	0.00	2.89	2.11	2.40	0.00					0.00	0.00
DS-09-202 Orig	< 0.5	39.3	80.5	8.73	35.6	7.4	2.11	7.7	1.2	7.3	1.4	4.1	0.66	4.5	0.64	7.4	1.3	< 1	< 0.1	9	< 0.4	8.7	2.5
DS-09-202 Dup	< 0.5	40.7	84.7	9.13	37.7	8	2.21	8.1	1.2	7.5	1.5	4.3	0.69	4.7	0.67	7.4	1.3	1	< 0.1	10	< 0.4	9.2	2.6
%RSD		2.47	3.60	3.17	4.05	5.51	3.27	3.58	0.00	1.91	4.88	3.37	3.14	3.07	3.24	0.00	0.00			7.44		3.95	2.77
DS-09-59 Orig	< 0.5	14.8	29.4	3.88	16.5	4.1	1.42	4.7	0.8	4.9	1	2.9	0.43	2.9	0.42	3.5	0.2	1	< 0.1	14	< 0.4	1.1	0.3
DS-09-205 Dup	< 0.5	16.6	35.6	4.1	18.9	4.3	1.55	5.4	0.8	5.2	1	2.9	0.43	2.7	0.37	3.7	0.2	2	< 0.1	14	< 0.4	1.1	0.2
DS-09-206 Trip	< 0.5	15.8	33.8	3.95	18.3	4.2	1.48	5.2	0.8	5.1	1	2.9	0.41	2.5	0.35	3.7	0.2	2	< 0.1	14	< 0.4	1.1	0.2
%RSD		5.73	9.68	2.83	6.98	2.38	4.39	7.07	0.00	3.01	0.00	0.00	2.73	7.41	9.49	3.18	0.00	34.64		0.00		0.00	24.74
DS-09-128 Orig	< 0.5	22	39	4.03	13.9	2.6	0.67	2.4	0.4	2.3	0.5	1.4	0.23	1.7	0.25	3.2	0.5	< 1	< 0.1	< 5	< 0.4	8.5	2.1
DS-09-207 Dup	< 0.5	24.7	45.8	4.23	15.8	2.8	0.7	2.7	0.4	2.3	0.5	1.4	0.21	1.4	0.21	3.3	0.5	2	< 0.1	< 5	< 0.4	8.6	2.1
DS-09-208 Trip	< 0.5	25.2	46.3	4.4	16.1	2.9	0.72	2.7	0.4	2.4	0.5	1.5	0.22	1.5	0.22	3.7	0.6	2	< 0.1	< 5	< 0.4	8.9	2.2
%RSD		7.18	9.33	4.39	7.81	5.52	3.61	6.66	0.00	2.47	0.00	4.03	4.55	9.96	9.18	7.78	10.83	0.00				2.40	2.71

E.2. Data Quality

During lithium metaborate/tetraborate fusion inductively coupled plasma (ICP) analysis at Actlabs, five standard reference materials (SRM) were run to evaluate the accuracy of major element analyses. In most cases, the percent relative difference (%RD) between the measured and certified values of each major element is less than 10%, indicating good accuracy overall. However, for standards in which certain major element contents approach the limit of detection, the %RDs between the measured and certified values of these elements are greater than 10%. These elements include K_2O in two SRMs (14%, 33%), MnO in one SRM (12%), MgO in one SRM (13%) and P_2O_5 in four SRMs (15-60%). Because four SRMs with certified P_2O_5 contents between 0.05-0.131 wt. % have high %RDs between measured and certified values, measurements of P_2O_5 that are less than or equal to 0.131 wt. % may not be accurate. This applies to all samples of granodiorite, feldspar porphyry (except for sample #177) and rhyolitic dykes.

The trace element concentrations of sixteen standard reference materials were analyzed during lithium metaborate/tetraborate fusion inductively coupled plasma (ICP) analysis at Actlabs. Since each standard reference material was analyzed for a select suite of trace elements, each trace element was analyzed in between 5 to 12 standard reference materials. The majority of %RDs between measured and certified values of trace elements are less than 10%, indicating good accuracy overall. For several trace elements, the %RDs between measured and certified values are above 10% in some standard reference materials. These high %RDs occur when the certified value of the element approaches the limit of detection, and the majority of SRM analyses for each of these elements have %RDs that are less than 10%. For Sn, Sb and Ge, the %RDs between

measured and certified values of the majority of SRM analyses are greater than 10% for certified values equal to and less than 3.6 ppm, 3.1 ppm and 1.88 ppm, respectively. Therefore, most Sn measurements, all Sb measurements and several Ge measurements in the dataset may be inaccurate. Because the %RDs between certified and measured values of Lu range from 13-24% in seven SRMs with 0.21-2.66 ppm Lu, Lu values in the dataset (0.21-1.03 ppm) may not be accurate. Ta values may also have decreased accuracy since four SRMs with 0.5-1.86 ppm Ta have %RDs between 14-60%. The %RDs between certified and measured values in Nb in SRMs suggest that Nb values in the range of 3-4 ppm may have poor accuracy. Samples containing 4 ppm Nb or less include all gabbro samples, some samples from andesitic dykes and one basaltic-andesitic dyke sample.

Several duplicate samples were analyzed during lithium metaborate/tetraborate fusion inductively coupled plasma (ICP) analysis at Actlabs, including duplicates of samples DS-09-75, -104, -146 and -202 and blind duplicates and triplicates of samples DS-09-59 and -128. Sample DS-09-146 was analyzed for trace elements only, while all other duplicate and triplicate samples were analyzed for both major and trace elements. The percent relative standard deviations (%RSD) between original and duplicate/triplicate analyses of major elements are less than 10%, indicating good precision overall, although the %RSD between the original, duplicate and triplicate analyses of P_2O_5 for DS-09-128 is 25%. Trace element analyses appear to have good precision overall, since the majority of percent relative standard deviations (%RSD) between original and duplicate/triplicate analyses of trace elements are less than 10%. Several trace elements (Co, Ni, Cu, Rb, Nb, Sn, Ta, W, U) have one or two duplicate/triplicate analyses with %RSD above 10%, ranging from 11-35%. In general, when the %RSD between original and

duplicate/triplicate analyses is greater than 10%, the measured value approaches the limit of detection.

XRF analysis was carried out on selected samples for the purpose of testing the extent of sample dissolution during lithium metaborate/tetraborate fusion inductively coupled plasma (ICP) analysis at Actlabs. Elements that may not be completely released from minerals such as zircon during sample dissolution include Zr, Y and Nb. Twenty samples, including 14 felsic rocks and 6 mafic to intermediate rocks, were analyzed at Memorial University of Newfoundland using the X-ray fluorescence (XRF) technique. The concentrations of Y obtained by the ICP method are up to 10% greater than the concentrations measured by XRF analysis, indicating that the ICP techniques are not producing artificially low concentrations of Y. In half of the samples, Nb concentrations measured by XRF are 5-24% lower than Nb concentrations measured by ICP. In the other half of the samples, Nb concentrations measured by XRF are 0.1-31% higher than those measured by ICP. The Zr concentrations measured using the ICP technique are, on average, 12% lower than those measured by the XRF method. Although the Zr data and some of the Nb data are lower when measured by ICP than by XRF, the 10-20% difference between XRF and ICP values of these elements can be attributed to differences in machine calibration, and sample dissolution appears to be complete.

E.3. Field of analytical uncertainty surrounding Nb/Th

This section describes the method used to determine the field of analytical uncertainty surrounding Nb/Th, and thus the boundaries of the "non-arc", "arc" and "transitional arc" fields on plots of Nb/Th in this study. The mean % relative difference

(%RD) between measured and certified values in standard reference materials (absolute values) was added to the mean % relative standard deviation (%RSD) between original and duplicate values to find the total uncertainty surrounding Nb and Th. The mean %RD and mean %RSD were calculated using only mafic-to-intermediate standards and duplicates/triplicates, respectively. These are standards WMG-1 (mineralized gabbro), W-2a (diabase) and BIR-1a (basalt), duplicates of samples DS-09-75, 104, 146 and duplicate and triplicate analyses of sample DS-09-59. As well, the %RD between the measured and certified values of Th for standard BIR-1a was not included in the mean calculation because the certified value for Th in BIR-1a (0.03 ppm) is below the limit of detection for Th (0.1 ppm). The sum of the mean %RD and mean %RSD for each element yielded estimates of 9.9% uncertainty surrounding Nb and 8.7% uncertainty surrounding Th. These values were used to calculate the maximum and minimum values of Nb and Th, within uncertainties, for each measured value. These limits of uncertainty were used to calculate the maximum and minimum Nb/Th values for each sample. If the maximum Nb/Th value of a given sample, within uncertainty, is less than 8.4, the Nb/Th value of the primitive mantle (Sun and McDonough, 1989), then the sample is considered to have a negative Nb anomaly. The "Transitional arc" field on plots of Nb/Th in this study represents the field of analytical uncertainty surrounding Nb/Th, which is defined by samples with Nb/Th values that are less than 8.4, but are greater than 8.4 at the limit of uncertainty, or vice versa.

APPENDIX F: METHODS OF ANALYSIS FOR ND ISOTOPIC DATA

Isotopic data were obtained at the TIMS laboratory at Memorial University of Newfoundland. A mixed $^{150}Nd/^{149}Sm$ spike was added to whole rock powders and they were dissolved in Teflon beakers using a solution of HF-HNO_3. After five days of digestion, the solutions were dried down on a hot plate and received 6N HCl. After the solutions were evaporated to dryness, 1 ml of 2.5N HCl was added to each sample and they were loaded on cationic exchange columns. The collected REE fractions were purified and loaded on secondary columns to isolate Sm and Nd. A multicollector Finnigan MAT 262 mass spectrometer was used in static mode to measure Sm and Nd concentrations and in dynamic mode to obtain Nd isotopic compositions. Nd isotopic ratios were normalized to $^{146}Nd/^{144}Nd=0.7219$ (O'Nions *et al.,* 1977) and corrected for the deviation from JNdi-1 $^{143}Nd/^{144}Nd =0.512115$ (Tanaka *et al.,* 2000). Replicates of the standard gave a mean value of $^{143}Nd/^{144}Nd = 0.512096 \pm 0.000007$ (2σ, n=11) for samples #74, 82, 89 and 141 and $^{143}Nd/^{144}Nd = 0.512091 \pm 0.000014$ (2σ, n=37) for samples #105, 181 and 184. Errors on the $^{147}Sm/^{144}Nd$ ratio are estimated to be less than 0.1%, and Nd isotopic compositions have <0.002% errors.

Epsilon Nd (ϵNd) values were calculated using an age of 580 Ma and a present-day chondritic uniform reservoir (CHUR) composition of $^{143}Nd/^{144}Nd = 0.512638$ (Goldstein *et al.* 1984) and $^{147}Sm/^{144}Nd = 0.1967$ (Jacobsen and Wasserburg, 1980). Model ages (T_{DM}), which represent the time of extraction from the depleted mantle, were calculated using the model of DePaolo (1981). Alternate model ages (T_{DM2}) were calculated based on a linear evolution for a mantle with a present-day ϵNd value of +10,

separated from the CHUR at 4.55 Ga, using the depleted mantle $^{147}Sm/^{144}Nd$ and $^{143}Nd/^{144}Nd$ values of Peucat *et al.* (1988).

APPENDIX G: GEOLOGY OF THE AVALON ZONE IN NEWFOUNDLAND

Tables G-1 to G-6, on the following pages, provide age control data and brief lithological descriptions of the main rock units and epithermal alteration systems in the Avalon Zone in Newfoundland, as summarized schematically in Figure 5.1.

Table G-1: Avalon Peninsula		
Unit	Age Control (Ma)	Dominant lithology
Signal Hill Group	younger than 565 ± 3 (G. Dunning, unpublished data; Benus, in King, 1988)	Molasse-like deposits with tuff interbeds.
St. John's Group	younger than 565 ± 3 (G. Dunning, unpublished data; Benus, in King, 1988)	Shallowing-upward, basinal-deltaic siliciclastic rocks with tuff interbeds.
Conception Group	ca. 580 (tuff beds in tillite in Gaskier's Formation, Bowring *et al.,* 2003), 565 ± 3 (ash bed in Mistaken Point Formation, G. Dunning, unpublished data; Benus, in King, 1988)	Turbidity flows and intermittent felsic pyroclastic activity.
Horse Cove Complex	581.7 ± 1.9 (rhyolitic dyke), 580.6 ± 2 (feldspar porphyry), 578.4 ± 2.3 (andesitic dyke) (this study)	Feldspar porphyry, fine-grained diorite and gabbro, and a mafic to felsic dyke swarm.
Wych Hazel Pond Complex	582 ± 1.5 (ash-flow tuff, Sparkes, 2005), 585 ± 5 (Fowler's Road Porphyry, Sparkes, 2005)	Subaerial and submarine siliciclastic rocks with tuff interbeds, intercalated with mafic volanic rocks. Hosts minor feldspar porphyry intrusions.
Manuels Volcanic Suite	584 ± 1 (Farmer's Field Rhyolite, O'Brien *et al.,* 2001, modified by Sparkes, 2005), 582 ± 4 (ash-flow tuff, Sparkes, 2005)	Felsic volcanic rocks.
Peak Tuff	606 ± 3 (Krogh *et al.,* 1988; O'Brien *et al.,* 2001)	Felsic volcanic rocks.
White Mountain Volcanic Suite	616 ± 2 (Sparkes, 2005)	Felsic volcanic rocks.
Turbidites	621 +5/-4 (tuff bed near base of succession, Israel, 1998)	Marine siliciclastic strata, dominated by turbidity flows, with rhyolite tuff interbeds.
White Hills Intrusive Suite	625 ± 2.5 (quartz-feldspar porphyry, Sparkes, 2005), 623.5 ± 3.5 (monzonite, Sparkes, 2005), 619 ± 3 (granite, Sparkes, 2005), 614 ± 2 (granite, Sparkes, 2005)	Monzonite, quartz-feldspar porphyry, granite.
Holyrood Intrusive Suite	640 ± 2 (monzonite; O'Brien *et al.,* 2001), 620 ± 2 (Krogh *et al.,* 1988), 623 ± 3 (granite; O'Brien *et al.,* 2001), 631 ± 2 (quartz-feldspar porphyry; Krogh *et al.,* 1988), 622.5 ± 1.3 (granite, Sparkes, 2005), 622 ± 2 (Butler's Pond Porphyry, Sparkes *et al.,* 2002)	Granite, monzonite, quartz-feldspar porphryry.
Hawke Hills Tuff	727 ± 7 (Israel 1998)	Felsic and minor intermediate pyroclastic flows and breccia.

Table G-2: Bonavista Bay - Bonavista Peninsula		
Unit	Age Control (Ma)	Dominant lithology
Signal Hill Group	565 ± 3 (ash bed in Mistaken Point Formation, G. Dunning, unpublished data; Benus, in King, 1988)	Molasse-like deposits with tuff interbeds.
St. John's Group	565 ± 3 (ash bed in Mistaken Point Formation, G. Dunning, unpublished data; Benus, in King, 1988)	Shallowing-upward, basinal-deltaic siliciclastic rocks with tuff interbeds.
Musgravetown Group	570 +5/-3 (rhyolite from base of succession, O'Brien *et al.,* 1989); 567 +5/-4 (Bull Arm Rhyolite, G. Dunning, unpublished data)	Marine to terrestrial volcano-sedimentary succession.
Louil Hills Intrusive Suite	572 +3/-2 (riebeckite granite, O'Brien *et al.,* 1989)	Gabbro, diabase dykes, granite and related felsic dykes.
Connecting Point Group	610 ± 1 (tuff near middle of succession, G. Dunning, unpublished, 1990, in Dec *et al.,* 1992)	Marine siliciclastic rocks, including shale-rich distal turbidites.
Love Cove Group	620 ± 2 (rhyolite, O'Brien *et al.* 1989); also two younger ages: 585 ± 5, 591 +6/-4 (G. Dunning, unpublished data, 1992)	Pyroclastic volcanic rocks, mostly intermediate, and arenaceous deposits.

Table G-3: Burin Peninsula		
Unit	Age Control (Ma)	Dominant lithology
Long Harbour Group	568 ± 5 (rhyolite from base of succession, Tucker, unpublished data, 1991, O'Brien *et al.,* 1994), 552 ± 3 (rhyolite from top of succession, Tucker, unpublished data, O'Brien *et al.,* 1994)	Subaerial bimodal volcanic rocks, marine siliciclastic rocks and redbeds.
Musgravetown Group	570 +5/-3 (rhyolite from base of succession, O'Brien *et al.,* 1989), 567 +5/-4 (Bull Arm Rhyolite, G. Dunning, unpublished data)	Marine to terrestrial volcano-sedimentary succession.
Swift Current, Cape Roger Mountain and Burin Knee Granites and associated intrusions	ca. 570-580 (in O'Brien *et al.,* 1999)	Granite, diorite, gabbro
Marystown Group	ca. 572 (pyroclastic rocks, Ketchum, unpublished data, 1998, in O'Brien *et al.* 1999), 608 +20/-7 (ash-flow tuff, Krogh *et al.* 1988)	Mafic to felsic subaerial flows and volcanic rocks.
Powder Horn Intrusive Suite	603 ± 2 (gabbro, Hinchey, 2002), 605 ± 5 (granite, Hinchey, 2002)	Medium- to coarse-grained gabbro to diorite.
Connecting Point Group	610 ± 1 (tuff near middle of succession, G. Dunning, unpublished, 1990, in Dec *et al.,* 1992)	Marine siliciclastic rocks, including shale-rich distal turbidites.
Burin Group	763 ± 2 (pegmatitic gabbro, Krogh *et al.,* 1998)	Submarine mafic volcanic rocks, gabbroic sills, tuff and sedimentary rocks.

Table G-4: Connaigre Peninsula		
Unit	Age Control (Ma)	Dominant lithology
Long Harbour Group	568 ± 5 (rhyolite from base of succession, Tucker, unpublished data, 1991, O'Brien *et al.,* 1994), 552 ± 3 (rhyolite from top of succession, Tucker, unpublished data, O'Brien *et al.,* 1994)	Subaerial bimodal volcanic rocks, marine siliciclastic rocks and redbeds.
Hardy's Cove Granite	568 ± 2 (granite, G. Dunning, unpublished data, 1994, in O'Brien *et al.,* 1995)	Granite, granodiorite and diorite.
Harbour Breton Intrusive Suite	570 ± 3 (granite, G. Dunning unpublished data, 1994, in O'Brien *et al.,* 1995)	Granite, porphyritic granite and microgranite.
Grole Intrusive Suite	567 ± 3 (quartz diorite, Tucker, unpublished data; O'Brien *et al.,* 1994)	Quartz diorite, diorite and gabbro.
Simmons Brook Intrusive Suite	621 ± 3 (granodiorite, Tucker, unpublished data; O'Brien *et al.,* 1994)	Tonalite, granodiorite and mafic and intermediate intrusive rocks.
Connaigre Bay Group	626 ± 3 (rhyolite, Tucker, unpublished data; O'Brien *et al.,* 1994)	Marine siliciclastic sedimentary rocks, mafic volcanic flows and pyroclastic rocks.
Furby's Cove Intrusive Suite	673 ± 3 (granite, Tucker, unpublished data, 1991; O'Brien *et al.,* 1994)	Co-magmatic granite and gabbro, and granitic and diabase dykes.
Tickle Point Formation	682 ± 3 (rhyolite, Tucker, unpublished data, O'Brien *et al.,* 1994), 682.8 ± 1.6 (rhyolite, Swinden and Hunt, 1991)	Rhyolite flows and pyroclastic rocks, mafic volcanic rocks, siliclastic and carbonate sedimentary rocks.

Table G-5: Cinq Cerf Bay - Grey River		
Unit	Age Control (Ma)	Dominant lithology
Grey River Tuff	544 ± 5 (felsic tuff, Dunning and O'Brien, 1989)	Felsic tuffs.
Intermediate and mafic intrusions	566 +2/-7 (gabbroic dyke, Dubé *et al.*, 1998), 565 ± 5 (intermediate dyke, Dubé *et al.*, 1998), 557 +14/-5 (gabbro/diorite, Valverde-Vaquero *et al.*, 2006)	Gabbro and diorite.
Roti Intrusive Suite	578 ± 10 (granodiorite, O'Brien *et al.*, 1991), 576 ± 2, 574 ± 3, 567 ± 2 (quartz-feldspar porphyry, Dubé *et al.*, 1998), 563 ± 4 (tonalite, Dunning and O'Brien, 1989)	Granodiorite, tonalite, quartz-feldspar porphyry.
Whittle Hill Sandstone - Third Pond Tuff succession	583 +7/-3 (lapilli tuff, Dubé *et al.*, 1998), 585 ± 5 (fine-grained intrusive rock or flow/tuff, Dubé *et al.*, 1998)	Conglomerate grading upward into sandstone and distal turbidites with felsic volcanic layers (Whittle Hill Sandstone) overlain by submarine mafic and felsic tuffs (Third Pond Tuff).
Granodiorite	584 +7/-6 (Valverde-Vaquero *et al.*, 2006)	Granodiorite.
Cinq Cerf Gneiss	675 +12/-11 (granitic orthogneiss, Valverde-Vaquero *et al.*, 2006)	Amphibole-rich banded gneiss, quartzo-feldspathic gneiss and schist, granitic orthogneiss and deformed mafic dykes.
Grey River Gneiss	686 +33/-15 (migmatite, Dunning and O'Brien, 1989)	Hornblende diorite migmatite, amphibolite, orthogneiss, migmatized schists.

Table G-6: Epithermal Alteration Systems in the Avalon Zone in Newfoundland			
System	Alteration Style	Age Control (Ma)	Host Rocks
Hickey's Pond and Stewart Prospects	high-sulphidation	ca. 572 and younger (Ketchum, unpublished data, 1998, in O'Brien *et al.*, 1999)	Marystown Group
Hope Brook Mine	high-sulphidation	574-578 (Dubé *et al.*, 1995)	Whittle Hill Sandstone - Third Pond Tuff succession, Roti Intrusive Suite
Steep Nap Prospect	low-sulphidation	586 and younger, but older than ca. 542 Ma, the Neoproterozoic-Cambrian boundary (Sparkes, 2005)	Manuels Volcanic Suite
Oval Pit Mine	high-sulphidation	585-580.5 (Sparkes, 2005)	Manuels Volcanic Suite
Lodestar Prospect	magmatic hydrothermal breccia	ca. 605-603 (Hinchey, 2002)	Adjacent to intrusive contact of the Powder Horn Intrusive Suite into the Connecting Point Group